UNIVERSIDAD DE CANTABRIA

La radiación del fondo cósmico de microondas a gran escala y la teoría de picos

por

Airam Marcos Caballero

Memoria presentada para optar al título de
Doctor en Ciencias Físicas

en el

Instituto de Física de Cantabria

Abril 2017

Declaración de Autoría

Enrique Martínez González, doctor en ciencias físicas y profesor de investigación del Consejo Superior de Investigaciones Científicas,

y

Patricio Vielva Martínez, doctor en ciencias físicas y profesor contratado doctor de la Universidad de Cantabria,

CERTIFICAN que la presente memoria,

La radiación del fondo cósmico de microondas a gran scala y la teoría de picos

ha sido realizada por **Airam Marcos Caballero** bajo nuestra dirección en el Instituto de Física de Cantabría, para optar al título de Doctor por la Universidad de Cantabria. Consideramos que esta memoria contiene aportaciones científicas suficientes para constituir la Tesis Doctoral del interesado.

En Santander, a 7 de abril de 2017,

Enrique Martínez González

Patricio Vielva Martínez

Agradecimientos

Ciertamente, esta tesis no podría haber sido posible sin la ayuda, apoyo, trabajo y consejos de mis dos directores, Enrique y Patricio. Gracias a ellos he podido adentrarme en el mundo de la cosmología, incluso en regiones que van mucho más allá de lo presentado en esta tesis. Muchas gracias por todo este tiempo en el que no he dejado de aprender.

No sería justo empezar estos agradecimientos sin mencionar también a los organismos que me han dado cobijo y apoyo económico: el Instituto de Física de Cantabria, la Universidad de Cantabria, el Consejo Superior de Investigaciones Científicas y el Ministerio de Economía y Competitividad. Detrás de todas estas instituciones se encuentra la imprescindible aportación de los contribuyentes, los mecenas de nuestro tiempo que permiten los avances científicos. En parte, esta tesis también es de todos ellos.

Por supuesto, también tengo que agradecer a mis compañeros (no solo de despacho) por todos estos años. Las discusiones y debates, científicos o no, son muchas veces la base y el germen de nuevas ideas y perspectivas. Gracias a Raúl por aguantar mis desvaríos y aportar ese contrapeso que equilibria la balanza del método científico, cuestionando hasta el más pequeño detalle. A Biuse, tambien conocida por ser la reina de Altamira, por ser fuente de inspiración, eficiencia y, sobretodo ahora que es madre, todo un ejemplo de mujer científica. Tambíen he apredido muchas cosas de David, al que cariñosamente apodo "el ingeniero". Gracias por enseñarme como funcionan todos esos cacharros. Cómo olvidar en estas líneas a "el gran chorbo", Luis Fernando, que nos dejó el legado de las generaciones anteriores de doctorandos. También a Andrés Curto, expatriado en "la pérfida Albión", donde parece que ha construido su nuevo hogar (qué gran científico pierde este país).

No solo de ciencia vive el hombre, y por ello mi más cariñoso agradecimiento es para mi familia y amigos. Empezando por mis abuelos, que han sido y son un gran ejemplo de vida. A mi madre, por ser ese gran apoyo imprescindible e incondicional, y a mi padre, por inculcarme la curiosidad por la ciencia desde pequeño. A mi hermana, que no por ser la única que tengo deja de ser la mejor. También a Carmen, Fernando y Vero, por hacer más grande esta familia y compartir muchos buenos momentos juntos. También tengo que agradecer a muchos amigos y personas cercanas, a los que no nombro personalmente por el miedo a dejarme alguno de ellos. Gracias a todos ellos. Y, cómo no, a Andrea, por estar siempre ahí, dándome todo su apoyo y compartiendo conmigo todos los buenos y los malos momentos.

UNIVERSIDAD DE CANTABRIA

The Cosmic Microwave Background radiation at large scales and the peak theory

by

Airam Marcos Caballero

A thesis submitted in partial fulfillment for the degree of
Doctor of Philosophy in Physics

in the

Instituto de Física de Cantabria

April 2017

Abstract

In this PhD thesis, the large-scale anisotropies in the Cosmic Microwave Background (CMB) radiation are analysed. In particular, the theory of peaks in a Gaussian random field on the sphere is reviewed and applied to the CMB temperature and polarization fields, including the eccentricity of the peaks in the formalism. Previous to the characterization of the large-scale peaks, a general study of the derivatives up to second order of the *Planck* CMB temperature data is performed at different scales, identifying the most significant deviations from the standard cosmological model prediction. A more detailed anaylsis is applied to the largest peaks on the CMB temperature and the Cold Spot. The formalism of the multipolar profiles is used to characterize the shape and geometry of those peaks. Finally, the large-scale anisotropies produced by the Integrated Sachs-Wolfe (ISW) effect are analysed in the last two chapters. In the first one, the claim that the Cold Spot can be originated by the imprint on the CMB temperature of a supervoid is analysed, considering different dark energy models and void geometries. On the other hand, in the last chapter, the ISW effect is detected from the cross-correlation between the CMB temperature and large-scale structure tracers. In particular, the redshift distribution and angular power spectrum of the NRAO VLA Sky Survey (NVSS) are studied in order to have a theoretical model of the angular cross-power spectrum between the CMB temperature and this galaxy catalogue. Some results presented in the latter chapter are included in the publications of the *Planck* collaboration on the integrated Sachs-Wolfe effect.

Contents

List of Figures

List of Tables

Abbreviations

BAO	Baryon Acoustic Oscillations
BICEP	Background Imaging of Cosmic Extragalactic Polarization
BOOMERanG	Balloon Observations Of Millimetric Extragalactic Radiation and Geomagnetics
CAMB	Code for Anisotropies in the Microwave Background
CBI	Cosmic Background Imager
CDM	Cold Dark Matter
CENSORS	Combined EIS-NVSS Survey Of Radio Sources
CIB	Cosmic Infrared Background
CMB	Cosmic Microwave Background
COBE	Cosmic Background Explorer
CPL	Chevallier-Polarski-Linder
CS	Cold Spot
CνB	Cosmic Neutrino Background
DASI	Degree Angular Scale Interferometer
DMR	Differential Microwave Radiometer
EIS	ESO Imaging Survey
ESA	European Space Agency
ESO	European Southern Observatory
FIRAS	Far-InfraRed Absolute Spectrometer
FLRW	Friedmann-Lemaître-Robertson-Walker
FWHM	Full Width at Half Maximum
GR	General Relativity
GUT	Grand Unified Theories
HEALpix	Hierarchical Equal Area isoLatitude Pixelization

HFI	High Frequency Instrument
HOD	Halo Occupation Distribution
ISW	Integrated Sachs-Wolfe
kSZ	kinetic Sunyaev-Zel'dovich
LFI	Low Frequency Instrument
LSS	Large Scale Structure
LTB	Lemaître-Tolman-Bondi
MASTER	Monte Carlo Apodized Spherical Transform Estimator
MAXIMA	Millimeter-wave Anisotropy eXperiment IMaging Array
MSSM	Minimal Supersymmetric Standard Model
NRAO	National Radio Astronomy Observatory
NVSS	NRAO VLA Sky Survey
OV	Ostriker-Vishniac
SSDS	Sloan Digital Sky Survey
SMHW	Spherical Mexican Hat Wavelet
SW	Sachs-Wolfe
SZ	Sunyaev-Zel'dovich
TH	Top Hat
VLA	Very Large Array
WIMP	Weakly Interacting Massive Particle
WISE	Wide-field Infrared Survey Explorer
WMAP	Wilkinson Microwave Anisotropy Probe
ΛCDM	CDM model with cosmological constant

Physical Constants

Speed of light	c	=	$2.997\ 924\ 58 \times 10^{8}$ m s^{-1} (exact)
Gravitational constant	G	=	$6.674\ 08(31) \times 10^{-11}$ m^{3} kg^{-1} s^{-2}
Planck constant	h	=	$6.626\ 070\ 040(81) \times 10^{-34}$ J s
Boltzmann constant	k	=	$1.380\ 648\ 52(79) \times 10^{-23}$ J K^{-1}
Stefan-Boltzmann constant	σ	=	$5.670\ 367(13) \times 10^{-8}$ W m^{-2} K^{-4}
Wien's displacement law constant	b	=	$2.897\ 7729(17) \times 10^{-3}$ m K
Electron mass	m_e	=	$9.109\ 383\ 56(11) \times 10^{-31}$ kg
Proton mass	m_p	=	$1.672\ 621\ 898(21) \times 10^{-27}$ kg
Planck length	L_p	=	$1.616\ 229(38) \times 10^{-35}$ m
Planck mass	M_p	=	$2.176\ 470(51) \times 10^{-8}$ kg

Symbols

$g_{\mu\nu}$	the space-time metric
$G_{\mu\nu}$	Einstein tensor
R	Ricci scalar
$T_{\mu\nu}$	Stress-energy tensor
U_μ	Velocity vector
Λ	Cosmological constant
Λ_{vac}	Vacuum cosmological constant
a	Scale factor
K	Curvature of the spatial sections
ρ	Energy density
ρ_γ	Photon energy density
ρ_ν	Neutrino energy density
ρ_Λ	Cosmological constant energy density
ρ_{de}	Dark energy density
ρ_c	Critical energy density
p	Pressure
w	Equation of state parameter
H	Hubble function
H_0	Hubble parameter
h	Reduced Hubble parameter ($H_0/100$ km s^{-1}Mpc^{-1})
Ω	Total density parameter
Ω_K	Curvature density parameter
Ω_γ	Photon density parameter
Ω_ν	Neutrino density parameter
Ω_Λ	Cosmological constant density parameter

Ω_m	Matter density parameter
Ω_b	Baryon density parameter
T	Temperature
T_{CMB}	CMB temperature
$T_{\mathrm{C}\nu\mathrm{B}}$	CνB temperature
T_γ	Photon temperture
T_ν	Neutrino temperture
N_{eff}	Effective number of neutrinos
V	Volume
S	Entropy
Φ	Newtonian potential
Ψ	Curvature of spatial sections
$\mathcal{R}$	Comoving curvature
δ_{ij}	Kronecker delta
h_{ij}	Tensor perturbations
$\delta\rho$	Density perturbations
$\delta\phi$	Inflaton perturbations
ζ	Spatial curvature of constant density hypersurfaces
$P_\zeta(k)$	Scalar power spectrum
$\Delta^2_\zeta(k)$	Dimensionless scalar power spectrum
A_s	Amplitude of the scalar perturbations
n_s	Spectral index of the scalar perturbations
α_s	Running of the spectral index n_s
A_t	Amplitude of the tensor perturbations
n_t	Spectral index of the tensor perturbations
k_0	Pivot wavenumber
r	tensor-to-scalar ratio A_t/A_s
ϕ	Inflaton
$V(\phi)$	Inflaton potential
N	Number of e-folds
$\varepsilon(\phi)$	Slow-roll parameter (slope of $V(\phi)$)
$\eta(\phi)$	Slow-roll parameter (flatness of $V(\phi)$)
$Y_{\ell m}(\mathbf{n})$	Spherical harmonics

$a_{\ell m}$	Spherical harmonic coefficients for temperature
$e_{\ell m}$	Spherical harmonic coefficients of E-mode polarization
$b_{\ell m}$	Spherical harmonic coefficients of B-mode polarization
C_ℓ	Angular power spectrum
Q and U	Stokes parameters for linear polarization
$E(\mathbf{n})$	Gradient component of the polarization
$B(\mathbf{n})$	Curl component of the polarization
Θ	Intrinsic CMB temperature fluctuations
v_γ	Photon fluid velocity
s_*	Sound horizon at the recombination epoch
σ_T	Total Thomson cross section
τ	Reionization optical depth
$\phi(\mathrm{n})$	Projected gravitational potential
$f_K(r)$	Transverse comoving distance
T_B	Brightness temperature
$B(\nu)$	Spectral radiance
$\eth$ and $\eth^*$	Spin raising and lowering operators
N_{ext}	Number of extrema
ν	Peak height
κ	Mean curvature
η	Gradient spinor
ϵ	Eccentricity tensor
σ_ν, σ_κ, σ_η and σ_ϵ	Standard deviation of the peak variables
b_ν, b_κ, b_η and b_ϵ	Peak biases
$X_m(\theta)$	Multipolar profiles
$P_\ell^m(\theta)$	Associated Legendre polynomials
Q_r and U_r	Stokes parameters in polar coordinates
w_ℓ	Fourier coefficients of the filter
b_ℓ	Fourier coefficients of the beam
N_{side}	HEALpix resolution parameter
z	Redshift
m	halo mass
R	Smoothing scale

$\bar{\rho}$	Mean matter density of the Universe
δ	Matter density fluctuations
δ_h	overdensity of halos
δ_g	overdensity of galaxies
$\delta_c(z)$	Critical overdensity for the spherical collapse at $z = 0$
$D(z)$	Linear growth factor of matter perturbations
$D(z)$	Linear growth suppression factor of matter perturbations
$P(k)$	Linear matter power spectrum at $z = 0$
$W_R(k)$	Fourier transform of the smoothing function
σ_R^2	Variance of the matter perturbations smoothed at the scale R
σ_m^2	σ_R^2 for $R = (3m/4\pi\bar{\rho})^{1/3}$
$n(m, z)$	halo mass function
$f(\nu)$	Multiplicity function
$b(m, z)$	Halo-matter bias
$b_g(z)$	Galaxy-matter bias
$M_{\min}$	Halo minimum mass in a catalogue
$N_g(m)$	Number of galaxies in a halo of mass m
$\Delta_\ell^t(k)$	Temperature transfer function
$\Delta_\ell^g(k)$	Galaxy transfer function

Chapter 1

Introduction

The standard cosmological model provides an accurate description of the evolution and shape of the Universe at large scales. This model is based on the cosmological principle, which states that the statistical properties of the Universe do not depend on the spatial location. Observations of the cosmic microwave background radiation and the large-scale structure of the Universe confirm that this statement is valid at cosmological distances.

The expansion of the Universe observed by measuring the radial velocities of the galaxies was the first evidence that, in the past, it was in an extremely hot and dense state. Measurements of the primordial abundances of the lightest atoms agree with the scenario in which they were formed in the early stages of the Universe, when the temperature was high enough to trigger nuclear reactions. The fact of having higher density and temperature at early times were confirmed by the discovery of the radiation emitted at the recombination epoch, when the free electrons and nuclei formed neutral atoms. This radiation is redshifted to the microwave frequencies due to the expansion of the Universe and forms the Cosmic Microwave Background (CMB) we observe today.

The evolution of the Universe at large scales is determined by applying the cosmological principle to the general relativity theory. The resulting equations, called Friedmann equations, relates the dynamics of the Universe with the energy content. However, the high isotropy observed in the CMB radiation is not explained by the current energetic components in the Universe. In the standard picture, a phase of an accelerated expansion taking place in the very early Universe is proposed to explain the large scale homogeneity, as well as the flatness geometry of the spatial sections. The mechanism causing this sudden expansion, which is called inflation, is supposed to be sourced by at least one scalar field, whose primordial quantum fluctuations are the seeds of the Large Scale Structure (LSS) of the Universe.

In this introductory chapter, the details of the standard cosmological model, including a summary of the energetic components present at each epoch, are introduced in the Section 1.1, whereas the basis of the inflationary mechanism are presented in Section 1.2. Finally, the physics of the cosmic microwave background is introduced in the Section 1.3.

1.1 The standard cosmological model

In the next subsections, the dynamics of the Universe is studied in the light of the Friedmann equations and the evolution of the cosmic fluid. The different energetic components which form the Universe according to the cosmological standard model are also reviewed, concluding the section with a brief introduction to the cosmological perturbations formalism.

1.1.1 The Friedmann equations

The modern cosmology is based on the General Relativity (GR) theory, developed by A. Einstein in a series of publications in 1915 [1]. This breakthrough in the history of physics changes the paradigm of the Newton's gravitation by describing the space-time as a curved four-dimensional manifold. In this scenario, the free-falling gravitating point-particles move along geodesics characterized by the particular geometry of the space-time, which in turn is determined by the energy-matter distribution. Therefore, in general relativity, the gravitation is seen as a pure geometrical effect, instead of a direct interaction between particles. Mathematically, the geometry of the space-time is described by the metric $g_{\mu\nu}$, a 2-rank non-degenerate symmetrical tensor with signature $(3,1)$. The metric defines a quadratic form characterizing the distance element:

$$\mathrm{d}s^2 = g_{\mu\nu}\ \mathrm{d}x^\mu \mathrm{d}x^\nu\ . \tag{1.1}$$

The geodesics along which the particles move, which are completely defined in terms of the metric tensor, can be calculated by minimizing the distance s between two points of the space-time. Following the prescriptions of GR, the metric, and therefore the gravitational field, is calculated from the Einstein equations:

$$G_{\mu\nu} + \Lambda\ g_{\mu\nu} = \frac{8\pi G}{c^4} T_{\mu\nu}\ , \tag{1.2}$$

where $G_{\mu\nu}$ is the Einstein tensor, which is a function of the metric and its derivatives, whereas the matter content of the Universe is described by the stress-energy tensor $T_{\mu\nu}$. Although, the gravity at small scales can be obtained without the term proportional to

Λ, it is included in these equations in order to explain the accelerated expansion of the Universe, which is endorsed by the current cosmological observations.

In general, the Einstein field equations are difficult to solve for situations with complex matter distribution. Fortunately, the cosmological principle allows one to consider solutions with high symmetry, which are simpler to characterize. It can be shown that the only metric compatible with the cosmological principle is the Friedmann-Lemaître-Robertson-Walker (FLRW) metric:

$$\mathrm{d}s^2 = -c^2\mathrm{d}t^2 + a(t)^2\left[\frac{1}{1-\kappa r^2}\,\mathrm{d}r^2 + r^2\left(\mathrm{d}\theta^2 + \sin^2\theta\,\mathrm{d}\phi^2\right)\right] . \tag{1.3}$$

In spherical coordinates, this metric has the property of being diagonal, which is guaranteed by the isotropy and homogenity of the space. In a universe described by the FLRW metric, the great amount of symmetry implies that the space only can grow or decrease in a homogeneous way, and therefore, the scale factor $a(t)$ is the only degree of freedom, which depends on the cosmic time t. Since this metric is degenerate when $a = 0$, the scale factor must have well-defined sign in order to avoid singular points and continuously describe the space-time evolution. Hereafter, we adopt the standard convention of $a(t) > 0$, for all values of t.

On the other hand, the constant κ in eq. (1.3) represents the curvature of the spatial sections, whose value can be considered to be -1, 0 or 1, after a proper redefinition of the radial coordinate r and the scale factor $a(t)$. Again, due to the isotropy of the Universe, the curvature κ must be a constant which depends neither on the time nor on the spatial location . This restricts the possible geometries of the spatial sections to be one of these three types: flat ($\kappa = 0$), spherical ($\kappa > 0$) or hyperbolic ($\kappa < 0$) geometries, which correspond to the flat, closed and open universe models, respectively. It is important to notice that, since GR only deals with the geometry of the space-time, the topological properties of the Universe are not constrained by the Einstein field equations. Although it is commonly assumed that the Universe is simply connected, different topologies are allowed for a given geometry. For instance, the Euclidean space with the standard flat geometry can be wrapped around in different directions in order to form a three-dimensional torus (this space is still flat, but with non-trivial topology). In the following, only the trivial topology is considered, and therefore, the different shapes for the Universe are restricted to be a 3-dimensional Euclidean space, a 3-sphere or a 3-hyperbolic space for $\kappa = 0, 1, -1$, respectively.

The metric in eq. (1.3) can be used as an *ansatz* in the Einstein equations in order to find GR solutions compatible with the cosmological principle. In this situation, the energy-matter content of the Universe is modelled as a perfect fluid, in which case the

stress-energy tensor has the following particular form:

$$T_{\mu\nu} = (\rho + p)\, U_\mu U_\nu + p g_{\mu\nu} \ , \tag{1.4}$$

where ρ and p are the energy density and pressure of the fluid, respectively. In a perfect fluid, other hydrodynamic parameters, as the heat conduction, viscosity and shear stresses, are neglected. For an isotropic universe, it is also assumed that the fluid is at rest with respect to a free-falling observer, and therefore, the fluid velocity field has the form $U^\mu = (1, 0, 0, 0)$, leading to a diagonal stress-energy tensor: $T^\mu{}_\nu = \mathrm{diag}(-\rho, p, p, p)$. Additionally, the pressure and energy density are considered to be functions of the cosmic time t, but, due to the homogenity of the Universe, not of the spatial coordinates. Depending on the hydrodynamic properties of the fluid, the density and the pressure are related by a particular equation of state.

Combining the FLRW metric (eq. (1.3)) and the stress-energy tensor for a perfect fluid (eq. (1.4)) into the Einstein field equations, we arrive to the Friedmann equations for the scale factor $a(t)$:

$$\left(\frac{\dot{a}}{a}\right)^2 = \frac{8\pi G}{3c^2}\rho - \frac{\kappa c^2}{a^2} + \frac{\Lambda c^2}{3} \ , \tag{1.5a}$$

$$\frac{\ddot{a}}{a} = -\frac{4\pi G}{3c^2}\,(\rho + 3p) + \frac{\Lambda c^2}{3} \ . \tag{1.5b}$$

These two differential equations describe the complete dynamics of an isotropic and homogeneous Universe with curvature κ and a particular matter content. In the simplest situation, consisting in a non-empty universe without the contribution of the cosmological constant, the Friedmann equations do not have fixed points for the scale factor, which implies that all the cosmological solutions consists in an expanding or contracting Universe. This relevant prediction of GR was confirmed by E. Hubble in 1929 measuring the velocity of remote galaxies and finding that they are moving away following a precise law [2]. Concretely, he found that the recessional speed and the distance of those galaxies are related in a proportional way. Although G. Lemaître previously derived a similar result in a publication in 1927 [3], this observational fact is widely known as the Hubble's law, whereas the particular proportionality constant is called the Hubble constant, which is commonly denoted by H_0. Since all the dynamical properties of the Universe are given by the scale factor, it is possible to see that the Hubble constant is equal to the quantity $\dot{a}/a$, evaluated at the present time. As a generalization of this constant, the Hubble function is defined to be the time-dependent function $H = \dot{a}/a$, which plays a important role in the background evolution.

Previously to Hubble's discovery, Einstein included the constant Λ in the gravitational

field equations in order to compensate the expansion derived from the Friedmann equations and obtain a static Universe. This particular situation is achieved with non-zero Λ and positive κ related in a very precise way. The main problem with this model (in addition to the disagreement with the current evidences of the expansion of the Universe) is that the scale factor is located in a critical point which is unstable, and any small perturbation leads to a expanding or contracting universe. Despite that the field equations admit a non-zero Λ without affecting the physical requirements for a consistent theory of gravity (e.g., the conservation of energy), finally, Einstein set its value to zero. Nowadays, after the discovery of the accelerated expansion of the Universe, the cosmological constant was again included in order to explain this unusual behaviour, which cannot be accomplished with standard material content satisfying the strong energy condition.

The first of the Friedmann equations (eq. (1.5a)) is the analog of a energy conservation equation for the scale factor, where the term corresponding to the kinetic energy is given by the square of the Hubble function $(\dot{a}/a)$ and the potential energy is proportional to the energy density ρ of the cosmic fluid. Besides this, the terms with the curvature κ and the cosmological constant Λ can be interpreted as additional sources of potential energy, which also affect to the scale factor dynamics. Furthermore, as it can be inferred from the Friedmann equations, the cosmological constant can be considered as a energetic component described by a time-independent density with negative pressure. More precisely, the equation of state of this hypothetical fluid is $p_\Lambda = -\rho_\Lambda$, where the density is given by $\rho_\Lambda = \Lambda c^4/8\pi G$. This analogy with a fluid can be used to construct generalizations of the cosmological constant model by considering modifications of the equation of state. Generically, in this class of models, the cosmic fluid responsible of the accelerated expansion of the Universe is referred to as dark energy.

1.1.2 Cosmic fluid and the Universe dynamics

Deriving with respect to the cosmic time the first Friedmann equation (eq. 1.5a) and using the second one (eq. (1.5b)) to eliminate second order derivatives of the scale factor, it can be derived the continuity equation for the energy:

$$\dot{\rho} + 3H\left(\rho + p\right) = 0 \ , \tag{1.6}$$

where we have introduced the Hubble function $H(t) = \dot{a}/a$. As it is expected, this equation is a direct consequence of the energy conservation implied by the Einstein's gravity, and alternatively, it can be also obtained vanishing the divergence of the stress-energy tensor (eq. (1.4)). Physically, the meaning of eq. (1.6) is that changes in the energy density are source by the term $3H\left(\rho + p\right)$, representing the flux of energy due to

the expansion of the Universe, in which case $\rho + p$ describes the relativistic inertial mass density. A direct application of the continuity equation is that, given a equation of state relating the pressure and the energy density, it can be solved in order to obtain the time evolution of the hydrodynamic variables of the cosmic fluid. In order to fully describe the Universe dynamics, only the first Friedmann equation (eq. (1.5a)) and the continuity equation (eq. (1.6)) are needed, whereas the second Friedmann equation (eq. (1.5b)) is not independent and it can be derived from these two.

One of the main consequences of the continuity equation is that the Universe expansion is adiabatic. Since the energy density is constant throughout the space, the total energy in a physical volume V is the product $E = \rho V$, where the volume grows proportional to a^3. It is possible to see from the first law of thermodynamics, $\mathrm{d}E = T\mathrm{d}S - p\mathrm{d}V$, that the time derivative of the total entropy S is a source for the energy density:

$$\dot{\rho} + 3H\left(\rho + p\right) = \frac{T}{V}\dot{S} \ , \tag{1.7}$$

where we have used that the volume expands accordingly to the Hubble function: $\dot{V} = 3HV$. The energy conservation, derived from the the Friedmann equations, implies that the left hand side vanish, which leads to $\dot{S} = 0$. Notice that, in this situation, the entropy density $s = S/V$, which is proportional to a^{-3}, depends on time because the evolution of the scale factor. The conservation of entropy plays an important role in the physical processes involving particle interactions and the expansion of the Universe.

In a realistic model of the Universe, the cosmic fluid is composed by different species of particles, as baryons, dark matter, radiation, or neutrinos, which have different hydrodynamic properties. In most of the cases, all these components can be modelled as a barotropic fluid for which the pressure only depends on the density, but not on any other hydrodynamic variables. In particular, the different species can be described by an equation of state which is linear, that is, $p = w\rho$, where the proportionality constant w is referred to as the equation-of-state parameter. The compatibility with the cosmological principle requires that w is, at most, a function of the time, parametrizing, in this case, a possible evolution of the equation of state. In the standard model of the Universe, it is assumed that the equation of state is time-independent for all the species, with the exceptions of some extensions of the dark energy model. With the information about the hydrodynamic behaviour given by the equation of state, the continuity equation can be solved in order to obtain the dependence of the energy densities as a function of the scale factor. Concretely, dividing eq. (1.6) by $\dot{a}$ in order to use the scale factor as the time variable, and integrating assuming that $p = w\rho$, it is found that the energy density

has a power-law dependence on a:

$$\rho(a) = \rho_0 \left(\frac{a}{a_0}\right)^{-3(1+w)} , \tag{1.8}$$

where ρ_0 is the density when the scale factor takes the value a_0. The tilt of the power-law depends on the particular value of the equation-of-state parameter w, which is assumed to be constant in the integration. It is observed that, unless $w < -1$, the energy density decrease as the Universe expands. Finally, assuming that the Universe is flat ($\kappa = 0$), the evolution of the scale factor can be calculated by solving the first Friedmann equation (eq. 1.5a) using the expression of the energy density in eq. (1.8):

$$a(t) = a_0 \left(\frac{t}{t_0}\right)^{\frac{2}{3(1+w)}} , \tag{1.9}$$

where a_0 is the scale factor at the time t_0, which has been chosen so that $a = 0$ at $t = 0$ (this is performed by requiring $H_0 t_0 = 2/3\,(1 + w)$). Notwithstanding that this equation is only valid for a flat universe, the existence of a singular time for which $a = 0$ is a general fact when the equation-of-state parameter is $w > -1$. Moreover, at early times, the curvature of the Universe can be ignored for fluids satisfying the strong energy condition ($w > -1/3$), and hence, the time dependence of the scale factor is $t^{\frac{2}{3(1+w)}}$, independently of the value of κ. Regarding the particular case of $w = -1$, the solutions of the Friedmann equations can be obtained by assuming that the energy density is constant, finding that the scale factor, in this case, grows exponentially (alternatively, the solution can be recovered by taking the limit in eq. (1.9), considering the implicit dependence of t_0 in w).

At the background level, the different components of the Universe are classified, by their equation-of-state parameter:

- *Radiation ($w = \frac{1}{3}$):*

  The radiation can be considered as a gas in equilibrium composed by ultrarelativistic particles, which can be both bosons (photons) or fermions (massless neutrinos). The equation of state for these kind of systems is obtained by requiring that the trace of the stress-energy tensor vanish. Since $T = -\rho + 3p$, as can be deduced from eq. (1.4), the radiation pressure is related to the energy density by $p = \frac{1}{3}\rho$. Therefore, the equation-of-state parameter for ultrarelativistic particles is $w = \frac{1}{3}$.

  Regarding to the evolution of the radiation fluid, there are two effects which contribute to the decreasing of the radiation density as the Universe expands. First, as in the case of matter, the energy density is reduced on account of the increment of the volume, which is proportional to a^{-3}. On the other hand, the energy

of relativistic particles, such as for instance the photons, decrease as a^{-1} due to the cosmological redshift. The combination of both effects leads to a dependence of the radiation density proportional to a^{-4}. As it is expected, this particular scaling for the radiation density is also obtained from the solution of continuity equation in eq. (1.8) for $w = \frac{1}{3}$. Finally, solving the Friedmann equations for a flat radiation-dominated universe, the scale factor grows as $t^{\frac{1}{2}}$.

- *Matter ($w = 0$):*

  In the standard cosmological model, the matter is supposed to be non-relativistic, which implies that the kinetic energy of the matter particles is small compared with their masses. Consequently, in this situation, the equation of state is assumed to satisfy $p \ll \rho$, or equivalently $w \ll 1$. Neglecting the equation-of-state parameter, this particular model of matter consists in a pressureless fluid, which reproduces the hydrodynamic properties of dust. Obviously, the matter particles inside collapsed objects, as galaxies or clusters, do not obey this equation of state, since the pressures are relevant in their hydrodynamic evolution. But, on the other hand, at cosmological scales, the matter halos can be interpreted as non-relativistic point particles constituting the cosmic fluid, and, in this case, the hydrodynamic variables behave as the ones of the dust model.

  Once the equation of state is determined, the evolution of a matter dominated universe can be calculated from the Friedmann equations. Concretely, imposing that $w = 0$ in eq. (1.8) leads to a energy density proportional to a^{-3}. Physically, this means that the dilution of matter as the Universe expands evolves accordingly to the growth of the volume. Finally, from eq. (1.9), the evolution of the scale factor in a flat and matter dominated universe is proportional to $t^{\frac{2}{3}}$.

- *Curvature ($w = -\frac{1}{3}$):*

  The curvature term in the first Friedmann equation (eq. (1.5a)) comes from the geometrical part of the Einstein field equations, and therefore, it is not a material component contributing to the stress-energy tensor. However, its dynamical properties over the background can be modelled as perfect fluid whose barotropic equation-of-state parameter is $w = -\frac{1}{3}$. Surprisingly, this particular equation of state implies that the absolute pressure of this hypothetical fluid can be negative, being the limit case of the strong energy condition. In addition, depending on the sign of the spatial curvature, the curvature density can be considered positive or negative, whose evolution, for this particular equation-of-state parameter, is proportional to a^{-2} (eq. (1.8)), recovering the dependence on the scale factor of the curvature term which appears in the Friedmann equation (eq (1.5a)). If κ is

negative, this type of cosmology is equivalent to the Milne model of the Universe, which corresponds to a evolution of the scale factor $a \propto t$.

- *Cosmological constant ($w = -1$):*

  The cosmological constant Λ, as the curvature, can be considered as a perfect fluid with negative pressure and constant energy density. In order to reproduce the Λ term in the Einstein field equation, the equation of state of this fluid must be $p = -\rho$. This kind of behaviour agrees with what is expected from a vacuum energy filling all the space. As deduced from the Friedmann equations for a constant energy density, the expansion of the Universe is exponential, that is, the scale factor grows as $e^{\sqrt{\frac{\Lambda}{3}}ct}$. The observed acceleration of the scale factor at late time is consistent with this strong evolution, being the cosmological constant the greater source of energy in the Universe. In the next section, the cosmological constant picture is generalised in order to describe a wide range of dark energy models.

In order to describe the evolution of the Universe, different species of matter have to be considered at the same time. Supposing that interactions between species can be neglected, at least at the level of the background evolution, the Dalton's law implies that the sum of the partial pressures is equal to the total pressure of the cosmic fluid. In the same way, this addition property is also valid for the energy densities of each component. Denoting by p_i, ρ_i and w_i, the partial pressure, energy density, and equation-of-state parameter of the species i, respectively, the corresponding hydrodynamic variables for the cosmic fluid are given by:

$$p = \sum_{i=1}^{N} p_i \ , \qquad\qquad \rho = \sum_{i=1}^{N} \rho_i \ , \tag{1.10}$$

where N is the total number of species used for describing the background dynamics. Assuming that the different fluid components do not interact among them, the continuity equation (eq. (1.6)) can be solved for the each species separately, and therefore, the scaling function in eq. (1.8) is valid for the energy density ρ_i, providing the equation-of-state parameter w_i.

An important parameter determining the geometry of the Universe is the critical density at a given time, which is defined as the density ρ_c needed for the first Friedmann equation (eq. (1.5a)) to hold when the Universe is flat ($\kappa = 0$) and the cosmological constant is ignored. This particular value depends on time through the Hubble function H and is given by $\rho_c = 3H^2c^2/8\pi G$. It is convenient to express the energy densities of the different components of the Universe relatively to the critical density, and for this reason, we introduce the density parameters as the ratios $\Omega_i = \rho_i/\rho_c$. Using the Friedman equation

(eq. (1.5a)), it is possible to deduce that the density parameters satisfy the following relation:

$$\sum_{i=1}^{N} \Omega_i + \Omega_\kappa = 1 \ , \tag{1.11}$$

where the space curvature is described by the parameter $\Omega_\kappa = -\kappa c^2/a^2H^2$. In this equation, the possible contribution of the cosmological constant Λ can be introduced by considering an additional energetic components defined by the density parameter $\Omega_\Lambda = \rho_\Lambda/\rho_c = \Lambda c^2/3H^2$. Denoting by Ω the sum of all density parameters Ω_i, the curvature of the Universe can be classified in closed, flat, or open depending if Ω is larger, equal, or smaller than 1.

Taking into account all the energetic components in the evolution of the Universe at the same time, different epochs can be distinguished. Because the densities of different types of energy have different dependence on the scale factor, their relative influences on the total energy density changes with time. As seen before, the energy densities scale as a^{-n}, with n being a natural number which depends on the energetic constituent considered. The greater the value of n, the greater the domination of the corresponding energy type at early times, whilst, conversely, the species with smaller n are the principal source of energy in the Friedmann equation at late times. Following this considerations, the photons and the ultrarelativistic particles form the dominant component in the primordial Universe (at least, after inflation), until the cosmological redshift suppressed the radiation energy compared with the non-relativistic matter, moment at which the matter domination epoch started. Whilst in models with non-zero κ, the matter domination epoch is succeeded by a period in which the Universe evolution is led by the curvature term, in a flat universe, the matter continues dominating the dynamics until very recent times, in which the cosmological constant drives the expansion.

1.1.3 Energetic components of the Universe

In this section, the energy content of the Universe and its physical implications for cosmology are considered. In particular, we describe the physical constituents of matter (baryonic and dark matter) and radiation (photons and neutrinos) , as well as, parametrizations of the different dark energy models.

- *Dark matter:*

  Unexpectedly, the first measurements of the virial mass of galaxy clusters, as well as, observations of rotational curves of galaxies evidenced the need of additional matter which is not traced by light [4–7]. Although alternative explanations for these observations based on modifications of the Newtonian gravity have been

proposed, additional measurements of the gravitational lensing effect, the growth of the large-scale structure and the anisotropies of the cosmic microwave background radiation support the consensus idea of the existence of a dark matter component in the Universe.

Depending on the velocities of the particles, the dark matter models are classified in three types: cold, warm, and hot dark matter. The main difference between these classes appear in the structure formation process. If the particles are relativistic, as in the case of hot dark matter, the collapse of structures is suppressed, obtaining that it is impossible to explain the current matter distribution from the evolution of the anisotropies observed in the CMB. On the other hand, whilst the hot dark matter requires relativistic velocities, the cold and warm dark matter can be explained with heavier particles moving slower. This kind of dynamics allows the dark matter to collapse and form halos whose abundance is within the observed bounds. Although, both cold and warm dark matter present the same behaviour at large scales, they diverge at distances comparable with the free streaming length of the warm dark matter particles. Below this characteristic scale, the halo formation in the warm model is suppressed due to the smoothing of the potential wells caused by the diffusion of dark matter particles. Additionally, other important difference between the cold and warm dark matter models concerns the formation process of the halo structures. Whilst the smaller cold dark matter halos are always formed before the larger ones, which leads to a hierarchical halo structure, the warm model predicts that this order is inverted for halos smaller than the free streaming length, implying, in this case, that small halos are formed by fragmentation. Since the current measurement of the large scale structure agree with the hierarchical halo formation model, most of the dark matter in the Universe must be cold.

Whereas it is evident that the dark matter does not have electromagnetic charge because it is not visible, some fundamental descriptions assumes that they interact through the weak force. In the standard model of particle physics, the only fundamental particles which have weak charge and are electromagnetically neutral are the neutrinos. However, they cannot constitute the most part of the observed dark matter because their masses are too small to be non-relativistic. Some extensions of the particle physics picture, as the Minimal Supersymmetric Standard Model (MSSM), includes neutrino-like particles which are heavy and stable. In general, these hypothetical particles responsible of the dark matter are called Weakly Interacting Massive Particles (abbreviated as WIMPs). If this is the case, the weak coupling of the dark matter with the standard model particles would imply that it decays producing radiation which could be detected in high density regions.

- *Baryonic matter:*

  In particle physics, the baryons are those subatomic particles which are composed by different combinations of three quarks (e.g. protons and neutrons). However, as an extension of this concept, in astrophysics, the baryonic matter is considered to be all particles composed primarily by baryons, as for instance the atoms. Rigorously, the electrons are not baryons, but they are included as a part of the baryonic matter since the are usually bounded to the protons. Nevertheless, other leptons, as the neutrinos, or the bosons are excluded from the definition of baryonic matter. Although, the contribution of the electrons in terms of gravity is small due to their low inertial mass, they have an important role in the dynamics of the baryons promoted by electromagnetic interactions.

  Whilst the dark matter does not feel the electromagnetic force, the baryonic matter particles have non-zero electromagnetic charge, implying that they can interact with photons. In the primordial Universe, when the temperature is large enough to ionize the media, the protons, electrons and photons form a plasma, which is supposed to behaves as a perfect fluid in thermal equilibrium. Because the mass of the proton is large compared with the electron mass, it is more likely that the photons interact with electrons rather than with protons. However, the Coulomb scattering between protons and electrons which takes place in the plasma allows photons to couple to protons, indirectly. These interactions are the basis of the Baryon Acoustic Oscillations (BAO) present in the CMB and the large scale structure.

- *Photons:*

  As a consequence of the annihilation between matter and anti-matter, the photons are the most abundant particle in the Universe. The observed values of number densities of different species confirm that there is roughly 10^9 photons per each baryonic particle. The small value of the baryon-to-photon ratio also shows that, in the primordial universe, there was an excess of only one matter particle per billion of particles (matter or antimatter) produced in the baryogenesis. Despite of the large number of photons, the present dynamic of the Universe is governed by matter due to the low energy density of photons.

  Apart from the non-thermal radiation produced in high energy events, the bulk of photons are in thermal equilibrium and form the cosmic microwave background radiation observed today. Since the distribution of this radiation is described by the black body spectrum, the total power radiated per unit area for all wavelengths is given by the Stefan-Boltzmann law, which can be used to calculate the energy

density of photons:

$$\rho_\gamma = \frac{4\sigma}{c} T_\gamma^4 \ , \tag{1.12}$$

where σ is the Boltzmann constant and T_γ is the photon temperature at a given time. Using the current value for the CMB temperature ($T_{\rm CMB} = 2.7255$ K), it is obtained that the present photon energy density parameter is $\Omega_\gamma h^2 \approx 2.473 \times 10^{-5}$.

- *Neutrinos:*

  At early times, when the temperature of the Universe was much greater than the electron mass, the positrons and electrons were in thermal equilibrium with neutrinos and photons. Notwithstanding that neutrinos and photons do not interact directly, they are thermalised by their respective interactions with the bulk of electrons and positrons through the weak and electromagnetic forces. Later, the Universe cooled down and the neutrino background decoupled from the rest of the particles, but maintaining its temperature equal to the photons temperature T_γ. Just after the neutrino decoupling, the temperature becomes smaller than the mass of the electron, and consequently, positrons and electrons annihilate producing high energy photons. The entropy and energy densities of photons increase at the end of the annihilation epoch, which leads to a difference of temperature between the neutrinos and photons.

  Supposing that this process is adiabatic, the entropy density, which is proportional to gT^3 for relativistic species, is conserved during the annihilation. The number of relativistic degrees of freedom g of the particles involved in the annihilation changes from the initial to the final state, implying a variation in T_γ. Therefore, the initial photons temperature, which is equal to the temperature of neutrinos T_ν, and the final CMB temperature T_γ are related by:

$$\frac{T_\nu}{T_\gamma} = \left(\frac{2}{2 + \frac{7}{8} \times 2 + \frac{7}{8} \times 2} \right)^{1/3} = \left(\frac{4}{11} \right)^{1/3} \ , \tag{1.13}$$

  where, in the second equality, the numerator represents the final number of degrees of freedom (g = 2, because the two polarization states of photons), whereas the denominator is the sum of all the degrees of freedom present before the annihilation (2 for the photons, and 2 for the two spin values of both electrons and positrons, weighted by 7/8 for being fermions). This equation implies that the neutrino temperature is 0.71 times lower than the photons one, which gives that the temperature of the Cosmic Neutrino Background (CνB) is $T_{\rm C\nu B} = 1.95$ K.

  As in the case of photons, the energy density of neutrinos is proportional to the fourth power of their temperature, which can be derived from a modification of

the Stefan-Boltzmann law for fermions:

$$\rho_\nu = \frac{7\sigma}{2c} N_{eff} T_\nu^4 \ . \tag{1.14}$$

As a consequence of using the Fermi-Dirac distribution for neutrinos instead of the Bose-Einstein statistics used in the derivation of the Stefan-Boltzmann law, the proportionality constant in this equation differs from the one in eq. (1.12) in a factor 7/8. Additionally, it is included the effective number of neutrinos species N_{eff}, which in the standard model of particles would be three. Nevertheless, in the derivation of the neutrino temperature in eq (1.13), it is assumed that neutrinos are completely decoupled from other leptons at the moment of the annihilation. Since this is not true for a realistic neutrino decoupling mechanism, there is a leakage of the positron and electron energy into the neutrinos, leading to an increment of T_ν. Besides this, a correction of the Fermi-Dirac statistics is needed in order to describe accurately the neutrino distribution after the decoupling. All these effects are taken into account in the definition of N_{eff}, whose value for the standard model is 3.046, rather than three. Using eqs. (1.13) and(1.14), the relativistic neutrino density parameter today is approximately $\Omega_\nu h^2 \approx 1.711 \times 10^{-5}$, whenever the neutrino masses are neglected.

Notice that neutrinos can only be considered relativistic, as previously, only at early times when the temperature is greater than their masses. However, the current constraints on the sum of the neutrino masses are consistent with the existence of non-relativistic neutrinos. Whilst the upper bound constraint on the sum of neutrino masses is $\sum_i m_i < 0.23$ eV [8], the present temperature of the cosmic neutrino background is three orders of magnitude lower ($T_{\mathrm{C}\nu\mathrm{B}} = 1.97$ K $= 1.68 \times 10^{-4}$ eV). Denoting by m_i the mass of the neutrino of the species i, the total neutrino density parameter is [9]:

$$\Omega_\nu h^2 = \frac{\sum_i m_i}{93.14 \text{ eV}} \ , \tag{1.15}$$

whose constraint is $\Omega_\nu h^2 < 0.0025$. Despite of their masses, the free streaming length of neutrinos is large, implying that they behave as hot dark matter. For this reason, as previously mentioned, the massive neutrinos have an important impact on the structure formation process.

- *Dark energy:*

  In the oldest cosmological models considered previously to the discovery of the accelerated expansion, the matter is the dominant energetic component of the Universe. These kind of cosmological models are based on the Friedmann-Einstein

universe, whose main parameter is the total density parameter Ω. However, observations of the cosmological structure on large scales suggested that the Universe is flat, where the 80% of the critical density is provided by a positive cosmological constant [10]. Despite of being unable to detect the possible contribution of the cosmological constant, supernovae observations suggested that $\Omega < 1$, concluding that we may live in a low mass-density universe [11, 12]. Just few months after these observations, in 1998, after obtaining accurate measurements of the Hubble's law using type Ia supernovae as standard candles, evidences of the accelerated expansion of the Universe caused by a cosmological constant were observed [13, 14]. Subsequently, this important discovery was confirmed by observations of the CMB and the large scale structure.

A possible physical interpretation of the cosmological constant is based on the quantum-mechanical description of the vacuum. As previously mentioned, the Λ-term in the Einstein equations can be seen as a fluid with constant energy density $\rho_\Lambda \propto \Lambda$ and negative pressure. It is, precisely, that constant-density behaviour as the Universe expands which allows one to consider the cosmological constant as a vacuum energy. The main problem with this interpretation is that, whilst the cosmological constant Λ_{vac} inferred from quantum field theory calculations is $\sim L_p^{-2}$, where L_p is the Planck length, the corresponding value implied by cosmological observations is much smaller ($\Lambda \sim H_0^2/c^2$). Taking values for these constants, it is obtained that both predictions for Λ differ in many orders of magnitude:

$$\frac{\Lambda_{\text{vac}}}{\Lambda} \sim 10^{121} \ , \tag{1.16}$$

while if the standard model of particle physics is extended including supersymmetry, this ratio is reduced to $\sim 10^{60}$. This inconsistency between the two fundamental standard models of physics in the determination of Λ is commonly known as the cosmological constant problem.

The explanation of the accelerated expansion based on the cosmological constant term of the Einstein field equations can be extended to include a more general type of energy. As it is shown from the Friedmann equations (eqs. (1.5)), it is possible to consider the cosmological constant as a fluid whose equation of state is $p_\Lambda = -\rho_\Lambda$, which corresponds to a equation-of-state parameter $w = -1$. Indeed, from the second Friedmann equation (eq. 1.5b), it is deduced that a fluid which violates the strong energy condition $1+3w \geq 0$ generates an accelerated expansion. Therefore, it is referred to as dark energy to any kind of energy whose equation-of-state parameter satisfies $w < 1/3$, at least at some time in the history of the Universe, and capable of explaining the accelerated expansion. Dynamically, the

different dark energy models are parametrized by a time-dependent equation-of-state parameter $w(t)$, By considering this dependence in the continuity equation (eq. 1.6), it is possible to see that the dark energy density scales as:

$$\rho_{de}(a) = \rho_{de,0} \left(\frac{a}{a_0}\right)^{-3} \exp\left(-3 \int_{a_0}^{a} \frac{\mathrm{d}a}{a}\, w(a)\right) \ , \tag{1.17}$$

where the scale factor a has been used as the time coordinate in the integral involving $w(a)$. As it is expected, the expression in eq. (1.8) is recovered if the equation-of-state parameter is assumed to be constant. A commonly used expression for the equation of state parameter is the Chevallier-Polarski-Linder (CPL) parametrization [15, 16], which assumes a linear dependence in the scale factor :$w(a) = w_0 + w_a\,(1 - a)$. It is important to notice that, unless $w = -1$, the dark energy is not a static fluid with constant density, implying that perturbations over the homogeneous background distribution have to be considered in the evolution of the cosmological structures. Since the current observations based on the baryon acoustic oscillations and the CMB are compatible with a constant equation-of-state parameter equal to $w = -1$, the cosmological constant is the preferred model for the dark energy.

The standard cosmological model is based on the ΛCDM model, which assumes a flat universe with the dark energy as a pure cosmological constant ($w = -1$), and the dark matter as a non-relativistic fluid ($w = 0$). This simple scenario is capable of explaining the most of the cosmological observations of the CMB and the large scale structure. However, different extensions including non-zero curvature or evolution of the dark energy are considered in order to explore models beyond the ΛCDM.

1.1.4 Cosmological perturbations

In the FLRW universe, it is considered that all the physical quantities depend on the time coordinate, but not on the spatial degrees of freedom. At large scales, this assertion seems to be true because the cosmological principle is approximately valid on cosmological scales. Nevertheless, different structures as galaxies or clusters are observed in the present Universe, which implies that there exists deviations from a completely uniform background. Moreover, the gravitational effects over matter overdensities lead to a non-linear growth of the initial perturbations, which collapse forming dark matter halos which in turn host baryonic matter in the form of galaxies. The complexity of the physical mechanism of structure formation is a matter of study in cosmology and it is a cornerstone in the comparison of theory and observations. However, as derived from

the CMB measurements, the cosmological perturbations are small in the early Universe, which allows one to use linear perturbation theory in this case.

In general, a physical quantity is determined by a space-time function $X(\mathbf{x}, t)$, which can be either a scalar or a tensor (indices labelling different components are omitted in this notation). In order to define the perturbations δX, it is needed to consider a background field $\bar{X}(t)$, depending only on the time coordinate, so that $\delta X(\mathbf{x}, t) = X(\mathbf{x}, t) - \bar{X}(t)$. An important issue concerning the definition of the perturbations is the selection of the coordinates, which in the end, means a choice of a particular background field $\bar{X}$. In the covariant formulation of GR, all the physical observables can be expressed in terms of tensor quantities, whose components depend on the coordinates defining the reference frame. The ambiguity in that coordinates can lead to unphysical degrees of freedom in the perturbation δX, which can be set to zero simply with a coordinate transformation. One of the problems in cosmological perturbation theory is to find *gauge* invariant quantities that represent real physical perturbations.

Different *gauges* are commonly used in the literature depending on the convenience to describe particular physical scenarios. Assuming for simplicity that the Universe is flat, one of the most popular is the conformal Newtonian *gauge*:

$$\mathrm{d}s^2 = a^2(\tau)\left\{-(1+2\Phi)\,\mathrm{d}\tau^2 + [(1-2\Psi)\,\delta_{ij} + h_{ij}]\,\mathrm{d}x^i \mathrm{d}x^j\right\}\ , \tag{1.18}$$

where the conformal time τ is used instead of the cosmic time and δ_{ij} represents the Kronecker delta. Whilst the scalar perturbations are parametrized by Φ and Ψ, the tensor modes are given by the components h_{ij}. In this *gauge*, the scalar Φ represents the Newtonian potential in the linear approximation, which plays an important role in the structure formation on the subhorizon scales. On the other hand, the curvature of the spatial sections is given by Ψ, which can be related to Φ using the linear approximation of the Einstein field equations (eq. (1.2)). In fact, in the matter dominated era, these two potentials are equal, since the shear stress in the cosmic fluid vanishes. However, the neutrinos do not behave as a perfect fluid after their decoupling, and hence, the non-zero shear causes that $\Phi \neq \Psi$ in the radiation-dominated era. Notwithstanding that the photons also have non-zero shear stress after the recombination due to their polarization, the two potentials are approximately equal, since, at that moment, the dominant component of the Universe is the matter, which behaves as a perfect fluid. One of the advantage of working with the conformal Newtonian metric (eq. (1.18)) is that the two scalars Φ and Ψ are equal to the Bardeen potentials (cite), which are *gauge* invariant.

Regarding the tensor perturbations in eq. (1.18), the trace and the divergence of h_{ij} must vanish ($h^i{}_i = \partial_i h^i{}_j = 0$) in order to have pure tensor modes. Indeed, these

perturbations correspond to gravitational waves propagating in the background space, whose polarization states are represented by the two remaining degrees of freedom of h_{ij} left after imposing the former constraints. Notice that, since these are the only tensor perturbations allowed in the metric, h_{ij} is *gauge* invariant at linear order.

Besides the perturbations of the metric in eq. (1.18), fluctuations in the cosmic fluid are also considered in terms of linear perturbations of the stress-energy tensor. In this case, the ambiguity in the *gauge* choice is physically evident, since, for instance, any density fluctuation $\delta\rho$ over the cosmic fluid can be removed by a change of coordinates. What is really happening in this transformation is that those perturbations on the matter fields are transformed in geometric fluctuations in the metric through the Einstein field equations. For this reason, it is necessary to construct *gauge* invariant quantities involving metric and matter degrees of freedom. In the case of scalars fluctuations, one of the most important *gauge* invariant quantities is the curvature of constant density hypersurfaces:

$$\zeta = -\Psi + \frac{1}{3}\frac{\delta\rho}{\rho + p} \,, \tag{1.19}$$

where ρ and p are the background energy density and pressure, respectively. On the one hand, ζ is simply the curvature of the spatial sections in the *gauge* in which $\delta\rho = 0$. But, on the other hand, by considering flat hypersurfaces ($\Psi = 0$), its value is proportional to the density perturbation $\delta\rho$. This duality in the definition of ζ is one the examples in which metric perturbations can be converted in matter fluctuations with just a *gauge* transformation.

The distribution of matter and radiation in the Universe is determined by the statistical properties of the primordial scalar curvature ζ. As derived from the simplest models of inflation, the distribution of the initial perturbations is nearly to a Gaussian, which implies that all the information about the statistics of ζ is in its second order moment. In order to separate different scales, it is convenient to work with the Fourier mode decomposition $\zeta_{\mathbf{k}}$, which depends on the wave vector $\mathbf{k}$. Moreover, if the cosmological principle is assumed, it is possible to prove that these modes are statistically independent: $\langle \zeta_{\mathbf{k}} \zeta^*_{\mathbf{k}'} \rangle = (2\pi)^3 \, \delta(\mathbf{k} - \mathbf{k}') P_\zeta(k)$, where the power spectrum $P_\zeta(k)$ only depends on the modulus of the wave vector $\mathbf{k}$ due to the isotropy of the space. It is convenient to express the amplitude of the fluctuations in terms of the power per logarithm interval of k:

$$\Delta^2_\zeta(k) = \frac{k^3}{2\pi^2} P_\zeta(k) = A_s \left(\frac{k}{k_0}\right)^{n_s - 1 + \frac{1}{2}\alpha_s \log k/k_0} \,, \tag{1.20}$$

where, in the right hand side, the power spectrum is modelled as a power law whose amplitude for the scale k_0 is given by A_s (s for scalar perturbations). The tilt is parametrized by the scalar spectral index n_s and its running α_s, which is included

in order to model possible deviations from the power law. Indeed, the expression in eq. (1.20) can be obtained by calculating the Taylor series expansion of the logarithm of $\Delta^2_\zeta(k)$ as a function of the logarithm of k up to second order. This simple model of the scalar power spectrum is adopted when the cosmological observations are compared with the prediction of inflation (see Section 1.2). Measurements of the CMB and the large scale structure favour the scale-invariant power spectrum ($n_s = 1$ and $\alpha_s = 0$) proposed by E. Harrison and Y. Zel'dovich [17, 18].

Similarly, the statistics of the primordial gravitational waves are described by the power spectrum of their amplitude for each polarization mode. Since different directions in the Universe are equivalent, the two polarization states have the same statistical properties. In this case, the dimensionless tensor power spectrum is commonly parametrized as

$$\Delta^2_t(k) = A_t \left(\frac{k}{k_0}\right)^{n_t} , \tag{1.21}$$

where the contributions of both polarization modes are taken into account in the definition of $\Delta^2_t(k)$. As in the case of scalars, A_t parametrizes the amplitude of the power spectrum at the scale k_0, and n_t is the tensor spectral index. Following the mechanism for the generation of the initial perturbations derived in the inflation model, the scalar and tensor power spectrum parameters are related in a precise way. For instance, in single-field slow-roll inflation, a consistency relation links the tensor-to-scalar ratio and the tensor spectral index: $A_t/A_s = -8n_t$.

1.2 Inflation

The classical cosmological model based on solutions of the Friedmann equation has two main problems which were pointed out in the late 1960s: the horizon and the flatness problems. The first who addressed the horizon problem was C. Misner in 1969 [19], showing the need of a mechanism for explaining the homogeneity of the cosmic microwave background on superhorizon scales. On the other hand, in the same year, R. Dicke mentioned that the density of the Universe must be close to the critical value in order to be consistent with the observations [20]. This fact, called the flatness problem, implies that the Universe must be flat at early times with high accuracy level. Whilst a high density leads to a universe which has already collapsed, the Universe would be nearly empty for low values of the density. These two problems are solved in the inflationary model.

In a paper in 1980, A. Guth and H. Tye proposed a mechanism for solving the monopole problem arising in Grand Unified Theories (GUT) [21]. In general, the GUT models applied to the hot Big Bang model predict the existence of topological defects, as magnetic monopoles and other topological relics, which would be very abundant today. Guth and Tye explained the lack of evidences on the existence of such monopoles by considering an exponential expansion of the Universe taking place after the monopoles were produced. At the end of this inflationary phase, the density of monopoles would be diluted to one monopole per Hubble volume or less. Approximately one year later, Guth also published a paper in which the same idea was applied for solving the horizon and the flatness problems [22]. Physically, the Guth's model is based on the existence of a false vacuum state with non-zero expectation value of the energy, which, dynamically, behaves as a cosmological constant. As long as the Universe is in this metastable state, the scale factor grows exponentially solving the cosmological problems mentioned above. At some later time, the Universe undergoes a phase transition from the false to the true vacuum state via quantum tunneling. This process generates bubbles settled in true vacuum state where the inflationary process stops. However, as notice by Guth himself, the bubbles are smaller than the observable Universe and they never percolate, resulting in a universe which is too inhomogeneous to be compatible with observations [23]. This class of models is referred to as old inflation in the literature.

In old inflation, the phase transition from the false vacuum to the true vacuum state is performed instantaneously, implying that most of the released energy is on the walls of the bubbles. In these models, the thermalization can be only done through bubble collisions, a process which does not allow the Universe to reheat properly. In order to solve the problems in these inflationary scenarios, A. Linde [24], and independently A. Albrecht and P. Steinhardt [25], proposed an alternative in which the phase transition towards the vacuum minimum occurs at particularly low velocity. In these models, the bubbles are larger than the observable Universe and no percolation process is needed to homogenize the energy density. These models are referred to as new inflation, or more commonly nowadays, slow-roll inflation.

If the inflationary phase is treated as a pure classical process, the Universe would be too homogeneous even for generating the anisotropies in the CMB and the large scale structures we observe today. However, taking into account quantum effects, the exponential expansion during inflation stretches the small quantum fluctuations up to macroscopic scales. These perturbations are frozen once their size is larger than the horizon, generating, in this way, the initial seed for the density fluctuations in the Universe. After inflation, the perturbations enter again into the horizon and they evolve following the standard laws of physics, leading to the formation of structures. The first who applied this mechanism to a de Sitter type universe were V. Mukhanov and G. Chibisov in 1981

[26]. Subsequently, in the next year, different papers were published on the subject, which generalize these ideas to the new inflationary model [27–31].

1.2.1 Problems of the classical Big Bang model

In this section, the horizon and flatness problems are studied in more detail, paying special attention to how an inflationary phase solves them.

- *Horizon problem:*

  The study of the causal structure of the space-time is performed by considering light trajectories from two given points. In special relativity, the causality in the Minkowski space is described simply by the light cones, however, in the general relativity, the curvature of the space-time results in more complicated causal structures. For this reason, different types of horizons are introduced in order to analyse causal relations between events. For example, the comoving particle horizon is defined as the comoving distance that the light travels from the Big Bang singularity to a given later time. From the FLRW metric (eq. 1.3), it is possible to see that this horizon also corresponds to c times the conformal time elapsed from the Big Bang:

  $$d(t) = c\int_{t_0}^{t}\frac{\mathrm{d}t}{a} = \int_{0}^{a(t)}\frac{\mathrm{d}a}{a}\,\frac{c}{aH}\ , \tag{1.22}$$

  where t_0 is the time associated with the initial singularity ($a(t_0) = 0$). Two points of the space are in causal contact at some time if the comoving distance between them is smaller than this length. Notice that, the comoving particle horizon depends on the cosmological parameters considered.

  Another important length scale is the Hubble radius, which is defined as c/H. As derived from the Hubble's law, this length can be interpreted as the distance at which the recessional velocity of free-falling galaxies is equal to the speed of light at some particular time. Notice that, because the Hubble function H can decrease with time, it is possible to observe points today which were beyond the Hubble radius in the past. For this reason, the Hubble radius does not define a proper causal horizon. Analogously, the comoving Hubble radius is defined as $c/(aH)$, where the scale factor is introduced in order to express distances in terms of the comoving quantities instead of the physical ones. In the last equality of eq. (1.22), the comoving particle horizon is expressed as the integral of the comoving Hubble radius with respect to the logarithm of the scale factor.

  Roughly speaking, the temperature of the Universe at the recombination epoch is given the the Saha equation [32], which, assuming the measured baryon density,

is $\approx$ 3000 K. Taken into account that the present value of the CMB photons temperature is $\approx$ 2.73 K and that the radiation temperature drops according to a^{-1} as the Universe expands, it is obtained that the scale factor at recombination is $\sim 10^{-3}$. By using this value in eq. (1.22), the comoving particle horizon at the time in which CMB anisotropies form is $\approx 195\ h^{-1}$Mpc, a distance corresponding to an angular size of $\approx 2^{\circ}$ in the last scattering surface. The fact that the CMB photons coming from any direction on the sky have approximately the same temperature evidences that the particle horizon at recombination must have been similar to the size of the observed Universe ($\sim 10\ h^{-1}$Gpc). This discrepancy between the predicted and the observed size of causally connected regions in the last scattering surface is called the horizon problem.

In order to have a larger particle horizon, the integral in eq. (1.22) must receive a contribution from early times caused by a large Hubble radius. This large primordial value of the Hubble radius is reconciled with the small length predicted by the observed matter and radiation abundances by assuming a rapid decrement of the Hubble length in the primordial epoch. Considering a primeval Universe with the energy content we observe today (matter, radiation and the cosmological constant), the comoving Hubble radius is an increasing function of time until the domination of the dark energy in the most recent epoch. Therefore, a energy density capable of reducing the comoving Hubble length is needed in order to explain the large value of the comoving particle horizon required for solving the horizon problem. From the second Friedmann equation (eq. (1.5b)), it is deduced that this behaviour can only be accomplished by a fluid which violates the strong energy condition.

- *Flatness problem:*

  From the Friedmann equations (eqs. (1.5a) and (1.5b)) and the continuity equation (eq. 1.6), it is obtained that the evolution of the total density parameter is given by

$$\dot{\Omega} + H\,(1+3w)\,\Omega\,(1-\Omega) = 0\ , \tag{1.23}$$

  where we have assumed that the Universe is dominated by a single component characterized by the equation of state parameter w. This equation has two critical points, $\Omega = 0$ and $\Omega = 1$, with opposite stability properties. In particular, if the fluid satisfies the strong energy condition ($1 + 3w \geq 0$), the flat solution, corresponding to $\Omega = 1$, is an unstable critical point, which means that any perturbation around the critical density moves outwards from the point $\Omega = 1$, leading to a non-flat universe. The constraints on the absolute value of the present curvature density parameter from the CMB and LSS observations is < 0.005 [8], which

implies that the Universe today is flat with accuracy below the one percent level. Moreover, assuming the standard evolution of the scale factor, the curvature density parameter is required to be $\sim 10^{-62}$ at the Planck epoch ($a \sim 10^{-32}$). This great fine-tuning in the initial conditions of the Universe at the Big Bang epoch is an evidence of the lack of naturalness in the model. The need of an alternative description of the primordial Universe capable of explaining the low value of the curvature density is referred to as the flatness problem.

Assuming the validity of the Friedmann equations, the only possibility to solve the flatness problem is to consider exotic forms of energy in the early Universe. For instance, for an energetic component violating the strong energy condition, the critical density is a stable critical point of eq. (1.23), and hence, only in this situation, the flat geometry is a dynamical attractor. Independently of the value of the curvature κ, the total density of the Universe approaches to its critical value during the period in which the effective equation of state parameter is $< -\frac{1}{3}$.

Since the difference $|1-\Omega|$ is proportional to $(c/aH)^2$ (see eq. (1.11)), the issue with the low value of the current curvature density, as the horizon problem described above, can be solved by considering an early epoch in which the comoving Hubble radius decreases with time.

As can be deduced from the second Friedmann equation (eq. 1.5b), the evolution of the scale factor is accelerated whenever the dominant energetic component does not satisfy the strong energy condition. Therefore, the solution of the horizon and flatness problems lies in considering an inflationary phase in the early Universe, which must stop at a given time in order to reconcile the model with the current observations. Nowadays, the only observed component of the Universe which does not satisfy the strong energy condition is the dark energy, however, its density only dominates at the most recent times. In the next section, the dynamics of the early Universe is modelled by introducing a scalar field which can explain the flatness and the large particle horizon size.

1.2.2 Physics of inflation

In the least action approach of the gravitational field, the dynamics of the metric is derived from the Einstein-Hilbert action, which is written in a covariant form as the integral of the Ricci scalar R in the world volume. By applying the Euler-Lagrange equations to this system, it is obtained that the metric which minimizes this action satisfies the Einstein field equations introduced in eq. (1.2), but with $\Lambda = 0$. The main advantage of working with this formalism is that it allows one to construct models of gravity with different interactions in the matter sector, respecting the principle of

relativity. For instance, in the simplest models of inflation, the accelerated expansion is driven by a scalar field, called the inflaton, which is minimally coupled to the gravity:

$$S[g_{\mu\nu},\phi] = \int \mathrm{d}^4x\ \sqrt{-|g|}\left[\frac{1}{16\pi G}R - \frac{1}{2}g^{\mu\nu}\partial_\mu\phi\ \partial_\nu\phi - V(\phi)\right]\ , \tag{1.24}$$

where all the effective interactions of the inflaton are modelled by the potential $V(\phi)$. Whilst the term proportional to the Ricci tensor represents the gravitational part, the matter-energy content is parametrized by the scalar field ϕ. In this action, it is assumed a standard quadratic kinetic term for the inflaton, which is coupled to gravity only through the inverse of the metric $g^{\mu\nu}$. The lack of higher order terms involving ϕ and the Ricci tensor causes that the inflaton has a minimal gravitational coupling. In fact, the action in eq. (1.24) describes the simplest model of a real scalar field propagating in a curved space.

The gravitational field equations are obtained by minimizing the action in eq. (1.24) with respect to the metric. Since the gravity part of eq. (1.24) is the standard Einstein-Hilbert action, the dynamics of the gravitational field is simply given by the Einstein field equations (eq. (1.2)) with the following stress-energy tensor:

$$T_{\mu\nu} = \partial_\mu\phi\ \partial_\nu\phi - g_{\mu\nu}\left[\frac{1}{2}\left(\partial\phi\right)^2 + V(\phi)\right]\ . \tag{1.25}$$

Comparing this expression with eq. (1.4), it is observed that the inflaton behaves as a perfect fluid. Moreover, if the cosmological principle is assumed, then the inflaton dynamics can be simplified, since, in this case, it is possible to consider ϕ as a function of only the cosmic time t. By neglecting the derivatives with respect to the spatial coordinates in eq. (1.25), it is derived that the energy density of this fluid is $\frac{1}{2}\dot{\phi}^2 + V(\phi)$, whereas its pressure is given by $\frac{1}{2}\dot{\phi}^2 - V(\phi)$. As discussed before, the accelerated expansion is only achieved if the inflaton violates the strong energy condition ($\rho+3p<0$), or equivalently, if

$$\dot{\phi}^2 \ll V(\phi)\ . \tag{1.26}$$

Since this expression implies that the kinetic energy of the inflaton is small compared with its potential energy, this dynamical requirement on the evolution of ϕ is referred to as the slow-roll condition. Whenever the dynamics of the inflaton satisfies this velocity condition, the expansion of the Universe is accelerated. Indeed, in the limit in which the kinetic energy can be completely neglected, the energy density of the inflaton is approximately constant, leading to a de Sitter universe whose expansion is exponential.

In order to solve the cosmological problems of the classical Big Bang model discussed in the previous section, inflation must last enough time so that the comoving Hubble radius decreases a desirable factor. A useful quantity that measures the efficiency of

the inflationary process at some time t is the number of e-folds, $N(t)$, which is defined as the natural logarithm of the ratio of the scale factor at the end of inflation over its corresponding value at the time t. This means that, for instance, if the number of e-folds when the inflation starts is N, the Universe has expanded e^N times during the inflationary epoch. Regarding the comoving Hubble radius, its value decreases a factor e^{-N} whenever the Universe behaviour during inflation is close to de Sitter ($\dot{H} \approx 0$). By considering this dynamical behaviour of the comoving Hubble radius, it is obtained that the horizon and the flatness problems are solved only if the inflation lasts, at least, ≈ 60 e-folds. Although this value can change depending on the details of the reheating and the energy at which inflation occurs, it is clear that the inflationary process cannot happen too swiftly in order to be consistent with the observations. This fact imposes constraints on the shape of the inflation potential $V(\phi)$ beyond the condition in eq. (1.26).

Since there are a lot of candidates for the potential of the inflaton arising in the formulation of different theories and models, the standard approach is to consider the expansion around a pure exponential inflation in terms of the derivatives of $V(\phi)$. In particular, the following quantities are introduced [33, 34]:

$$\varepsilon(\phi) = \frac{1}{2}\left(\frac{V'(\phi)}{V(\phi)}\right)^2 , \qquad \eta(\phi) = \frac{V''(\phi)}{V(\phi)} , \tag{1.27}$$

which are called the slow-roll parameters. Whilst ε measures the slope of the potential at some point, the parameter η quantifies the flatness of $V(\phi)$, whose shape can be concave or convex depending on its sign. In the regime in which the slow-roll parameters are small, the inflationary expansion is close to be exponential. More precisely, it is possible to see that $\varepsilon \approx -\dot{H}/H^2$ whenever the slow-roll approximation is valid, which means that ε quantifies the rate of change of the Hubble function. As long as ε approaches zero, H is constant, recovering a de Sitter universe with exponential expansion. On the other hand, besides the condition on the first derivative of the potential ($\varepsilon \ll 1$), constraints on the second derivative ($|\eta| \ll 1$) are imposed in order to keep the velocity of the inflaton ($\dot{\phi}$) small during a period of time long enough, such as inflation can last to generate a large number of e-folds. In addition, beyond the determination of the inflationary conditions on the background, the slow-roll parameters in eq. (1.27) have an important role in the description of the initial power spectrum of the cosmological perturbations.

1.2.3 Initial perturbations from inflation

Inflation provides a natural mechanism for the generation of the initial scalar and tensor perturbations. One important fact is that, in the slow-roll approximation, the evolution

of the linear perturbations freezes at scales above the Hubble length. Because, as it has been shown in the preceding sections, the comoving Hubble length decreases at least a factor $\sim 10^{26}$ during the inflationary phase, a wide range of scales are frozen before the end of the inflation. In particular, the quantum fluctuations of the inflaton, and hence, the curvature perturbations induced by them, remain fixed after the Hubble radius becomes smaller than the wavelength of the perturbation.

The quantization of scalar fluctuations of the metric are better formulated in terms of the comoving curvature $\mathcal{R}$, instead of the curvature of constant density hypersurfaces ζ introduced in eq. (1.19). However, this change of the variable defining the scalar perturbations is not important, since both curvatures, $\mathcal{R}$ and ζ, are equal on superhorizon scales. More precisely, the comoving curvature perturbation $\mathcal{R}$ can be expressed as a function of the spatial curvature Ψ (eq. (1.18)) and the inflaton perturbation $\delta\phi$:

$$\mathcal{R} = \Psi + \frac{H}{\dot{\phi}}\delta\phi \ , \tag{1.28}$$

where $\dot{\phi}$ refers to the derivative of the unperturbed inflaton. Since $\delta\phi$ vanishes in a inertial frame, $\mathcal{R}$ represents the spatial curvature seen by comoving observers. It is important to notice that, as well as ζ in eq. (1.19), the combination which defines $\mathcal{R}$ is *gauge* invariant. On the other hand, by considering the flat *gauge* ($\Psi = 0$) in eq. (1.28), it is possible to see that the scalar mode $\mathcal{R}$ is directly related to the inflaton perturbation $\delta\phi$. Since a variation of the inflaton corresponds to a shift of the time in which the fluctuation exits the horizon, the comoving curvature perturbations $\mathcal{R}$ can be seen as a fluctuation in the time coordinate (more precisely, $\mathcal{R} = -H\delta t$, or equivalently, in terms of the number of e-folds perturbation, $\mathcal{R} = \delta N$). In this alternative picture, the initial density perturbations are generated by a delay in time at end of inflation $\delta t(\mathbf{x})$, which depends on the space location, and hence, some regions of the Universe have been inflated more than others, leading to a difference in their densities. This time-delay formalism has been used for the calculation of the primordial power spectra [27, 28].

After inflation, any field involved in the inflationary expansion is supposed to decay in the standard model particles during a process called reheating. As a consequence, in single field inflation, the perturbations in the density (and pressure) of all the cosmological species come from the same curvature perturbation $\mathcal{R}$. This fact is one of the most important predictions of the simplest models of inflation, in which the primordial fluctuations are purely adiabatic. In general, any perturbation of the cosmic fluid can be decomposed in adiabatic and isocurvature modes, where the latter, in contrast to the adiabatic fluctuations, do not generate curvature perturbations by definition ($\mathcal{R} = 0$). The isocurvature modes might arise in multi-field inflationary models, in which different

density perturbations are generated non-thermally through the decaying of several fields [35].

By considering comoving linear perturbations of the metric in the action in eq. (1.24), the Mukhanov-Sasaki equation gives the evolution of the Fourier modes of the fluctuations:

$$u_{\mathbf{k}}'' + \left(k^2 - \frac{z''}{z}\right) u_{\mathbf{k}} = 0 \ , \tag{1.29}$$

where the prime notation indicates derivatives with respect to the conformal time. In this equation, the Mukhanov variable is introduced, which is defined as $u = z\mathcal{R}$ for scalar perturbations, where $z = a\dot{\phi}/H$ is a time-dependent function, which depends only on background quantities. The wavelength of the mode, represented by the vector $\mathbf{k}$, is given in comoving coordinates. In the slow-roll approximation, since the Hubble function H and $\dot{\phi}$ can be considered constant, it is obtained that the quantity z''/z in eq. (1.29) is approximately the comoving Hubble length. In this regime, the Mukhanov-Sasaki equation has a simple physical interpretation: for scales smaller than the Hubble length ($k^2 \gg z''/z$), the term involving the derivatives of z can be ignored, obtaining that fluctuations oscillate following the standard wave equation. On the other hand, the Mukhanov-Sasaki equation for scales larger than the Hubble radius ($k^2 \ll z''/z$) admits only two solutions: an irrelevant decaying mode and a growing mode which leads to a constant curvature $\mathcal{R}$. It is precisely this last solution which causes the freezing of perturbations whose size is larger than the Hubble radius.

Additionally, the primordial gravitational waves can be also generated following the Mukhanov-Sasaki equation (eq. (1.29)), where, in this case, the Mukhanov variable is $u = zh$, where h the amplitude of one of the polarization modes and $z = a/2$. As for the scalar perturbations, the mechanism which generates the primordial tensor modes, is based on the freezing of superhorizon perturbations. The importance of measuring the amplitude of the primordial gravitational waves is that it is directly related to the energy scale of inflation.

According to the inflationary mechanism, it is supposed that the seed of the primordial perturbations arise from the freezing of quantum vacuum fluctuations. Therefore, the Mukhanov variable u in eq. (1.29) must be quantized following the standard prescriptions of quantum mechanics. For this purpose, the Mukhanov-Sasaki equation can be interpreted as a quantum oscillator, but with a time-dependent frequency caused by the term z''/z. The main challenge in the quantization of this type of systems is the ambiguity in the definition of the vacuum state, which leads to an indeterminacy on the amplitude of the perturbations. The standard approach to this problem is to consider an early enough time such that the mode is deep inside the horizon ($k^2 \ll z''/z$), and

then choose the vacuum state as the one corresponding to the usual harmonic oscillator. This particular initial condition for the modes in the Mukhanov-Sasaki equation is called the Bunch-Davies vacuum [36]. Obviously, this choice is not unique and inflation might start in an excited state, leading to non-Gaussian perturbations [37].

One of the most important consequences of the slow-roll inflation is that the primordial power spectrum is nearly flat ($n_s \approx 1$ and $n_t \approx 0$), with some corrections due to the evolution of the inflaton. In particular, the scalar and tensor spectral indices can be written as a function of the slow-roll parameters [34]:

$$n_s - 1 = 2\eta - 6\varepsilon \ , \qquad\qquad n_t = -2\varepsilon \ , \tag{1.30}$$

where higher order terms of ε and η are neglected. Notice that, in a generic inflation model, the slow-roll parameters depend on the value of the inflaton at a given time (see eq. (1.27)). In order to describe the primordial power spectra we observe today, both ε and η must be evaluated at the time at which the scale k crosses the horizon ($k \sim aH$). This can introduce a scale dependence on the spectral indices, which would modify the power law behaviour of the primordial fluctuations amplitude (in the case of the scalar power spectrum, this dependence is modelled by the spectral index running α_s defined in eq. (1.20)). However, in slow-roll inflation, it is expected that the slow-roll parameters are nearly constant.

Besides the tilt of the power spectra, the ratio between the amplitudes of the tensor and scalar modes can be also related to the slow-roll parameters. More precisely, it is obtained that the tensor-to-scalar ratio at first order is given by

$$r = \frac{A_t}{A_s} = 16\varepsilon \ . \tag{1.31}$$

From this equation and the expression of the tensor spectral index in eq. (1.30), it is possible to derive the consistency relation $r = -8n_t$, which holds whenever the slow-roll approximation is valid. This constraint between r and n_t can be used to check the inflation hypothesis as the mechanism to generate the primordial perturbations. The best constraints on the tensor-to-scales ratio are obtained from measurements of the polarization of the cosmic microwave background. The primordial gravitational waves have not yet been detected and the current upper limit is $r < 0.07$ at 95% confidence, for the pivot scale $k_0 = 0.05$ Mpc^{-1} [38].

1.3 Cosmic Microwave Background

In the hot Big Bang model, the temperature of the Universe in the past was greater than today, diverging as the scale factor goes to zero ($T \propto a^{-1}$). As a consequence of this fact, the baryonic matter (composed by electrons and atomic nuclei) must be ionised in the primordial Universe, and therefore, the free charged particles (especially the electrons) were strongly coupled to the photons, implying that the mean free path of the photons was small compared with the typical cosmological distances. In this epoch, the information carried by photons cannot travel between regions whose relative distance is larger than this mean free path. One of the implications of the evolution of the Universe is that the temperature drops as the Universe expands, causing that neutral atoms could form when the temperature is low enough. In this later stage, the probability that a photon collide with a free particle is small due to the absence of free charged particles in the medium. This process, in which the electrons are captured by the atomic nuclei, is called recombination. Since the cross section of the photon scattering is reduced after the recombination, the photons undergo a phase transition in which their mean free path grows up to cosmological scales. In this case, the photons are able to travel freely throughout the Universe being observed today as a background radiation.

The first references to the existence of the CMB radiation were published by A. Alpher, R. Herman and G. Gamow in 1948 [39–42]. In these publications, the CMB is referred to as "the temperature in the Universe" and "the background temperature" [41, 42]. Moreover, in the short letter [41], where some wrong calculations on the matter density presented in the Gamow's paper [40] are corrected, the temperature of the CMB today is estimated to be 5 K, which corresponds to a temperature of ≈ 600 K at the epoch of matter-radiation equality. This prediction is very close to the present measurements of the CMB temperature (2.73 K). Since the relic photons can be considered to be in a equilibrium state, the spectral energy density of the background radiation follows a black body spectrum. By using the Wien's displacement law[1], it is found that the peak of the spectral radiance is around the microwave spectrum. In 1964, A. Penzias and R. Wilson measured the CMB for the first time using a Dicke radiometer, which was built for radio astronomy purposes and satellite communication experiments [43]. In the first instance, the detected signal was thought to be instrumental noise, but later, the astrophysicists R. Dicke, J. Peebles, P. Roll and D. Wilkinson interpreted this radiation as the Cosmic Microwave Background [44].

[1]The Wien's displacement law gives the wavelength at which the spectral radiance of a black body has the maximum:

$$\lambda_{\max} = \frac{b}{T} \, .$$

For a given density, the Saha equation determines the ionization fraction of the hydrogen atoms at some temperature [32]. Using the measured value of the baryonic matter density, the temperature at which the ionization fraction is one half is about 3000 K. This calculation implicitly assumes that the recombination reaction is instantaneous and the thermal equilibrium is maintained during the process. Additionally, in the Saha approach, it is considered that the protons capture an electron and produce a Hydrogen atom in the fundamental state, directly. However, this recombination mechanism is inefficient, since this reaction creates also a photon with enough energy to ionise again a nearby atom. A more accurate approximation is to consider that the fundamental state of the Hydrogen is reached through an intermediate excited state. In this case, the photons produced do not have the energy required to ionise the medium again [45, 46]. Assuming that the recombination took place at $T = 3000$ K and the observed CMB temperature is around 3 K today, the redshift at which the CMB was emitted is $z \approx 1000$. This distance defines a sphere around us, called the last scattering surface, from which the CMB photons can travel freely.

1.3.1 The CMB angular power spectra

The observed CMB anisotropies coming from a given direction on the sky can be seen as a scalar field on the sphere. Analytically, the temperature field can be expanded in terms of the spherical harmonics:

$$\frac{\Delta T}{T}(\mathbf{n}) = \sum_{\ell=0}^{\infty} \sum_{m=-\ell}^{\ell} a_{\ell m} Y_{\ell m}(\mathbf{n}) \ , \tag{1.32}$$

where $a_{\ell m}$ are the spherical harmonic coefficients describing the field $\Delta T/T$. This expansion can be understood as a Fourier transform for fields on the sphere, where the multipole ℓ represents the angular size of the perturbations (as the wavenumber k is associated to the wavelength in the standard Fourier transform on the Euclidean space). In particular, the multipole ℓ is inversely proportional to the angular scale θ. On the other hand, the number m for a fixed value of ℓ represents different possible orientations of the anisotropy pattern. Alternatively, the eq. (1.32) can be inverted in order to express the spherical harmonic coefficients in terms of the temperature field:

$$a_{\ell m} = \int \mathrm{d}^2 n \ \frac{\Delta T}{T}(\mathbf{n}) \ Y^*_{\ell m}(\mathbf{n}) \ , \tag{1.33}$$

as can be derived from the orthogonality relations of the spherical harmonics. The statistical distribution of the temperature field can be translated to a distribution of the $a_{\ell m}$'s. For instance, the spherical harmonic coefficients with $\ell \neq 0$ have zero mean, since

the average of the temperature field is supposed to be isotropic. Furthermore, if the the monopole is subtracted, the mean of the coefficient a_{00} also vanishes. Additionally, the linearity of eq. (1.33) assures that the $a_{\ell m}$'s are Gaussianly distributed, whenever the temperature is also Gaussian.

On the other hand, it is possible to describe the polarization of the CMB in a similar way as the temperature. In this case, the linear polarization of the CMB photons is represented as a headless vector field on the sphere, corresponding to the polarization direction of the incoming photon. Since headless vectors are only determined by the orientation and magnitude, the polarization is described by a 2-spin quantity. Assuming the helicity basis as the system of reference of the tangent space on the sphere, the two components of the polarization are given by $Q \pm iU$, where Q and U are the Stokes parameters. The 2-spinor can be expanded in terms of the spin-weighted spherical harmonics:

$$Q(\mathbf{n}) \pm iU(\mathbf{n}) = \sum_{\ell=0}^{\infty} \sum_{m=-\ell}^{\ell} (e_{\ell m} \pm i b_{\ell m})\, {}_{\pm 2}Y_{\ell m}(\mathbf{n}) \ , \tag{1.34}$$

where the coefficient $e_{\ell m}$ and $b_{\ell m}$ describe the even and odd components of the spinor under parity transformations, respectively. As in the case of vectors, the 2-spinor can be decomposed in the gradient and curl parts. Whereas the coefficients $e_{\ell m}$ describe the scalar field E representing the gradient part of the polarization, the $b_{\ell m}$'s are the spherical harmonic coefficients of the pseudo-scalar field B, which corresponds to the curl part. This particular decomposition also have physical interest: the primordial curl or B-mode of polarization is only non-zero if there exists primordial tensor perturbations. After removing the contribution of the gravitational lensing and the galactic and extra-galactic contaminants, the signal of the B-mode can be used to measure the amplitude of the primordial gravitational waves.

The statistical properties of the CMB radiation can be described in terms of the different moments of the probability distribution. We have seen before that the first-order moment (or the mean) is zero by definition, and hence, the first moment with physical interest is the second-order moment or correlation function. In terms of the spherical harmonic coefficients, the second-order moments of the spherical harmonics coefficients of temperature and polarization are written as

$$\langle a_{\ell m} a^*_{\ell' m'} \rangle = \delta_{\ell\ell'} \delta_{mm'} C_\ell^{TT} \ , \tag{1.35a}$$

$$\langle a_{\ell m} e^*_{\ell' m'} \rangle = \delta_{\ell\ell'} \delta_{mm'} C_\ell^{TE} \ , \tag{1.35b}$$

$$\langle e_{\ell m} e^*_{\ell' m'} \rangle = \delta_{\ell\ell'} \delta_{mm'} C_\ell^{EE} \ , \tag{1.35c}$$

$$\langle b_{\ell m} b^*_{\ell' m'} \rangle = \delta_{\ell\ell'} \delta_{mm'} C_\ell^{BB} \ , \tag{1.35d}$$

where C_ℓ^{XY} with $X, Y = T, E, B$ are the angular power spectra. In the right-hand-side of this equations, it is assumed that the spherical harmonic coefficients with different values of ℓ and m are independent. This fact is a direct consequence of the rotational invariance of the moments derived from the cosmological principle. Moreover, the power spectrum only depends on the multipole ℓ, but not on m, since different values of m represents different orientations of the spherical harmonics. The parity invariance of the correlation functions, implied by the cosmological principle, assures that the primordial cross-power spectra between the B-mode and any other scalar field (as T or E) vanish. However, these power spectra could be non-zero due to the foreground emission, or the rotation of the polarization angle induced by the gravitational lensing effect.

Assuming that the CMB temperature and the primordial perturbations are Gaussian, higher-order moments are either zero or a function of the power spectra C_ℓ^{XY}. Therefore, all the information about the statistics of the CMB temperature and polarization is represented by the angular power spectra in eqs. 1.35. The CMB power spectra for temperature, the E polarization mode and the correlation between them, measured by the *Planck* experiment [47], are depicted in Figures 1.1 and 1.2, whereas the angular power spectrum of the B-mode obtained from the BICEP/*Keck* data [48–50] is shown in Figure 1.3.

1.3.2 CMB physics

In this section, the physical mechanisms that created the fluctuations on the CMB are studied. The CMB anisotropies are classified as primary and secondary, depending whether they are generated at the last scattering surface or not.

- *Sachs-Wolfe effect:*

  The initial perturbations of the gravitational potential affect to the radiation background modifying its density distribution, and therefore, its temperature. According to the expansion of the Universe, the radiation temperature decreases as the inverse of the scale factor ($T \propto a^{-1}$), whose particular evolution depends on the background dynamics (see eq. (1.9)). On the other hand, the adiabatic perturbations, parametrised by the Newtonian potential Φ, can be interpreted as a shift in the time coordinate ($\Phi = \delta t/t$), as can be deduced from the expression of the metric in the Newtonian conformal gauge (eq. (1.18)). The fluctuations in the cosmic time can be translated to small variations in the scale factor, which in turn lead to perturbations in the density and temperature of the photons. Using the above considerations and the particular expression of the scale factor in eq. (1.9),

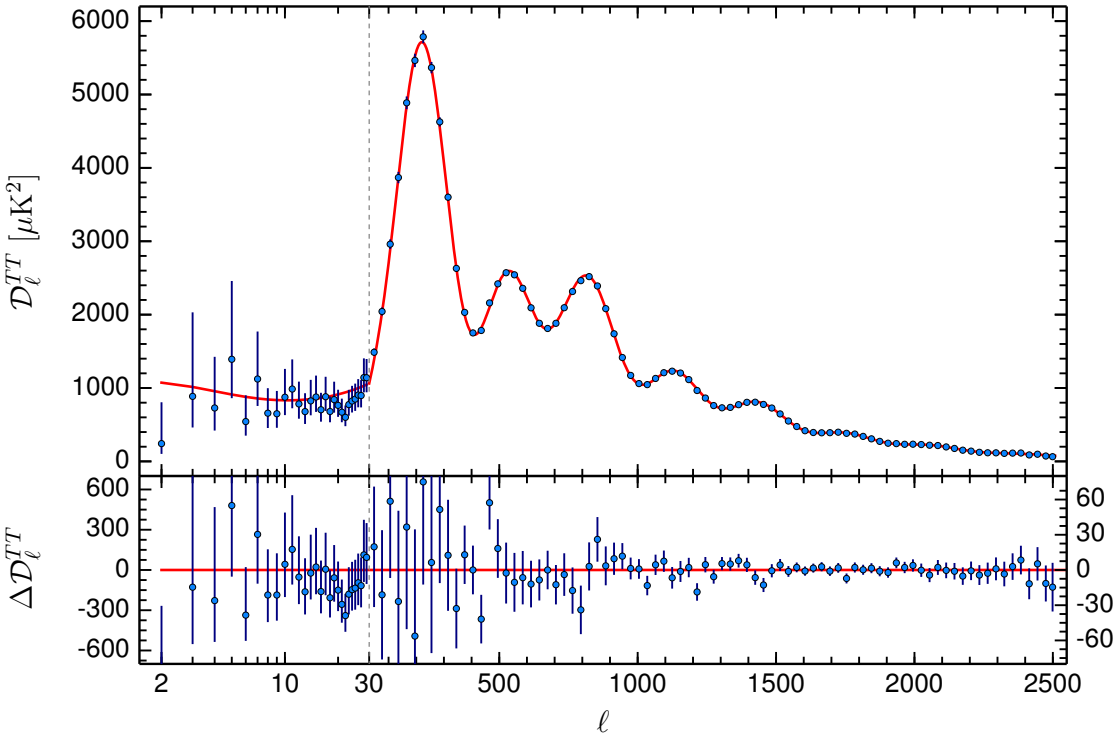

FIGURE 1.1: CMB temperature power spectrum measured by the *Planck* experiment [47] (Upper panel). The vertical axis corresponds to $D_\ell^{TT} = \ell(\ell+1)C_\ell^{TT}/2\pi$, where C_ℓ^{TT} is the angular power spectrum defined in eq. (1.35a). The solid red lines depict the theoretical power spectrum, and the residuals with respect to this model are shown in the bottom panel. The error bars correspond to the 1σ uncertainties. Reprinted from [8].

the CMB temperature fluctuations Θ can be written as [51, 52]:

$$\Theta = \frac{\delta T}{T} = -\frac{\delta a}{a} = -\frac{2}{3\,(1+w)}\frac{\delta t}{t} = -\frac{2}{3\,(1+w)}\Phi \ , \tag{1.36}$$

where the value of the equation-of-state parameter w is given by the energy component dominating the Universe at the moment at which the fluctuations are considered. For instance, considering a matter dominating Universe ($w = 0$), the temperature fluctuations are given by $\Theta = -2\Phi/3$. However, since the photons are redshifted in the presence of a gravitational potential, the observed CMB temperature fluctuations $\Delta T/T$ are given by $\Theta + \Phi$, a quantity which is called effective temperature [53]. This effect arises from the fact that the photons must climb the potential well (or roll down a potential hill), with the consequent loss (or gain) of energy, before they are observed at later times. Therefore, from eq. (1.36) and assuming that the Universe is matter-dominated at the recombination epoch, it is obtained that the observed CMB temperature is [51, 52]:

$$\left.\frac{\Delta T}{T}\right|_{\rm SW} = \frac{1}{3}\Phi \ . \tag{1.37}$$

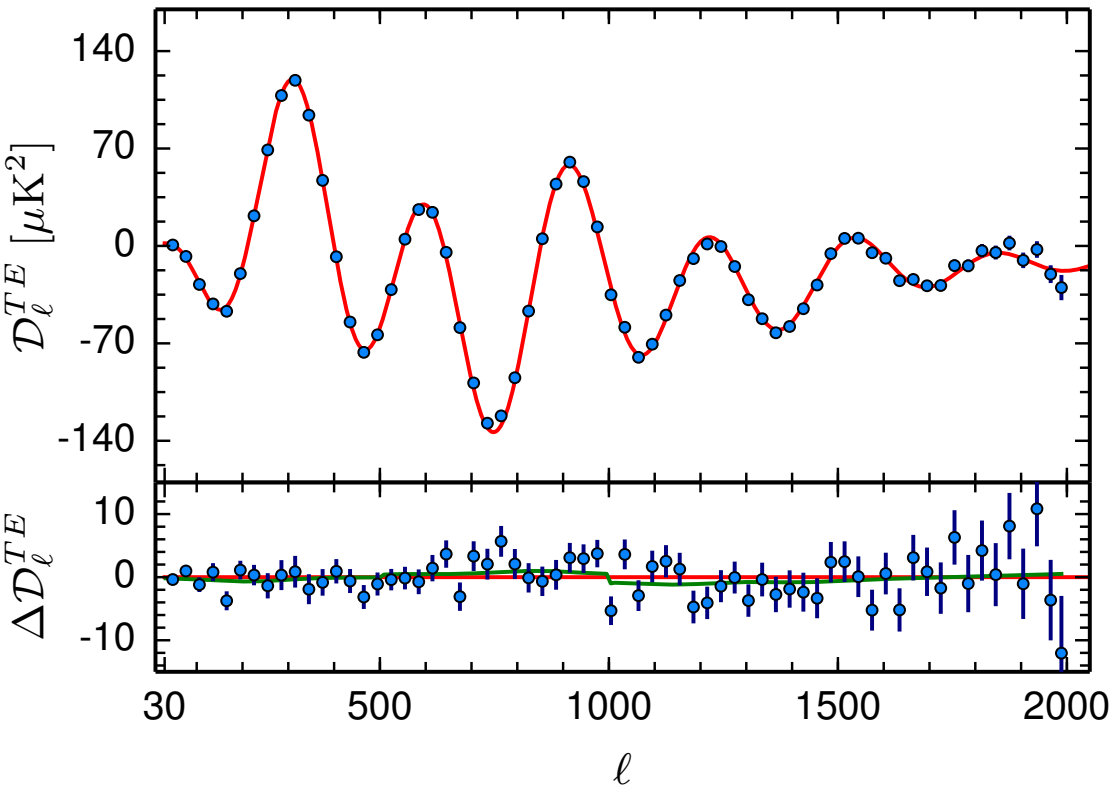

(A) TE cross-power spectrum

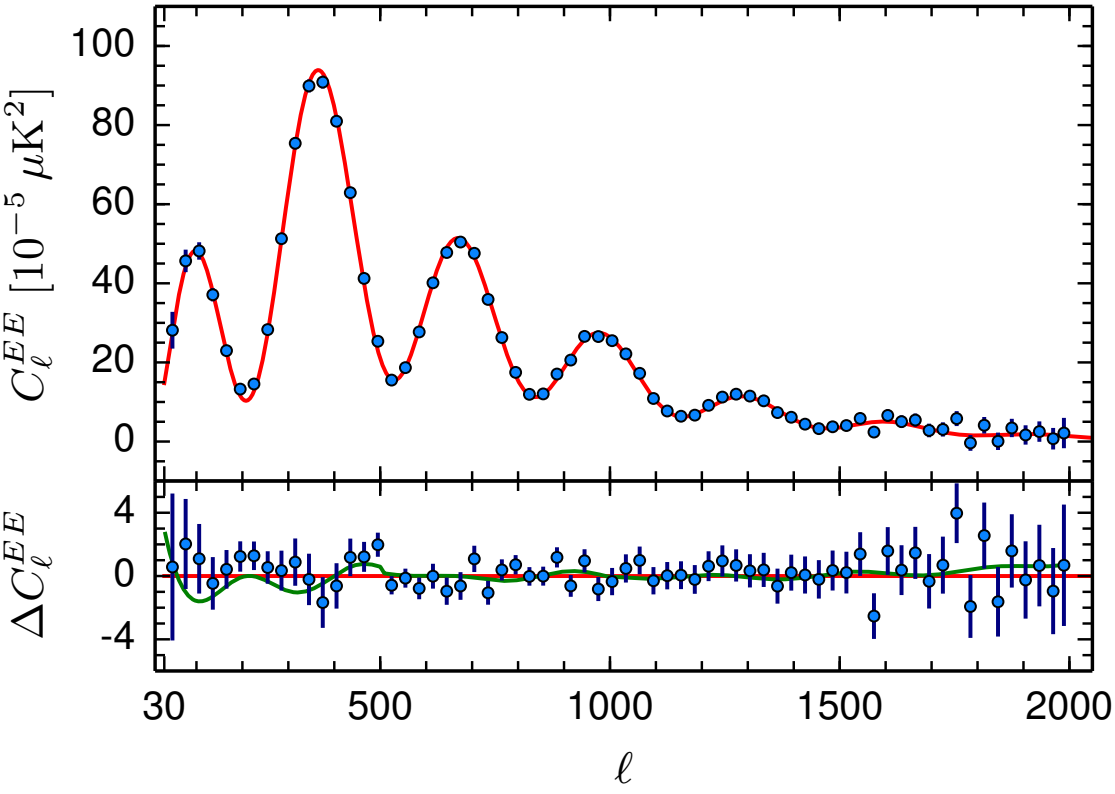

(B) EE power spectrum

FIGURE 1.2: EE and TE power spectra measured by the *Planck* experiment [47] (Upper panel). The vertical axis corresponds to $D_\ell^{XY} = \ell(\ell+1)C_\ell^{XY}/2\pi$, where C_ℓ^{XY} is the angular power spectra defined in eqs. (1.35b) and (1.35c). The solid red lines depict the theoretical power spectra, and the residuals with respect to these models are shown in the bottom panel. The green solid lines models the systematic effect caused by the temperature-to-polarization leakage. The error bars correspond to the 1σ uncertainties. Reprinted from [8].

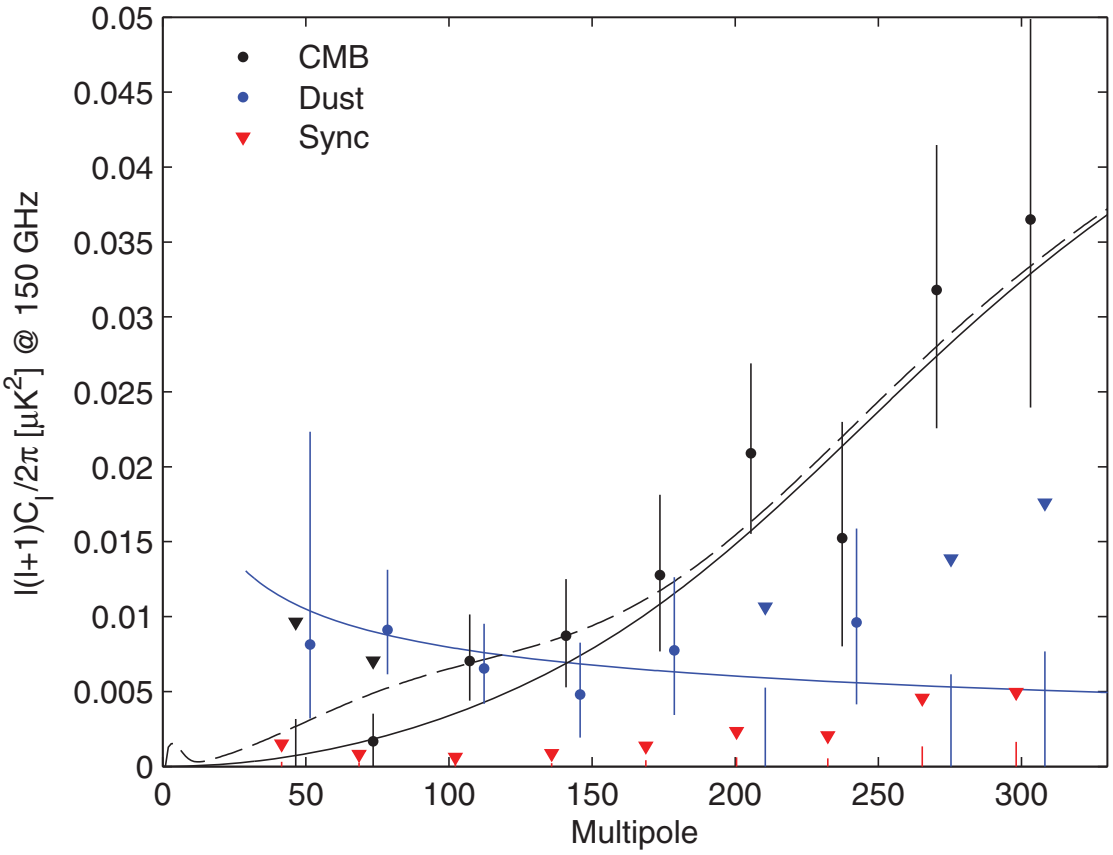

FIGURE 1.3: BB power spectrum per logarithm interval of ℓ measured by the BICEP/*Keck* array experiments [48–50]. Different colours represent different components: CMB (black), dust (blue) and synchrotron (red). The error bars denote the 68% confidence intervals, and the downward triangle indicate the 95% upper limits. The solid black line shows the theoretical expectation from the ΛCDM model, considering only the gravitational lensing effect ($r = 0$), whereas the dashed line assumes a contribution of primordial gravitational waves whose amplitude is $r = 0.05$ at $k = 0.05$ Mpc^{-1}. The solid blue line depicts a model for the dust contribution. Reprinted from [38].

This mechanism for the generation of CMB temperature fluctuations is called Sachs-Wolfe effect [51]. Since the Newtonian potential, and hence the CMB fluctuations, are related to the primordial curvature perturbations (see eq. (1.19)), the nearly scale-invariant power spectrum predicted from inflation is translated to the CMB temperature power spectrum as well. However, the Sachs-Wolfe effect does not account for other physical effects, as the ones caused by the particular dynamics of the photon fluid, interactions between photons and baryons or the time evolution of the gravitational field. Notice that in the derivation of the Sachs-Wolfe (SW) effect in eq. (1.37), it is assumed implicitly that the initial perturbations are adiabatic. On the other hand, it can be proven that $\Delta T/T = 2\Phi$ for isocurvature modes on superhorizon scales, in which case the potential Φ vanishes initially [52].

- *Acoustic peaks:*

The physics of the baryon plasma before recombination has an important role in the observed CMB anisotropies. In the early Universe, when the plasma is fully ionised, the photons and baryons are tightly coupled through the Thomson scattering. As mentioned in Section 1.1.3, it is more likely that a photon collides with an electron rather than a proton, since the cross section of the Thomson scattering is inversely proportional to the squared mass of the charged particle. Nevertheless, the photons are also tightly coupled to protons, because electrons and protons interact through the Coulomb scattering as well, and in this way, the bulk of electrons acts as a glue between the photon and proton fluids. On the other hand, the protons are the main contribution to the gravitational potential due to their high mass. All these interactions cause that the CMB photon distribution affects to the gravitational potential, and vice versa, in a way determined by the physics of the photon-baryon plasma.

After recombination, the photons decouple from the baryons, and hence the photon temperature anisotropies are frozen at the last scattering surface. As a consequence, the acoustic waves in the photon fluid leave an imprint over the CMB, which can be seen as peaks in the temperature angular power spectrum (see Figure 1.1). For adiabatic initial perturbations, the oscillation modes of the photon temperature have an extremum at the last scattering surface when the value of ks_* is a multiple of π, where s_* is the sound horizon at the recombination epoch. This condition select the modes k which contribute most to each peak in the power spectrum. For instance, the lowest mode, which corresponds to the first peak in the power spectrum, is $k = \pi/s_*$, that is, its wavelength is one half of the sound horizon. The next one, associated to the second peak, is the mode whose wavelength equals to the sound horizon ($k = 2\pi/s_*$), and so on. Moreover, the isocurvature modes also generate acoustic waves on the photon fluid, but, in this case, their phase is shifted $\pi/2$ with respect to the adiabatic modes [54], moving the acoustic peaks towards smaller scales.

Even in the absence of couplings to baryons, the photon fluid presents acoustic oscillations, which are caused by the particular dynamics of the pressure and density of the photons, and whose sound speed is $1/\sqrt{3}$ times the speed of light [53]. But, when the interaction with baryons is taken into account, the behaviour of these oscillations change in different ways: the sound speed decreases on account of the extra inertia introduced by the baryons, and the equilibrium point and amplitude of the acoustic oscillations are modified such that the magnitude of the compression phase is enhanced with respect to the rarefaction one [53, 55]. This last phenomenon causes an observable effect over the CMB temperature power spectrum, implying that the amplitude of the even and odd peaks are relatively

modified. In particular, the odd peaks are enhanced with respect to the even ones. On the other hand, the change in the sound speed due to baryons shifts the position of the acoustic peaks in the angular power spectrum, since the acoustic horizon scale at recombination is also modified.

Besides the effect of the baryons and the gravitational potential, the CMB perturbations are also affected by photon diffusion, which causes deviations from the perfect fluid approach (as non-zero shear viscosity and heat conduction). The diffusion of photons induce a smearing of the perturbations whose scale is smaller than the characteristic diffusion length, and consequently, a damping of the acoustic oscillations for large values of k is observed [56, 57]. On the other hand, since the gravitational potential decays with time in the radiation-dominated era, the acoustic oscillations whose scale is larger than the sound horizon at the matter-radiation equality are driven [58]. Both effects can be observed in the CMB power spectrum [59].

In addition, acoustic oscillations also induce a non-zero bulk velocity in the photon fluid, which causes a Doppler shift on the observed CMB temperature. Since the density and velocity oscillations are out of phase, the acoustic peaks are smeared when this effect is taken into account [53]. However, due to the drag of the baryons, the density fluctuations are enhanced with respect to the velocity ones, which prevents the acoustic peaks from being completely cancel out by the Doppler effect [55].

- *Polarization:*

  At recombination, photons are coupled to the bulk of electrons through the Thomson scattering, whose cross section depends on the relative polarizations of the incoming and outgoing photons. More precisely, the differential cross section of the Thomson scattering is [60]:

$$\frac{\mathrm{d}\sigma}{\mathrm{d}\Omega} = \frac{3\sigma_T}{8\pi} \left(\boldsymbol{\epsilon} \cdot \boldsymbol{\epsilon}'\right)^2 \ , \tag{1.38}$$

  where σ_T is the total Thomson cross section, whereas $\boldsymbol{\epsilon}$ and $\boldsymbol{\epsilon}'$ are the polarization vectors of the incoming and outgoing photons, respectively. The differential cross section quantifies the probability that a photon scatters in a direction within the differential solid angle $\mathrm{d}\Omega$. If the incoming radiation is isotropic and unpolarised, the term $\left(\boldsymbol{\epsilon} \cdot \boldsymbol{\epsilon}'\right)^2$ in eq. (1.38) average out leading to scattering probability independent of the scattered polarization vector $\boldsymbol{\epsilon}'$, and therefore, the outgoing radiation is also unpolarized in this situation. However, if the distribution of the incoming photons is anisotropic the resulting radiation could be polarized. Supposing that the electron is at rest in the system of reference, the directional pattern of the

incoming radiation is expanded in terms of the spherical harmonics. The only pattern which produce non-zero polarization through Thomson scattering is the quadrupole ($\ell = 2$).

The shear stress in the photon fluid is a source for the quadrupolar moment, and hence causes the polarization of the CMB photons. There is no polarization in the perfect fluid approach, since the shear stress vanishes in this case. However, imperfections caused by the photon fluid diffusion at recombination generate a shear stress, which is proportional to the velocity gradient and suppressed by the scattering. More precisely, the quadrupolar moment is proportional to kv_γ/τ', where v_γ is the photon velocity (which can be related to the dipolar moment of the temperature) and τ' is the derivative of the optical depth with respect to the conformal time [53, 54]. In terms of the multipole expansion of the temperature, the diffusion process can be understood as transfer of power from the dipole ($l = 1$) to the quadrupole ($l = 2$). Since the amplitudes of the velocity v_γ and the temperature have the same order of magnitude, it is found that the polarization is suppressed a factor k/τ' with respect to the temperature. This fact makes the polarization to affect smaller scales, due to the extra k factor.

The acoustic oscillations are also observed in the different polarization spectra. However, these oscillations are out-of-phase with respect to the temperature in the E and B modes, since the amplitude of polarization signal is sourced by the velocity of the photon fluid v_γ, instead of the temperature. On the other hand, the acoustic oscillations in the TE cross-spectrum have a phase shift of $\pi/2$ with respect to the oscillations in the EE angular spectrum, as it is predicted by taking the product of the temperature and velocity oscillations.[2]

- *Integrated Sachs-Wolfe effect (ISW):*

  Another source of temperature anisotropies comes from the fact that the gravitational potential vary over time. Considering distances larger than the sound horizon, the precise dynamics caused by the interaction between photons and baryons can be neglected. In this situation, the evolution of the intrinsic temperature Θ at superhorizon scales is simply given by $\Theta' = \Psi'$ [54, 61, 62]. Therefore, the derivative of the effective temperature with respect to the conformal time is $\Theta' + \Phi' = \Psi' + \Phi'$. By integrating this expression, it is obtained that the observed

[2] In a simplified model of the acoustic oscillations, and assuming adiabatic initial conditions, it is possible to consider that the temperature oscillates as $\cos ks_*$, whereas the E-mode follows $\sin ks_*$ (it is sourced by the velocity). Therefore, the TT power spectrum presents oscillation as $\cos^2 ks_* \sim \cos 2ks_*$, and the E-mode as $\sin^2 ks_* \sim \cos(2ks_* + \pi)$. On the other hand, the TE cross-spectrum behaves as $\cos ks_* \sin ks_* \sim \cos(2ks_* + 3\pi/2)$.

temperature fluctuations are given by [51]:

$$\left.\frac{\Delta T}{T}\right|_{\rm ISW} = \int_{\tau_*}^{\tau_0} {\rm d}\tau \ \left[\Psi'(\tau) + \Phi'(\tau)\right] \ , \tag{1.39}$$

where τ_* and τ_0 are the conformal times at the last scattering surface and today, respectively. Notice that this expression can be simplified in the absence of shear stress, since $\Phi \approx \Psi$. The eq. (1.39) admits a simple explanation: when the CMB radiation falls down in a potential well (or climbs a potential hill) during its propagation from the last scattering surface to the observer, it suffers a gravitational redshift which changes its temperature. If the potentials do not evolve ($\Psi' + \Phi' = 0$), then the net effect over the photons cancel out, and the temperature fluctuations vanishes. However, if the value of $\Psi + \Phi$ when the photon starts crossing the potential well (or hill) is different from the corresponding value when the photon leaves the gravitational field, there is an overall non-zero redshift which changes the temperature of the CMB radiation.

The potentials are constant in the matter domination era, and hence the ISW effect vanishes during this period. However, the radiation is the main component of the Universe at early times, where the photon pressure makes the potentials decay inside the sound horizon. Since the radiation still has influence on the background dynamics at the recombination epoch, there exists a non-zero contribution to the integral in eq. (1.39) from times between τ_* and the matter domination epoch. Likewise, the ISW effect generated in this period affects only to the range of scales corresponding to the sound horizon between these two times. This effect on account of the evolution of the potentials near the last scattering surface is called early ISW.

Moreover, the potential also decays due to the influence of the dark energy at recent times. The accelerated expansion in this period prevents the growth of the density perturbations and, as in the case of the radiation-dominated era, the gravitational potential decays generating temperature fluctuations from the ISW effect. Since the dark energy density started to drive the background dynamics recently, the ISW anisotropies from the dark energy peaks at the largest scales observed today. This particular effect is called late ISW, in contrast to the ISW caused by the variation of the potentials at the last scattering surface at earlier times.

Finally, the integrated Sachs-Wolfe effect applied to tensor perturbations leads to temperature anisotropies at large scales, which are caused by the time evolution of the metric due to the gravitational waves.

- *Gravitational lensing:*

One of the consequences of general relativity theory is that the light trajectories are curved when the photons pass through a gravitational source. In the weak lensing approach, the observed photons coming from the direction $\mathbf{n}$ are deviated to the position $\mathbf{n}+\nabla\phi(\mathbf{n})$, where $\phi(\mathbf{n})$ is the projected potential given by [63, 64]:

$$\phi(\mathbf{n}) = -2\int_0^{r_*} \mathrm{d}r \; \frac{f_\kappa(r_*-r)}{f_\kappa(r_*)f_\kappa(r)}\Psi(r\mathbf{n}, r_0-r) \; , \tag{1.40}$$

where $f_\kappa(r)$ is the transverse comoving distance as a function of the curvature of the FLRW universe κ at the comoving distance r. In this equation, $\Psi(\mathbf{r},\tau)$ is the gravitational potential at the comoving position $\mathbf{r}$ and conformal time τ. The deflection angle given by $\nabla\phi$ causes distortions on the CMB which affect to the smaller scales.

Besides the deflection, the gravitational lensing rotates the polarization of the CMB photons such that the power is transferred from the E-mode to the B-mode, and vice versa. Moreover, this fact creates a non-zero cross-power spectrum between E and B, which initially vanishes due to parity invariance.

- *Reionization effects:*

  After recombination, the photons do not scatter with other particles, since there is no free electrons in the medium. During this era, known as dark ages, the Universe expands and the CMB radiation becomes colder. However, the gravity forms structures and high-density regions by gravitational collapse, where atoms are ionised again. This reionization process occurs around $z \sim 8$ [65]. The scattering of photons erases the CMB perturbations, leading to a rescaling of the amplitude by $e^{-\tau}$, where τ is the reionization optical depth. Besides, Thomson scattering from reionization generates linear polarization in the CMB photons, which enhances the power at large scales in the E and B polarization modes. By using combined temperature and polarization data, the effect of reionization can be distinguished from a change in the amplitude of the primordial perturbations.

  Moreover, energy is transferred from the hot gas of electrons in galaxy clusters to the CMB photons through the inverse Compton scattering. This process, called Sunyaev-Zel'dovich effect (or simply SZ effect), results in a change of the frequency of the photons causing distortions in the black-body spectrum of the CMB [66, 67]. Depending whether the high energy of the electrons comes from the gas temperature or the peculiar motion of the cluster, two different SZ effects are differentiated: thermal and kinetic. The kinetic Sunyaev-Zel'dovich (kSZ) effect in the linear regime is also known as the Ostriker-Vishniac (OV) effect [68].

1.3.3 CMB observations

In the harmonic decomposition of the CMB temperature, the monopole ($\ell = 0$) has the greatest amplitude (~ 1 K), which evidences the high level of isotropy of the CMB radiation. But additionally, the movement of the solar system with respect to the comoving frame of the CMB introduces a Doppler effect on the CMB photons, which also dominates over the primordial perturbations. This effect is observed as a dipolar pattern ($\ell = 1$) aligned with our peculiar velocity [69], whose direction corresponds to $(l, b) = (264°, 48°)$ in Galactic coordinates. Whilst the amplitude of the dipole is $\sim 10^{-3}$ K, the level of the primordial fluctuations is around $\sim 10^{-5}$ K. Moreover, the deflection of photons due to the aberration and modulation effects caused by our peculiar velocity induces distortions on the CMB at small scales and affects at all the multipoles [70].

The CMB is observed in the microwave range of the electromagnetic spectrum. At these wavelengths, there are different foreground emissions from our Galaxy besides the primordial CMB fluctuations, as the synchrotron, free-free or dust. In addition, there exists extragalactic radiation, as the Cosmic Infrared Background (CIB) or the emission from point sources. The general procedure to remove all these contaminants is to exploit the fact that their temperature depends on the frequency, unlike the CMB, whose thermodynamic temperature is independent of the frequency band. The r.m.s. of the brightness temperature[3] as a function of the frequency for the different foregrounds components and the CMB are shown in Figure 1.4. For this reason, it is important that the CMB experiments measure the temperature and polarization at different frequencies in order to characterize the foreground emission and separate the CMB signal from other components.

The first detection of the primordial CMB fluctuations was in 1992 by the Cosmic Background Explorer (COBE) satellite [71]. The resolution of the Differential Microwave Radiometer (DMR) instrument aboard COBE was around 7°, allowing the measurement of the multipoles up to 20. The amplitude of the temperature perturbations found by COBE was around 6×10^{-6} with an spectral index $n_s = 1.1 \pm 0.5$[4], which is in agreement with the scale invariant power spectrum proposed by Harrison and Zel'dovich

[3] The brightness temperature is defined as:

$$T_B = \frac{c^2}{2k\nu^2} B(\nu) \ ,$$

where $B(\nu)$ is the spectral radiance of the source. If $B(\nu)$ is the black-body radiance corresponding to the thermodynamic temperature T, then $T_B \approx T$ for frequencies satisfying that $h\nu \ll kT$.

[4] The amplitude of the curvature power spectrum, in terms of the temperature fluctuations found by COBE, was

$$A_s = 25 \left(\frac{\Delta T}{T} \right)^2 \sim 10^{-9} \ ,$$

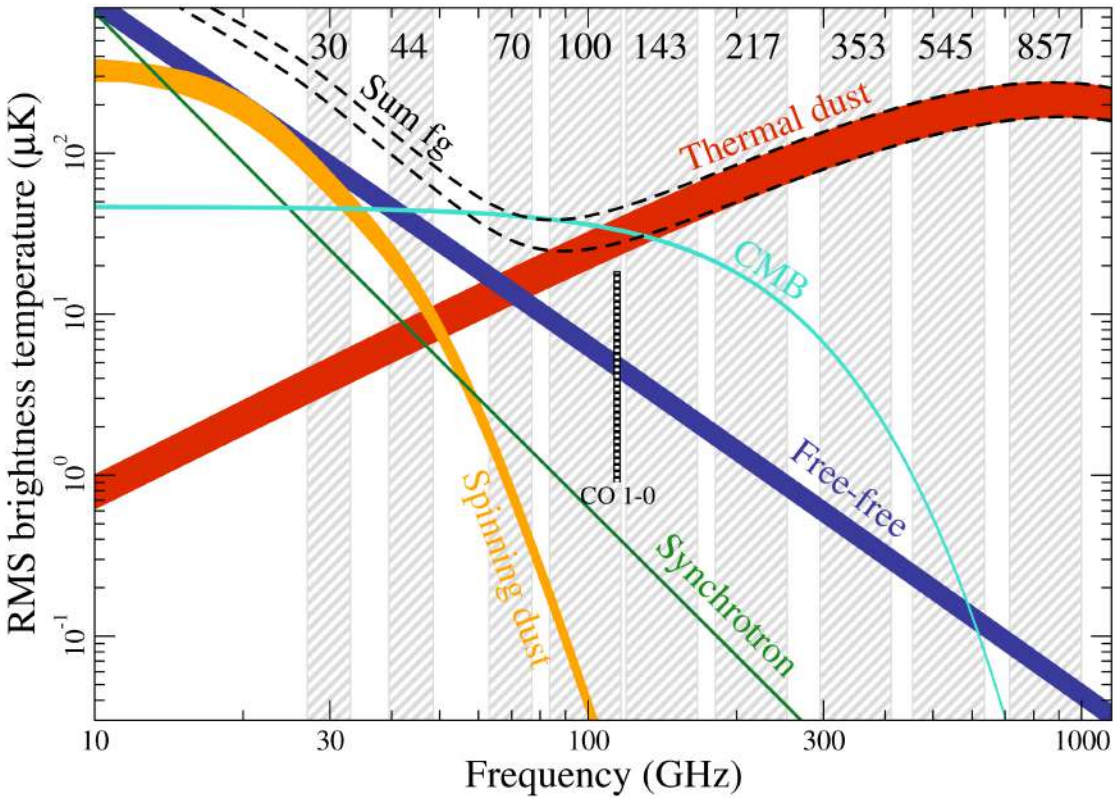

FIGURE 1.4: Brightness temperature as a function of the frequency for the CMB and the Galactic foregrounds. The frequency bands correspond to the ones used in the *Planck* experiment [47]. Reprinted from the ESA image archive.

[17, 18]. Additionally, COBE was provided with the Far-InfraRed Absolute Spectrometer (FIRAS), an instrument which was able to measure the CMB spectrum and temperature with high precision [72–75]. The CMB black body temperature obtained by combining different experiments is [75]:

$$T_{\rm CMB} = 2.72548 \pm 0.00057 \text{ K} \ . \tag{1.41}$$

In 2006, G. Smoot and J. Mather (the principal investigators of the DMR and FIRAS instruments, respectively) were awarded the Nobel prize in physics due the measurements of the CMB performed by the two experiments.

After the important detection of the CMB temperature anisotropies, the next step was to detect the acoustic peaks caused by the interactions in the photon-baryon plasma before recombination. A detection of the first acoustic peak would imply that the primordial perturbations are mostly adiabatic, as it is derived from inflation. On the contrary, other models for structure formation, as topological defects, predict incoherent isocurvature modes, leading to a suppression and a shift of the first acoustic peaks to smaller scales

where we have used that the temperature perturbations are given by the Sachs-Wolfe effect, which gives $\Delta T/T = \Phi/3 = \mathcal{R}/5$ in the matter domination epoch.

($\ell \approx 400 - 500$) [76–78]. Finally, the first acoustic peak was observed at $\ell \approx 200$ with an amplitude around 75 μK by the Toco [79], Balloon Observations Of Millimetric Extragalactic Radiation and Geomagnetics (BOOMERanG) [80] and the Millimeter-wave Anisotropy eXperiment IMaging Array (MAXIMA) [81] experiments, constraining the curvature of the Universe to be nearly flat. Subsequently, the second and third peaks were detected at multipoles $\ell \approx 550$ and $\ell \approx 800$, respectively, by the Degree Angular Scale Interferometer (DASI) [82] and other experiments [83, 84]. All these observations favour the hypothesis that the primordial perturbations could be mainly caused by inflation rather than cosmic defects.

On the other hand, the amplitude of the temperature perturbations at small scales ($\ell = 400 - 1500$) was measured for the first time by the Cosmic Background Imager (CBI), providing a detection of the Silk damping effect [56].

After the launch of COBE, the next satellite in orbit whose purpose is to measure the CMB anisotropies was the Wilkinson Microwave Anisotropy Probe (WMAP) [85], whose instrument measures the microwave radiation in the 5 frequency bands in the range $23 - 94$ GHz. The full-sky maps provided by this experiment allowed constraining the cosmological parameters with high precision, confirming the ΛCMB as the preferred cosmological model [86, 87]. Nevertheless, the WMAP team found evidences of some anomalies in the CMB at large scales [88], which have been studied deeply in the literature (see Section 1.3.4).

The resolution and sensitivity of WMAP were improved by the *Planck* satellite [47], launched in 2009. In this mission, the spacecraft includes two instruments: the High Frequency Instrument (HFI) and the Low Frequency Instrument (LFI), with a total of 9 frequency bands within the range from 30 to 857 GHz (the frequency bands considered in the *Planck* experiment are shown in Figure 1.4). The large number of bands in a wide range of frequencies allows *Planck* to accurately characterize the foreground emission, obtaining high quality CMB maps. Moreover, the resolution of the *Planck* mission is enough to measure the temperature angular power spectra up to $\ell \approx 2500$ [89], improving the constraints on the parameters of the standard cosmological model. Despite that the ΛCMB is still the most likely model, *Planck* confirmed the presence of anomalies at large scales [90, 91], which were first detected in the WMAP data.

Regarding polarization, the first experiment in detecting the CMB polarization signal was DASI [92], which measured the amplitude of the E-mode at 4.9σ confidence level. Later, the same experiment improved these constraints, obtaining a detection of 6.3σ of the EE angular power spectrum, and 2.9σ of the TE cross-spectrum [93]. Moreover, the CBI experiment [94] provided a significant detection of the CMB polarization, observing for the first time the acoustic oscillations in the E-mode and confirming the standard

model prediction that the acoustic peaks in polarization are out-of-phase with respect to the temperature ones. On the other hand, the WMAP team measured the TE cross-power spectrum with high accuracy in the first-year results [95], observing that there exists an anticorrelation between temperature and polarization on degree angular scales ($\ell \sim 150$). This fact is a distinctive signature of adiabatic superhorizon fluctuations at decoupling, as predicted by inflationary models [96, 97].

Since the effect of the reionization optical depth on the intensity is degenerated with the amplitude of the primordial perturbations, the determination of the shape of the polarization spectra is especially important to constrain the value of τ. In TE angular cross-power spectrum measured by WMAP, it is observed an excess of power at large scales ($\theta > 10^{\circ}$). When these data are used to constrain the reionization optical depth, a best-fit of $\tau = 0.17 \pm 0.04$ is obtained, corresponding to a reionization redshift $11 < z_r < 30$ [95]. However, in the next release, the excess in the TE spectrum was reduced by improving the map making and the power spectrum estimation [98], leading to a value the optical depth $\tau = 0.09 \pm 0.03$ ($z_r = 10.9$) by adding also the information of the EE and the TT power spectra. Recently, the *Planck* collaboration published a significant lower value, $\tau = 0.058 \pm 0.012$, determining that the reionization occurs at the average redshift within the interval $z_r = 7.8 - 8.8$ [65].

On the other hand, the secondary B-mode due to the gravitational lensing effect was detected by South Pole Telescope (SPT) [99] for the first time, and later measured by other experiments [100, 101]. However, the B-mode coming from the primordial tensor perturbations is only constrained with upper limits. Constraints on the tensor-to-scalar ratio from measurements of the BB spectrum lead to an upper bound $r < 0.09$ at 2σ level, for the pivot scale $k_0 = 0.05$ Mpc^{-1} [38].

1.3.4 CMB anomalies and beyond the standard model

The anisotropies in the Cosmic Microwave Background (CMB) are described inside the standard model of cosmology, which assumes that the initial perturbations are distributed according to a Gaussian in a homogeneous and isotropic Universe. The recent measurements of the CMB allow one to determine the cosmological parameters with high precision [8], showing an overall agreement between data and the concordance cosmological model. Although, in general, this agreement is good, some anomalies are found in the CMB at large scales. The characterization of these deviations have an important role in understanding the process which leads to the initial perturbations, and hence, in the characterization of the inflationary model.

Different large-scale anomalies are found in the CMB, which were first detected in the WMAP data ([88], see also references below) and confirmed later by *Planck* [91]. All these anomalies have the common property that are especially dominated by the large scale behaviour of the CMB.

- *Hemispherical asymmetry*

  An hemispherical asymmetry is observed aligned with the ecliptic axis in terms of the amplitudes of the power spectrum in opposing hemispheres [102]. In particular, it is noticed a lack of power at large scales ($\ell \leq 64$) in the northern ecliptic hemisphere. Moreover, the hemispherical asymmetry is also detected when smaller scales are considered ($\ell \leq 600$), obtaining that the region with maximum power is located at $(l, b) = (226^\circ \pm 10^\circ, -17^\circ \pm 10^\circ)$ [103].

- *Dipole modulation:*

  A dipole modulation of the CMB signal was proposed as an explanation of the hemispherical asymmetry [104]. In this model, the observed temperature is parametrised as:

  $$T(\mathbf{n}) = [1 + A\,(\mathbf{p} \cdot \mathbf{n})]\, T_{\rm iso}(\mathbf{n}) \ , \tag{1.42}$$

  where A is the amplitude of the modulation, $\mathbf{p}$ is the unit vector indicating the dipole direction and $T_{\rm iso}$ is an auxiliary temperature field, which is supposed to be isotropic. The observed dipole direction is $(l, b) = (224^\circ, -22^\circ)$ in Galactic coordinates with an amplitude $A = 0.072 \pm 0.022$ [105] by using multipoles $\ell \leq 64$. A more detailed analysis was performed in the harmonic space taking into account the scale dependence in [91, 106], finding similar results. The direction of the dipolar modulation is consistent with the location of the region with maximum power inferred from the hemispherical asymmetry analysis [102, 103].

- *Parity asymmetry:*

  Parity asymmetries have been also analysed concluding that there exists a difference in the variance of the odd and even components of the temperature field [107–109]. In these studies, the parity components are defined as:

  $$T^{\pm}(\mathbf{n}) = \frac{T(\mathbf{n}) \pm T(-\mathbf{n})}{2} \ . \tag{1.43}$$

  The multipoles contributing to the fields T^+ and T^- are the even and odd multipoles, respectively. Therefore, the estimators of the parity asymmetry are based on the comparison of the angular power spectrum C_ℓ for values of ℓ with different parity [107, 108]. The results indicate that the odd component of the temperature field has more power than the even one, finding that this asymmetry is particularly

important at large scales ($\ell \leq 22$). However, the same analysis applied to E and B do not reveal a parity asymmetry in polarization [109].

Since the correlation function at π radians is given by

$$C(\pi) = \sum_{\ell=0}^{\ell_{\max}} \frac{2\ell+1}{4\pi} (-1)^{\ell} C_{\ell} \ , \tag{1.44}$$

and the value of C_ℓ is higher for the odd multipoles, the parity asymmetry anomaly can be related to the lack of power at large scales [110].

Additionally, the parity asymmetry studies have been extended including a directional dependence in several works [111, 112], indicating that the preferred axis for parity violations could correspond to the quadrupole and octopole alignment direction [113].

- *Quadrupole and octopole alignment:*

  When the temperature field is expanded in terms of the spherical harmonics, an unlikely alignment between the quadrupole and the octopole is observed [90, 113]. In general, the direction $\mathbf{n}_\ell$ associated to each multipole can be calculated by maximising the quantity [114]:

$$\sum_{m=-\ell}^{\ell} m^2 |a_{\ell m}(\mathbf{n})|^2 \ , \tag{1.45}$$

  which represents the angular momentum dispersion. In this expression, $a_{\ell m}(\mathbf{n})$ are the spherical harmonic coefficients corresponding to the system of reference in which the z axis is oriented in the direction given by $\mathbf{n}$. For the quadrupole and octopole, these directions are aligned such that its scalar product is very close to one ($\mathbf{n}_2 \cdot \mathbf{n}_3 \approx 0.99$), whose probability is 1% [90]. The direction of alignment of these two vectors is $(l, b) \approx (240°, 65°)$ in Galactic coordinates.

  The interference between the quadrupole and the octopole produce large-scale features in the CMB temperature aligned with the ecliptic plane, which, in particular, have more power in the southern hemisphere [113]. Therefore, the asymmetry induced by the quadrupole-octopole alignment may be related to the hemispherical asymmetry [102, 103].

- *Low variance:*

  A variance of the CMB temperature field lower than expected from Gaussian simulations is observed in the data [115], which is especially evident at largest scales with a p-value of $\approx 0.5\%$. In terms of the angular power spectrum, the low variance anomaly can be seen as a deficit of power in the lowest multipoles, in particular,

the quadrupole and octopole have an important impact on the analysis [116]. This kind of suppression could be explained with by an early fast-roll phase of the inflaton, which reduces the primordial power spectrum at large scale, preceding the standard slow-roll phase [117, 118].

- *Lack of correlation at large scales:*

  In addition, the two-point correlation function of the CMB temperature presents a deficit of power at scales $\theta > 60°$ [119, 120]. This anomaly can be quantified by the estimator [88]:

  $$S_x = \int_{-1}^{x} \mathrm{d}\cos\theta \; C(\theta)^2 \; , \tag{1.46}$$

  where $C(\theta)$ is the correlation function. In particular, the quantity $S_{1/2}$ (for which the integration limits are within the $60° - 180°$ interval) has been used previously in the literature [88, 91, 120]. The p-value for the estimator $S_{1/2}$ is around 0.5% [91].

- *The Cold Spot:*

  A non-Gaussian deviation is observed at the scale $R \approx 5°$ by performing a multi-scale analysis using the Spherical Mexican Hat Wavelet (SMHW) [121]. This deviation is associated to a particular peak, called the Cold Spot (CS), [122, 123] located at $(l, b) = (210°, -57°)$, whose significance of the CS anomaly is about 1% [91, 124]. The CS shows unusual properties in terms of the mean angular profile or the area of wavelet coefficients above a certain threshold [91]. Regarding its shape, it is found that the Cold Spot is essentially circular by using a modification of the SMHW for the study of non-spherical features [124].

  Different physical mechanisms have been proposed to explain the Cold Spot anomaly, as cosmic bubble collision [125–127], the gravitational evolution of a cosmic texture [128], and alternative inflationary models [129]. In addition, the temperature fluctuations on the CMB caused by voids through the ISW effect have been also studied in the literature as possible explanations of the Cold Spot [130–137]. Analysis of the ISW effect for different modelling of the void underdensity and modifications of the dark energy equation of state are addressed in Chapter 5.

Chapter 2

The shape of CMB temperature and polarization peaks on the sphere

We present a theoretical study of CMB temperature peaks, including its effect over the polarization field, and allowing nonzero eccentricity. The formalism is developed in harmonic space and using the covariant derivative on the sphere, which guarantees that the expressions obtained are completely valid at large scales (i.e., no flat approximation). The expected patterns induced by the peak, either in temperature or polarization, are calculated, as well as their covariances. It is found that the eccentricity introduces a quadrupolar dependence in the peak shape, which is proportional to a complex bias parameter b_ϵ, characterizing the peak asymmetry and orientation. In addition, the one-point statistics of the variables defining the peak on the sphere is reviewed, finding some differences with respect to the flat case for large peaks. Finally, we present a mechanism to simulate constrained CMB maps with a particular peak on the field, which is an interesting tool for analysing the statistical properties of the peaks present in the data.

2.1 Introduction

The cosmic microwave background (CMB) radiation is one of the most important sources of cosmological information. In particular, the statistical properties of the CMB fluctuations are essential to understand the primordial Universe. In order to explain the observations, a phase of inflationary expansion in the early Universe has been postulated. Within the standard frame, this inflation mechanism also generates the initial matter

perturbations which are the seeds of the cosmic structures observed nowadays. It is believed that the initial perturbations generated by the standard inflationary models are nearly Gaussian. For this reason, the 2-point correlation functions of the temperature and polarization CMB anisotropies have most of the cosmological information which can be obtained from the primordial fluctuations. The temperature angular power spectrum of the CMB has been recently determined by the Planck mission with high accuracy [89]. Regarding the primordial CMB polarization, only the gradient part of the polarization field (E-mode) has been detected up to $\ell \sim 2000$. Although the effect of the gravitational lensing on the curl of the polarization field (B-mode) has been observed [99, 100], there is still no evidence of the primordial B-mode induced by the tensor perturbations [138, 139]). On the whole, the agreement of the CMB data with the cosmological standard model is high [8]. However, there are several anomalies at large scales which are still unexplained [91].

One of the alternative observables which can be used to study the perturbations is the statistical properties of peaks. In the case of the matter field, it is important to understand the properties of overdensity peaks because that is where the collapse of structures takes place. In a seminal work [140], the statistics of peaks for Gaussian fields in three dimensions is developed. There are several aspects of peaks which can be analysed, for instance, the number of peaks, the peak shape or their correlation function. One important result from peak theory is that the peak correlation function is related to the underlying matter distribution through a non-local bias [141]. The understanding of the peak correlation function and its bias relation to the matter field is also important to study the baryon acoustic oscillations [142].

In order to study the CMB temperature extrema, the three-dimensional formalism of peaks was later particularised in [143] to the case of scalar fields on the sphere (see also [144]). However, a full analysis including polarization is needed for a complete understanding of the CMB fluctuations. The radial profiles of the Stokes parameters were described in [145]. Nevertheless, these profiles are calculated using the small-angle limit and the peaks are considered spherically symmetric. Recently, an analysis of the CMB temperature and polarization Planck data, including peak eccentricity, has been published [91]. The studies in [145] and [91] based on the stacking of peaks do not reveal significant deviations from the standard model, except a shift in the temperature profile which could be associated to the power deficit at large scales. Non-standard scenarios including parity violations [146] or cosmological birefringence [147] can also be tested using the stacking of temperature peaks in polarization.

In this chapter, we present a comprehensive study of the CMB peaks on the sphere including polarization and allowing different eccentricities. The derivation followed in

this work is based on the spherical harmonic coefficients, instead of the real space. This allows one to obtain expressions which are completely valid at large scales, where the flat approximation breaks. In addition, the formalism in harmonic space opens the possibility of generating constrained CMB simulations with a peak at some point of the sphere with the desired characteristics. Besides the peak shapes, the extrema statistics is reviewed for the case of a Gaussian scalar field on the sphere. It is found that the probability and the number density of large peaks is modified with respect to the calculations in [143]. Finally, we notice that the approach addressed in this work is completely general and it can be applied to any scalar Gaussian field on the sphere, taking into account its correlation with any other scalar or spin-2 field.

This chapter is organized as follows: in section 2.2, we introduce the covariant derivatives in terms of the spherical harmonic coefficients in order to define the peak degrees of freedom on the sphere. In section 2.3, it is explained the methodology used to separate the variables defining the peak from the rest of the Gaussian random field. Additionally, the statistics of extrema on the sphere is reviewed in section 2.4, finding some differences with respect to previous calculations. The shape of CMB peaks including polarization for different values of mean curvature and eccentricity is analysed in section 2.5, whilst its covariance is calculated in section 2.6. The expressions of the peak patterns are given in terms of the angular power spectra, which allows calculating them in a simple way. The physical description of the peak profiles is discussed in section 2.7. Furthermore, in section 2.8, a way to simulate peaks on the sphere, which is one of the applications of the formalism developed in this work, is derived.

2.2 Derivatives of a scalar field on the sphere

A peak on the sphere is defined through its derivatives up to second order. In general, any field on the sphere can be expanded in terms of the spherical harmonics:

$$T(\theta,\phi) = \sum_{\ell=0}^{\infty} a_{\ell m}\, Y_{\ell m}(\theta,\phi)\ . \tag{2.1}$$

The first step in our analysis is to express the derivatives in terms of the spherical harmonic coefficients $a_{\ell m}$. For simplicity, we consider that the peak is located at the north pole. The value of the field at this point can be written in the following way:

$$T = \sum_{\ell=0}^{\infty} \sqrt{\frac{2\ell+1}{4\pi}} a_{\ell 0}\ . \tag{2.2a}$$

In order to calculate derivatives on the sphere, we use the spin raising and lowering operators $\eth$ and $\eth^*$, which are proportional to the covariant derivatives in the helicity basis (see Appendix A.1 for a more detailed description of the derivatives on the sphere). If we consider the local system of reference at any point of the sphere, then the derivatives with respect to the Cartesian coordinates correspond to the real and imaginary parts of the lowering operator, that is $\eth^* = -\partial_x + i\partial_y$ (similarly, the spin raising operator verifies $\eth = -\partial_x - i\partial_y$). Here, we have assumed that the basis vectors $\mathbf{e}_x$ and $\mathbf{e}_y$ correspond to the vectors $\mathbf{e}_\theta$ and $\mathbf{e}_\phi$ of the spherical coordinate system, respectively. Thus, the first derivatives at this point are written as

$$\eth^* T = \sum_{\ell=0}^{\infty} \sqrt{\frac{2\ell+1}{4\pi}} \sqrt{\frac{(\ell+1)!}{(\ell-1)!}} a_{\ell 1} \ . \tag{2.2b}$$

This quantity is a complex number whose real and imaginary parts correspond to the derivatives in each orthogonal direction at the north pole. Finally, the second derivatives are encoded in the Hessian matrix (see eq. (A.6)). It is convenient to separate the trace and the traceless parts of this matrix, because these two quantities transform in a different way under rotations. The trace corresponds to the Laplacian,

$$\nabla^2 T = \eth^* \eth T = -\sum_{\ell=0}^{\infty} \sqrt{\frac{2\ell+1}{4\pi}} \frac{(\ell+1)!}{(\ell-1)!} a_{\ell 0} \ , \tag{2.2c}$$

and the traceless part is given by

$$(\eth^*)^2 T = \sum_{\ell=0}^{\infty} \sqrt{\frac{2\ell+1}{4\pi}} \sqrt{\frac{(\ell+2)!}{(\ell-2)!}} a_{\ell 2} \ . \tag{2.2d}$$

In the local system of reference, this operator is given by $(\eth^*)^2 = \partial_x^2 - \partial_y^2 - i2\partial_x\partial_y$. Although this operator is a complex quantity, the imaginary part can be set to zero with a rotation of the xy plane. Physically, this corresponds to choose the principal axes of the peak as the reference system. From the real part, it can be shown that the operator $(\eth^*)^2$ represents a measure of the anisotropy at the centre of the peak.

The $a_{\ell m}$ coefficients are m-spin quantities under rotations of the z axis. That is, if we rotate by an angle α, the $a_{\ell m}$ coefficient transforms as $a_{\ell m} e^{im\alpha}$. Looking at the expression of the field derivatives in terms of the spherical harmonic coefficients, it is possible to deduce that, whilst T and $\nabla^2 T$ are scalars, $\eth^* T$ is a vector and $(\eth^*)^2 T$ is a 2-spin tensor. Since tensors with different rank are statistically independent under the assumption of isotropy, then only the scalars T and $\nabla^2 T$ are correlated, while $\eth^* T$ and $(\eth^*)^2 T$ are uncorrelated with the rest of the field derivatives.

For simplicity, we normalize the field derivatives in order to have unit variance:

$$\nu \equiv \frac{T}{\sigma_\nu} \ , \qquad \kappa \equiv -\frac{\nabla^2 T}{\sigma_\kappa} \ , \tag{2.3a}$$

$$\eta \equiv \frac{\eth^* T}{\sigma_\eta} \ , \qquad \epsilon \equiv \frac{(\eth^*)^2 T}{\sigma_\epsilon} \ , \tag{2.3b}$$

where the expressions of the variances are given in the Appendix A.2. These parameters denote the peak degrees of freedom throughout the chapter. The parameter ν represents the peak height, whereas the normalized Laplacian κ is the mean curvature of the peak. The parameter η is a complex number whose components are the first derivatives at the peak location. Hereafter, we set $\eta = 0$ in order to have a critical point. Finally, the value of ϵ gives information about the eccentricity of the peak. In particular, its modulus is proportional to the square of the eccentricity, and its phase is twice the orientation angle with respect to the reference system (see more details in Appendix A.2).

Using eqs. (2.2), the peak variables can be expanded in terms of the spherical harmonic coefficients, which are normalized to have unit variance:

$$\nu = \sum_{\ell=0}^{\infty} \nu_\ell a_{\ell 0} \ , \qquad \kappa = \sum_{\ell=0}^{\infty} \kappa_\ell a_{\ell 0} \ , \tag{2.4a}$$

$$\eta = \sum_{\ell=0}^{\infty} \eta_\ell a_{\ell 1} \ , \qquad \epsilon = \sum_{\ell=0}^{\infty} \epsilon_\ell a_{\ell 2} \ , \tag{2.4b}$$

where the multipolar coefficients ν_ℓ, κ_ℓ, η_ℓ and ϵ_ℓ are defined in the Appendix A.2 (eqs. (A.9)).

2.3 Uncorrelating the peak variables

The aim of this section is to separate the peak degrees of freedom from the rest of the information of the field. For this purpose, we transform the $a_{\ell m}$ coefficients into a new set of variables containing the peak degrees of freedom (ν, κ, η and ϵ) and an ensemble of new variables $\hat{a}_{\ell m}$ without any peak information. The $\hat{a}_{\ell m}$ variables are defined for all values of ℓ except for four given multipoles ℓ_ν, ℓ_κ, ℓ_η and ℓ_ϵ, in order to preserve the total number of degrees of freedom.[1] We choose the variables $\hat{a}_{\ell m}$ such that its correlation with the peak variables vanishes, using an orthogonalization process. For convenience, we normalize the $a_{\ell m}$ coefficients such that they have unit variance. The

[1] In principle, the multipoles ℓ_ν, ℓ_κ, ℓ_η and ℓ_ϵ are chosen arbitrarily with the condition that $\nu_{\ell_\nu}, \kappa_{\ell_\kappa}, \eta_{\ell_\eta}, \epsilon_{\ell_\epsilon} \neq 0$, such that the change of variables is not singular.

change of variables is given by:

$$\hat{a}_{\ell 0} = a_{\ell 0} - \begin{pmatrix} a_{\ell_\nu 0} & a_{\ell_\kappa 0} \end{pmatrix} P^{-1} \begin{pmatrix} \nu_\ell \\ \kappa_\ell \end{pmatrix} \quad (\ell \neq \ell_\nu, \ell_\kappa) \ , \tag{2.5a}$$

$$\hat{a}_{\ell 1} = a_{\ell 1} - a_{\ell_\eta 1} \frac{\eta_\ell}{\eta_{\ell_\eta}} \quad (\ell \neq \ell_\eta) \ , \tag{2.5b}$$

$$\hat{a}_{\ell 2} = a_{\ell 2} - a_{\ell_\epsilon 2} \frac{\epsilon_\ell}{\epsilon_{\ell_\epsilon}} \quad (\ell \neq \ell_\epsilon) \ , \tag{2.5c}$$

$$\hat{a}_{\ell m} = a_{\ell m} \quad (m > 2) \ . \tag{2.5d}$$

The peak variables only affect to the multipoles $m = 0, 1, 2$, and therefore the $a_{\ell m}$ coefficients with $m > 2$ remain unchanged. The matrix P in eq. (2.5a) is the pivot matrix given by

$$P = \begin{pmatrix} \nu_{\ell_\nu} & \nu_{\ell_\kappa} \\ \kappa_{\ell_\nu} & \kappa_{\ell_\kappa} \end{pmatrix} \ . \tag{2.6}$$

Notice that the variables $\hat{a}_{\ell m}$ are not the coefficients of the standard spherical harmonics expansion. The inverse relations between $a_{\ell m}$ and $\hat{a}_{\ell m}$ are calculated from eqs. (2.5) with a little bit of algebra:

$$a_{\ell 0} = \hat{a}_{\ell 0} + \begin{pmatrix} \nu_\ell & \kappa_\ell \end{pmatrix} \Sigma^{-1} \left[\begin{pmatrix} \nu \\ \kappa \end{pmatrix} - \sum_{\ell'=0}^{\infty} \begin{pmatrix} \nu_{\ell'} \\ \kappa_{\ell'} \end{pmatrix} \hat{a}_{\ell' 0} \right] \ , \tag{2.7a}$$

$$a_{\ell 1} = \hat{a}_{\ell 1} + \eta_\ell \left(\eta - \sum_{\ell'=0}^{\infty} \eta_{\ell'} \hat{a}_{\ell' 1} \right) \ , \tag{2.7b}$$

$$a_{\ell 2} = \hat{a}_{\ell 2} + \epsilon_\ell \left(\epsilon - \sum_{\ell'=0}^{\infty} \epsilon_{\ell'} \hat{a}_{\ell' 2} \right) \ , \tag{2.7c}$$

$$a_{\ell m} = \hat{a}_{\ell m} \quad (m > 2) \ . \tag{2.7d}$$

For simplicity, we have assumed that these equations are valid for all ℓ with the prescription that the pivot coefficients $\hat{a}_{\ell_\nu 0}$, $\hat{a}_{\ell_\kappa 0}$, $\hat{a}_{\ell_\eta 1}$, $\hat{a}_{\ell_\epsilon 2}$ are zero. The matrix Σ in eq. (2.7a) is the covariance matrix between ν and κ. As the peak variables are uncorrelated with the $\hat{a}_{\ell m}$ coefficients, it is possible to put constraints in ν, κ, η and ϵ without affecting the rest of the degrees of freedom of the temperature, given by the variables $\hat{a}_{\ell m}$. Once the peak constraints are imposed, the original $a_{\ell m}$ coefficients are recovered using the inverse relation. Notice that this inversion process is analytical and therefore no numerical inversion is needed.

In addition to the temperature field, we can also consider the E and B polarization fields. Although the peak selection is still done in T, the E and B-modes will be affected due to the corresponding correlation between both fields and T. Once we have specified the

peak conditions on the temperature, we need to know what is the conditional probability of E and B, in order to calculate their statistical properties. Although the primordial fluctuations do not introduce correlation between the B-mode and the scalar fields, there could be different physical effects which break the parity invariance of the field and lead to the TB and EB correlations [146, 147]. Within the formalism established in this chapter, we consider the general case where these correlations are non-zero. If the distribution of the temperature and polarization fields is Gaussian, then the conditional probability of E and B given T is a bivariate Gaussian with the following mean values and covariance:

$$\langle e_{\ell m}\rangle = \frac{C_\ell^{TE}}{\sqrt{C_\ell^{TT}}} a_{\ell m} \ , \qquad \langle b_{\ell m}\rangle = \frac{C_\ell^{TB}}{\sqrt{C_\ell^{TT}}} a_{\ell m} \ , \tag{2.8a}$$

$$\mathbf{C} = \begin{pmatrix} C_\ell^{EE} & C_\ell^{EB} \\ C_\ell^{EB} & C_\ell^{BB} \end{pmatrix} - \frac{1}{C_\ell^{TT}} \begin{pmatrix} \left(C_\ell^{TE}\right)^2 & C_\ell^{TE} C_\ell^{TB} \\ C_\ell^{TE} C_\ell^{TB} & \left(C_\ell^{TE}\right)^2 \end{pmatrix} \ , \tag{2.8b}$$

where $e_{\ell m}$ and $b_{\ell m}$ are the spherical harmonic coefficients of E and B respectively. The mean values of the polarization modes are affected by the temperature field, which is described by the $a_{\ell m}$ coefficients in these equations. The constraints on the temperature due to the peak induce a non-zero pattern in the polarization fields. This fact is used in section 2.5 to calculate the shape of peaks in polarization.

2.4 Extrema statistics

In this section we show how to select minima or maxima using the peak variables ν, κ, η and ϵ. In order to have a critical point, the only requirement is to fix the first derivatives to zero, that is, $\eta = 0$. In addition, if we want to have an extremum, additional constraints in the mean curvature κ and in the eccentricity ϵ are needed. In particular, we ensure that the critical point is an extremum by requiring that the eigenvalues of the Hessian matrix have the same sign. This is done by imposing that $|\epsilon| \leq \sqrt{a}|\kappa|$, where $a = \sigma_\kappa^2/\sigma_\epsilon^2$ is the ratio of the variance of the Laplacian $\nabla^2 T$ and that of $(\eth^*)^2 T$. Whether that extremum is a minimum or maximum depends on the sign of the curvature. If $\kappa > 0$, the field will have a maximum, and, if $\kappa < 0$, a minimum (in the case of $\kappa = 0$, the point would be flat up to second order, but the probability of this is zero). These extremum constraints can be imposed by considering the probability of the peak degrees of freedom:

$$P(\nu,\kappa,\epsilon)\ \mathrm{d}\nu\ \mathrm{d}\kappa\ \mathrm{d}^2\epsilon = \frac{2|\epsilon|}{2\pi\sqrt{(1-\rho^2)}} \exp\left[-\frac{\nu^2 - 2\rho\nu\kappa + \kappa^2}{2(1-\rho^2)} - |\epsilon|^2\right]\ \mathrm{d}\nu\ \mathrm{d}\kappa\ \mathrm{d}|\epsilon|\ \frac{\mathrm{d}\alpha}{\pi} \ , \tag{2.9}$$

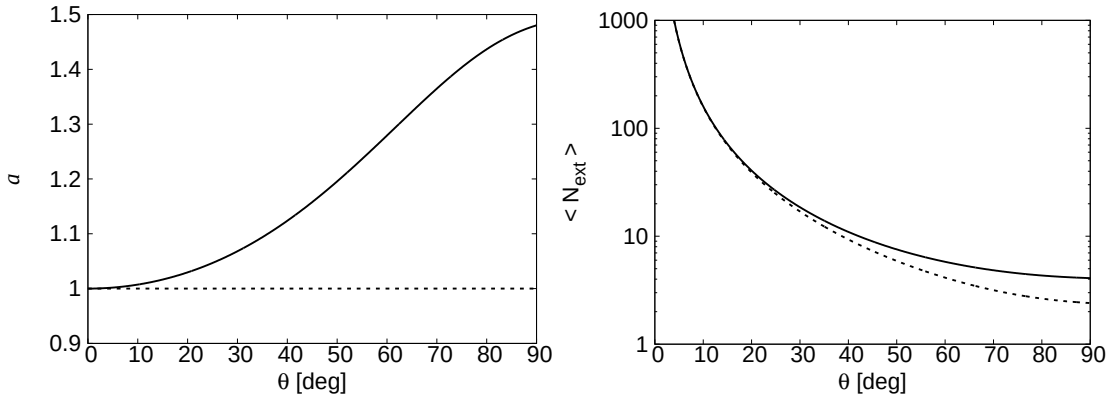

FIGURE 2.1: The parameter $a = \sigma_\kappa^2/\sigma_\epsilon^2$ and the expected number of extrema are depicted as a function of the angluar size of the peak. The solid lines represent the calculation for the sphere, whereas the dashed lines correspond to the flat approximation. In order to select peaks with a given size, the temperature field is filtered by a Gaussian whose FWHM corresponds to the peak scale considered. Notice that in the case of large peaks, for which the flat approximation breaks, it is necessary to use the sterographic projection to relate the FWHM of the Gaussian and the angular size of the peak ($R = 2\tan\theta/2$).

where the eccentricity is given by $\epsilon = |\epsilon|e^{i2\alpha}$, that is, $|\epsilon|$ is the modulus and α is the orientation of the ellipse. Notice that the peak height and the curvature are not independent, with a joint probability given by a multivariate Gaussian, where ρ is the correlation. It is possible to write the correlation as a function of the field variances: $\rho = \sigma_\eta^2/\sigma_\nu\sigma_\kappa$. As the eccentricity is a Gaussian complex number, its modulus follows the Rayleigh distribution, and the orientation angle α is distributed uniformly in the interval $[0, \pi]$.

It is possible to calculate the number density of peaks from the probability density in eq. (2.9). The density of peaks depends on the particular size of the peak, in addition to its probability. For instance, the number of big spots is suppressed because they occupy an area larger than the small ones. Hence, it is expected that small spots are more abundant than large ones. The spot size dependence is introduced through the determinant of the Hessian matrix, which is proportional to the inverse of the square of the spot size. The number density of peaks is given by

$$n(\nu,\kappa,\epsilon)\ \mathrm{d}\nu\ \mathrm{d}\kappa\ \mathrm{d}^2\epsilon = \frac{1}{2\pi\theta_*^2}\left(a\kappa^2 - |\epsilon|^2\right) P(\nu,\kappa,\epsilon)\ \mathrm{d}\nu\ \mathrm{d}\kappa\ \mathrm{d}^2\epsilon\ , \tag{2.10}$$

where $\theta_*^2 = 2\sigma_\eta^2/\sigma_\epsilon^2$. This expression differs from the one in [143] in the a parameter, but we recover it when $a \approx 1$. It is possible to show that there exists the constraint relation $a = 1 + \theta_*^2$ between both parameters. In the small-scale limit, it is possible to consider that $\theta_* \ll 1$, and then $a \approx 1$. Nevertheless, this limit is not valid if the sample is dominated by large spots (see figure 2.1).

The expected total number of extrema on the sphere is obtained by integrating eq. (2.10) over all possible values of ν and κ. However, the integration over the eccentricity ϵ must be done in the region where $|\epsilon| \leq \sqrt{a}|\kappa|$, in order to guarantee that the point is an extremum. The expected total number of extrema is

$$\langle N_{\rm ext} \rangle = 2 \left(1 + \frac{1}{\theta_*^2 \sqrt{3 + 2\theta_*^2}} \right) . \tag{2.11}$$

This number only depends on the value of θ_*. When θ_* is small, the number of extrema is proportional to θ_*^{-2}. In this case, we obtain the result in [143]. But we need to consider the exact formula when the number of peaks is small, or equivalently, when the field is dominated by large peaks. In figure 2.1, the expected number of extrema is represented as a function of the peak size, where it is possible to see that the flat approximation breaks for peaks larger than 30°. In practice, there are only several of such large peaks on the sphere, and therefore the cosmic variance is not significantly reduced by performing a stacking analysis. However, the study of particularly large peaks is still useful to test the properties of the CMB at large scales.

As concrete examples of eq. 2.11, it is possible to check this expression analytically for dipolar and quadrupolar patterns. In the case of the dipole, we assume that $C_1^{TT} \neq 0$ and $C_\ell^{TT} = 0$ for all $\ell \neq 1$. Therefore, the field will have a dipole with random orientation and amplitude. The small-scale limit cannot be taken in this case, since $\theta_*^2 = \infty$. The number of extrema in a dipolar pattern is always 2, independently of the randomness of the field. This fact agrees with the prediction from eq. (2.11) for a random dipole, which is $\langle N_{\rm ext} \rangle = 2$. Repeating the same reasoning for a random quadrupole ($C_2^{TT} \neq 0$ and $C_\ell^{TT} = 0$, for $\ell \neq 2$), we find that $\langle N_{\rm ext} \rangle = 4$, as expected from a quadrupolar pattern which always has 2 maxima and 2 minima. In general, from eq. (2.11) follows that $\langle N_{\rm ext} \rangle \geq 2$, reflecting the fact that there will be always one minimum and one maximum in the sphere at least. This is a consequence of the extreme value theorem applied to the sphere.

We finish this section commenting that there are two ways of assigning probabilities to the peak variables, depending on the physical problem we are addressing. If we are interested in studying the statistical properties of a single peak on the sphere, then we have to use the probability in eq. (2.9). This probability gives the distribution of the peak variables in a single point, independently of any other location on the sphere. On the other hand, sometimes it is useful to sum over a given population of peaks in order to enhance the signal we want to measure. The distribution of the peak variables in this stacking-like procedure is different from the one-point distribution. In this case, the correct way to assign probabilities is given by the number density in eq. (2.10). The

peak variables of the stacked points are distributed on the sphere following the number density, instead of the one-point probability of the peak variables.

2.5 Multipolar profiles

The expected 2-dimensional shape of peaks on the sphere depends on how the peak variables are constrained. Indeed, if the peak degrees of freedom are randomly distributed without any additional constraint, then the expected pattern is zero. It is possible to see the peak shape as an effect of a bias in the peak variables. For instance, if we impose a threshold for the peak height ν, then the randomness of the field is broken and the value of $\langle\nu\rangle$ is different from zero. This bias in the expected value of the peak height generates a non-trivial pattern on the sphere. In this section we only consider the peak height ν, the mean curvature κ and the eccentricity ϵ as the peak degrees of freedom, because the first order derivatives are fixed to zero ($\eta = 0$) by definition of a peak.

The fact that the expected value of the eccentricity $\langle\epsilon\rangle$ could be biased introduces a ϕ dependence in the peak pattern on the sphere. In order to take into account these angular dependence, we expand a generic field on the sphere $X(\theta,\phi)$ in the following way:

$$X(\theta,\phi) = \sum_{m=-\infty}^{\infty} X_m(\theta)\; e^{im\phi}\;. \tag{2.12}$$

The profiles $X_m(\theta)$ represent contributions to the peak with different rotational symmetry. Since the field X is real, it is satisfied that $X_m(\theta)^* = X_{-m}(\theta)$, where the number m is the spin of the profile. The fact that peaks are determined through their derivatives up to second order implies that the profiles with spin $m > 2$ vanish. The dipolar profile with $m = 1$ is also zero because the first derivatives are zero by definition. Only the scalar ($m = 0$) and quadrupolar ($m = 2$) profiles contribute to this expansion.

The inverse transform of eq. (2.12) is

$$X_m(\theta) = \frac{1}{2\pi}\int \mathrm{d}\phi\; X(\theta,\phi)\; e^{-im\phi}\;. \tag{2.13}$$

In particular, the scalar profile $X_0(\theta)$ is the ϕ-average of the field, that is, the standard profile when spherical symmetry is assumed. The quadrupolar profile $X_2(\theta)$ is a correction term due to the asymmetry introduced by the eccentricity of the peak. It is useful to write the multipolar profiles by using the associated Legendre polynomials:

$$X_m(\theta) = \sum_{\ell=m}^{\infty} \sqrt{\frac{2\ell+1}{4\pi}}\sqrt{\frac{(\ell-m)!}{(\ell+m)!}}\; a^X_{\ell m}\; P^m_\ell(\cos\theta)\;. \tag{2.14}$$

In the particular case when the peak is located in the north pole, the coefficients $a^X_{\ell m}$ in this expansion coincide with the spherical harmonics coefficients of the field X.

2.5.1 Profiles in harmonic space

In this subsection, the multipolar profiles for the CMB temperature and polarization are calculated in harmonic space. For simplicity, it is convenient to use the Stokes parameters in polar coordinates with the origin at the centre of the peak. These polar parameters Q_r and U_r are a rotated version of the standard Q and U ones (see [148]). The Q_r field represents radial or tangential polarization patterns around the spot. If the sign of Q_r is positive the polarization is radial, and tangential in the case in which Q_r is negative. On the other hand, U_r represents the polarization rotated 45° with respect to Q_r, as in the standard Stokes parameters. If the peaks are not oriented, then a polarization field with rotational symmetry is expected, and therefore, Q_r and U_r will not depend on ϕ. This is not the case when the polarization field is described using the Cartesian Stokes parameters (examples of the expected patterns in this particular case can be seen in [145] and [91]). The azimuthal dependence introduced in this way is due to the inappropriate choice of the coordinate system, and it does not reflect the rotational symmetry of the polarization field.

The expected value of the multipolar profiles is calculated from eqs. (2.7) and eq. (2.14), taking into account that $\langle \hat{a}_{\ell m} \rangle = 0$. We also assume that the first derivatives are zero ($\langle \eta \rangle = 0$). Therefore, the multipolar profiles $\langle T_m(\theta) \rangle$ only depend on the average of the peak height, mean curvature and eccentricity. Depending on how these mean values are constrained, different shapes are obtained. In order to have a peak, the condition imposed on the expected values of κ and ϵ is the extremum constraint ($|\epsilon| \leq \sqrt{a}|\kappa|$), which guarantees to have a maximum or minimum. In general, there is more freedom in choosing the value of ν. For instance, if we are interested in peaks above a given threshold ν_t, then its expected value must be calculated with the condition that $\nu > \nu_t$. Another possibility is to fix ν to a given value and study the pattern induced by the peak with that particular height. Since in this chapter we are interested in the qualitative behaviour of peaks, this latter approach is used in the calculations.

Additionally, the polarization field of the peak in terms of Q_r and U_r is calculated from the E and B modes. Notice that, if the peak is located at the north pole, then Q_r and U_r coincide with the standard Stokes parameters on the sphere. Therefore, they can be calculated using its expansion in terms of the spin-weighted spherical harmonics.

Firstly, we consider peaks with rotational symmetry. In this case, the only expected contribution comes from the $m = 0$ profile in the multipolar expansion (eq. (2.12)). The

monopolar profiles are therefore given by

$$\langle T_0(\theta)\rangle = \sum_{\ell=0}^{\infty} \frac{2\ell+1}{4\pi} \left[b_\nu + b_\kappa \ell(\ell+1)\right] C_\ell^{TT}\ P_\ell(\cos\theta)\ , \tag{2.15a}$$

$$\langle Q_{r0}(\theta)\rangle = -\sum_{\ell=2}^{\infty} \frac{2\ell+1}{4\pi} \sqrt{\frac{(\ell-2)!}{(\ell+2)!}} \left[b_\nu + b_\kappa \ell(\ell+1)\right] C_\ell^{TE}\ P_\ell^2(\cos\theta)\ , \tag{2.15b}$$

$$\langle U_{r0}(\theta)\rangle = -\sum_{\ell=2}^{\infty} \frac{2\ell+1}{4\pi} \sqrt{\frac{(\ell-2)!}{(\ell+2)!}} \left[b_\nu + b_\kappa \ell(\ell+1)\right] C_\ell^{TB}\ P_\ell^2(\cos\theta)\ , \tag{2.15c}$$

These profiles depend on the bias parameters b_ν and b_κ, which can be calculated from the expected value of ν and κ:

$$\begin{pmatrix} b_\nu \sigma_\nu \\ b_\kappa \sigma_\kappa \end{pmatrix} = \Sigma^{-1} \begin{pmatrix} \langle \nu \rangle \\ \langle \kappa \rangle \end{pmatrix}\ . \tag{2.16}$$

The matrix Σ relating these quantities is the covariance matrix of ν and κ, described in Section 2.3 (see also eq. (A.11)). These profiles obtained for spherical symmetric peaks represent the generalization of the expressions in [145] for large angular distances (see Appendix A.3). As it is expected, the temperature profile depends on the angular power spectrum C_ℓ^{TT}. On the other hand, the coefficients in the multipolar expansion of the Stokes parameters are given by the cross-correlation between the temperature and the polarization fields. In the case of a spherically symmetric peak, it is possible to see that Q_{r0} describes the gradient of the polarization field, while U_{r0} represents the curl contribution. For this reason, Q_{r0} depends exclusively on the correlation of the temperature with E, which is the gradient of the polarization field, and U_{r0} depends on the correlation of T with B, which is the curl contribution. If it is assumed that there is not any physical effect capable of rotating the polarization angle (e.g., birefringence [147]) or violating parity conservation [146] then the correlation between T and B vanishes, and hence the expected value of U_{r0} is zero.

The monopolar temperature profiles for maxima and different values of the peak height are represented in figure 2.2, showing the two effects due to the peak height and curvature biases. The curvature term contributes to the peak only at small scales, just modifying the peakedness of the profile. For large values of ν, the monopolar peak profile tends to be proportional to the temperature correlation function, since the curvature bias becomes negligible (see figure 2.9 and the discussion in section 2.5.3 about the behaviour of the bias parameters). In the case of polarization, we consider only Q_{r0} because the TB power spectrum is zero in the standard model. The monopolar profiles of Q_r for maxima, conditioned to the value of ν, are represented in figure 2.3. As in the temperature case, the contribution to the Q_{r0} profile for high ν comes from the correlation between the

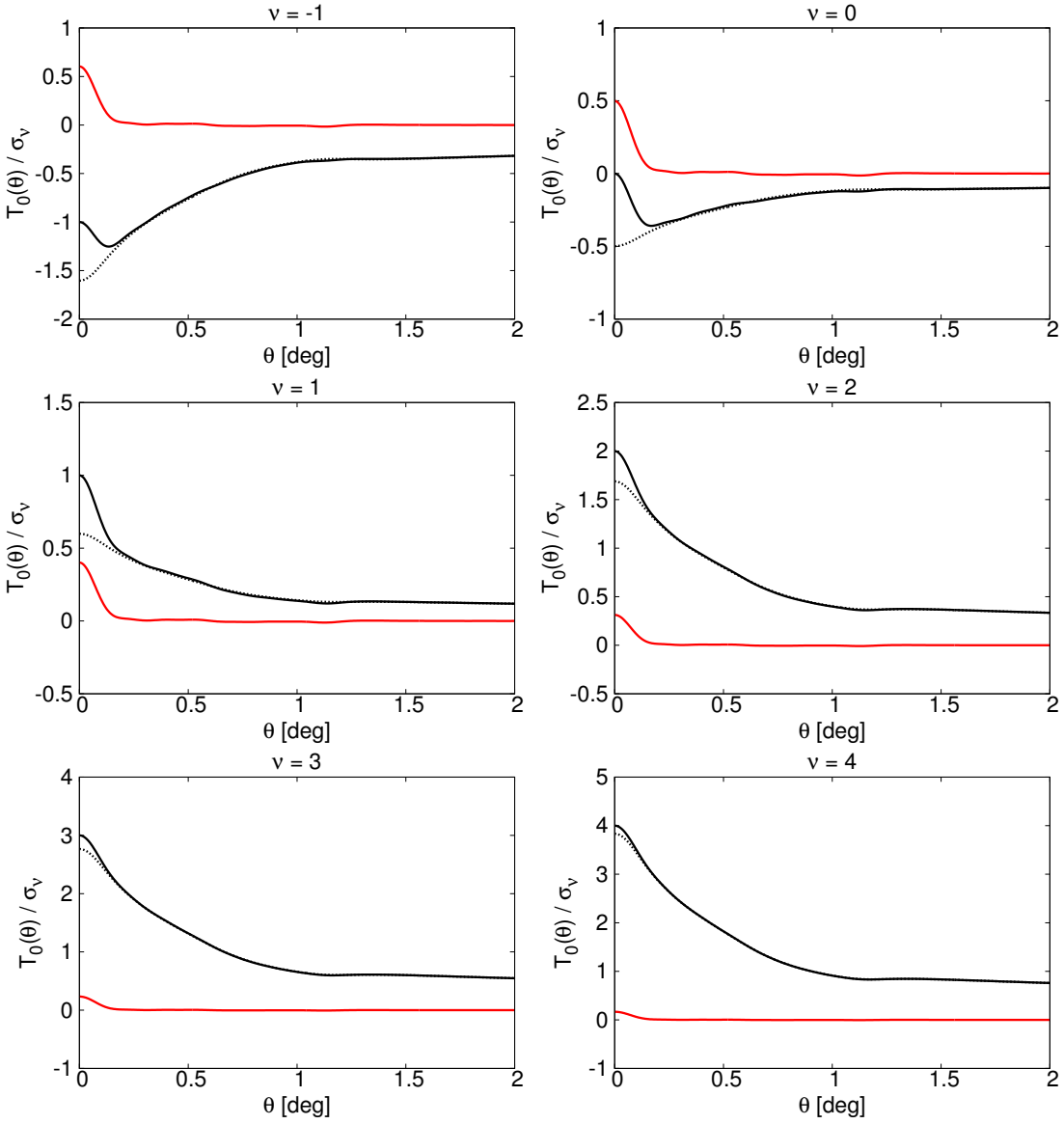

FIGURE 2.2: Spherically symmetric temperature profiles $T_0(\theta)$ for maxima conditioned to different peak heights. The dotted black lines depicts the contribution proportional to the temperature correlation function (peak height bias b_ν), while the red line corresponds to the modification due to its Laplacian (mean curvature bias b_κ). The black solid line represents the total profile.

temperature and Q_r. The effect due to the curvature bias, present in profiles with small ν, tends to modify the peaks of the Q_{r0} profile. The profiles represented in figures 2.2 and 2.3 are calculated for maxima, but equivalent results are obtained for minima.

In the case that $\langle\epsilon\rangle \neq 0$ (e.g., when the peaks are oriented towards some direction), then there is also a contribution to the quadrupolar profile ($m = 2$) in eq. (2.12):

$$\langle T_2(\theta)\rangle = b_\epsilon \sum_{\ell=0}^{\infty} \frac{2\ell+1}{4\pi} C_\ell^{TT}\ P_\ell^2(\cos\theta)\ , \tag{2.17a}$$

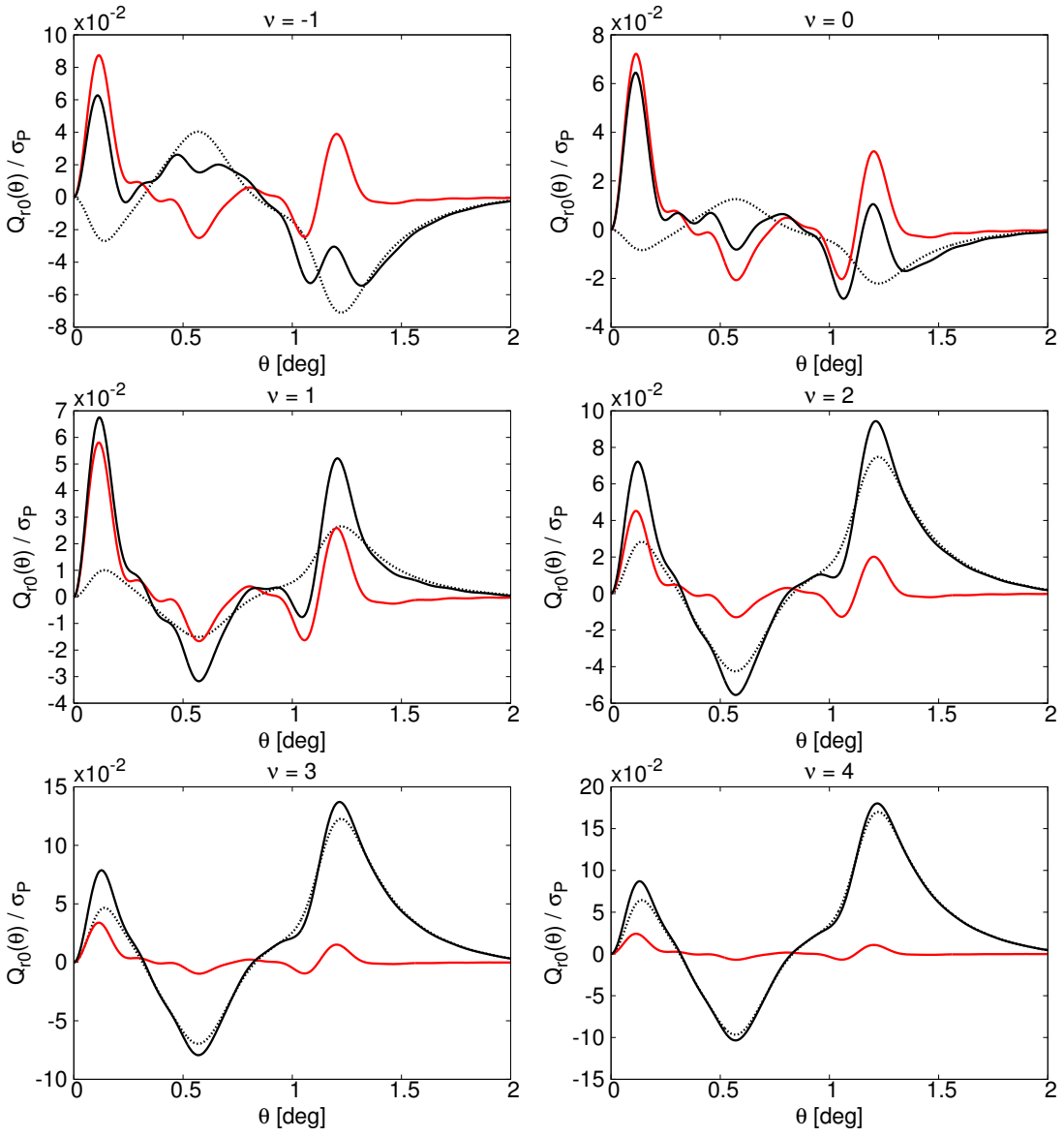

FIGURE 2.3: Monopolar profiles $Q_{r0}(\theta)$ for different peak heights. The dotted black lines show the contribution due to the peak height bias (b_ν), while the red line is the modification caused by the mean curvature bias (b_κ). The black solid line corresponds to the total profile. All these profiles are normalized by $\sigma_P = \sqrt{\langle Q^2\rangle + \langle U^2\rangle}$.

$$\langle Q_{r2}(\theta)\rangle = -2b_\epsilon \sum_{\ell=0}^{\infty} \frac{2\ell+1}{4\pi}\sqrt{\frac{(\ell-2)!}{(\ell+2)!}}\left[C_\ell^{TE}\ P_\ell^{+}(\cos\theta) + iC_\ell^{TB}\ P_\ell^{-}(\cos\theta)\right]\ , \quad (2.17b)$$

$$\langle U_{r2}(\theta)\rangle = 2ib_\epsilon \sum_{\ell=0}^{\infty} \frac{2\ell+1}{4\pi}\sqrt{\frac{(\ell-2)!}{(\ell+2)!}}\left[C_\ell^{TE}\ P_\ell^{-}(\cos\theta) + iC_\ell^{TB}\ P_\ell^{+}(\cos\theta)\right]\ . \quad (2.17c)$$

In this case, the bias of the quadrupolar profiles is defined as $b_\epsilon = \langle\epsilon\rangle/\sigma_\epsilon$, which is proportional to the expected value of the eccentricity. The θ dependence in eqs. (2.17b)

and (2.17c) is described by the functions:

$$P_\ell^+(x) = -\left[\frac{\ell-4}{1-x^2} + \frac{1}{2}\ell\,(\ell-1)\right] P_\ell^2(x) + (\ell+2)\,\frac{x}{1-x^2} P_{\ell-1}^2(x)\ , \tag{2.18a}$$

$$P_\ell^-(x) = -2\left[(\ell-1)\,\frac{x}{1-x^2} P_\ell^2(x) - (\ell+2)\,\frac{1}{1-x^2} P_{\ell-1}^2(x)\right]\ . \tag{2.18b}$$

These functions arise in the analysis of any 2-spin field on the sphere (e.g., CMB polarization or weak lensing). They define the θ dependence of the 2-spin spherical harmonics with $m = 2$ as a function of ℓ [148, 149]. These expressions are undetermined in $\theta = 0$ ($x = 1$), but they have a continuous limit if the following values are adopted (see [149]):

$$P_\ell^\pm(1) = \pm\frac{1}{4}\frac{(\ell+2)!}{(\ell-2)!} \tag{2.19}$$

The quadrupolar profiles in eqs. (2.17) are complex quantities whose phase represents a rotation of the system of reference. The principal axes coincide with the xy axes when the eccentricity bias b_ϵ is real. Regarding the CMB polarization, one difference with respect to the spherically symmetric case is that the polarization fields E and B contribute to both Stokes parameters Q_r and U_r. The Stokes parameters in polar coordinates describe properly peaks with rotational symmetry. However, when the peak has nonzero eccentricity, the gradient and curl contributions are mixed due to the elongation of the peak. The effect of the eccentricity bias on the temperature and polarization peak shapes is represented in figures 2.4-2.6 as a function of the peak height. In these figures, the mean value of the eccentricity has been calculated from the probability density distribution in eq. (2.9), imposing the condition that ϵ is real ($\alpha = 0$). Geometrically, this is equivalent to orient the peak, such that the principal axes coincide with the Cartesian system of reference. Additionally, the 2-dimensional shape of temperature peaks and its effect on the Stokes parameters are shown in figures 2.7 and 2.8.

Let us remark that the multipolar profiles have already been used to test the standard cosmological model with the Planck temperature and polarization data [91].[2] The orientation of peaks in that work is performed by selecting the principal axes in the inverse Laplacian of the temperature. This allows one to reduce the noise contribution in order to have a better estimation of the orientation axes. On the other hand, the theoretical

[2] In [91], the multipolar profiles of polarization are defined expanding the quantity $Q + iU$, where the Stokes parameters are given in Cartesian coordinates (only valid in the flat approximation). The profiles P_m arising in this expansion are related to the ones used in this work as follows:

$$P_0 = Q_{r2} - iU_{r2}\ ,$$
$$P_2 = Q_{r0}\ ,$$
$$P_4 = Q_{r2} + iU_{r2}\ .$$

calculations in the present chapter are done directly in the temperature field, but the formalism can be trivially generalized so that the peak is selected and oriented in any derived field. For instance, it is possible to select the peak in a smoothed version of the temperature (in particular the inverse Laplacian), in order to reduce the noise or study the physics of peaks at different scales. In this sense, the work in this chapter complements the study in [91] giving a theoretical background, which is completely general and can be applied to many situations.

2.5.2 Profiles in real space

In this subsection, we provide an alternative description of the peak profiles, in which they are expressed in terms of derivatives of different correlation functions, depending on which field is considered and where the peak is selected. In the following, it is assumed that the peak is located in the temperature field and its effect on a general field X, which can be T, E, B, Q_r or U_r, is studied. It is straightforward to generalize this formalism for peaks selected in any other field replacing T by that field. Using vector notation we have that $\langle X_m(\theta)\rangle$ can be written as the following dot products:

$$\langle X_0(\theta)\rangle = \mathbf{b}_0^\dagger\ \mathbf{C}_0^{TX}(\theta)\ , \tag{2.20a}$$

$$\langle X_2(\theta)\rangle = \mathbf{b}_2\ \mathbf{C}_2^{TX}(\theta)\ , \tag{2.20b}$$

where the biases $\mathbf{b}_0$ and $\mathbf{b}_2$ are defined as

$$\mathbf{b}_0 \equiv \begin{pmatrix} b_\nu \\ b_\kappa \end{pmatrix}\ , \qquad \mathbf{b}_2 \equiv b_\epsilon\ . \tag{2.21}$$

The biases concerning the scalar degrees of freedom ν and κ are combined in the vector $\mathbf{b}_0$, while the bias related to the eccentricity is denoted by $\mathbf{b}_2$ for convenience. The θ-dependence of the multipolar profiles is calculated from the correlation function $C^{TX}(\theta)$:

$$\mathbf{C}_0^{TX}(\theta) = \begin{pmatrix} 1 \\ -\nabla^2 \end{pmatrix} C^{TX}(\theta)\ , \qquad \mathbf{C}_2^{TX}(\theta) = (\eth^*)^2 C^{TX}(\theta)\ . \tag{2.22}$$

The first component of the vector $\mathbf{C}_0^{TX}$ is the correlation function itself, while the second one is minus its Laplacian. On the other hand, the function $\mathbf{C}_2^{TX}$ defining the quadrupolar profile is written as a second order covariant derivative of the correlation function.

The quantities defined in eq. (2.22), which determine the shape of the peak, are different derivatives of the correlation function. Indeed, these derivatives are the cross-correlations

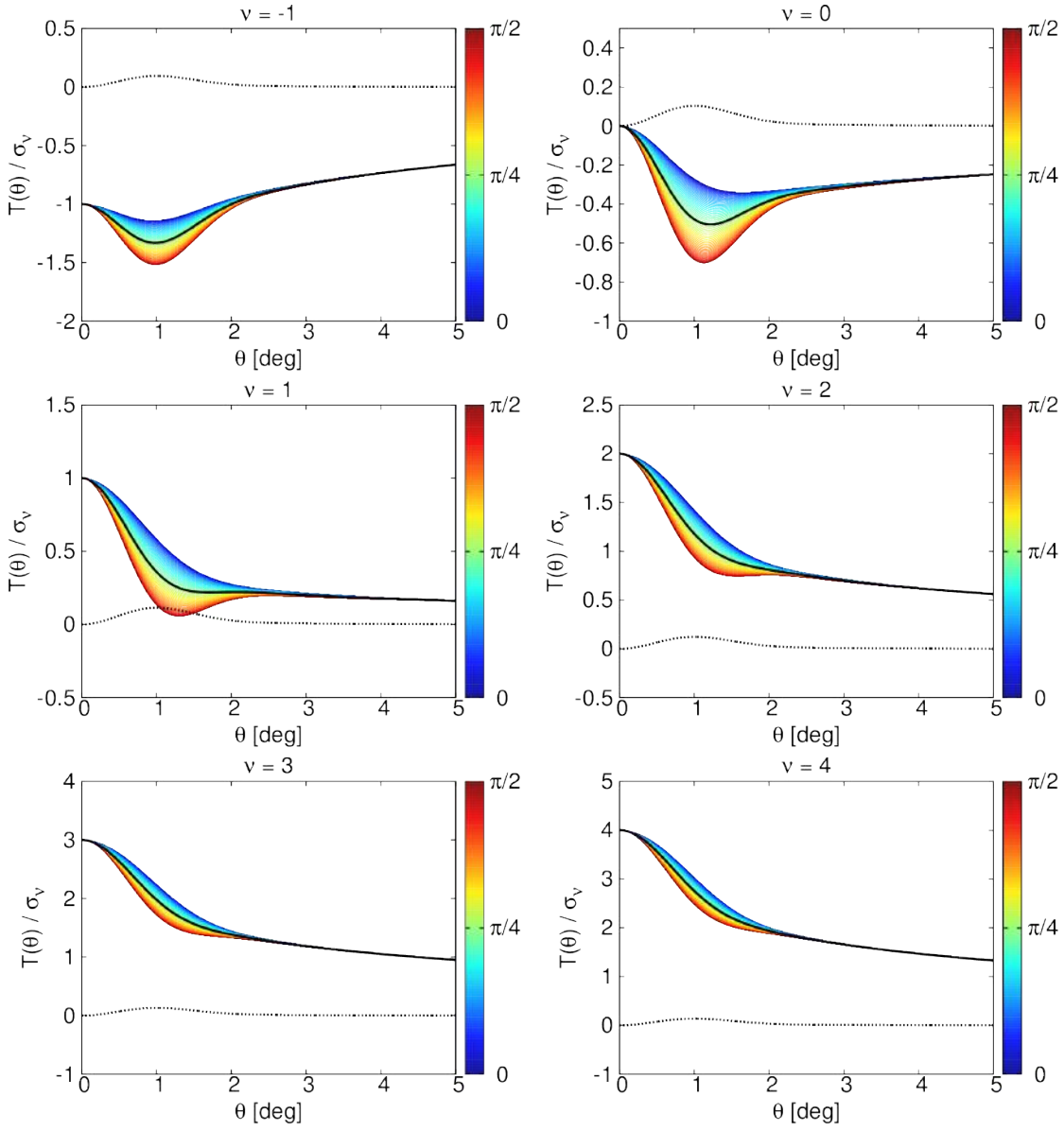

FIGURE 2.4: The effect of the eccentricity on the temperature profile for different ν. The principal axes of the peak are oriented according to the Cartesian system of reference, which implies that ϵ is real and the eccentricity bias is given by $b_\epsilon = \langle|\epsilon|\rangle/\sigma_\epsilon$. The black solid line depicts the spherically symmetric profile ($m = 0$). The color scale represents how the peak profile varies as a function of the azimuthal angle ϕ. The maximum and minimum elongations are reached at $\phi = 0$ and $\phi = \pi/2$ respectively. The quadrupolar profiles ($m = 2$) are represented by black dotted lines. In this figure, the temperature field is filtered by a Gaussian of FWHM 1°.

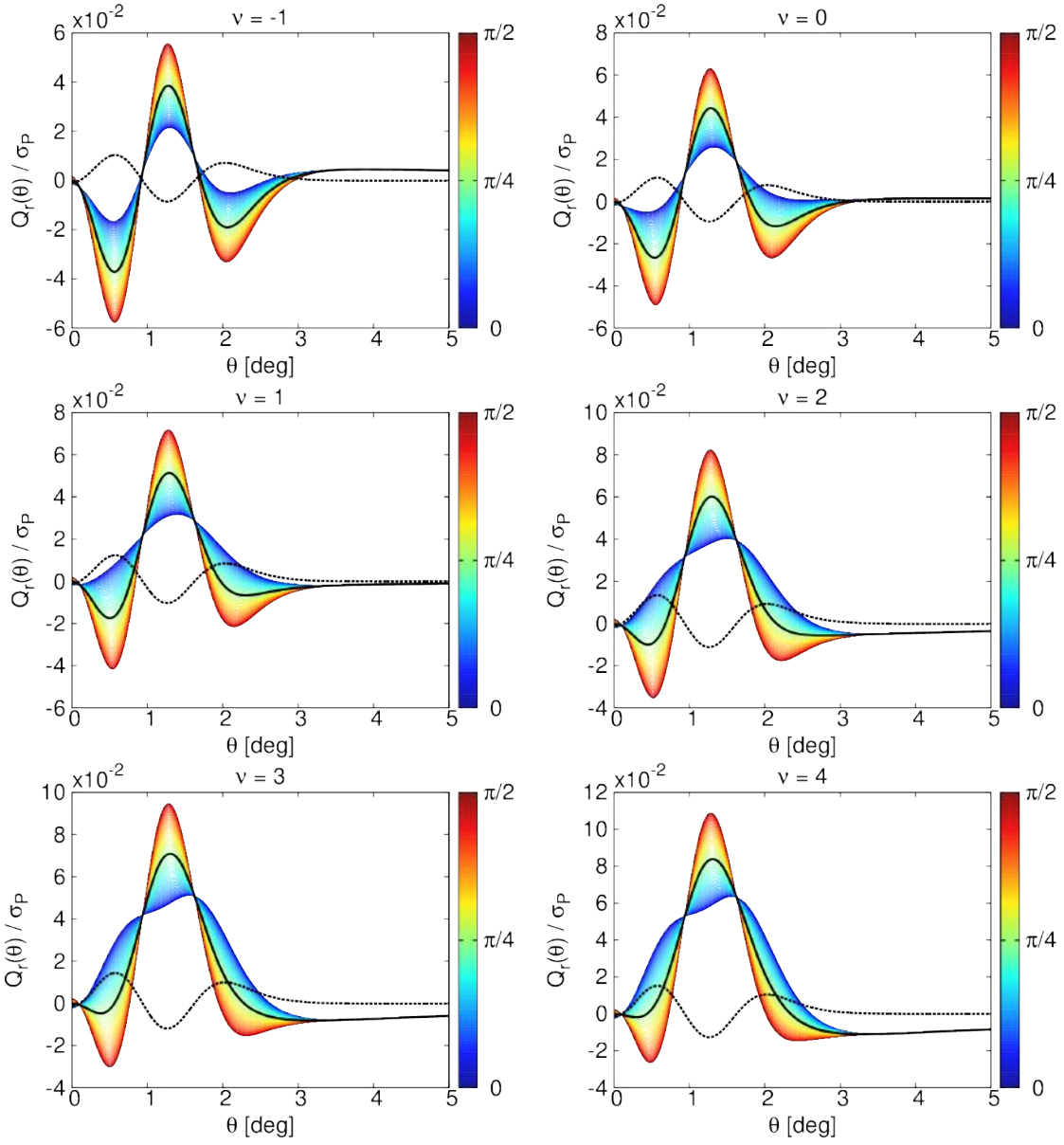

FIGURE 2.5: The effect of the eccentricity on the Q_r profile for different ν. The peaks are oriented in the same way than in figure 2.4. The black solid line corresponds to the spherically symmetric profile ($m = 0$). The color scale represents how the profile varies as a function of the azimuthal angle ϕ. The maximum and minimum elongations are reached at $\phi = 0$ and $\phi = \pi/2$ respectively. The quadrupolar profiles $Q_{r2}(\theta)$ are represented by black dotted lines. In this figure, the peak is selected in the temperature field, filtered by a Gaussian of FWHM 1°. All these profiles are normalized by $\sigma_P = \sqrt{\langle Q^2 \rangle + \langle U^2 \rangle}$.

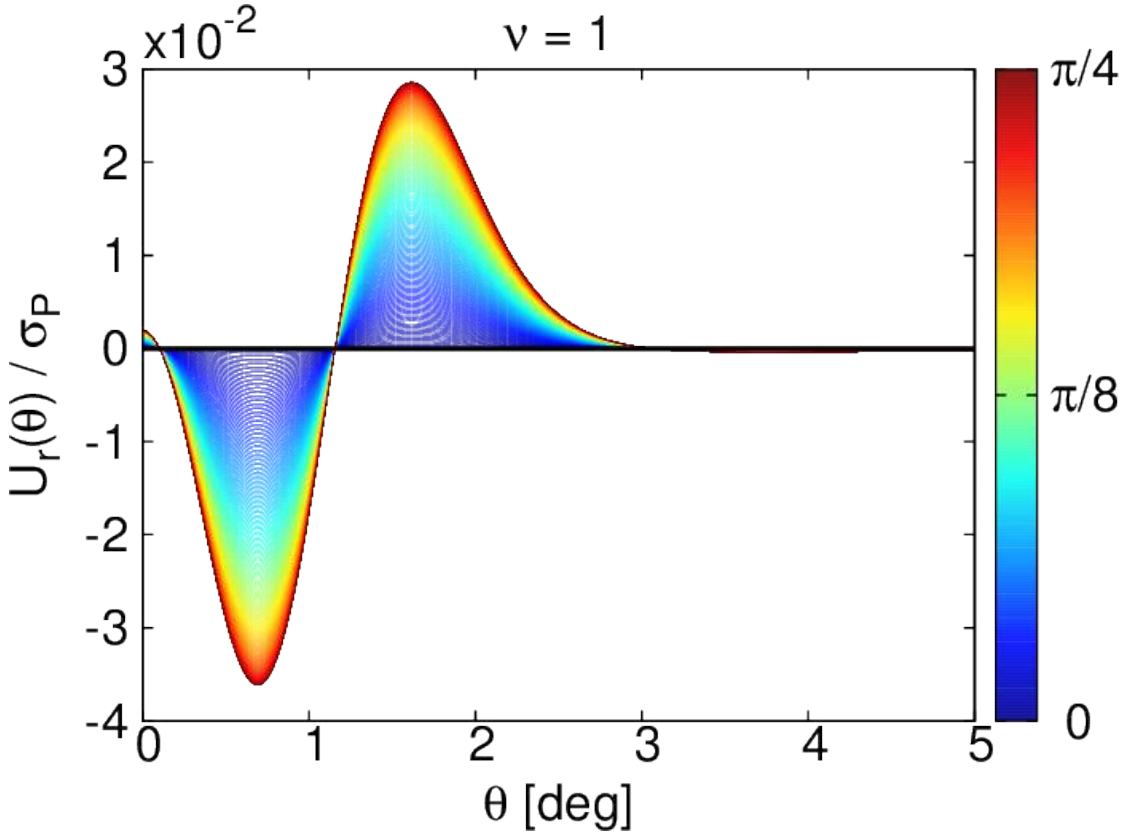

FIGURE 2.6: The effect of the eccentricity on the U_r profile for $\nu = 1$. The peaks are oriented in the same way than in figure 2.4. The color scale represents how the profile varies as a function of the azimuthal angle ϕ. This profile vanishes for $\phi = 0$ and it increases until reaching the maximum contribution at $\phi = \pi/4$. Different values of ν only change the amplitude of this profile following the dependence of $|b_\epsilon|$ as a function of the peak height (see figure 2.9). In this figure, the peak is selected in the temperature field, filtered by a Gaussian of FWHM 1°. The profile is represented normalizing by $\sigma_P = \sqrt{\langle Q^2 \rangle + \langle U^2 \rangle}$.

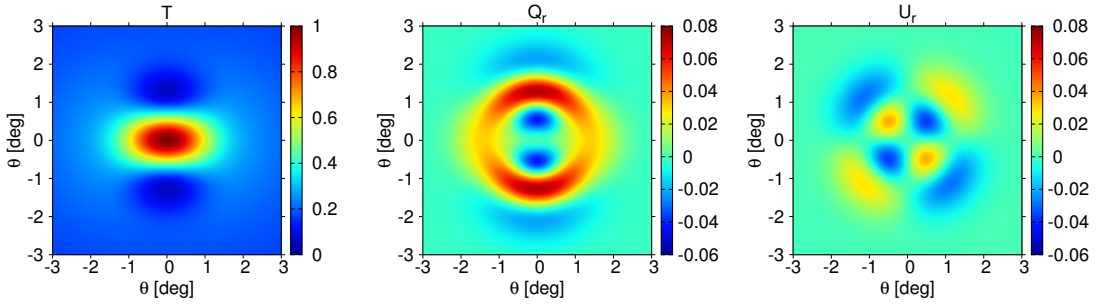

FIGURE 2.7: The 2-dimensional shape of peaks with eccentricity for oriented peaks with $\nu = 1$. The panels from left to right represents T, Q_r and U_r. In this figure, only the temperature field is filtered with a Gaussian of FWHM 1°. The units of color scales are given in terms of σ_ν for the temperature, and σ_P for the Stokes parameters.

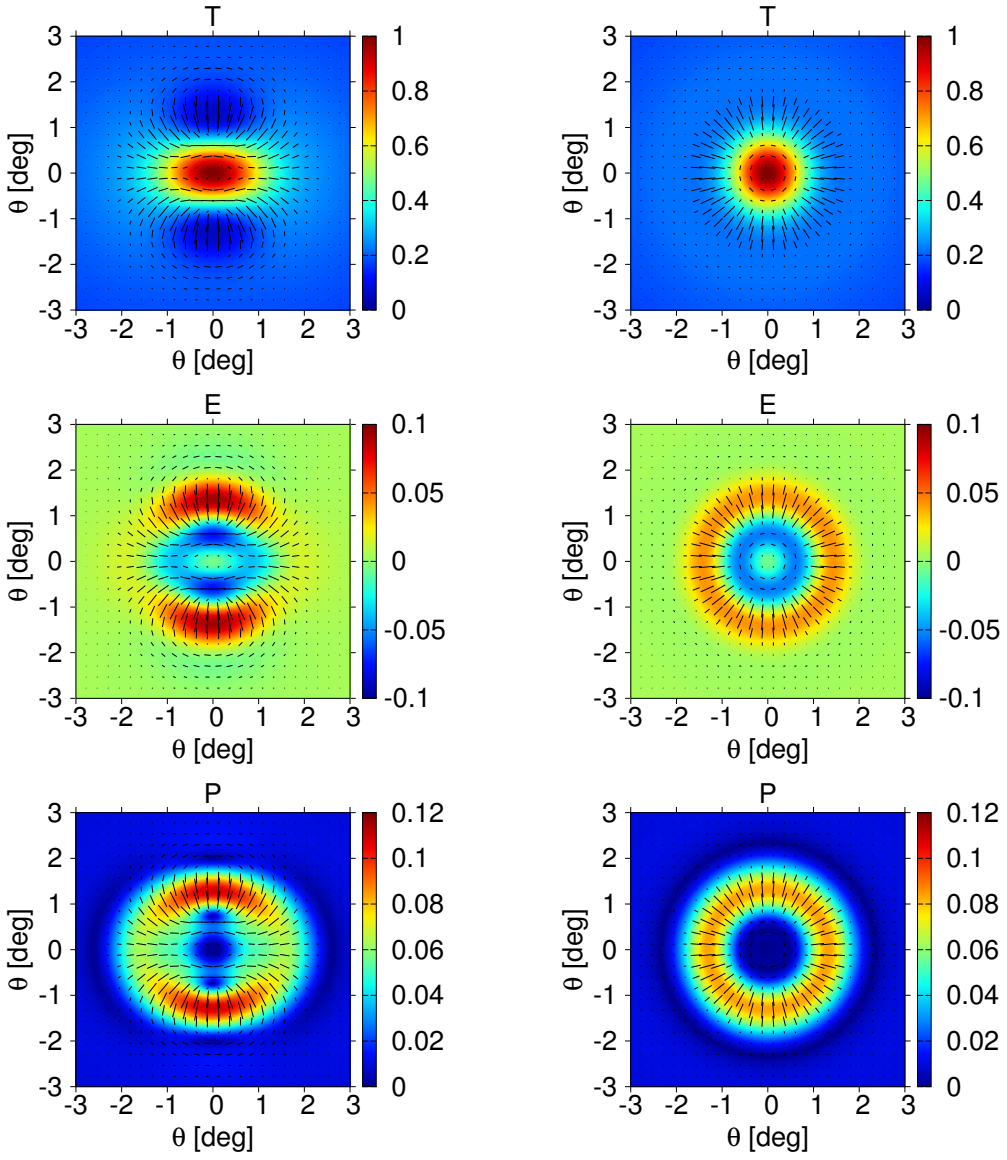

FIGURE 2.8: The 2-dimensional shape of peaks for $\nu = 1$. In the left panels, it is considered a oriented peak with eccentricity, whilst in the right panels it is represented a spherical symmetric peak. In all these figures, the polarization directions are drawn over it. The length of the headless vectors is proportional to the polarization degree. *Upper row*: the color map represents the temperature pattern induced by the peak. *Middle row*: in this case the color map depicts the E-mode polarization. *Lower row*: it is represented $P \equiv \sqrt{Q^2 + U^2}$, which describes the degree of polarization. In this figure, only the temperature field is filtered with a Gaussian of FWHM 1°. The units of color scales are given in terms of σ_ν for the temperature, and σ_P for the E-mode and P.

of the field X with the peak degrees of freedom. For instance, the Laplacian of the correlation function $\nabla^2 C^{TX}(\theta)$ is proportional to the correlation of the mean curvature κ and the field X, that is, $\langle \kappa X \rangle$. On the other hand, the derivative $(\eth^*)^2 C^{TX}(\theta)$ is proportional to the correlations $\langle \epsilon X \rangle$, while the correlation function itself is proportional to $\langle \nu X \rangle$. The fact that the field X is correlated with the peak degrees of freedom is the reason why any constraint on the peak variables ν, κ and ϵ modifies the shape of the peak.

2.5.3 Bias discussion

The terms contributing to the multipolar profiles in eqs. (2.20) arise from different peak selection biases. There are three conditions that can be imposed on peaks: constraints on the peak height, the condition of being a maximum or minimum and constraints on the orientation of the peak. The condition of being an extremum affects to the mean curvature and the eccentricity (see section 2.4). Hereafter, the bias parameters are calculated conditioning to the value of ν.

The biases for maxima are represented in figure 2.9 as a function of the peak height. In the high- peak limit, the maximum selection has no effect on the profile because it is more likely that a peak with high ν is a maximum, without any additional bias on the curvature. Therefore, the curvature bias b_κ approaches to zero for high ν (the expected value of the mean curvature is $\langle \kappa \rangle \sim \rho\nu$ for large values of ν). We arrive at the same conclusion if we consider minima with extreme negative values of ν. On the other hand, the peak height bias b_ν approaches to ν/σ_ν in the high-peak limit (see figure 2.9). Hence, the radial profile of high peaks is proportional to the correlation function.

Finally, we consider constraints on the eccentricity. If the peaks are oriented according to its principal axes, then the mean value $\langle \epsilon \rangle$ is not zero, introducing a bias in the value of ϵ. The quadrupolar profile ($m = 2$) in eq. (2.20b), which breaks the rotational symmetry and introduces an azimuthal dependence in the peak shape, is proportional to the bias $b_\epsilon = \langle \epsilon \rangle / \sigma_\epsilon$. As this bias is a complex number whose argument only has information about the orientation angle, then the statistical properties of the eccentricity are only in its modulus $|b_\epsilon|$. In the high-peak limit, the modulus of the eccentricity bias approaches to $|b_\epsilon| = \sqrt{\pi}/2\sigma_\epsilon$.

In figure 2.9, we consider two different ways of calculating the biases. In one case, the one-point probability (eq. (2.9)) is used for averaging the peak variables and, in the other case, it is used the number density of peaks (eq. (2.10)). Each of these approaches are useful in different situations (see Section 2.4 for a discussion). Although the biases

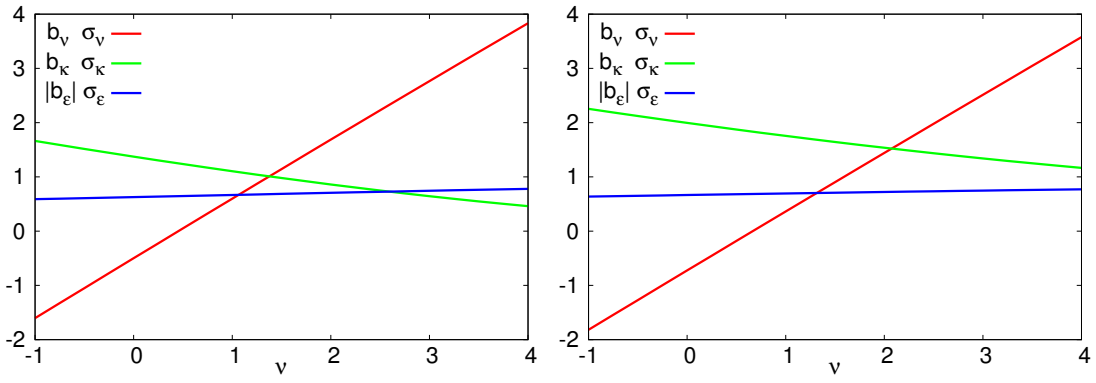

FIGURE 2.9: Biases of the peak profile for maxima as a function of the peak height ν. The curvature and the eccentricity are marginalised, while the peak height is conditioned to a given value. *Left*: The one-point probability is used for averaging the peak variables and calculating the biases. *Right*: The biases are calculated using the peak number density.

must be independent of the probability used for their calculation in the high-peak limit, differences can be seen for large values of ν.

The eccentricity is a complex number whose phase describes the orientation of the peak. It is possible to remove this phase choosing the principal axes of the peak as the reference system. In this particular case, both the eccentricity ϵ and the bias b_ϵ are real. Combining eqs. (2.20), it can be shown that the expected value $\langle T(\theta,\phi)\rangle$ is a biased correlation function, where the bias can be seen as the operator

$$b = b_\nu - (b_\kappa - 2|b_\epsilon|)\,\partial_x^2 - (b_\kappa + 2|b_\epsilon|)\,\partial_y^2 \,, \tag{2.23}$$

where we consider the principal axes as the xy-coordinates. This bias is non-local because it contains partial derivatives. Furthermore, it is non-isotropic due to the fact that the derivatives along the principal directions have different bias. Only when there is no eccentricity bias ($b_\epsilon = 0$), we recover isotropy. The bias in eq. (2.23) is a generalization of the one in [142] for peaks with eccentricity.

2.6 Covariance of the multipolar profiles

In this section, the covariance of the multipolar profiles are calculated. As in the previous section, both the temperature and the Stokes parameters are expanded in terms of the multipolar profiles. In the case of peaks with spherical symmetry, only the scalar profile ($m = 0$) contributes to the peak local shape. Conversely, if peaks are selected with eccentricity, then the quadrupolar profile ($m = 2$) is also non-zero. In this case,

obviously, the multipolar profiles with $m = 0$ and $m = 2$ have all the information concerning the peak shape.

In general, the covariance between the multipolar profiles of the field X and Y can be written as the sum of two contributions:

$$\langle X^*_{m'} Y_m \rangle = \langle X^*_{m'} Y_m \rangle_{\text{intr.}} + \langle X^*_{m'} Y_m \rangle_{\text{peak}} \ , \tag{2.24}$$

where the intrinsic covariance $\langle X^*_{m'} Y_m \rangle_{\text{intr.}}$ represents the correlations of the multipolar profiles, independently whether a peak is selected or not. The second part $\langle X^*_{m'} Y_m \rangle_{\text{peak}}$ is a modification of the intrinsic covariance due to the fact that a peak is present in the field. In general, the contribution of the peak is a suppression of the intrinsic covariance caused by the reduction of the field randomness when the peak variables are constrained.

The intrinsic covariance is given by

$$\langle X^*_{m'}(\theta') Y_m(\theta) \rangle_{\text{intr.}} = \delta_{mm'} \sum_{\ell=m}^{\infty} \frac{2\ell+1}{4\pi} \frac{(\ell-m)!}{(\ell+m)!} \, C_\ell^{XY} \, P_\ell^m(\cos\theta) P_\ell^m(\cos\theta') \ . \tag{2.25}$$

Whilst this covariance is only determined by the angular cross-power spectrum of the fields and affects to the whole range of m-values, the peak covariance depends on how the peak variables are selected. In addition to the covariance of the $m = 0$ and $m = 2$ profiles, the peak also modifies the covariance of the multipolar profile with $m = 1$, which is associated to the first derivative. The condition of having a critical point ($\eta = 0$) implies that the expected value of the dipolar profile is zero, and for this reason we have not considered the $m = 1$ profile in the peak shape analysis (see Section 2.5). However, as the covariance of the field is affected by the constraint on the first derivative, the parameter η must be included in the analysis of this section.

The contribution of the peak to the field covariance is caused by the particular constraints on the peak degrees of freedom (for instance, imposing the extremum constraint, the peak height above a given threshold, or the first derivative equal to zero). These constraints modify how the peak variables are distributed with respect to the case without peak selection. In the following, the covariance matrix of ν, κ, η and ϵ, when peak variables are unconstrained, is denoted by S. Once the peak is selected, the change in this covariance is parametrized by the matrix ΔS, which is defined as the difference between the covariance of ν, κ, η and ϵ, with and without the peak constraints imposed. The bias of S is defined as the matrix:

$$B_S = B \ (\Delta S) \ B^\dagger \ , \tag{2.26}$$

where the four-dimensional matrix B is given by the inverse of S, normalizing the rows by the corresponding variances of the peak variables. That is,

$$B = \begin{pmatrix} \sigma_\nu^{-1} & 0 & 0 & 0 \\ 0 & \sigma_\kappa^{-1} & 0 & 0 \\ 0 & 0 & \sigma_\eta^{-1} & 0 \\ 0 & 0 & 0 & \sigma_\epsilon^{-1} \end{pmatrix} S^{-1} \ . \tag{2.27}$$

The bias of the covariance B_S in eq. (2.26) is a linear transformation of the matrix ΔS. Therefore, if the peak variables are not constrained (i.e., $\Delta S = 0$), the bias B_S is also zero. For convenience, the bias matrix B_S is separated in different blocks taking into account the different spin of the peak variables:

$$B_S = \begin{pmatrix} B_{00} & B_{01} & B_{02} \\ B_{10} & B_{11} & B_{12} \\ B_{20} & B_{21} & B_{22} \end{pmatrix} \ . \tag{2.28}$$

This matrix is Hermitian by construction, and therefore $B_{ij} = B_{ji}^*$. The reason of this decomposition is that the peak variables affect to the different multipolar profiles depending on their spin. The two-dimensional matrix B_{00} represents the bias of the covariance of the scalar degrees of freedom (ν and κ), while B_{11} and B_{22} are the biases of the variances of the first derivative (η) and the eccentricity (ϵ), respectively. Likewise, due to the peak selection process, it is possible to have correlations between different peak variables, which are described by the off-diagonal terms of B_S (for instance, the extremum constraint $|\epsilon| \leq |\sqrt{a}|\kappa|$ introduces correlations between κ and ϵ). In the particular case of peaks where the first derivative is set to zero by definition, the bias in the covariance of η is $B_{11} = -1/\sigma_\eta^2$ and there is no correlation between η and the rest of degrees of freedom, which leads to $B_{01} = B_{12} = 0$. Finally, the peak covariance is calculated using the bias matrix B_S:

$$\langle X_{m'}^*(\theta') Y_m(\theta) \rangle_{\rm peak} = \mathbf{C}_{m'}^{TX}(\theta')^\dagger B_{m'm} \mathbf{C}_m^{TY}(\theta) \ , \tag{2.29}$$

where $\mathbf{C}_m^{TX}$ for $m = 0, 2$ are defined in eq. (2.22). In the particular case of $m = 1$, this quantity is given by the covariant derivative of the correlation function:

$$\mathbf{C}_1^{TX}(\theta) = \eth^* C^{TX}(\theta) \ . \tag{2.30}$$

In eq. (2.29), it is assumed that the peak is selected in temperature, but it can be generalized for peaks in any other field replacing T by that field.

When a peak is present in the field, the covariance is reduced coherently depending

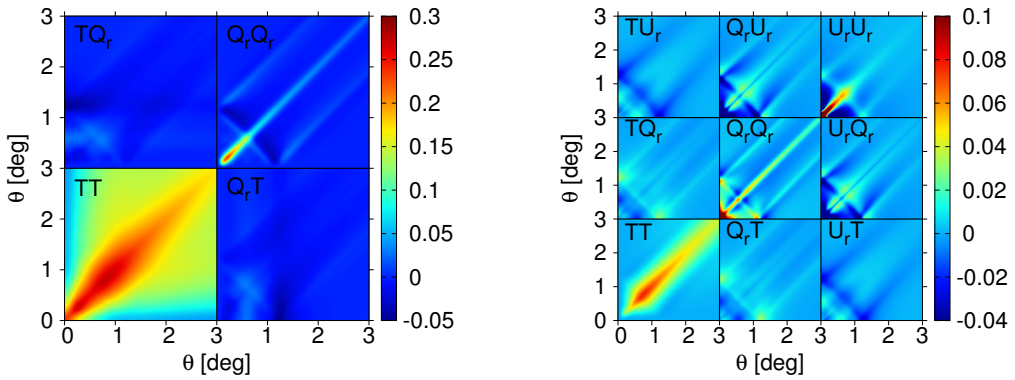

FIGURE 2.10: Covariance of the $m = 0$ (left) and $m = 2$ (right) profiles for peaks selected in temperature with $\nu > 1$. Each field is normalized by the corresponding standard deviation (σ_ν for the temperature and $\sigma_P/\sqrt{2}$ for each of the Stokes parameters).

on how the peak variables are constrained. For instance, if the peak height ν is fixed to a given value or selected above a threshold, the field at the centre is constrained, and therefore it is expected that the variance at $\theta = 0$ is reduced. In figure 2.10, it is represented the covariance of the $m = 0$ and $m = 2$ profiles for peaks selected in temperature with $\nu > 1$. It is possible to see that the effect of the peak on the covariance mainly affects the TT part, while the covariances concerning the Stokes parameters are dominated by the intrinsic term. This fact is produced because the peak covariance of the Stokes parameters is proportional to the square of the TE correlation, which is subdominant with respect to the intrinsic fluctuations of the field. This is not the case for temperature, where the presence of a peak modifies drastically the covariance around the centre and introduces correlations between different θ. Additionally, it is possible to consider the covariance between the monopolar and the quadrupolar profiles. However, the intrinsic part vanishes and the effect of the peak is small in this case.

If we are interested in analysing the two-dimensional pattern instead of the individual multipolar profiles, it is necessary to calculate the covariance of the field $X(\theta, \phi)$. Since all the information of the field is contained in the multipolar profiles, the field covariance can be calculated from the covariance of the multipolar profiles:

$$\langle X(\theta', \phi') X(\theta, \phi) \rangle = \sum_{m,m'=-\infty}^{\infty} \langle X^*_{m'}(\theta') X_m(\theta) \rangle \, e^{i(m\phi - m'\phi')} \, . \tag{2.31}$$

This covariance can also be split into the intrinsic and the peak contributions. As it is expected, the intrinsic part obtained from eq. (2.25) leads to the field correlation function, depending on the separation of the two points. On the other hand, the peak contribution is modelled by the covariance of the multipolar profiles with $m = 0, 1, 2$ in eq. (2.29). These terms introduce a inhomogeneous correlation function around the

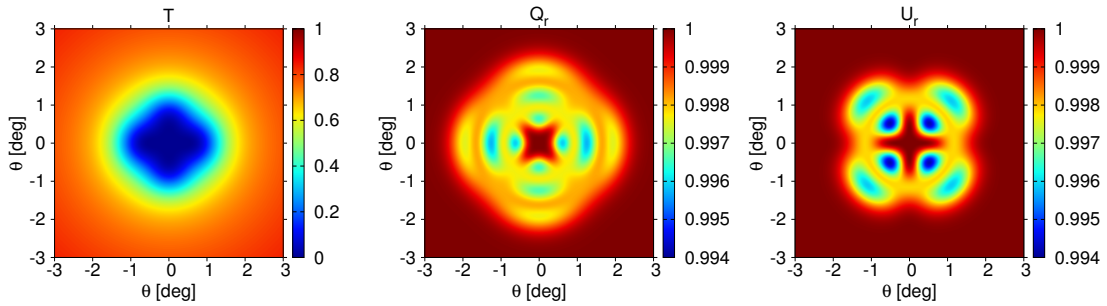

FIGURE 2.11: Variance of the temperature (left), Q_r (middle) and U_r (right) fields around a peak selected in T smoothed by a Gaussian of FWHM 1°. The peak height is conditioned to be $\nu = 1$, and therefore these variances correspond to the patterns in figure 2.7. Each field is normalized by its variance corresponding to the case of no peak selection. It is possible to see that the peak barely alters the variance of the Stokes parameters ($< 1\%$), whilst the temperature variance is drastically decreased in the region of the peak.

peak, which can be also anisotropic if the peak has eccentricity. In figure 2.11, it is represented the variance of each point around an oriented peak selected in temperature. In the region close to the centre, the variance is suppressed with respect to the intrinsic variance. The quadrupolar pattern present in this figure is a consequence of the peak eccentricity. Whilst the peak has a strong effect on the variance of the temperature field, the variances of the Stokes parameters are modified in less than 1%.

2.7 Physical interpretation of the peak patterns

The azimuthally averaged temperature peak patterns, where the effect of the eccentricity has been averaged out at zero, are essentially given by the correlation function between T and the field where the pattern is imprinted, which can be either T or the polarization fields. Modifications due to the peak curvature can arise in the low-peak limit, but this effect is only manifested in the region close to the centre of the peak and it has not influence in the physical behaviour of the profiles at large scales. In the high-peak limit, or for distances greater than the correlation of $\nabla^2 T$, the physics of peaks is the same as the one causing the shape of the corresponding temperature cross-correlation functions. For instance, the ring structure seen in the Q_r profile (figure 2.3) is an effect of the baryon acoustic oscillations produced at scales smaller than the sound horizon size at the decoupling epoch, which are also present in the TQ_r (or TE) correlation [91, 145].

In this chapter, we analyse the effect of the eccentricity in both temperature and polarization patterns. In the case of the temperature, the eccentricity of the peak affects to the second order derivatives at the centre adding a directional dependence. This effect modifies essentially the small scales since the eccentricity term is proportional to

$\sim \ell^2$. However, the eccentricity is noticeable at scales up to the sound horizon size. The acoustic oscillations produced inside of a non-spherical potential propagate the anisotropy from the centre to the horizon size. In contrast, for scales greater than the horizon, the physics is dominated by gravity, which is not sensitive to the local geometry of the potential well, and the spherical symmetry is therefore recovered. In figure 2.4, we can see this effect, where the peak profile is represented for different azimuthal angle. The quadrupolar profile $T_2(\theta)$ characterizes the effect of the eccentricity on the temperature peak as a function of θ. The eccentricity does not alter the peak height at the centre, and therefore $T_2(\theta)$ vanishes at $\theta = 0$. However, this term contributes at scales within the sound horizon. For larger scales, $T_2(\theta)$ goes to zero and the peak becomes spherically symmetric.

In addition, the peak orientation in temperature also affects to the polarization pattern. As described in [145], the polarization direction characterizes the flow of the photons. Whilst the polarization direction is radial when the velocity field is converging, it shows a tangential configuration for a divergent flow [150]. In the case of peaks, its shape depends on the correlation between T and polarization. Therefore, in addition to the divergence of the photon flow, the sign of the temperature is also important to describe the polarization pattern. The oscillations in Q_r represent changes both in the sign of the temperature and in the velocity field (see [145], for a more detailed explanation). When the peak has eccentricity, it is possible to distinguish two different effects on the velocity field which modify the polarization pattern: a change in the direction of the flow and azimuthal variations of the modulus of the velocity field. Both effects modify the local quadrupole moment of the photon distribution, which causes the CMB polarization. The fact of having a non-spherically symmetric potential makes the flow to deviate from being purely radial. This introduces a nonzero U_r field, even if the curl contribution is zero (see figure 2.7). In the principal axes directions, the flow is radial as in the spherical case, and therefore U_r vanishes. However, the deviation from the radial flow due to the peak deformation reaches its maximum value in directions at 45° with respect to the principal axes. For this reason, the azimuthal dependence of U_r is a quadrupolar pattern rotated 45° with respect to the orientation axis. The alternating sign in each quadrupolar lobe indicates that the deviation angle between the velocity field and the radial direction has different signs in each quadrant. In addition, the U_r pattern also presents a radial dependence (see figure 2.6). The changes on the sign in the radial profile is produced by the acoustic oscillations present in the correlation function of the temperature and polarization fields. In addition to the flow direction, the modulus of the velocity field is also affected by the peak eccentricity. In regions where the peak pattern is compressed with respect to the spherical case, the pressure of the photons is higher, and on the contrary, the pressure is lower in the direction of elongation. The pressure

of the photon fluid modifies the velocity field, and hence also the polarization pattern. The directions of elongation and compression correspond to the major and minor axes, respectively. This introduces a quadrupolar pattern aligned with the principal axes of the peak, which can be seen in both, Q_r and P. In some cases, the pressure in the elongation axis is not enough to reverse the flow, and therefore the change of sign in Q_r due to the velocity reversion is not present (see figure 2.5).

In order to enhance the elliptical patterns, the peaks represented in figures 2.4-2.8 are selected in the temperature field smoothed with a Gaussian of FWHM 1°, which implies that the inner acoustic oscillations in the Q_r profile are suppressed by the filter (compare with figure 2.3). A calculation of the profiles at high resolution indicates that any source of power at small scales different from the baryon acoustic oscillations (e.g. lensing or noise) produce a smearing of the ring pattern present in the polarization field due to the fact in this situation the peaks do not trace properly the potential wells at the last scattering surface.

2.8 Peak simulations

In this section, we use the formalism developed in section 2.3 to generate constrained simulations having a peak with given characteristics. For simplicity, we consider the case in which the peak height ν is fixed to a given value, but it is possible to generalize the procedure for random values of ν. The simulations are generated in the spherical harmonic space. The first step is to generate the variables $\hat{a}_{\ell m}$ defined in eqs. (2.5), which are given as a linear combination of the standard spherical harmonic coefficients $a_{\ell m}$. This property allows us to consider that the $\hat{a}_{\ell m}$ variables are Gaussian under the assumption that the field where the peak is selected is also Gaussian. These new variables obtained after the orthogonalization process are not independent. Their covariance matrix is given by

$$\langle \hat{a}_{\ell 0} \hat{a}_{\ell' 0} \rangle = \delta_{\ell\ell'} + \begin{pmatrix} \nu_\ell & \kappa_\ell \end{pmatrix} C^{-1} \begin{pmatrix} \nu_{\ell'} \\ \kappa_{\ell'} \end{pmatrix} \quad (\ell \neq \ell_\nu, \ell_\kappa) \ , \tag{2.32a}$$

$$\langle \hat{a}_{\ell 1} \hat{a}_{\ell' 1} \rangle = \delta_{\ell\ell'} + \frac{\eta_\ell \eta_{\ell'}}{\eta^2_{\ell_\eta}} \quad (\ell \neq \ell_\eta) \ , \tag{2.32b}$$

$$\langle \hat{a}_{\ell 2} \hat{a}_{\ell' 2} \rangle = \delta_{\ell\ell'} + \frac{\epsilon_\ell \epsilon_{\ell'}}{\epsilon^2_{\ell_\eta}} \quad (\ell \neq \ell_\epsilon) \ , \tag{2.32c}$$

$$\langle \hat{a}_{\ell m} \hat{a}_{\ell' m} \rangle = \delta_{\ell\ell'} \quad (m > 2) \ , \tag{2.32d}$$

where $C = PP^t$, being P the pivot matrix defined in eq. (2.6). Using the Cholesky decomposition of the covariance matrix, it is possible to simulate the $\hat{a}_{\ell m}$ coefficients.

The next step is to simulate the peak variables. Using the probability in eq. (2.9), we have to put constraints in order to have a minimum or maximum. In practice, the easiest way to do this is by using a Montecarlo approach. Conditioning the peak height to ν, random values of κ and $|\epsilon|$ are generated. The eccentricity ϵ is generated from the two independent Gaussian variables which characterize its real and imaginary parts, while the curvature κ is generated as a Gaussian with mean $\rho\nu$ and variance $1-\rho^2$ (as it can be deduced from eq. (2.9)). If these numbers satisfy the extremum constraint $|\epsilon| \leq \sqrt{a}|\kappa|$ and $\kappa > 0$ ($\kappa < 0$) for maximum (minimum) selection, these values are preserved. Otherwise, they are rejected and generated again until obtaining a pair of values which satisfy the extremum constraint. The sign of κ is chosen to be positive or negative depending whether we are selecting minima or maxima respectively.

Once the peak variables κ, ϵ and the $\hat{a}_{\ell m}$ variables are simulated, the standard spherical harmonic coefficients $a_{\ell m}$ are recovered using eqs. (2.7). Given a simulation of the temperature, it is possible to generate the polarization fields E and B correlated with it. In order to do this coherently, we simulate the spherical harmonics coefficients $e_{\ell m}$ and $b_{\ell m}$, which correspond to E and B respectively, following a Gaussian distribution with mean and variance given in eqs. (2.8). The influence of the peak in the polarization fields is given by the correlation between both fields and the temperature.

Notice that although, using this formalism, the peak is located at the north pole, it can be set at any position on the sphere by performing the proper rotation. The last step is to construct the maps from the spherical harmonic coefficients $a_{\ell m}$, $e_{\ell m}$ and $b_{\ell m}$. A simulation produced following this procedure is given in figure 2.12.

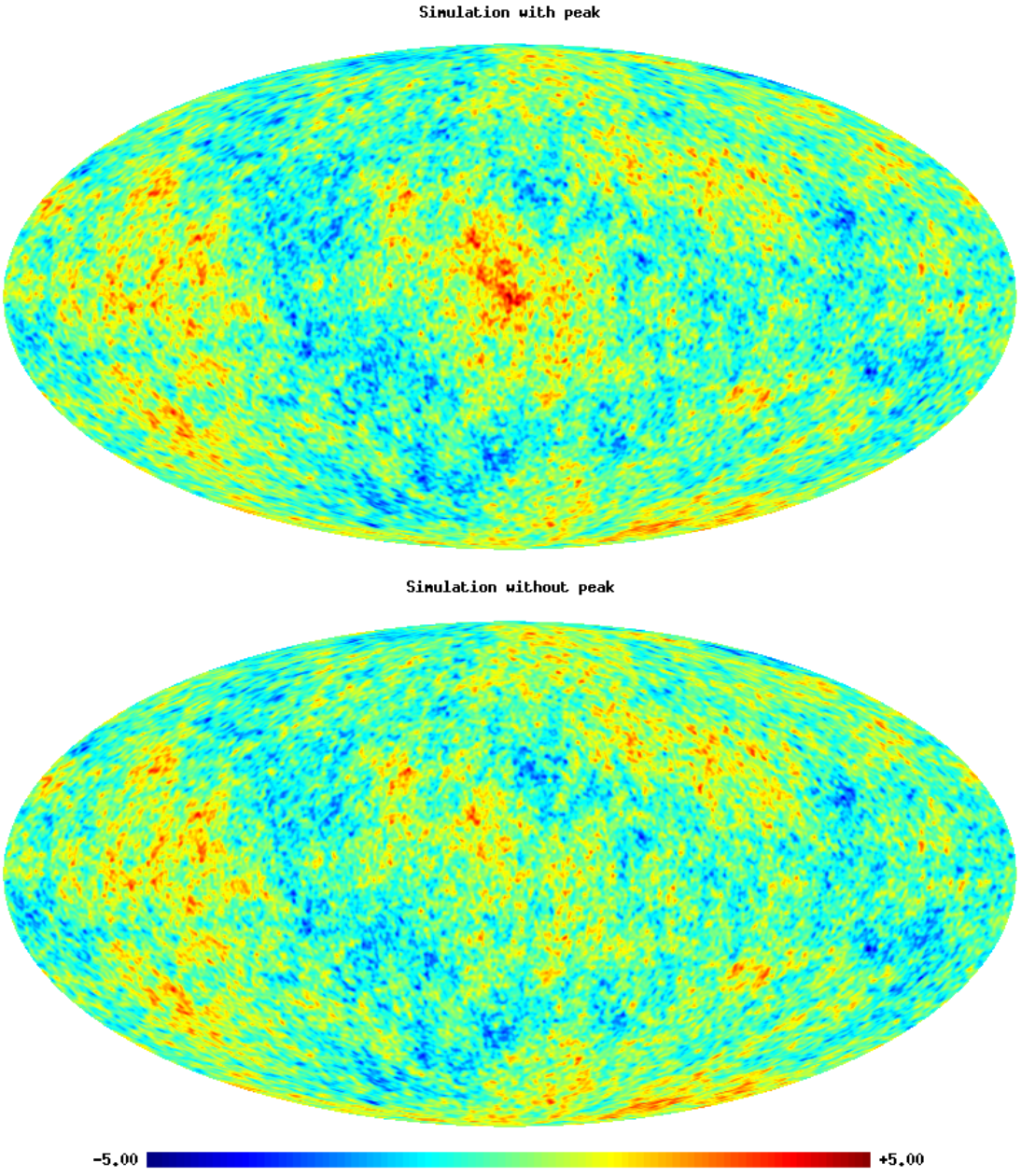

FIGURE 2.12: Simulations of the CMB temperature field with a peak with $\nu = 5$ located at the centre of the image (upper map), and without a peak (lower map). Both simulations only differ in the peak variables (the variables $\hat{a}_{\ell m}$ are the same), and therefore it is possible to see similar structures in regions away from the peak. One can notice that the presence of the peak affects to the area around it, attending to the properties of the temperature correlation function. In these maps, the temperature is filtered with a Gaussian whose FWHM is 1°, and the color bar indicates the value of the map normalized by the standard deviation.

Chapter 3

Multiscale analysis of the CMB temperature derivatives

We study the Planck CMB temperature at different scales through its derivatives up to second order, which allows one to characterize the local shape and isotropy of the field. The problem of having an incomplete sky in the calculation and statistical characterization of the derivatives is addressed in this chapter. The analysis confirms the existence of a low variance in the CMB at large scales, which is also noticeable in the derivatives. Moreover, deviations from the standard model in the gradient, curvature and the eccentricity tensor are studied in terms of extreme values on the data. As it is expected, the Cold Spot is detected as one of the most prominent peaks in terms of curvature, but additionally, when the information of the temperature and its Laplacian are combined, another feature with similar probability at the scale of 10° is also observed. However, the p-value of these two deviations increase above the 6% when they are referred to the variance calculated from the theoretical fiducial model, indicating that these deviations can be associated to the low variance anomaly. Finally, an estimator of the directional anisotropy for spinorial quantities is introduced, which is applied to the spinors derived from the field derivatives. An anisotropic direction whose probability is $< 1\%$ is detected in the eccentricity tensor.

3.1 Introduction

In the standard cosmological model, the high level of isotropy of the Cosmic Microwave Background (CMB) observations are explained by evoking a phase of exponential expansion in the early Universe, called cosmic inflation. Following the standard predictions of inflation, the initial perturbations are Gaussianly distributed in a homogeneous flat

space. Deviations in the isotropy and Gaussianity of the CMB temperature field are important to constrain the particular model of inflation, or even to explore new physics in the primordial Universe.

The analysis of the temperature gradient and higher order derivatives are useful for the characterization of the CMB anisotropies. For instance, at small scales, the temperature gradient have been used to reconstruct the matter density power spectrum using the gravitational lensing effect over the CMB photons [151], as well as to study the beam asymmetry systematic introduced by the scanning strategy [152]. In the previous chapter, the shape of the large-scale peaks are analysed by considering the value of the Laplacian and the eccentricity tensor at the centre of the peak [153]. In this work, we are interested in the large scale behaviour of the CMB temperature derivatives, for which different scales are analysed. If the scaling function is a Gaussian filter, the multiscale analysis based on the scalar curvature (the Laplacian) is equivalent to the Spherical Mexican Hat Wavelet [121, 122]. On the other hand, the spinorial derivatives (the gradient and the eccentricity tensor) have information about the local directionality of the CMB temperature, which have been studied previously by using the steerable wavelets formalism [154–156]. We present here a joint analysis of the derivatives field for a wide range of scales (from 1° to 30°), paying attention to the extreme deviations with respect to the standard model expectation.

The scalar curvature, as well as the temperature itself, allow one to analyse the CMB in terms of rotational invariant quantities, which, in particular, characterizes Cold Spot-like features on the sky. Besides the scalar derivatives, the modulus of the gradient and the eccentricity tensor can be studied in order to localize regions on the sky with anomalous dipolar or quadrupolar local shape. Moreover, due to the directional character of these derivatives, the gradient and the eccentricity tensor can be also used to measure the isotropy of the field. For this purpose, an estimator for spinorial quantities based on the geodesic projection on a particular direction on the sphere is introduced.

This chapter is organised as follows: in Section 3.2, the calculation of the field derivatives in terms of the spherical harmonic coefficients is introduced, whereas the data processing is described in Section 3.3. A new formalism regarding the statistics of the derivative fields in the presence of a mask is introduced in Section 3.4. The first analysis of this work is performed in Section 3.5, which consists in the calculation and study of the covariance of the different derivatives components. On the other hand, extreme values of the derivative fields are analysed and compared with the standard model prediction in Section 3.6. In addition, the directional analysis of the spinorial derivatives is considered in Section 3.7, in order to quantify the isotropy of the CMB temperature field.

3.2 Theoretical framework

A field on the sphere is commonly described by the spherical coordinates, and consequently, its derivatives are taken along the directions determined by the local basis vectors $\mathbf{e}_\theta$ and $\mathbf{e}_\phi$. Additionally, it is useful to coordinate the tangent plane in terms of the helicity basis $\mathbf{e}_\pm = \mathbf{e}_\theta \pm i\mathbf{e}_\phi$, particularly when the derivatives are expressed in the spherical harmonic space. The reason for using this system of reference is that the covariant derivatives in the helicity basis modify the spherical harmonics as the spin raising/lowering operators, which simplifies the calculations. This implies, in particular, that the derivatives of a field on the sphere can be spanned in terms of the spin-weighted spherical harmonics, whose spin depends on which type of derivative is considered. Since spinors with different rank are statistically independent, we classify the derivatives up to second order in two scalars ($s = 0$), one vector ($s = 1$) and one tensor ($s = 2$), which allows one to make an independent analysis for each spin. The scalar derivatives are the temperature field itself (zero-order derivative) and its Laplacian, which are mutually correlated, specially at large scales. On the other hand, the components of the gradient form a vector, while the local eccentricity is a 2-spin tensor determined by the second order derivatives. Following the notation in [157], the derivatives are given by

$$\nu_R(\mathbf{n}) = \frac{1}{\sigma_\nu(R)} \sum_{\ell=0}^{\infty} w_\ell(R)\; a_{\ell m}\; Y_{\ell m}(\mathbf{n}) \;, \tag{3.1a}$$

$$\kappa_R(\mathbf{n}) = \frac{1}{\sigma_\kappa(R)} \sum_{\ell=0}^{\infty} \frac{(\ell+1)!}{(\ell-1)!}\; w_\ell(R)\; a_{\ell m}\; Y_{\ell m}(\mathbf{n}) \;, \tag{3.1b}$$

$$\eta_R(\mathbf{n}) = \frac{1}{\sigma_\eta(R)} \sum_{\ell=1}^{\infty} \sqrt{\frac{(\ell+1)!}{(\ell-1)!}}\; w_\ell(R)\; a_{\ell m}\; {}_{+1}Y_{\ell m}(\mathbf{n}) \;, \tag{3.1c}$$

$$\epsilon_R(\mathbf{n}) = \frac{1}{\sigma_\epsilon(R)} \sum_{\ell=2}^{\infty} \sqrt{\frac{(\ell+2)!}{(\ell-2)!}}\; w_\ell(R)\; a_{\ell m}\; {}_{+2}Y_{\ell m}(\mathbf{n}) \;, \tag{3.1d}$$

where $w_\ell(R)$ represents the Fourier coefficients of the window function corresponding to a particular angular scale R (see Section 3.3 for the precise definition of this filter). In the equations above, the scalar quantities ν and κ are real fields, while the spinors η and ϵ are complex numbers, since they have a directional character. The corresponding complex conjugates are expressed in terms of the spherical harmonics with spin -1 and -2, respectively. The derivatives in eqs. (3.1) are normalized by their corresponding theoretical variances, which are calculated assuming a fiducial model. They are expressed

in terms of the angular power spectrum in the following way:

$$\sigma_\nu^2(R) = \sum_{\ell=0}^{\infty} \frac{2\ell+1}{4\pi} w_\ell^2(R)\ C_\ell\ , \tag{3.2a}$$

$$\sigma_\kappa^2(R) = \sum_{\ell=0}^{\infty} \frac{2\ell+1}{4\pi} \left[\frac{(\ell+1)!}{(\ell-1)!}\right]^2 w_\ell^2(R)\ C_\ell\ , \tag{3.2b}$$

$$\sigma_\eta^2(R) = \sum_{\ell=1}^{\infty} \frac{2\ell+1}{4\pi} \frac{(\ell+1)!}{(\ell-1)!} w_\ell^2(R)\ C_\ell\ , \tag{3.2c}$$

$$\sigma_\epsilon^2(R) = \sum_{\ell=2}^{\infty} \frac{2\ell+1}{4\pi} \frac{(\ell+2)!}{(\ell-2)!} w_\ell^2(R)\ C_\ell\ . \tag{3.2d}$$

The fact of normalizing the data by using a concrete theoretical model does not introduces a bias in the analysis, since it can been seen as a change of units in order to have unit variance quantities. The theoretical fiducial model assumed throughout the chapter is $\Omega_b h^2 = 0.2222$, $\Omega_c h^2 = 0.1197$, $H_0 = 67.31$ km/s Mpc^{-1}, $\tau = 0.078$, $n_s = 0.9655$ and $\ln(10^{10} A_s) = 3.089$, which represent the Planck TT-lowP best-fit cosmological parameters ([8], table 3).

3.3 Data processing

The CMB temperature data analysed in this chapter correspond to the cleaned maps delivered by the Planck collaboration. Since we are studying large scale structures, the foreground contamination may be important in the analysis and could introduce spurious signals. For this reason, two of the four official temperature maps provided by Planck are considered, namely, SEVEM and SMICA [158]. These two maps are given in the Healpix pixelation scheme with resolution $N_{\text{side}} = 2048$ [159], and filtered by a Gaussian beam whose FWHM is $5'$ and the corresponding pixel window function. In terms of the spherical harmonic coefficients, these maps have a band limit of $\ell_{\max} = 4000$.

In order to consider CMB anisotropies at different scales, the maps are filtered by a Gaussian function. The corresponding filter on the sphere is obtained from the stereographic projection of the two-dimensional Euclidean Gaussian distribution, whose Fourier coefficients are given by:

$$w_\ell(R) = \exp\left[-\frac{\ell\,(\ell+1)}{2R^2}\right]\ , \tag{3.3}$$

where the scale R, characterizing the width of the filter, represents the standard deviation of a two-dimensional Gaussian function in the Euclidean space. The linear scale R is related to the angular size θ on the sphere by $R = 2\tan\frac{\theta}{2}$. However, the difference

id	R [deg]	$N_{\rm side}$	$\ell_{\rm max}$
1	1.00	256	767
2	1.20	256	767
3	1.43	256	767
4	1.71	256	767
5	2.04	128	383
6	2.44	128	383
7	2.92	128	383
8	3.49	128	383
9	4.17	64	191
10	4.99	64	191

id	R [deg]	$N_{\rm side}$	$\ell_{\rm max}$
11	5.96	64	191
12	7.13	64	191
13	8.53	32	95
14	10.21	32	95
15	12.22	32	95
16	14.65	32	95
17	17.57	16	47
18	21.11	16	47
19	25.42	16	47
20	30.71	16	47

TABLE 3.1: Different scales considered in this chapter. The first column indicates the labels used in Figure 3.6 to refer to that scale. The second column is the angular scale size R measured in degrees. Finally, the third and fourth columns represent the resolution ($N_{\rm side}$) and the band limit ($\ell_{\rm max}$) used in the calculations of that particular scale, respectively.

between these two quantities is only important at large scales. Throughout the chapter, twenty angular scales from 1° to 30°, which are chosen with logarithmic steps, are considered in the analysis (see table 3.1).

The data maps at the different scales are calculated by performing the spherical harmonic transform of the temperature field up to the given multipole and applying the filter $w_\ell(R)$ for each scale. Before calculating the spherical harmonic coefficients, the maps are masked with their respective confidence masks, and subsequently, the monopole and dipole are removed in the remaining area. In this procedure, the maps are deconvolved in order to remove the effective beam and pixel window function present initially in the data. The derivative fields are computed from the spherical harmonic coefficients following eqs. (3.1a-3.1d). The resulting maps are generated again in the Healpix pixelisation scheme whose resolution depends on the scale R considered. This optimal resolution (in the sense of working at the lowest resolution that retains all the useful information of the filtered signal) is defined by taking into account the properties of the stereographic projection:

$$N_{\rm side} \gtrsim \sqrt{\frac{1}{12}\left(1+\frac{4N}{R^2}\right)}\,, \tag{3.4}$$

where N represents the number of pixels in the area defined by a circle of radius R. Since the values of $N_{\rm side}$ are only powers of 2, the Healpix resolution whose value is immediately greater than the right-hand-side of eq. (3.4) is taken. The gradient, the curvature and the eccentricity tensor require larger resolution than the temperature field, and, for this reason, the value of $N = 56$ is chosen, which we have tested that provides maps with the optimal resolution. Finally, the maps are generated considering only multipoles up to $\ell_{\rm max} = 3N_{\rm side} - 1$, once the corresponding pixel window function

is applied. Of course, the same procedure is applied to the simulations used in the characterization of the statistical properties of the data.

3.4 Pixel covariance in the presence of a mask

Since we are considering a field smoothed at different scales, the mask applied to the data introduces different spurious correlations, and reduces the variance in the region close to it for each convolved version of the signal. In general, if the signal that we want to analyse presents correlations, the particular geometry of the mask becomes important and this effect is not trivial to consider analytically. For this reason, the systematics introduced by the mask are estimated by using a Monte Carlo methodology. Simulations of the CMB anisotropies are generated and masked accordingly to the observed sky in the data, and subsequently, the covariance of the derivatives at different scales are calculated in each pixel. Since the maps are smoothed after the mask is applied, the zeros imposed on unobserved pixels affects to the unmasked region depending on the size of the filter. For the largest scales considered in the chapter, this effect may be especially important.

We have developed a formalism in which the effect of the mask in each pixel can be taken into account. The method is based on the decomposition of the covariance between different masked fields at each pixel as a linear transformation of the corresponding theoretical covariance obtained in the full-sky limit:

$$\hat{\mathbf{C}}(p) = \mathbf{R}(p)\ \mathbf{C}\ \mathbf{R}^t(p), \tag{3.5}$$

where $\hat{\mathbf{C}}(p)$ is the covariance in the pixel p for the masked map, $\mathbf{C}$ is the full-sky covariance, which is independent of the map location, and $\mathbf{R}(p)$ is the transformation matrix relating them. As it is expected, this transformation depends on the sky location due to the anisotropy introduced by the mask. Since the mask geometry can be complicated, the matrix $\mathbf{R}(p)$ is estimated by calculating simulations of the particular masked fields under consideration.

The matrix which defines the linear transformation in eq. (3.5) is unique, imposing the condition that it is lower triangular, in which case, it can be expressed as the product $\mathbf{R}(p) = \hat{\mathbf{L}}(p)\mathbf{L}^{-1}$, where $\hat{\mathbf{L}}(p)$ and $\mathbf{L}$ are the lower triangular matrices obtained from the Cholesky decomposition of $\hat{\mathbf{C}}(p)$ and $\mathbf{C}$, respectively. In the particular case of two-dimensional covariances, the matrix $\mathbf{R}(p)$ is explicitly given by

$$\mathbf{R}(p) = \begin{pmatrix} \frac{\hat{\sigma}_1}{\sigma_1} & 0 \\ \frac{\hat{\sigma}_2}{\sigma_1}\left(\hat{\rho} - \rho\sqrt{\frac{1-\hat{\rho}^2}{1-\rho^2}}\right) & \frac{\hat{\sigma}_2}{\sigma_2}\sqrt{\frac{1-\hat{\rho}^2}{1-\rho^2}} \end{pmatrix}, \tag{3.6}$$

where σ_1 and σ_2 are the r.m.s. of the two considered random variables, and ρ is the correlation coefficient between them. The same quantities, but with the hat notation, indicates the corresponding variables when the field is masked. Notice that $\hat{\sigma}_1$, $\hat{\sigma}_2$ and $\hat{\rho}$ depend on the sky location due to the anisotropy introduced by the mask. Since the components of the matrix $\mathbf{R}(p)$ are formed by ratios of masked and unmasked quantities, it converges faster than $\hat{\mathbf{C}}(p)$ when they are estimated with simulations. For instance, for pixels away from the mask, where the effect of the smoothing on the derivatives is negligible, the matrix $\mathbf{R}$ approaches to the identity with practically zero variance. On the other hand, if the covariance $\hat{\mathbf{C}}(p)$ is calculated directly, it is needed more simulations to converge with a desired precision, even in points for which the mask has no effect. For this reason, the covariance of the the masked fields $\hat{\mathbf{C}}(p)$ is calculated from eq. (3.5), where the transformation matrix $\mathbf{R}(p)$ is estimated with simulations and the full-sky covariance $\mathbf{C}$ is computed theoretically.

Besides for the calculation of $\hat{\mathbf{C}}(p)$, the matrix $\mathbf{R}(p)$ in eq. (3.6) is used to construct an estimator of the one-point covariance of the derivative fields (see Section 3.5), and, additionally, to take into account the observed low variance of the CMB [115] in the analysis performed in Sections 3.6 and 3.7.

3.5 Covariance of the derivatives

One of the anomalies in the CMB data is the low variance of the temperature field at large scales, which have been confirmed by several analyses [91, 115, 116, 160]. In this work, these studies are extended to the variance of each derivative field and the correlation between ν and κ. In order to take into account the smoothing effects on a incomplete sky, it is proposed an estimator that considers the different variance at each pixel. In particular, for two correlated variables given by the vector $\mathbf{x}(p) = (x_1(p), x_2(p))$, the estimator of their covariance matrix is

$$\mathbf{S}^2_{\mathbf{x}} = \frac{1}{N_{\rm pix}} \sum_p \mathbf{R}^{-1}(p)\mathbf{x}(p) \left[\mathbf{R}^{-1}(p)\mathbf{x}(p)\right]^t =$$

$$= \frac{1}{N_{\rm pix}} \sum_p \mathbf{R}^{-1}(p) \begin{pmatrix} x_1^2(p) & x_1(p)x_2(p) \\ x_1(p)x_2(p) & x_2^2(p) \end{pmatrix} \left[\mathbf{R}^{-1}(p)\right]^t \,, \tag{3.7}$$

where the anisotropy of the field due to the mask is considered by using the matrix $\mathbf{R}(p)$ defined in eq. (3.6) and $N_{\rm pix}$ represents to number of observed pixels. This expression is obtained by inverting eq. (3.5) to express the full-sky covariance as a function of the covariance from the data, which is estimated as the product of the two fields at each pixel, and averaging over the observed sky, once the correction given by the inverse of

the matrix $\mathbf{R}(p)$ is applied. From eq. (3.7), it is possible to see that the estimator of the variance of the field x is

$$S_x^2 = \frac{\sigma_x^2}{N_{\rm pix}} \sum_p \frac{|x(p)|^2}{\hat{\sigma}_x^2(p)} \ , \tag{3.8}$$

where we have included the modulus of x in order to generalize this expression for complex fields, like the gradient and the eccentricity tensor. These variances are calculated as a sum over all observed pixels weighted by the ratio $\sigma_x^2/\hat{\sigma}_x^2(p)$, which represents the anisotropy introduced by the mask. In the case of pixels away from the mask, the weights approach to unity, recovering the standard variance estimator for full sky maps. Averaging eq. (3.8), the variance of the field x is obtained, which implies that the estimator S_x^2 is unbiased.

In addition to the variances, the cross-correlation between the variables x and y can be calculated using the following estimator, which is obtained from the off-diagonal component of eq. (3.7):

$$S_{xy} = \frac{\sigma_x \sigma_y}{N_{\rm pix}} \sum_p \frac{x(p)y(p)}{\hat{\sigma}_x(p)\hat{\sigma}_y(p)} \sqrt{\frac{1-\rho^2}{1-\hat{\rho}^2(p)}} + \frac{\sigma_x \sigma_y}{N_{\rm pix}} \sum_p \frac{x^2(p)}{\hat{\sigma}_x^2(p)} \left(\rho - \hat{\rho}(p) \sqrt{\frac{1-\rho^2}{1-\hat{\rho}^2(p)}} \right) \ . \tag{3.9}$$

The fact that the mask modifies the correlation coefficient of the two variables introduces a second term on the right-hand-side of this equation in order to prevent a biased estimation of the cross-correlation. In the particular case of having full-sky maps, S_{xy} coincides with the standard estimator of the cross-correlation of two variables.

In figure 3.1, it is represented the variance of the derivatives fields as a function of the scale. The variance of the normalized temperature field ν presents a low variance with significance greater than 2-σ for scales $> 2^\circ$. This result is in agreement with previous analyses of the low variance of the CMB temperature at large scales [91]. Regarding the derivatives, the gradient η and the curvature κ also have a low variance at large scale, which are significant for $R > 15^\circ$, whereas the eccentricity remains below the 2-σ level for all scales. Additionally, the low variance is also manifested in the cross-correlation of ν and κ for scales $R > 5^\circ$, but, on the other hand, this anomaly is no present in the cross-correlation coefficient, which is calculated normalizing by the observed standard deviations instead of their theoretical values (figure 3.2). This is an indication that, despite of low variance in ν and κ, the correlation of these two variables is compatible with the theoretical expectation. Both CMB Planck maps, SEVEM and SMICA, give similar results in terms of the variance of the derivative fields.

In addition to the analysis of the variance, it is possible to study the local isotropy of the field looking at the variance of the different components of the spinorial derivatives. Since the cosmological principle implies that any statistical quantity does not depend

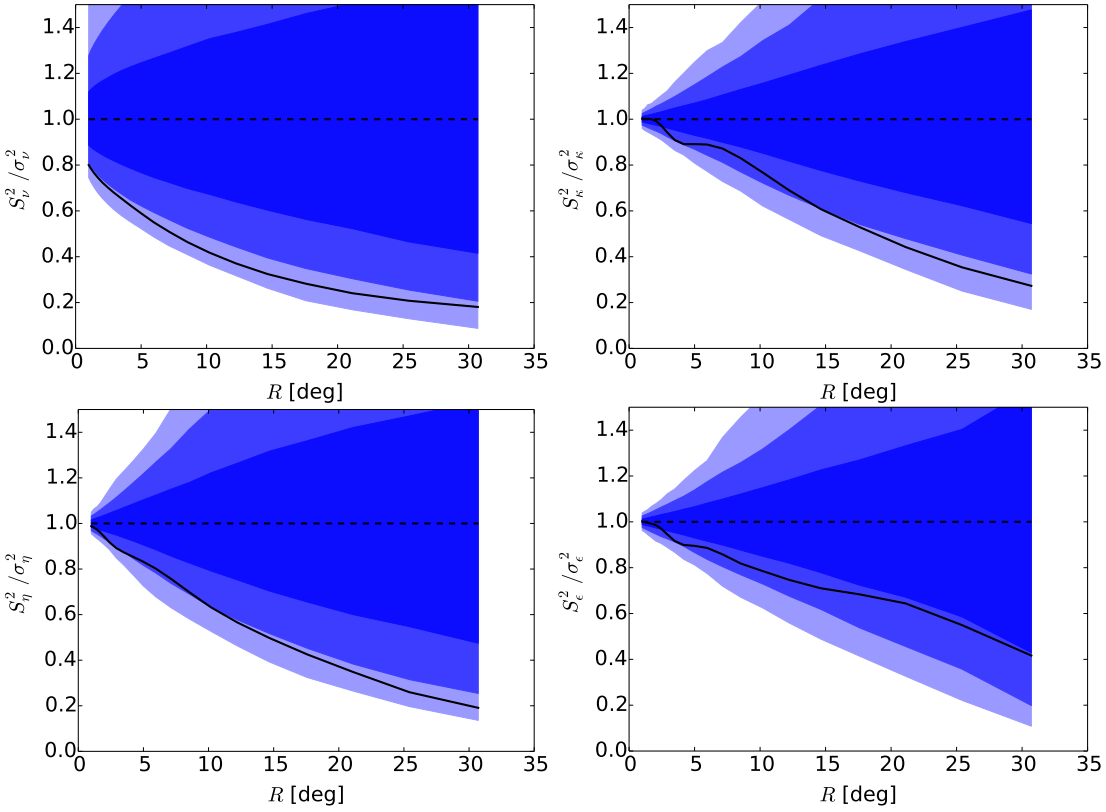

FIGURE 3.1: Variances of the derivatives fields ν, κ, η and ϵ as a function of the scale R, for the Planck SEVEM map. The three contours correspond to the one, two and three sigma regions.

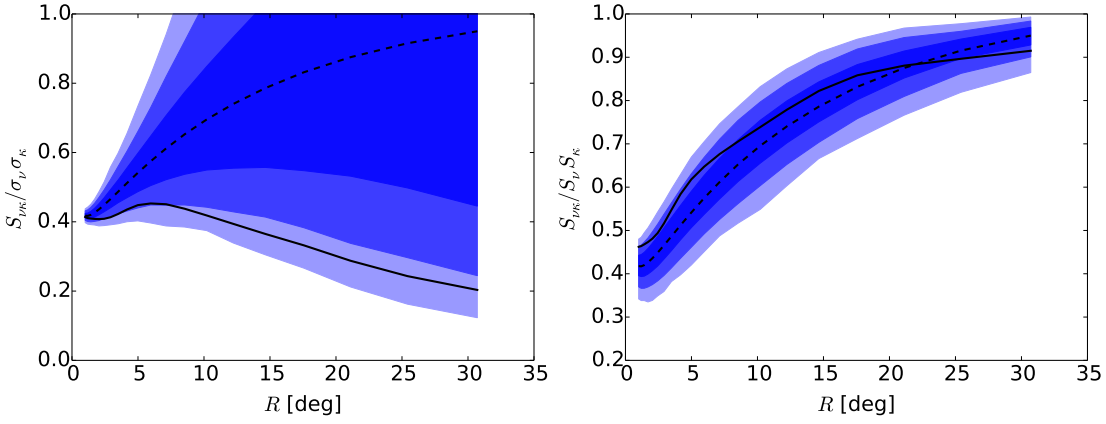

FIGURE 3.2: Cross-correlation $S_{\nu\kappa}$ between the temperature and the curvature (left), and its corresponding correlation coefficient (right) as a function of the scale, obtained from the Planck SEVEM map. The contours correspond to the one, two and three sigma regions.

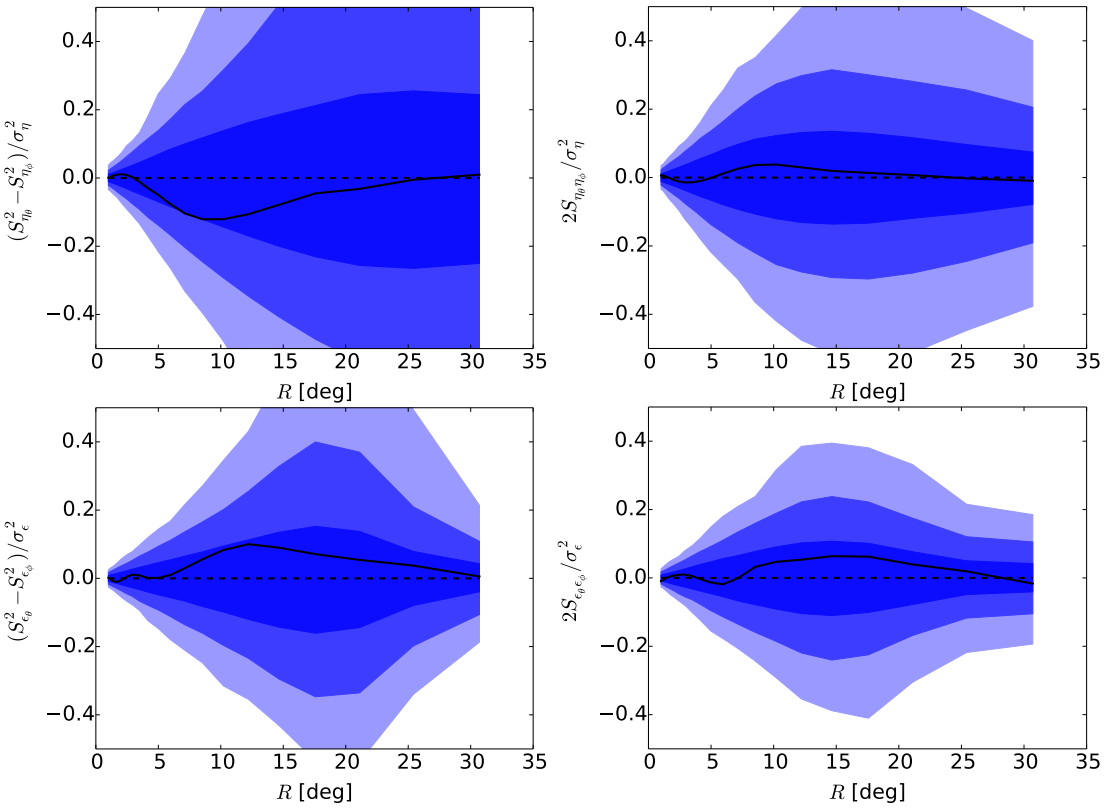

FIGURE 3.3: Difference of the variances (left) and cross-correlation (right) of the two component of the spinors η (upper row) and ϵ (bottom row). The curves are obtained from the Planck SEVEM data. The contours correspond to the one, two and three sigma regions.

on the direction considered, the variance of each component must be the same as well as the correlation between them must vanish. In figure 3.3, the difference of the variances and the cross-correlation between the two components of η and ϵ are depicted, showing that the data are compatible with the isotropy of the field. Notice that these quantities depend on the particular choice of the coordinate system, indicating in this case, an alignment with the galactic north-south direction, which corresponds to the z-axis of the spherical coordinates. A more general analysis of the statistical isotropy of the derivatives, which is independent of the particular coordinate system assumed, is performed in Section 3.7.

3.6 Extreme deviations in the derivatives fields

In order study deviations of the CMB temperature field and its derivatives from the standard model prediction, the tail probability of the one-point distribution for each pixel is calculated. Assuming the predictions of the simplest models of inflation, the CMB fluctuations are Gaussianly distributed and, therefore, the variables ν, κ and the

components of the spinors η and ϵ are also Gaussian variables, since they are calculated applying linear operators over the CMB temperature field.

For the scalar degrees of freedom ν and κ, we define the following quantities:

$$\chi^2_\nu(p) = \frac{\nu^2(p)}{\hat{\sigma}^2_\nu(p)}\sigma^2_\nu \ , \tag{3.10a}$$

$$\chi^2_\kappa(p) = \frac{\kappa^2(p)}{\hat{\sigma}^2_\kappa(p)}\sigma^2_\kappa \ , \tag{3.10b}$$

$$\chi^2_s(p) = \mathbf{s}(p)\hat{\mathbf{C}}^{-1}_s(p)\mathbf{s}(p) \ , \tag{3.10c}$$

where the vector $\mathbf{s} = (\nu, \kappa)$ is composed by the temperature and curvature fields, and $\hat{\mathbf{C}}_s(p)$ denotes the covariance of $\mathbf{s}$ in the pixel p, which is calculated from eq. (3.5). If the temperature field is Gaussian, these quantities are distributed according to the χ^2 probability density. Whilst the χ^2 distribution has one degree of freedom in the case of χ^2_ν and χ^2_κ, the combination χ^2_s has two degrees of freedom. In a similar way, it is computed the χ^2 quantities for the gradient and the eccentricity tensor:

$$\chi^2_\eta(p) = \boldsymbol{\eta}(p)\hat{\mathbf{C}}^{-1}_\eta(p)\boldsymbol{\eta}(p) \ , \tag{3.11a}$$

$$\chi^2_\epsilon(p) = \boldsymbol{\epsilon}(p)\hat{\mathbf{C}}^{-1}_\epsilon(p)\boldsymbol{\epsilon}(p) \ , \tag{3.11b}$$

where, in this case, the vectors $\boldsymbol{\eta}$ and $\boldsymbol{\epsilon}$ denote the components of the spinors η and ϵ, respectively.

In order to quantify deviations from the standard model, we compute the logarithm of the tail probability of χ^2 variables defined in eqs. (3.10-3.11):

$$r_x(p) = -\ln \mathrm{P}\{\chi^2 > \chi^2_x(p)\} \ , \tag{3.12}$$

where x represents the field considered (ν, κ, s, η or ϵ). One advantage of this quantity is that it is distributed following the exponential probability density, independently of the degrees of freedom of the χ^2 variable considered (the logarithm of a variable that is uniformly distributed has an exponential probability density). Possible anomalies on the derivative fields are identified by looking at large values of $r_x(p)$, which correspond to large deviations of $\chi^2_x(p)$. In particular, the maximum of $r_x(p)$ can be computed:

$$r_x = \max_p\{r_x(p)\} \ . \tag{3.13}$$

Due to the intrinsic correlations on the field, the values of $r_x(p)$ for different pixels are correlated, which modifies the distribution of the maximum r_x, particularly at large

scales, where the correlations dominates the field. For this reason, the probability distribution of r_x is calculated using a Monte Carlo method with 5000 simulations.

In figures 3.4 and 3.5, the upper and lower tail probabilities of r_x for each derivative are represented. Since a low variance in the derivative fields is observed, there is a preference for small values of the lower tail probability, especially at the largest scales. For instance, at $R = 30^\circ$ the probability of having a value of r_ν lower than the observed value is about 3% in both SEVEM and SMICA data. The low variance is also manifested in η and ϵ, in which case the lower tail probability is below 3% for $R = 18^\circ$. Additionally in figures 3.4 and 3.5, in order to take into account this anomalous variance in the data, the statistics r_x are calculated using the observed covariance, instead of the covariance obtained from the theoretical fiducial model. In this case, the anisotropy introduced by the mask is also modelled using eq. (3.5), but replacing the matrix $\mathbf{C}$ by the estimated covariance from the data. Once this correction for the low variance is done, the probabilities of r_η and r_ϵ are within the 2σ limits, while some values of r_ν and r_κ with upper tail probabilities $< 5\%$ are found.

The statistical deviation caused by the Cold Spot is observed at $R = 5^\circ$ as a decrement in the upper tail probability of r_κ. Since we are filtering the temperature with a Gaussian, the curvature map of the smoothed field is equivalently calculated by applying the Spherical Mexican Hat Wavelet (SMHW) [121], and therefore, the study of κ at different scales is equivalent to a multiscale analysis using the SMHW (see Appendix D). In previous works [123] with the SMHW, the Cold Spot is characterized as the extreme value at 5°, which causes a deviation in the skewness at this scale. When the upper tail probability is computed using the theoretical fiducial model, the CS represents a relatively likely event with a probability of 6-8%, but if the low variance correction is done and the CS fluctuation is normalized by the observed variance instead of the theoretical one, this probability falls to $< 3\%$, as previously reported in [123] and [91]. Consequently, there is a statistical connection between the CS and the low variance anomaly, being a rare event having a large fluctuation as the CS in a field with such a low variance. Besides the curvature field, the combined analysis of ν and κ, where the correlation between them is taken into account, also presents a deviation at the scale of the CS and above. In particular, a fluctuation with similar significance to the CS (p-value about 1.2%) at the scale of $R \approx 10^\circ$ is observed. At this particular location in the sky, there is no a extremum in the temperature field filtered with that scale, since the gradient is different than zero. However, at smaller scales, there is a hot spot at the same location. This peak and the Cold spot are the most prominent extrema in the κ field at the scale $R \approx 5^\circ$, which were previously identified in the SMHW analysis with a smaller probability in [91]. It is important to notice that these deviations may be caused by the low variance of the CMB temperature field at large scales, since when the

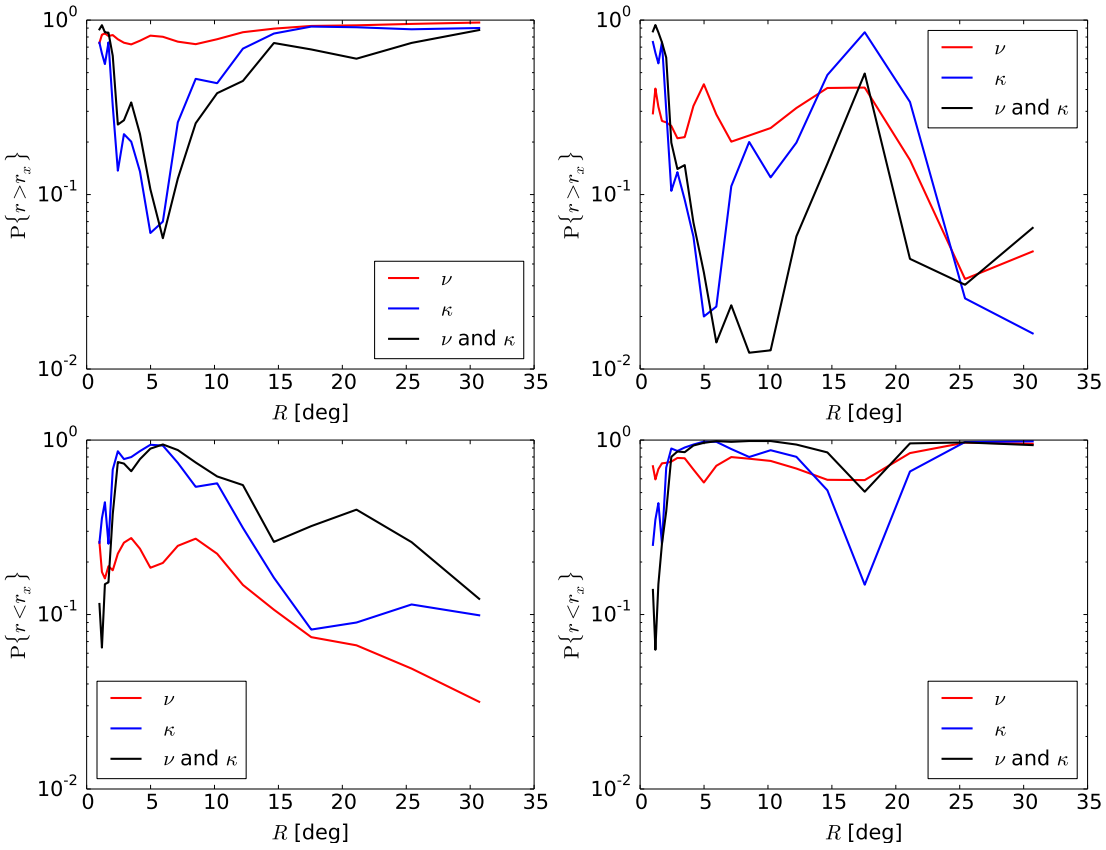

FIGURE 3.4: Upper tail probability (upper row) and lower tail probability (bottom row) of the maximum value r_x for the temperature, the curvature and the combination of both, obtained from the Planck SEVEM map. In the first column, the covariance is calculated from the theoretical fiducial model, whereas the probabilities in the second column are calculated using the covariance obtained from the data, in order to take into account the low variance.

analysis is performed comparing with the fiducial theoretical model, these fluctuations are less significant (see figure 3.4).

The locations of the maximum values of $r_x(p)$ for different scales are represented in figure 3.6. It is possible to see that, with the exception of the eccentricity ϵ, all the maxima lie in the Galactic southern hemisphere, and most of them in the particular quadrant coinciding with the CMB power asymmetry [102, 103]. It is important to remark that, in the case of the temperature ν, all the maxima for scales $R > 1^\circ$ are located in two of the largest spots in the sky, one cold and other hot. On the other hand, the gradient and the second order derivatives trace other large scale features (e.g. the Cold Spot, traced by the κ field). In the case of η and κ, the maximum deviation from the standard model are located near to the largest peaks observed in the temperature map, whereas deviations of the eccentricity tensor ϵ are spread along the field without any particular clustering around the largest structures. The excess of clustering of the ν maxima compared with high-order derivatives is caused by the particular scale

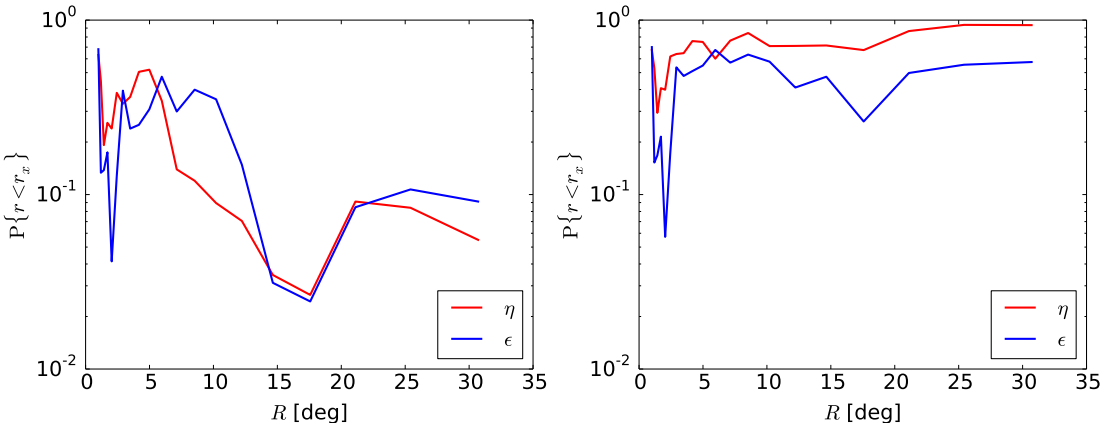

FIGURE 3.5: Lower tail probability of r_η and r_ϵ as a function of the scale, derived from the Planck SEVEM map. Whilst in the left figure the corresponding covariances are calculated from the theoretical fiducial model, the probabilities in the right figure are computed using the estimated covariance from the data.

dependence of the derivatives, which introduces extra ℓ factors, obtaining, in this way, less correlated extrema.

3.7 Directional analysis

The gradient and the eccentricity tensor are spinorial quantities with non-zero spin, and therefore they have directional dependence which can be used to study alignment directions and the local isotropy of the field. In this section, an estimator of preferred directions in the sky for spinorial quantities is introduced. Given a particular point p on the sphere, we can construct all the geodesics connecting it with any other arbitrary point (see figure 3.7). This system of geodesics define a particular directional scheme associated to p, which can be used to project the spinorial field along this geodesics. The projected field is averaged using a particular weight function W, which depends on the size of the region around the point p where the isotropy is tested. If this process is repeated for all the possible points on the sphere, we get an estimator depending on the point p which define the anisotropy direction. For instance, in the case of the gradient, this estimator measures a possible excess of vectors pointing to a particular location on the sphere. This concept can be generalized for arbitrary spin quantities, maintaining a similar interpretation. In the case of the eccentricity tensor, which is a 2-spinor, this estimator indicates the existence of predominant directions where the local elongations of peaks are oriented. A similar analysis of the alignment of the eccentricity tensor (equivalent to the steerable wavelet basis formed by the second Gaussian derivatives) based on the intersection of great circles was applied to WMAP data in [155, 161].

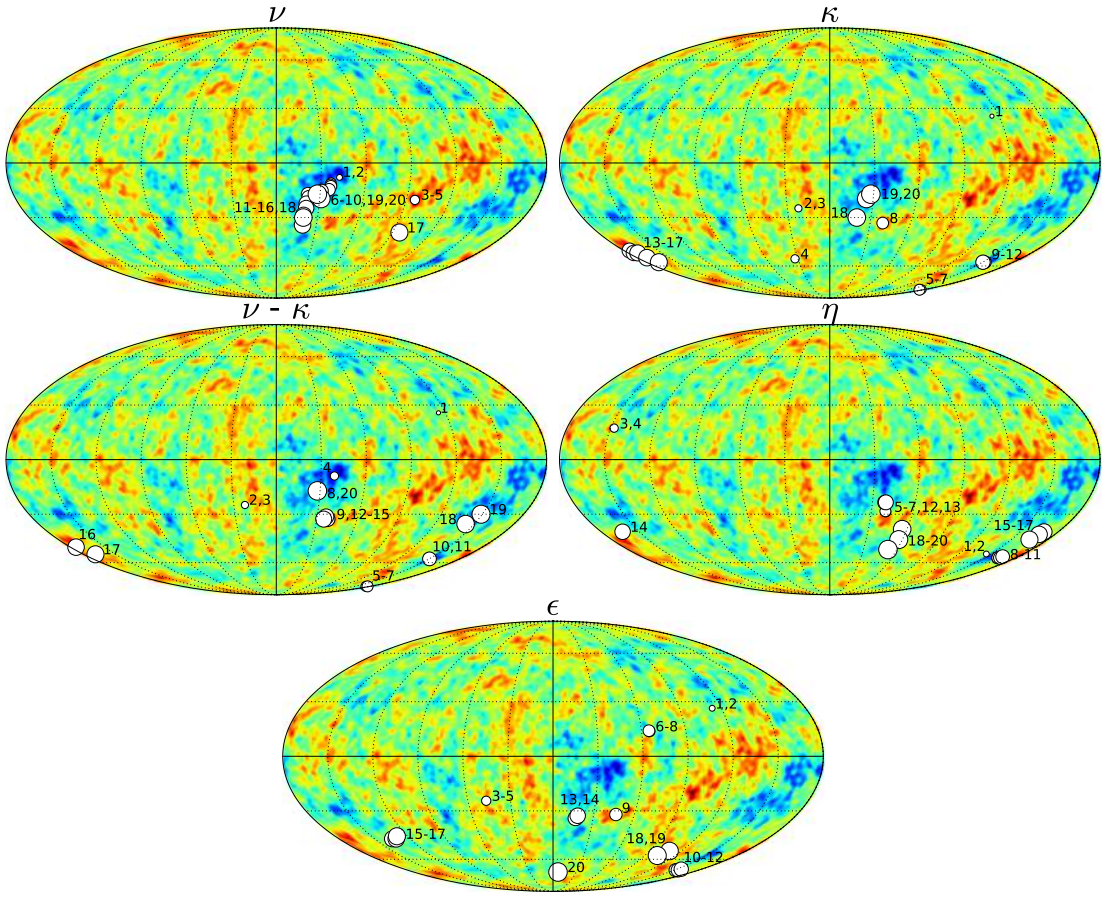

FIGURE 3.6: Locations of the maximum values of $r_x(p)$ for the derivatives fields at different scales. The locations are represented by white circles, whose size is proportional to the scale R considered. The field corresponding to each map is indicated in the title. The CMB temperature field corresponds to the Commander Planck map [158] smoothed by Gaussian with $R = 1°$.

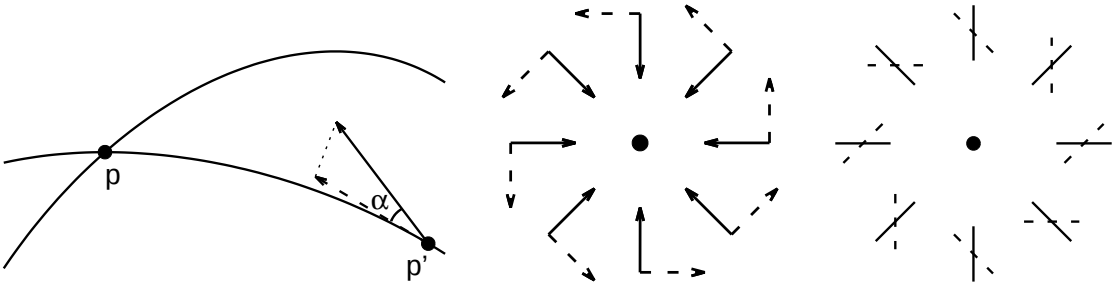

FIGURE 3.7: *Left:* projection of a vector field ($s = 1$) along the geodesic connecting p and p' as it is considered for the definition of the directional asymmetry estimator in eq. (3.14). *Right:* the two pictures represent the contribution of the spinor ${}_s\zeta$ field to the real and imaginary parts of ${}_s\bar{\zeta}(\mathbf{x})$. For simplicity, only the particular cases of $s = 1$ (vectors) and $s = 2$ (headless vectors) are depicted in the figure. The reference point $\mathbf{x}$ used for the projection is indicated at the centre of a small flat patch of the sphere. The spinor components which have even parity (solid lines) contribute to the real part of ${}_s\bar{\zeta}$, whereas its imaginary part measures the contribution of the odd parity components (dashed lines). A change in the sign of ${}_s\bar{\zeta}$ can be seen a rotation of π/s in the spinor field.

Concretely, given a spinorial field ${}_s\zeta$ with spin s defined in the Galactic coordinates, the isotropy estimator associated to the direction defined by the point $\mathbf{x}$ is:

$$ {}_s\bar{\zeta}(\mathbf{x}) = \int \mathrm{d}^2\mathbf{y}\; W(\mathbf{x}\cdot\mathbf{y})\,{}_s\zeta(\mathbf{y})e^{is\alpha(\mathbf{x},\mathbf{y})} \;, \tag{3.14} $$

where $\alpha(\mathbf{x},\mathbf{y})$ is the angle between the Galactic north direction and the geodesic connecting the points $\mathbf{x}$ and $\mathbf{y}$. The function W in this integral weights the contribution of the spinor at $\mathbf{y}$ in the anisotropy direction defined by $\mathbf{x}$. In this way, the function W has information about the region around the point $\mathbf{x}$ where the directional analysis performed. It is possible to see that the directional estimator ${}_s\bar{\zeta}(\mathbf{x})$ is a scalar field, which can be expanded in terms of the spin zero spherical harmonics. In general, this field is complex, and its real and imaginary parts correspond to the projection of different parity components of the spinor (see figure 3.7).

The estimator in eq. (3.14) can be written in the spherical harmonic space as:

$$ {}_s\bar{\zeta}(\mathbf{x}) = \sum_{l=|s|}^{\infty}\sum_{m=-\ell}^{\ell} D_\ell^s \sqrt{\frac{(\ell-|s|)!}{(\ell+|s|)!}}\; {}_s\zeta_{\ell m}\; Y_{\ell m}(\mathbf{x}) \;, \tag{3.15} $$

where ${}_s\zeta_{\ell m}$ are the spherical harmonics coefficient associated to the spinor ${}_s\zeta(\mathbf{x})$. The spin dependent quantities D_ℓ^s in eq. (3.15) are given by:

$$ D_\ell^s = \sum_{\ell'=0}^{\infty} M^s_{\ell\ell'} W_{\ell'} \;, \tag{3.16} $$

where W_ℓ represents the coefficients of the filter W in eq. (3.14) in harmonic space and the coupling matrix $M^s_{\ell\ell'}$ is given by

$$ M^s_{\ell\ell'} = s(-1)^s\left(2\ell'+1\right)\sqrt{\frac{(\ell+|s|)!}{(\ell-|s|)!}}\sum_{L=|\ell-\ell'|}^{\ell+\ell'}(2L+1)\sqrt{\frac{(L-|s|)!}{(L+|s|)!}}\begin{pmatrix}\ell & \ell' & L\\ 0 & 0 & 0\end{pmatrix}\begin{pmatrix}\ell & \ell' & L\\ s & 0 & -s\end{pmatrix}A^s_L \;. \tag{3.17} $$

In this expression, the numbers A_ℓ are related with integral of the spin-weighted spherical harmonics, which are defined in the Appendix B.

In the particular case of the gradient and the eccentricity tensor, it is possible to see that the estimator in eq. (3.14) can be obtained by filtering the temperature map with the filters D^s_ℓ:

$$ \bar{\eta}(\mathbf{x}) = \sum_{\ell=1}^{\infty}\sum_{m=-\ell}^{\ell} D^1_\ell a_{\ell m} Y_{\ell m}(\mathbf{x}) \;, \tag{3.18a} $$

$$ \bar{\epsilon}(\mathbf{x}) = \sum_{\ell=2}^{\infty}\sum_{m=-\ell}^{\ell} D^2_\ell a_{\ell m} Y_{\ell m}(\mathbf{x}) \;. \tag{3.18b} $$

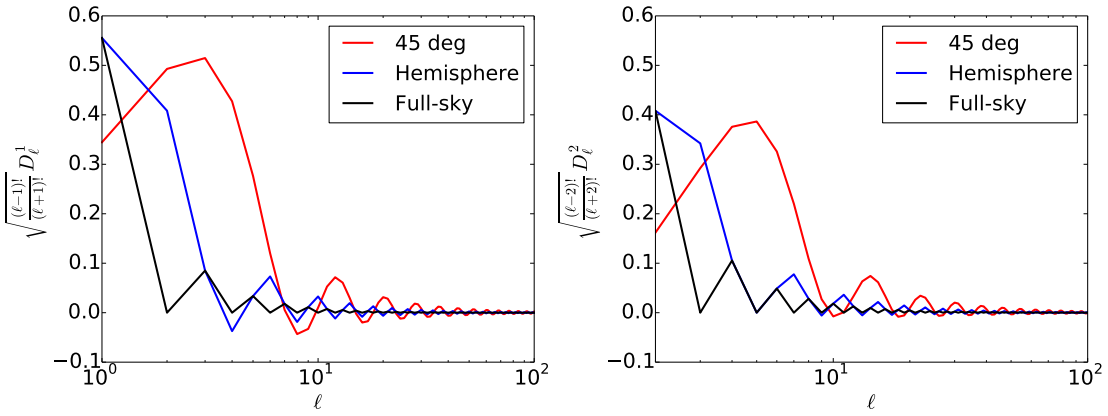

FIGURE 3.8: Filters D^s_ℓ for $s = 1$ (left) and $s = 2$ (right) used in the analysis of the directionality of spinors. Different curves correspond to different averaged area in the estimator.

Notice that the directional estimators for the derivatives $\bar{\eta}(\mathbf{x})$ and $\bar{\epsilon}(\mathbf{x})$ are real scalar fields. Moreover, since they have a linear dependence on the temperature field, it is assumed that they are Gaussianly distributed, which simplify the calculations and the subsequent statistical analysis.

In this work, the weight function W used for averaging of the projected spinor in eq. (3.14) is assumed to be a disc centred at the point $\mathbf{x}$[1]. Particularly, discs with different radius are considered: 180° (full-sky average), 90° (one hemisphere) and 45°. The resulting filters D^s_ℓ for these three cases are represented in figure 3.8, for $s = 1$ and $s = 2$. The asymmetry in the multipoles with different parity, which is more evident in the filters with the largest averaging window, is a consequence of the transformation rules of the spinors under the rotation group. For instance, when a s-spinor is projected and averaged over the full sphere, the multipoles with parity different from s vanish because the field ${}_s\bar{\zeta}(\mathbf{x})$ has well-defined parity given by $(-1)^s$. More precisely, in this particular case, the value of ${}_s\bar{\zeta}$ at the point $\mathbf{x}$ and at its antipode $-\mathbf{x}$ are related by a rotation of π radians, which introduces a factor -1 depending on the parity of the spinor (odd for the vector η and even for 2-spinors ϵ).

Within this formalism, the points on the sphere which present higher directional asymmetry in the derivatives correspond to extrema in the scalar fields $\bar{\eta}(\mathbf{x})$ and $\bar{\epsilon}(\mathbf{x})$, which, in particular, are a maximum or a minimum depending on whether the spinor tends to be aligned or anti-aligned with the direction given by $\mathbf{x}$. From this point of the

[1]In the harmonic space, the weight function W corresponding to a disc with radius θ is given by

$$W_\ell(\mu) = \begin{cases} -\sqrt{\frac{1+\mu}{1-\mu}}\frac{P^1_\ell(\mu)}{\ell(\ell+1)}\,, & \ell \neq 0 \\ 1\,, & \ell = 0 \end{cases},$$

where $\mu = \cos\theta$ and $P^1_\ell(\mu)$ is the associated Legendre polynomial with $m = 1$.

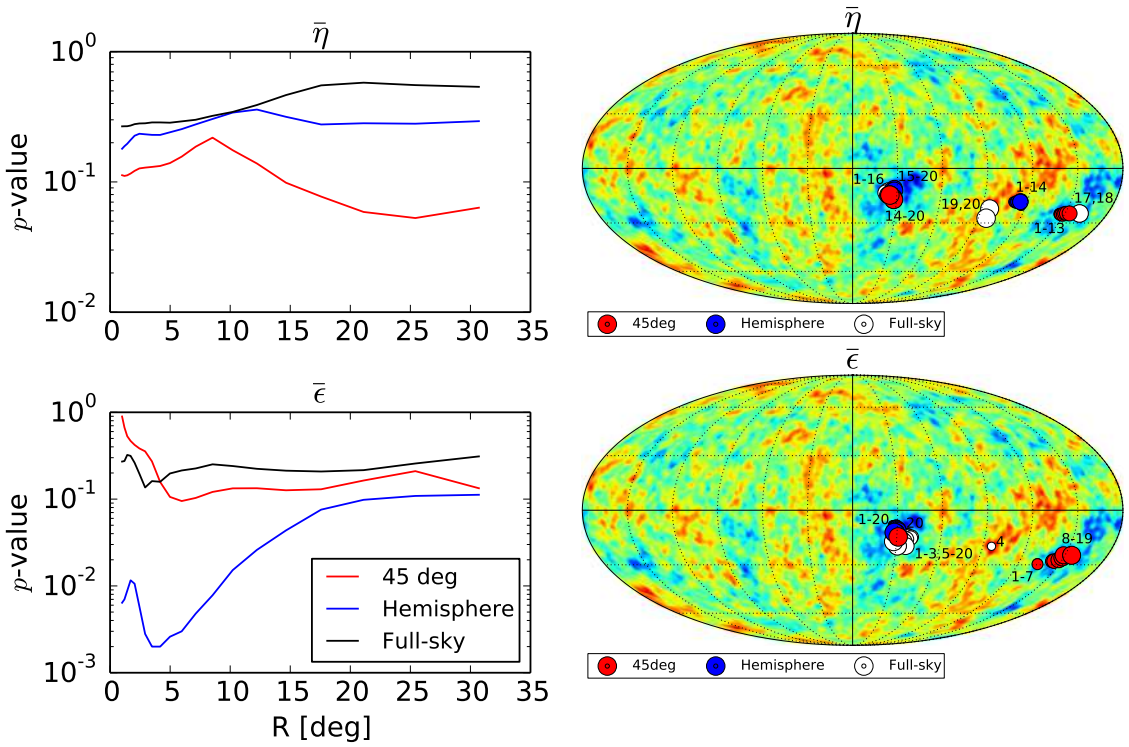

FIGURE 3.9: Directional analysis of the spinors η and ϵ using the three cases considered: full-sky, hemispherical and 45° averages. *Left:* the probabilities of finding a value of $\bar{\eta}$ (upper figure) and $\bar{\epsilon}$ (lower figure) as extreme as the maximum observed in the data for different scales. *Right:* the locations of these maxima on the CMB map are indicated with circles whose size is proportional to the scale R. The results presented in this figure are obtained from the Planck SEVEM map.

study, these extrema are calculated and characterized in the same way as the analysis performed in Section 3.6, and with the same considerations for the mask derived in Section 3.4. The results are shown in figure 3.9, where we represent the p-value of the extrema in $\bar{\eta}$ and $\bar{\epsilon}$ observed in the data as a function of the scale R, as well as their corresponding location on the CMB field. The same three cases represented in figure 3.8 for the weight function are considered in the analysis. Whilst the gradient is compatible with the standard model prediction, the eccentricity tensor has a preferred directionality when the spinor is averaged over an hemisphere. The probability of this deviation is only 0.2% for $R = 4°$ in the SEVEM map, whereas this values increases up to 0.9% for the SMICA data. The corresponding anisotropic direction is located near the Galactic plane on one of the largest peaks of the CMB (see figure 3.9). However, notice that the main contribution to this deviation come from a strip between 45° and 90° from the centre of this structure, since the estimator $\bar{\epsilon}$ for the 45° averaging is within the standard model limits.

Chapter 4

Local properties of the large-scale peaks of the CMB temperature

In the present work, we study the largest structures of the CMB temperature measured by Planck in terms of the most prominent peaks on the sky, which, in particular, are located in the southern galactic hemisphere. Besides these large-scale features, the well-known Cold Spot anomaly is included in the analysis. All these peaks would contribute significantly to some of the CMB large-scale anomalies, as the parity and hemispherical asymmetries, the dipole modulation, the alignment between the quadrupole and the octopole, or in the case of the Cold Spot, to the non-Gaussianity of the field. The analysis of the peaks is performed by using their multipolar profiles, which characterize the local shape of the peaks in terms of the discrete Fourier transform of the azimuthal angle. In order to quantify the local anisotropy of the peaks, the distribution of the phases of the multipolar profiles is studied by using the Rayleigh random walk methodology. Finally, a direct analysis of the 2-dimensional field around the peaks is performed in order to take into account the effect of the galactic mask. The results of the analysis conclude that, once the peak amplitude and its first and second order derivatives at the centre are conditioned, the rest of the field is compatible with the standard model. In particular, it is observed that the Cold Spot anomaly is caused by the large value of curvature at the centre.

4.1 Introduction

In the present chapter, we study the large-scale features on the CMB temperature by identifying the most prominent peaks and analysing their statistical properties. These largest peaks correspond to structures located in the galactic southern hemisphere, more

precisely, in the quadrant where the south ecliptic pole is located. This region of the sky corresponds to the direction where some of the above mentioned anomalies are located (power asymmetry or dipole modulation). Besides this directional asymmetries, the interference of the quadrupole and the octopole induces an excess of power in the ecliptic southern hemisphere which is caused by their particular alignment [162]. Additionally, although it is not a peak as large as the others we consider, the Cold Spot [122, 123] is also included in the analysis since it presents an anomalous peak curvature. All these structures correspond in part to the "fingers" and spots studied in [163]. Moreover, in the previous chapter [164], a multiscale analysis reveals that these peaks are the most outstanding large-scale deviations in terms of either the amplitude or the curvature.

The chapter is organized as follows: in Section 4.2, the large-scale peaks are selected in the temperature field, characterizing their local shape through the derivatives up to second order. The analysis of the peaks is performed in terms of the radial shape of the multipolar profiles in Section 4.3, whereas the study of their phase correlations is considered in Section 4.4. In order to implement a partial sky coverage properly, the work is completed with an analysis of the peaks directly in real space.

4.2 Characterization of the large-scale peaks

The peaks in the CMB correspond to local maxima or minima in the temperature field, and they had been considered as useful geometrical descriptors of the statistical properties of the primordial radiation [140, 143–145, 157]. In order to have an extremum, constraints on the field derivatives have to be imposed. Firstly, the critical point condition implies that the gradient of the temperature must vanish at the peak location, but additionally, in order to exclude possible saddle points, it is imposed that the Hessian matrix is positive or negative definite, depending whether the extremum is a minimum or a maximum. Therefore, it is natural to characterize the peaks theoretically by conditioning the first and second derivatives at the centre of the peak, as well as the corresponding peak height. Following the notation in [157], the derivatives on the sphere are calculated by using the spin raising and lowering operators:

$$\nu = \frac{T}{\sigma_\nu} \,, \tag{4.1a}$$

$$\eta = \frac{\eth^* T}{\sigma_\eta} \,, \tag{4.1b}$$

$$\kappa = -\frac{\eth^* \eth T}{\sigma_\kappa} \,, \tag{4.1c}$$

$$\epsilon = \frac{(\eth^*)^2 T}{\sigma_\epsilon} \ , \tag{4.1d}$$

where the derivatives are normalized in order to have dimensionless quantities with unit variance. This set of parameters corresponds to our peak degrees of freedom, which consist in two scalars (ν and κ), one vector (η) and one 2-spinor (ϵ). Whilst the value of the temperature at the extremum is given by the peak height ν, the local curvature is described by the Laplacian, which is proportional to κ. On the other hand, the spinorial quantities η and ϵ represent the gradient and the eccentricity tensor, respectively. The components of these two spinors expressed in the helicity basis are given by complex numbers, whose real and imaginary parts describe geometrical aspects of the peak. For instance, the local eccentricity of the peak is proportional to the modulus of ϵ, whereas its phase represents the particular direction of the principal axes on the sky. Regarding the gradient, the real and imaginary parts of η correspond to the components of the first derivatives in the orthogonal local system of reference. Theoretically, the gradient at the peak location must vanish by definition, but we maintain this degree of freedom as non-zero in the formalism because, in practice, there is a residual gradient due to the fact that we are selecting peaks as local extrema in a discretised field, which prevents us to impose $\eta = 0$. Although this non-null value of the first derivative is very small compared to its standard deviation, analysis based on conditioning the derivatives are very sensitive to small variations of the conditioned values. In terms of the peak shape, this effect causes a dipolar asymmetry at distances larger than the peak size (see figure 4.8 in Section 4.5).

In this work, we consider the five large-scale peaks given in figure 4.1. In the previous chapter [164], a complete analysis of deviations on the derivatives fields is performed at different scales, concluding that these peaks are the most anomalous structures at large scales. The peaks labeled by 1-4 correspond to two maxima and two minima selected in the CMB temperature field filtered with a Gaussian with $R = 10°$. These peaks are the most prominent large-scale structures in the sky, which are located in the same ecliptic hemisphere. The particular value of $R = 10°$ is chosen so that these large-scale fluctuations are highlighted. On the other hand, the peak labeled by 5 is the well-known CMB anomaly called the Cold Spot [123], which is included in the analysis because is the most outstanding large-scale deviation in terms of the curvature [164], contributing to the non-Gaussianity of the temperature field [122, 123]. The Cold spot is usually characterized as a minimum in the Spherical Mexican Hat Wavelet (SMHW) [121] coefficient map at the scale $R \approx 5°$. As the SMHW is obtained from the Laplacian of the Gaussian function (see Appendix D), the coefficients map is equivalent to the curvature field κ of the temperature, filtered with a Gaussian with the same scale than the SMHW. Since there is a strong correlation between ν and κ at large scales, a minimum in the curvature corresponds to a minimum in the temperature field itself.

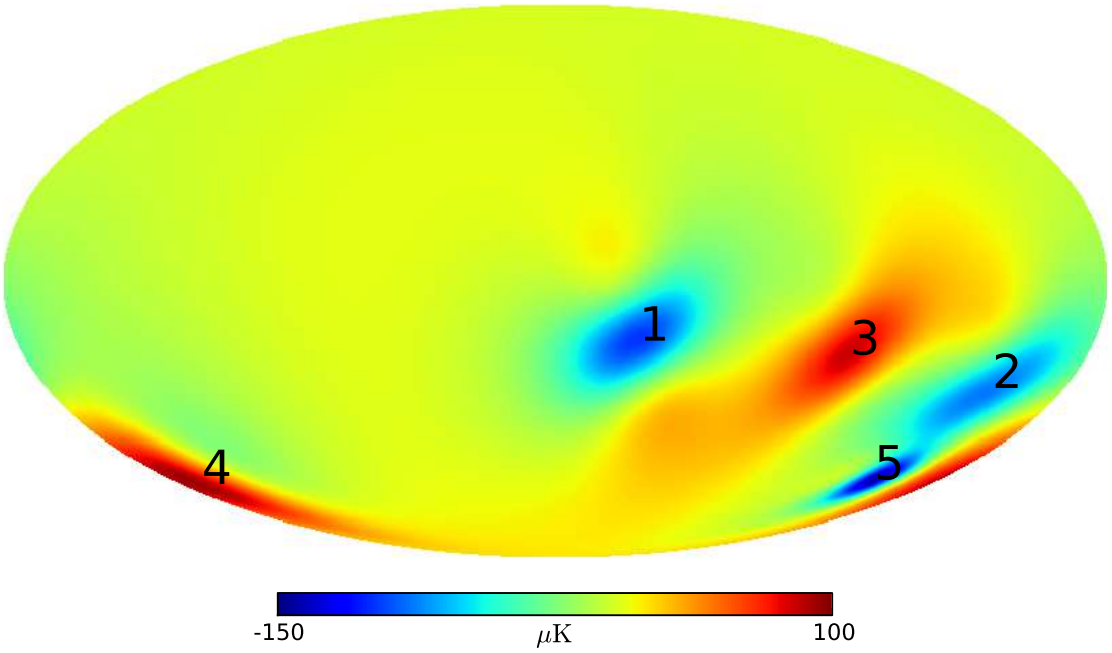

FIGURE 4.1: Locations of the large-scale peaks considered in this chapter, which are labeled with the numbers as referred in the text. The color map represents the theoretical mean field produced by conditioning the derivatives at the centre of the peaks. Notice that the correlation between peaks are not taken into account in this figure, causing that the derivatives do not correspond exactly to the observed values.

For this reason, we equivalently define the Cold Spot as a minimum in ν at the scale $R = 5°$.

In order to calculate the variances of the derivatives and other theoretical quantities, a particular model has to be considered. The following fiducial model is assumed: $\Omega_b h^2 = 0.2222$, $\Omega_c h^2 = 0.1197$, $H_0 = 67.31$ km/s Mpc^{-1}, $\tau = 0.078$, $n_s = 0.9655$ and $\ln(10^{10} A_s) = 3.089$, which represent the Planck TT-lowP best-fit cosmological parameters ([8], table 3).

The values of the derivatives at the centre of the peaks obtained from the Planck Commander map [158] are represented in figure 4.2. The scalar degrees of freedom ν and κ are depicted in the same plane, showing the contours of the one-point probability density function. Since the correlation between ν and κ depend on the scale where the peak is selected, it is expected that the ellipses for the peaks 1-4 ($R = 10°$) are narrower than the ones for the peak 5, whose scale is smaller ($R = 5°$). On the other hand, the one-point distribution of the eccentricity tensor does not depend on the scale R [157], and therefore the probability contours are the same of all the peaks. The Cold Spot (peak 5) is the peak which presents a higher deviation in the ν-κ plane, mainly caused by the large value of $\kappa \approx 4$. This value differs from the SMHW coefficient $\kappa \approx 4.7$ reported in [123] and confirmed by [91] for the same scale, giving a lower probability of

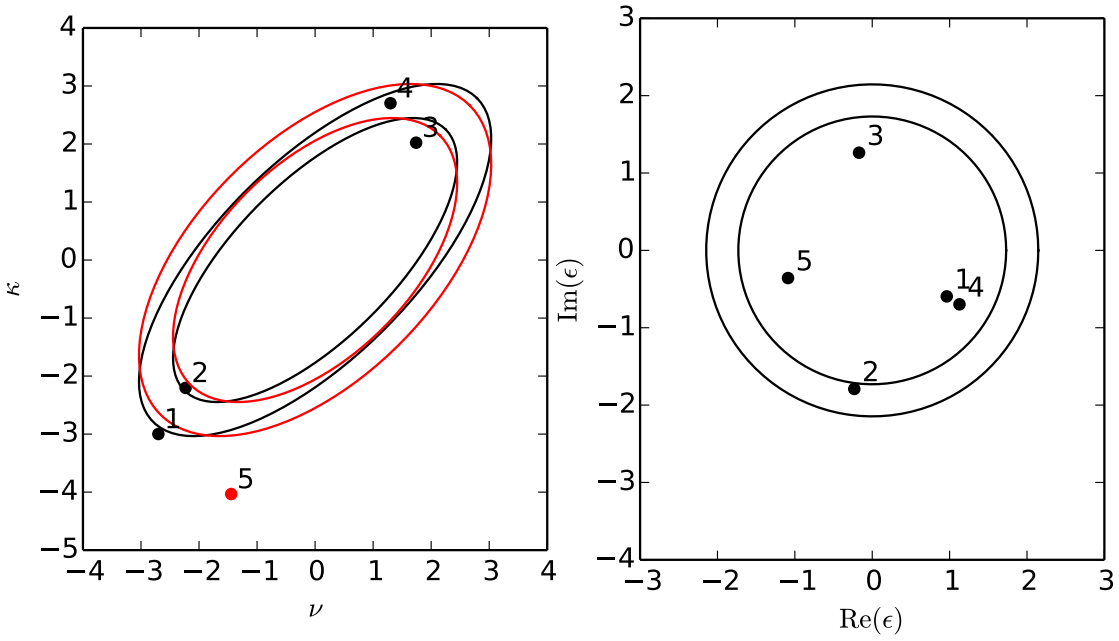

FIGURE 4.2: The peak degrees of freedom labeled with the numbers which identify each peak throughout the chapter. Whilst the peak height ν and the curvature κ are shown in the left panel, the values of the eccentricity tensor ϵ are depicted in the complex plane in the right panel. The ellipses represent the probability contours at 95% and 99% levels. In the case of the ν-κ plane, the contours for the peaks 1-4 are represented in black, and the corresponding ellipses for the Cold Spot (peak 5) are shown in red.

finding a Cold Spot in the CMB temperature. The main difference between these calculations is that, whereas in this work the value of κ is calculated by normalizing by the theoretical variance σ_κ, in [123] and [91] the value of the SMHW coefficient is calculated by using the variance estimated from the data, which is affected by the low variance of the measured CMB field at large scales [91, 115]. On the other hand, the eccentricity of the Cold Spot is within the 2σ level, which implies that its shape is almost circular [124].

The deviation of the peaks derivatives with respect to the standard model is considered by calculating the expected number of peaks with ν and κ as extreme as the corresponding observed values which are present in one realization of the temperature field (see [157] for the expression of the number density of peaks on the sphere). These numbers are 0.054 for the Cold Spot and 0.14 for the largest cold spot at $R = 10^\circ$ (peak 1), whereas the rest of the peaks have an expected number per realization ≈ 1. This implies that a peak as extreme as the Cold Spot in terms of ν and κ is expected in every 19 realizations of the CMB temperature, given a more likely probability for the Cold Spot than the calculation in [123], which considers a larger value for the curvature κ at the centre of the peak, as explained above.

4.3 Multipolar profiles

In this section, we study the shape of the largest peaks observed in the CMB temperature. Following the formalism of [157], the shape of the peaks can be studied through the multipolar profiles, which consist in the coefficients of the Fourier transform of the azimuthal angle around the peak:

$$T_m(\theta) = \frac{1}{2\pi} \int \mathrm{d}\phi \; T(\theta, \phi) e^{-im\phi} \; , \tag{4.2}$$

where the coordinates θ and ϕ represent the radial and azimuthal coordinates, respectively, centered at the peak location. The monopolar profile with $m = 0$ corresponds to the standard profile, which takes into account the spherical symmetric component of the peak. On the other hand, the higher order profiles describe different asymmetrical shapes, depending on the multipole m. For instance, the profiles with $m = 1$ and $m = 2$ represent a dipole and a quadrupole around the peak, respectively.

The derivatives at the centre of the peak affects to the local shape depending on its spin. In particular, if the values of ν, κ, η and ϵ are fixed at the centre, it is obtained the following mean profiles [157]:

$$\langle T_0(\theta) \rangle = \sum_{\ell=0}^{\infty} \frac{2\ell+1}{4\pi} \left[b_\nu + b_\kappa \ell(\ell+1) \right] \; b_\ell w_\ell C_\ell \; P_\ell(\cos\theta) \; , \tag{4.3a}$$

$$\langle T_1(\theta) \rangle = b_\eta \sum_{\ell=0}^{\infty} \frac{2\ell+1}{4\pi} \; b_\ell w_\ell C_\ell \; P_\ell^1(\cos\theta) \; , \tag{4.3b}$$

$$\langle T_2(\theta) \rangle = b_\epsilon \sum_{\ell=0}^{\infty} \frac{2\ell+1}{4\pi} \; b_\ell w_\ell C_\ell \; P_\ell^2(\cos\theta) \; , \tag{4.3c}$$

and $\langle T_m(\theta) \rangle = 0$ for $m \neq 0, 1, 2$. In these equations, we have assumed that the peak is selected in the temperature field filtered with the window function w_ℓ, whereas the profiles are calculated from a field observed with a beam b_ℓ. The bias parameters characterizing the mean profiles depend on the particular values of the derivatives at the centre:

$$b_\nu = \frac{\nu - \rho\kappa}{\sigma_\nu(1-\rho^2)} \; , \tag{4.4a}$$

$$b_\kappa = \frac{\kappa - \rho\nu}{\sigma_\kappa(1-\rho^2)} \; , \tag{4.4b}$$

$$b_\eta = \frac{\eta}{\sigma_\eta} \; , \tag{4.4c}$$

$$b_\epsilon = \frac{\epsilon}{\sigma_\epsilon} \; , \tag{4.4d}$$

where ρ is the correlation coefficient between ν and κ. As it is mentioned before, despite the fact that we are selecting maxima and minima, the gradient at peak location does not vanish because of the discretization of the field. This particular residual affecting to the dipolar profile can be modelled as a small bias b_η depending on the measured value of η. This simple modelization of the bias is enough to correct all the systematic effect appearing in the subsequent analysis.

Additionally, when the local shape of the peak is fixed, the covariance of the multipolar profiles are given by [157]:

$$\langle T_m(\theta) T^*_{m'}(\theta')\rangle = \langle T_m(\theta) T^*_{m'}(\theta')\rangle_{\text{intr.}} + \langle T_m(\theta) T^*_{m'}(\theta')\rangle_{\text{peak}} \ . \tag{4.5}$$

Whilst the intrinsic part $\langle T_m(\theta) T_m(\theta')\rangle_{\text{intr.}}$ represents the covariance of the profile when the derivatives at the centre are not constrained, the term $\langle T_m(\theta) T_m(\theta')\rangle_{\text{peak}}$ is the modification of the covariance due to the fact of conditioning the values of the derivatives. It is important to notice that the covariances of the multipolar profiles do not depend on the specific values at which the derivatives are conditioned. The intrinsic covariance can be calculated from the angular power spectra in the following way [157]:

$$\langle T_m(\theta) T^*_{m'}(\theta')\rangle_{\text{intr.}} = \delta_{mm'} \sum_{\ell=m}^{\infty} \frac{2\ell+1}{4\pi} \frac{(\ell-m)!}{(\ell+m)!}\, b_\ell^2 C_\ell\, P_\ell^m(\cos\theta) P_\ell^m(\cos\theta') = \delta_{mm'} C_m^{\text{intr.}}(\theta,\theta') \ . \tag{4.6}$$

On the other hand, the contribution of the peak to the covariance of the multipolar profiles is different form zero for $m = 0, 1, 2$. In general, it can be written as:

$$\langle T_m(\theta) T^*_{m'}(\theta')\rangle_{\text{peak}} = \delta_{mm'} \sum_{\ell,\ell'=m}^{\infty} \frac{2\ell+1}{4\pi} \frac{2\ell'+1}{4\pi} B^m_{\ell\ell'}\, b_\ell w_\ell C_\ell\, b_{\ell'} w_{\ell'} C_{\ell'}\, P_\ell^m(\cos\theta) P_{\ell'}^m(\cos\theta') = \\ = \delta_{mm'} C_m^{\text{peak}}(\theta,\theta') \ , \tag{4.7}$$

where the matrices $B^m_{\ell\ell'}$ are given by:

$$B^0_{\ell\ell'} = -\frac{1}{1-\rho^2}\left\{\frac{1}{\sigma_\nu^2} - \frac{\rho}{\sigma_\nu\sigma_\kappa}\left[\ell(\ell+1)+\ell'(\ell'+1)\right] + \frac{\ell(\ell+1)\ell'(\ell'+1)}{\sigma_\kappa^2}\right\} \ , \tag{4.8a}$$

$$B^1_{\ell\ell'} = -\frac{1}{\sigma_\eta^2} \ , \tag{4.8b}$$

$$B^2_{\ell\ell'} = -\frac{1}{\sigma_\epsilon^2} \ , \tag{4.8c}$$

and $B^m_{\ell\ell'} = 0$ for $m > 2$. Since conditioning the derivatives reduces the variance of the field, these coefficients are always negative. These expressions can be generalised to consider scenarios where only the amplitude or the curvature are conditioned. In this

case, we have that $B^0_{\ell\ell'}$ equals to $-\sigma_\nu^{-2}$ or $-\sigma_\kappa^{-2}$, depending on whether ν or κ is the conditioned variable.

As it is described in Section 4.2, the peaks 1-4 are selected in a map filtered with a Gaussian with a scale $R = 10°$, whereas the Cold Spot is defined as a peak in $R = 5°$. Therefore, the window function w_ℓ, which characterizes the smoothing of the field where the amplitude and its derivatives are calculated, is a Gaussian filter whose scale R depends on the peak considered. On the other hand, the filter b_ℓ corresponds to the effective resolution of the maps over which the multipolar profiles are calculated.

In order to analyse the shape of the peaks, the values of ν, κ, η and ϵ are conditioned to the measured values at the centre of the peak. The observed monopolar, dipolar and quadrupolar profiles are compared with the theoretical predictions in figures 4.3-4.5. In the case of the quadrupolar profile, a rotation is performed in order to align the principal axes with the system of reference of the peak, such that only the real part has non-zero expectation value. Statistical deviations from the standard model are quantified using a χ^2 test as a function of the maximum value of θ considered in the analysis. Assuming that the CMB temperature is a Gaussian random field, the conditional probability of the multipolar profiles obtained fixing the values of the derivatives at the centre is also Gaussian, therefore the χ^2 test is appropriate for the analysis. It is computed the following quantity for each χ^2 value, which is approximately normally distributed for a large number of degrees of freedom:

$$z_m(\theta_{\max}) = \frac{\chi^2_m(\theta_{\max}) - n_f(\theta_{\max})}{\sqrt{2n_f(\theta_{\max})}} \ , \tag{4.9}$$

where $\theta_{\max}$ represents the maximum value of θ considered in the test, and n_f is the number of degrees of freedom of the χ^2 variable corresponding to that value of $\theta_{\max}$. Whereas for $m = 0$ the value of n_f is equal to the number of bins considered, for any other multipole m it is twice the number of bins due to the fact that the profiles take complex values. In this equation, the statistics $\chi^2_m(\theta_{\max})$ is computed from the measured profiles and the theoretical mean profiles and covariances:

$$\chi^2_m(\theta_{\max}) = (2 - \delta_{m0}) \sum_{\theta_i,\theta_j \leq \theta_{\max}} \left[T^*_m(\theta_i) - \langle T^*_m(\theta_i)\rangle\right] C^{-1}_m(\theta_i,\theta_j) \left[T_m(\theta_j) - \langle T_m(\theta_j)\rangle\right] \ , \tag{4.10}$$

where the matrix $C_m(\theta_i,\theta_j) = C^{\text{intr.}}_m(\theta_i,\theta_j) + C^{\text{peak}}_m(\theta_i,\theta_j)$ is the covariance between the different bins of the multipolar profiles, which is given by the sum of eq. (4.6) and eq. (4.7). The summations in this expression are extended over the indices for which the centre of the bins θ_i take values up to the $\theta_{\max}$. Regarding the theoretical estimation, the mean profiles and covariance must be also averaged in each bin in order to compare with

the data. This operation is equivalent to calculate the integral of the associated Legendre functions in each interval of θ. In the literature [165], there exists analytical formulae which allow one to calculate these integrals recursively (see appendix C). Notice that both the real and the imaginary parts of the multipolar profiles $T_m(\theta)$ are considered in the calculation of $\chi^2_m(\theta_{\max})$. Commonly, the peaks are oriented along the principal axes, in which case the mean value of the imaginary parts vanishes.

Since we are interested in large-scale peaks, the galactic mask is a problem in the calculation of the profiles, specially in the ones with $m > 0$, where the break of the isotropy of the field is critical. Deconvolution techniques based on the Toeplitz matrix can be used in order to correct the mask effect, but in the case of aggressive masking the resulting profiles are not accurately calculated. For this reason, we use an inpainted map without missing pixels, more precisely, the CMB temperature field used in the analysis of the multipolar profiles is the Planck Commander map [158], whose galactic mask region has been filled by calculating a constrained Gaussian realization. On the other hand, in Section 4.5, the peaks are analysed directly in real space, where the missing pixels are not problematic, and therefore the inpainting techniques are not required.

Following the expression in eq. (4.2), the multipolar profiles are calculated by averaging the pixels in rings whose width is 1° and are centred at the different values of θ. Since the size of these bins is large compared with the resolution of the Planck Commander map (FWHM $5'$), the contribution of the instrumental noise can be ignored in our analysis. On the other hand, the filter b_ℓ used in the calculation of the theoretical profiles and covariance is the product of a Gaussian filter characterizing the resolution of the data and the corresponding pixel window function.

In figures 4.3-4.5, it is represented the values of $z(\theta_{\max})$ for the monopolar, dipolar and quadrupolar profiles, respectively. We can see that the deviation of these profiles is less than 2σ in all the peaks considered. Moreover, the multipolar profiles with values of m up to 10 have been analysed, obtaining values which are compatible at 3σ level with what is expected in the standard model.

Particularly, in the Cold Spot analysis, it is found that the monopolar profile agrees with the standard model prediction when the values of ν and κ are conditioned. On the other hand, if only the value of ν is fixed to the observed value whereas κ is averaged out using its probability density distribution (see [157]), the Cold Spot profile presents a 4.7σ deviation for $\theta < 10^\circ$. This result implies that the Cold Spot anomaly is mainly caused by the extremely large value of κ at the centre, whereas when κ is conditioned, no anomaly is found in the monopolar profile. In figure 4.6, it is represented the monopolar profiles of the Cold Spot obtained by conditioning, the peak height ν, the curvature κ, or both. Notice that the ring-shape in the Cold spot at $\approx 15^\circ$ is only recovered when

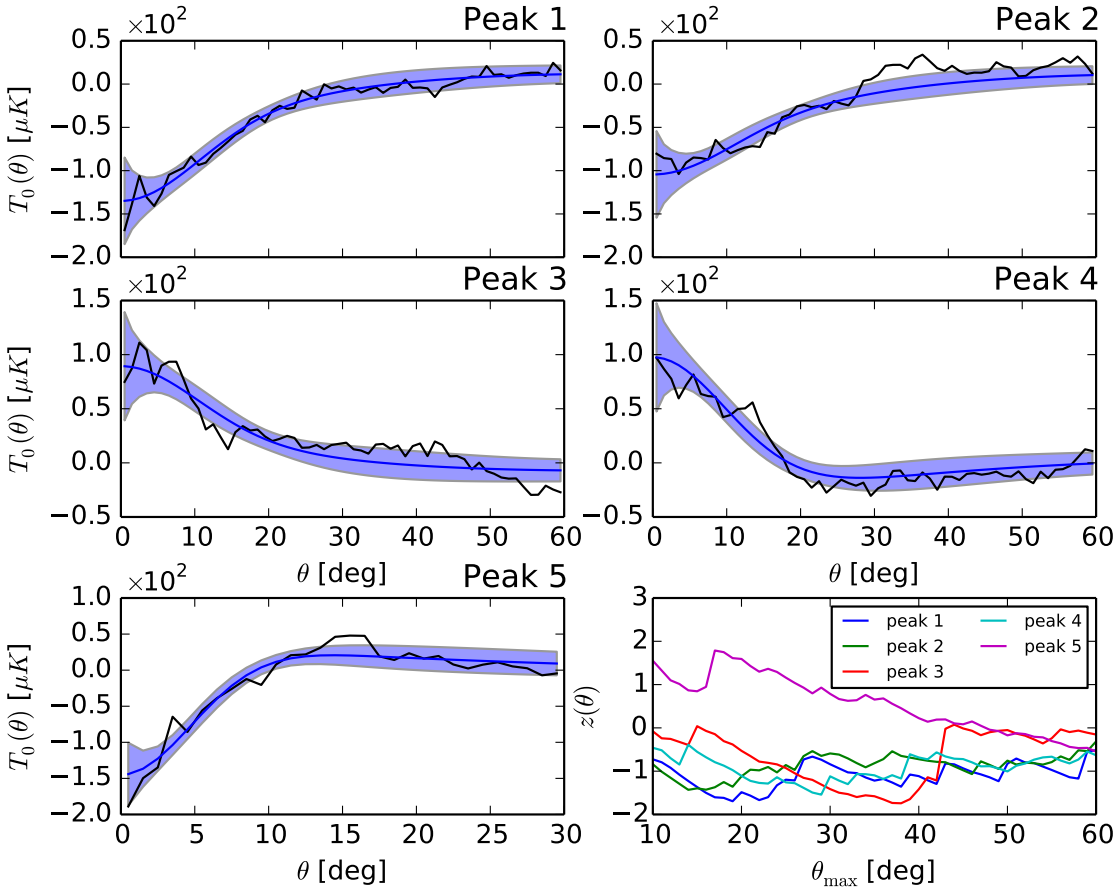

FIGURE 4.3: Monopolar profiles ($m = 0$) and their fit parameters z (see the text for details) for the different peaks considered. The blue line represents the theoretical mean profiles conditioned to the values of ν and κ at $\theta = 0$ observed for each peak, and the shaded regions show the 1σ error bars. The fit parameter z is depicted as a function of $\theta_{\max}$, the maximum value of θ of the profile considered in the fit.

both degrees of freedom are fixed, which implies that this distinctive feature is produced by a combined effect of a large value of κ with a relatively small absolute value of ν.

4.4 Phase correlations of the multipolar profiles

In order to detect deviations from the standard model, the statistical properties of the phases of the spherical harmonics coefficients have been studied in several works. If the CMB temperature field is non-Gaussian or anisotropic, correlations in the phases of the $a_{\ell m}$'s may exists, which causes that they are not uniformly distributed in the interval $[0, 2\pi]$. There are different statistical tests which can be applied to study the randomness of this kind of periodic variables. For instance, the Kuiper's test, which is a generalization of the KS test for circular data, has been used in the analysis of the phases [166]. On the other hand, in [167], the study of the Rayleigh statistics and the random

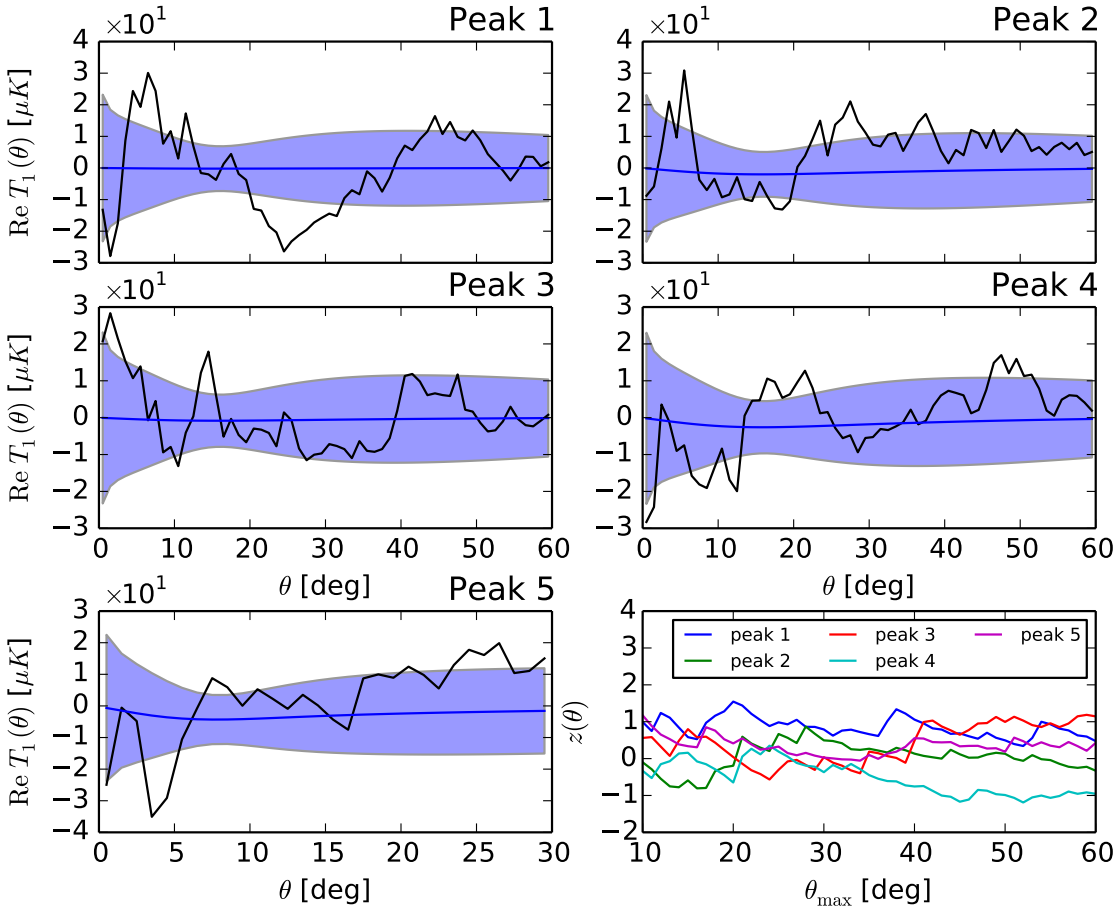

FIGURE 4.4: Real part of the dipolar profiles ($m = 1$) once the peaks are oriented in the direction of the residual gradient introduced by the pixelization. The blue line represents the theoretical mean profiles conditioned to the value of η at $\theta = 0$ observed for each peak, and the shaded regions show the 1σ error bars. Additionally, the fit parameter z is depicted as a function of $\theta_{\max}$, the maximum value of θ considered in the fit.

walk performed by the $a_{\ell m}$'s in the complex plane are applied to the CMB temperature data. All the analyses considered in these works are based on the spherical harmonics coefficients, which describe the field in a particular system of reference, and therefore their results could depend on the direction of the z axis. Additionally, in a previous work [168], the genus of the largest structures on the CMB ($\ell \leq 8$) are analysed concluding that they corresponds to the ones derived from Gaussian field with random phases. In the following, the phases of the multipolar expansion centred at different peak locations are studied in terms of the multipolar profiles.

The decomposition of the field around the peaks in terms of the profiles $T_m(\theta)$ gives information about the contribution of each multipolar pattern to the peak shape. In particular, the phases of the multipolar profiles represent the orientation of each multipole in the local system of reference centred at the peak. Given a multipole m, the

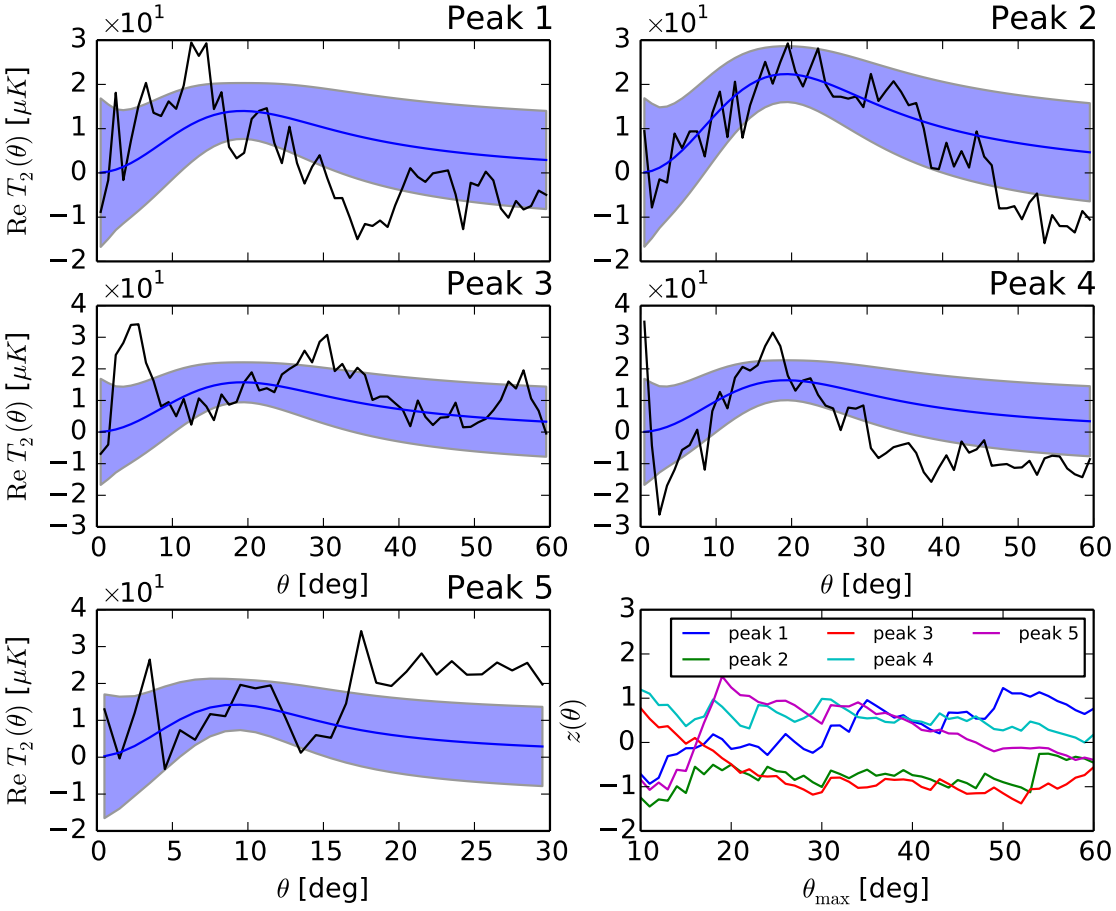

FIGURE 4.5: Real part of the quadrupolar profiles ($m = 2$) oriented along the principal axis for the different peaks considered. The blue line represents the theoretical mean profiles conditioned to the value of ϵ at $\theta = 0$ observed for each peak, and the shaded regions show the 1σ error bars. Additionally, the fit parameter z is depicted as a function of $\theta_{\max}$, the maximum value of θ considered in the fit.

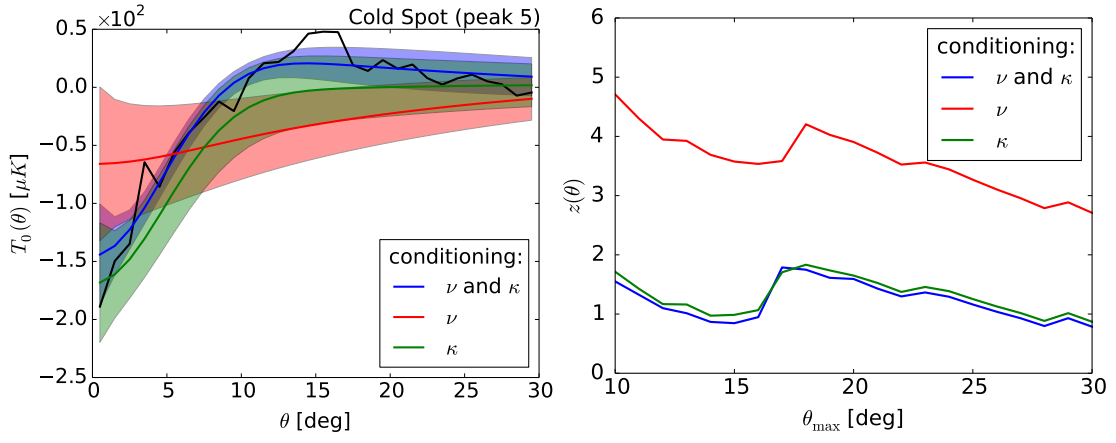

FIGURE 4.6: *Left:* Monopolar profiles of the Cold Spot obtained by conditioning the amplitude ν, the curvature κ, or both. The shaded region represent the 1σ error bar in each case. *Right:* χ^2 test performed over these profiles measured in terms of the normal variable z as a function of the maximum value of θ considered in the analysis.

phases of $T_m(\theta)$ for different values of θ are not independent due to the intrinsic correlations in the field, and therefore an alignment of the multipoles is expected. In order to test whether these correlations follow the standard model or not, profiles whose bins in θ are independent are defined. More precisely, considering n bins of the radial angle labeled by θ_a, the following profiles are calculated:

$$\hat{T}_m(\theta_a) = \sum_{b=1}^{a} \lambda_{ab}^m \left[T_m(\theta_b) - \langle T_m(\theta_b)\rangle\right] \ , \tag{4.11}$$

where the coefficients λ_{ab}^m are chosen such that $\hat{T}_m(\theta_a)$ have unit variance and no correlation for different values of a. In practice, for each value of m, the coefficients λ_{ab}^m correspond to the components of the lower triangular matrix obtained from the Cholesky decomposition of the inverse covariance given in eq. (4.5). Additionally, the mean profile $\langle T_m(\theta_b)\rangle$ is subtracted to the data in eq. (4.11) in order to remove the peak degrees of freedom from the phases analysis, since otherwise the phases can be correlated because we are centred in a particular point of the field with a peak. Notice that the cumulative sum in eq. (4.11) implies that $\hat{T}_m(\theta_a)$ only depends on the values of the temperature with radial distance from the peak centre smaller that θ_a.

As the phases of $\hat{T}_m(\theta_a)$ are independent, they describe a Rayleigh random walk in the complex plane for each value of m. At the time step N, the position of this random walk is given by

$$Z_N^m = \sum_{a=1}^{N} \frac{\hat{T}_m(\theta_a)}{|\hat{T}_m(\theta_a)|} \ . \tag{4.12}$$

In these models of random walks, the time step N corresponds to the maximum radial angle θ_N considered in the multipolar profile. Notice that, if a rotation of the system of reference around the peak is performed with an angle α, the positions of the random walk transform as $Z_N^m e^{im\alpha}$, as can be deduced from the transformation properties of the multipolar profiles. This is just a rotation of angle $m\alpha$ of the complex plane where the random walk moves on. Since the action of the rotation group on the steps Z_N^m is different for each value of m, we consider a random walk for different multipolar profile separately. In previous works [167] based on the spherical harmonics coefficients, different values of m contribute to the steps, which implies that the resulting random walk analysis is not invariant under rotations of the z axis. On the other hand, in the scenario considered in this chapter, the analysis of the random walks performed by the phases of each multipolar profile only depends on the position of the peak, and not on the orientation of the local system of reference.

The distance between the random walk position at the step N and the origin of the complex plane is approximately distributed following the probability density

$$P_N(r) = \frac{2r}{N}\, e^{-r^2/N} \,, \tag{4.13}$$

which is valid for large values of N. From this equation, it can be deduced that the variable $\sqrt{2/N}r$ is distributed according to the Rayleigh distribution (or equivalently, $2r^2/N$ follows a χ^2 with two degrees of freedom). In order to achieve better precision with this formula, the value of r is calculated as follows [169]:

$$r_N^m = \sqrt{\left(1 - \frac{1}{2N}\right)|Z_N^m|^2 + \frac{|Z_N^m|^4}{4N^2}} \,. \tag{4.14}$$

For large values of N, the variable r_N^m approach to the distance travelled by the random walk $|Z_N^m|$. Considering this definition, the variable r_N^m follows the probability in eq. (4.13) with $O(N^{-2})$ accuracy, instead of the $O(N^{-1})$ error achieved with the standard definition of the distance ($r_N^m = |Z_N^m|$).

The analysis is based on the fact that if the phases of the profiles $\hat{T}_m(\theta_a)$ are correlated, the distances travelled by the random walks will be greater than the ones expected from eq. (4.13). The paths followed by the random walks obtained from the phases of the multipolar profiles of the different peaks considered are represented in figure 4.7. In addition, the lower tail probability of the distance travelled by the random walk at the time step N is depicted.

It is possible to see some evidences of correlation of the phases for the multipole $m = 8$ in the peaks 2 and 4, whereas in the case of the peaks 3 and 5, the most correlated multipoles are $m = 4$ and $m = 5$, respectively. Regarding the Cold Spot (peak 5), it is important to notice that the maximum correlation is reached at $\approx 15°$, the angular distance which coincides with the position of a hot ring around the centre of the Cold Spot. On the other hand, the lack of anomalies in this analysis can be seen as evidence of the low level of residuals in the Planck Commander map at full-sky.

4.5 Real space analysis

In the case of having an incomplete sky, the multipolar profiles with $m \neq 0$ are very sensitive to the geometry of the mask. This is not the case of the monopolar profiles ($m = 0$), for which the standard sky fraction correction is enough to have a good estimation of the profile. Since we are interested in large-scale structures, it is very unlikely to avoid the effect of the galactic mask in the analysis of the peaks. In this

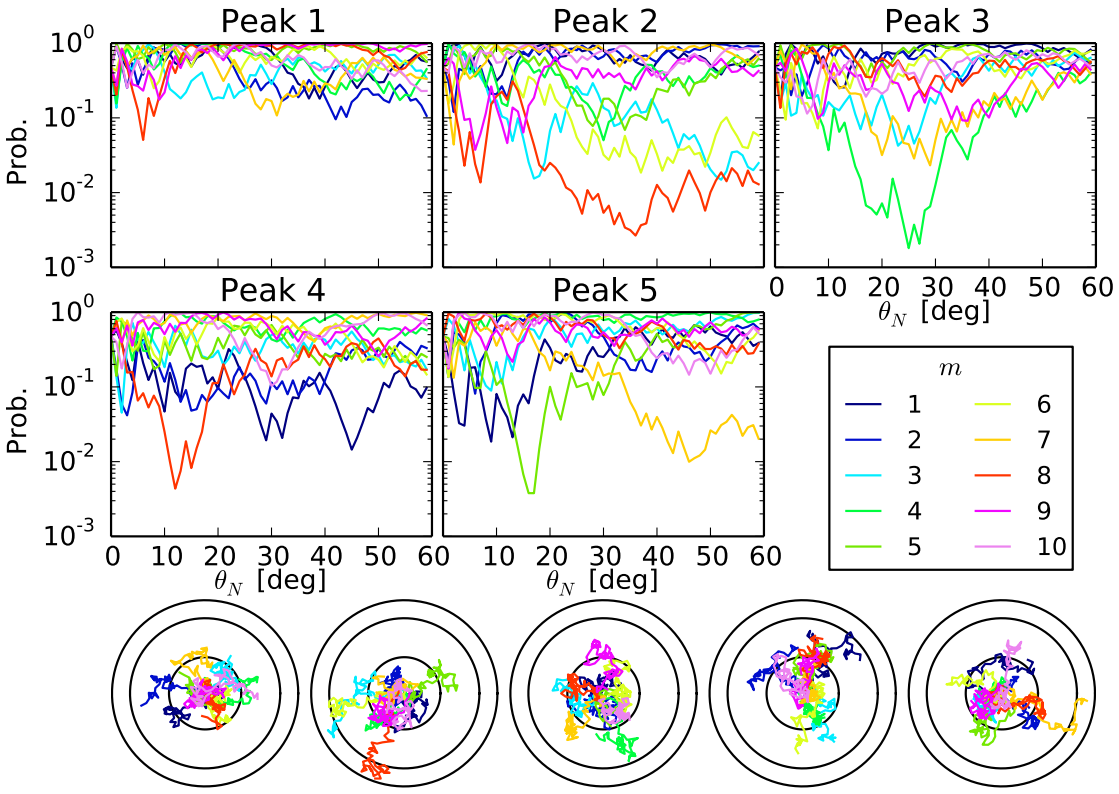

FIGURE 4.7: *First and second rows:* Lower tail probabilities of the distance travelled by the Rayleigh random walks Z_N^m as a function of the time step N, which corresponds to the angle θ_N as labeled in the x axis. Different colours represent the multipole m of the profile as described in the legend. *Bottom row:* Paths followed by the Rayleigh random walks derived by the phases of the multipolar profiles of the large scale peaks considered in this chapter (numbers of the peaks are ordered from left to right). The black solid circles define the positions at which the probability distribution of the total travelled distance takes the values 0.50, 0.95 and 0.99, from inner to the outer circle.

section, we consider a real space approach, analysing 2-dimensional patches around the peaks in a pixel-based formalism. This allows one to take into account the mask in a simple way, as compared with the Fourier analysis provided by the multipolar profiles.

As in the previous sections, the patches around the peaks are parametrized by the polar coordinates (θ, ϕ) with the peak located at the centre of the system of reference. If the peak is described by its derivatives up to second order, the mean value of the field is given as Fourier expansion in terms of the multipolar profiles with $m = 0, 1, 2$ [157]:

$$\langle T(\theta,\phi)\rangle = \langle T_0(\theta)\rangle + \langle T_1(\theta)\rangle e^{i\phi} + \langle T_1^*(\theta)\rangle e^{-i\phi} + \langle T_2(\theta)\rangle e^{i2\phi} + \langle T_2^*(\theta)\rangle e^{-i2\phi} \qquad (4.15)$$

On the other hand, the covariance of the temperature around the peak can be decomposed in terms of the intrinsic covariance of the field, and the covariance due to the

effect of the peak selection [157]:

$$C(\theta,\phi,\theta',\phi') = C_{\text{intr.}}(\theta,\phi,\theta',\phi') + C_0^{\text{peak}}(\theta,\theta') + 2C_1^{\text{peak}}(\theta,\theta')\cos(\phi-\phi') + 2C_2^{\text{peak}}(\theta,\theta')\cos[2(\phi-\phi')]\,, \tag{4.16}$$

where $C_{\text{intr.}}$ is the standard correlation function between the points (θ,ϕ) and (θ',ϕ') of the temperature field, which does not consider the contribution of the peak, and C_m^{peak} for $m = 0, 1, 2$ (defined in eq. (4.7)) represents the contribution to the covariance due to the fact that we are conditioning to the values of the derivatives at the location of the peak.

The data used to study the peaks directly in the real space are the Planck SEVEM and SMICA temperature maps, masked with their confidence masks [158]. The analysis of the 2-dimensional patches is based on the HEALPix pixelization scheme [159] of the regions around the peaks. For the largest peaks labelled by 1-4, the CMB data is filtered with a Gaussian of FWHM 2° in harmonic space and mapped at the resolution corresponding to $N_{\text{side}} = 32$. On the other hand, the Cold Spot (peak 5) is analysed at $N_{\text{side}} = 64$ with a FWHM of 1°. The masks for the two resolutions are calculated by smoothing the full resolution mask with the corresponding Gaussian, and masking pixels below a given threshold (in our case, 0.9). The resulting patches consist in disc-shape regions centred at the peaks with maximum radii of 60° for the largest peaks, and 30° for the Cold Spot, which leads to a total number of pixels ~ 3000 for each of the peaks. The gnomic-projected CMB data at the peaks locations are represented in figure 4.8. Finally, the covariance and the theoretical profiles are calculated by using eqs. (4.7) and (4.3), where, as in the case of the multipolar profiles, the window function b_ℓ is given by the map resolution considered and the pixel window function.

The patches obtained from the data are compared with the theoretical models of the peaks obtained after conditioning to the values of the derivatives at the centre. The goodness of fit is evaluated by using a χ^2 test as a function of the maximum value of the radius considered in the analysis. No significant deviations from the theoretical models are found in the data for any of the peaks, a result which is consistent with the analysis of the multipolar profiles in Section 4.3. Finally, in order to check the consistency between the real space and multipolar profile methodologies, the analysis of patches is repeated with the full-sky Commander map, finding that both analysis are compatible with the standard model.

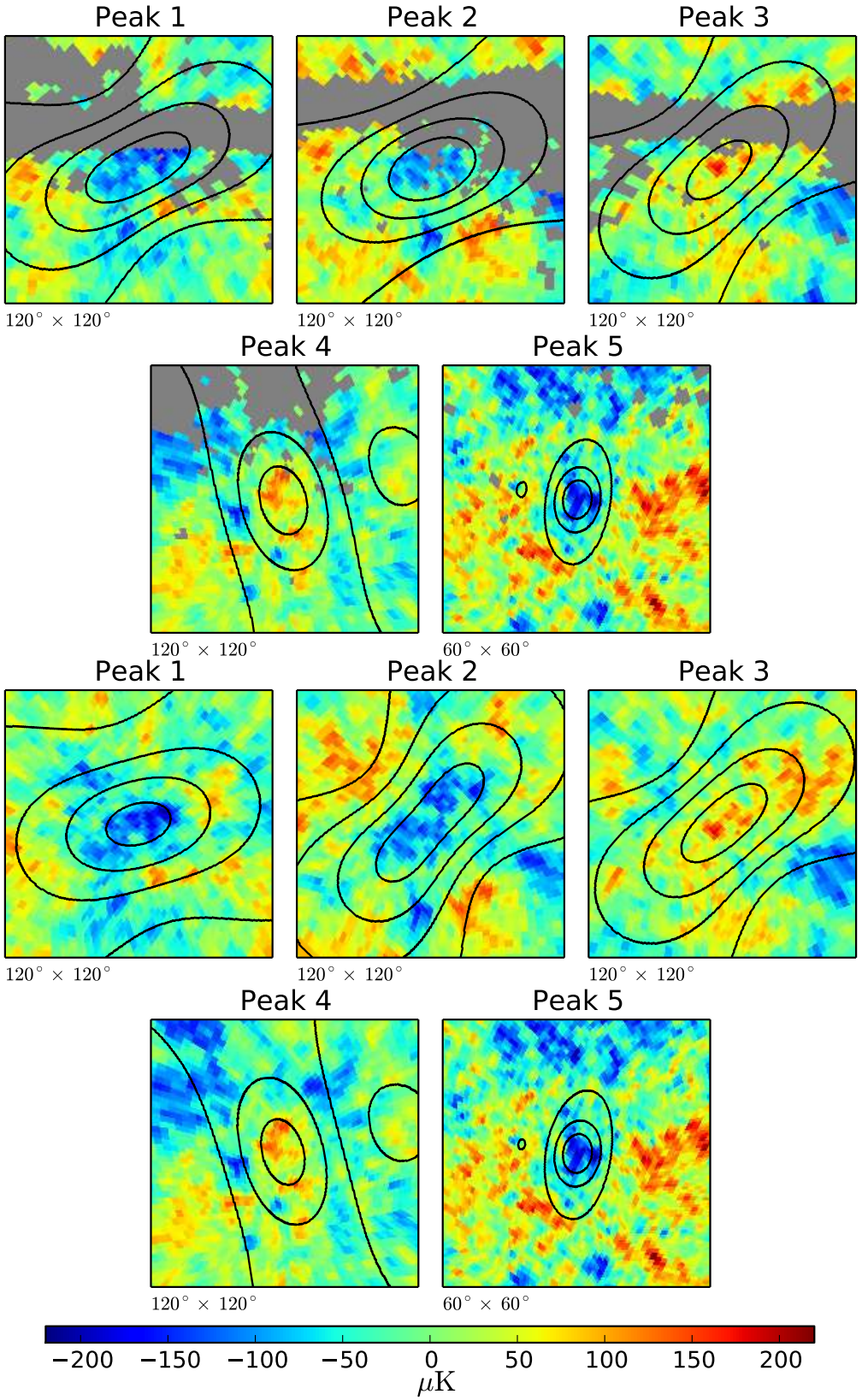

FIGURE 4.8: Temperature patches of the Planck SEVEM (first and second rows) and Commander (third and fourth rows) maps around the peaks considered in the 2-dimensional analysis, where, in the case of SEVEM, the missing pixels due to the galactic mask are represented in gray. The contours depicts the theoretical mean temperature field obtained by conditioning the values of the derivatives at the centre of the peak.

Chapter 5

On the void explanation of the Cold Spot

The integrated Sachs-Wolfe (ISW) contribution induced on the cosmic microwave background by the presence of a supervoid as the one detected by [136] is reviewed in this chapter in order to check whether it could explain the Cold Spot (CS) anomaly. Two different models, previously used for the same purpose, are considered to describe the matter density profile of the void: a top-hat function and a compensated profile produced by a Gaussian potential. The analysis shows that, even enabling ellipticity changes or different values for the dark energy equation of state parameter w, the ISW contribution due to the presence of the void does not reproduce the properties of the CS.

5.1 Introduction

The Cold Spot (CS), an extremely cold region centred on $(b, \ell) = (210°, -57°)$, was discovered in the Wilkinson Microwave Anisotropy Probe (WMAP) data using a multiscale analysis of the Spherical Mexican Hat Wavelet (SMHW) coefficients [122, 123]. Within the ΛCDM model, the significance of the occurrence of this feature in the cosmic microwave background (CMB) anisotropies was estimated between 1% and 2% [124]. As the Planck Collaboration confirmed, the CS shows unusual properties which come to light when the mean angular profile or the area of wavelet coefficients above a certain threshold on angular scales around 10° are analysed [91]. Besides the possibility that the CS could be a statistical fluke, different explanations have been proposed. Although this chapter is focused on the void hypothesis, other physical mechanisms include a cosmic bubble collision [125–127], the gravitational evolution of a cosmic texture [128], and alternative inflationary models [129].

Recently, there has been a debate on whether the CS could be explained as a consequence of the presence of a large void, which was detected in the WISE-2MASS galaxy survey at the same direction [136, 137]. Actually, this is not the first time in which a void arises as the possible origin of the CS (see e.g. [130–135]). This low-density region is consistent with a supervoid centred at $z \approx 0.15 - 0.25$, depending on its characterization. The alignment of the void and the CS is pointed out as a hint of a physical connection between both phenomena. They built their argument based on a probabilistic discussion about this alignment and a particular case of the Lemaître-Tolman-Bondi (LTB) model with a Gaussian potential [137] to infer the angular profile of the CMB imprint of a spherically symmetric supervoid in the number density of galaxies. In this latter paper, the connection between the supervoid detected in WISE-2MASS and the CS was analysed in the light of the integrated Sachs-Wolfe (ISW) and the Rees-Sciama contributions. However, [170] and [171] show independently that the first-order ISW contribution from the presence of this type of void is actually dominant with respect to the non-linear component (Rees-Sciama effect), and therefore the corresponding temperature decrement induced in the CMB by the presence of a void as the one mentioned above (≈ -19 μK) would not be intense enough to account for the depth of the CS (≈ -150 μK).

In this chapter, we explore the latter argument through a supplementary analysis in the SMHW coefficients [121] at the specific CS angular scale, since the anomaly is detected in the SMHW space. In addition, we extend the void models enabling ellipticity changes to check that a different geometry could not produce an ISW contribution which accounts for the CS. We also show that alternative simple models of dark energy cannot reconcile the CMB contribution from a supervoid and the observed CS temperature. Finally, we discuss the previous analyses.

5.2 The void influence on the CMB

As it is known, within the standard cosmological model, the contribution of any possible supervoid is already included in the total CMB anisotropies (as a part of the linear ISW contribution) and therefore the presence of a standard and linear underdensity cannot explain the anomalous temperature decrement of the CS. The assumption that the effect on the CMB photons due to the nonlinear evolution of the potential is negligible with respect to the ISW contribution is based on previous analyses of the Rees-Sciama contribution, which becomes noticeable at multipoles $\ell > 80$ ($\lesssim 2^\circ$), and even at these angular scales, its value is much lower than the ISW component at large scales (see e.g. [172]). Therefore, a rare void is needed in order to explain the CS with the ISW

and Rees-Sciama effects. These non-standard scenarios are explored varying the void eccentricity up to very unlikely values. In any case, the angular size of the ISW effect of the voids considered in this work is greater than several degrees.

Besides the amplitude of this decrement, the profile of the CS is also important to characterize the anomaly because a particular shape is preferred when it is selected in the SMHW coefficients. In this section, we first review the main conclusions about the ISW contribution expected from the presence of a void as that detected by [136]. Subsequently, the impact of varying the ellipticity of the void is also explored. In addition, non-standard scenarios with different values of w are considered to check whether the void prediction is able to cause a temperature decrement as that observed in the CS.

5.2.1 Spherical model

Because of symmetry assumptions, the ISW contribution to the CMB anisotropies caused by a large-scale structure (LSS) fluctuation can be written as:

$$\frac{\Delta T}{T}(\theta) = -2 \int \mathrm{d}z \frac{\mathrm{d}G(z)}{\mathrm{d}z} \Phi \left(\sqrt{r^2(z) + r_0^2 - 2r(z) r_0 \cos\theta} \right), \tag{5.1}$$

where θ denotes the angular distance from the centre of the void at $r_0 = r(z_0)$, in comoving distance. The gravitational potential $\Phi(\mathbf{r}, z)$ is factorized into the growth suppression factor $G(z)$ and a spatial dependence $\Phi(r)$ which, assuming $G(0) = 1$, represents the potential at $z = 0$.

In this chapter, two different density profiles, which have been already used to the same purpose, are considered. On the one hand, a spherical top-hat (TH) model [136], parametrized by its radius R. In this case, the potential can be written as

$$\Phi(r) = \begin{cases} \phi_0 R^2 \left(3 - \dfrac{r^2}{R^2} \right), & \text{if } r \leq R \\ \phi_0 \dfrac{2R^3}{r}, & \text{if } r > R, \end{cases} \tag{5.2}$$

where r denotes the comoving distance from the centre of the void.

When distances greater than R are considered, this model behaves as a point-like particle: it presents an inverse dependence on distance, and therefore the gravitational effect is extended far beyond distances as the size of the void.

On the other hand, a particular case of LTB model is considered [137, 171]. The potential is described in this case by a Gaussian profile:

$$\Phi(r) = \phi_0 {r_0}^2 \exp\left(-\frac{r^2}{{r_0}^2}\right), \tag{5.3}$$

where r_0 accounts for the scale. Hereafter, this profile is referred to as the Gaussian model, although the matter underdensity profile is not Gaussian in this case[1].

It is easy to show that, whilst the density profile associated to the Gaussian potential is compensated, that associated to the TH model is not.

In both cases, the amplitude ϕ_0 is proportional to the matter density fluctuation at the void centre δ_0:

$$\phi_0 = \frac{\Omega_m \delta_0}{4G(0)} \left(\frac{H_0}{c}\right)^2, \tag{5.4}$$

where, in a flat universe, $\Omega_m = 1 - \Omega_\Lambda$ denotes the matter energy density (in our case, with a fixed dark energy density $\Omega_\Lambda = 0.685$), H_0 is the Hubble constant at present time and c is the speed of light in vacuum.

The best-fitting set of parameters is considered for each model. In particular, we take $R = (220 \pm 50)\mathrm{h}^{-1}\mathrm{Mpc}$, $\delta_0 = 0.14 \pm 0.04$ and $z_0 = 0.22 \pm 0.03$, for the TH model [136]; and $r_0 = (195 \pm 35)\mathrm{h}^{-1}\mathrm{Mpc}$, $\delta_0 = 0.25 \pm 0.10$ and $z_0 = 0.155 \pm 0.037$, in the case of the LTB Gaussian model [137, 171].

In order to characterize the feature induced in the CMB temperature anisotropies by the presence of a supervoid, we compute its 1-dimensional shape. This profile can be expanded in terms of the Legendre polynomials:

$$\frac{\Delta T}{T}(\theta) = \sum_{\ell=0}^{\infty} \sqrt{\frac{2\ell+1}{4\pi}} a_\ell P_\ell(\cos\theta), \tag{5.5}$$

where a_ℓ denotes the coefficients of the expansion. In the particular case in which the void is aligned with the z-axis, the coefficients a_ℓ are equivalent to the spherical harmonic coefficients with $m = 0$. They can be therefore computed from the theoretical profile of Eq. (5.1) as

$$a_\ell = \sqrt{(2\ell+1)\,\pi} \int_{-1}^{1} \mathrm{d}(\cos\theta) \frac{\Delta T}{T}(\theta) P_\ell(\cos\theta). \tag{5.6}$$

The corresponding ISW profiles induced by each void model and the CS data are depicted in Figure 5.1. The profiles are very different in terms of the amplitude. Within the considered ΛCDM model, the standard deviation of the ISW temperature fluctuations is estimated to be $\sigma_{\mathrm{ISW}} = 19.58\ \mu\mathrm{K}$. Whilst the Gaussian model induces a profile whose

[1] Notice that this model is denoted simply as LTB in previous papers [136, 137, 171].

value at $\theta = 0$ lies at the 1σ level when the standard deviation due exclusively to the ISW contribution is taken as reference, the TH profile at the centre reaches a 4.5σ level.

In terms of the standard deviation of the matter field convolved by a top-hat function of scale R, the corresponding value of δ_0 for the TH best-fit profile lies at the $\approx 6\sigma$ level[2]. This could give a hint that the TH model is not a realistic description of a void expected within the standard model, although it is shown closer –but not enough yet– to explain the CS anomaly. Actually, this void description would imply an anomaly larger than the one that is expected to be explained. For the Gaussian model, the value of δ_0 is only at a $\approx 2\sigma$ level.

In addition to the amplitude, a deeper insight can be obtained by paying attention to the shape of the profile. The SMHW coefficient of the CS with scale $R = 5^\circ$ describes both the temperature at the centre and the hot ring at 15°, since the specific shape of the SMHW at this scale weighs these features in a single number. Therefore, if the theoretical profiles fit the CS data, they will have a similar value of the SMHW coefficient. It is also important to remark that the CS represents a $\approx 4.7\sigma$ fluctuation in terms of this coefficient, which implies that any theoretical model assumed for the CS must explain this large deviation. The value of the SMHW coefficient can be computed as

$$W_0 = \sum_{\ell=0}^{\infty} \sqrt{\frac{2\ell+1}{4\pi}} w_\ell a_\ell. \tag{5.7}$$

The standard deviation of the SMHW coefficients with $R = 5^\circ$ (the scale at which the CS anomaly is manifested) due to the ISW contribution is $\sigma_{\rm ISW}(W_0) = 0.94\ \mu$K. We obtain W_0 values at around $-1.07\ \mu$K for the TH description and $-0.54\ \mu$K for the Gaussian model, and both lie within the $\approx 1\sigma$ level when only the ISW contribution is taken into account. On the other hand, the SMHW coefficient associated to the CS is a 20σ fluctuation with respect to the ISW effect, and therefore is very unlikely to explain the CS only taking into account the ISW fluctuations of linear standard voids. Other possible scenario is that the CS is the sum of a primordial CMB fluctuation and the ISW effect of a void, but even in this case the probability of this event is small. The SMHW coefficient of the observed data, once the effect of the void is subtracted, is still a $\approx 4.5\sigma$ fluctuation. Therefore, whilst the effect predicted by the theoretical models for this particular void is shown compatible with the expected ISW signal from typical LSS fluctuations within the ΛCDM, the CS appears anomalous in relation to both properties: shape and amplitude.

[2]Notice that [136] provide a value of at least 3.3σ based on a more conservative estimate of the rareness of the void which takes into account a 1σ deviation of the TH best-fit parameters.

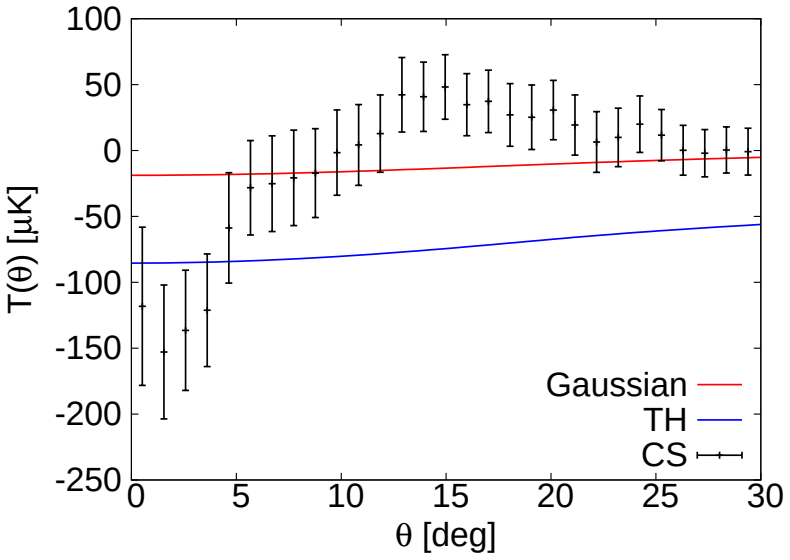

FIGURE 5.1: CMB temperature profiles induced by the presence of a supervoid modelled as a TH (in blue) and a Gaussian model (in red). The data points correspond to the CS profile from the Planck SMICA map, and the error bars represent the cosmic variance.

In principle, to consider the void as explanation of the CS, it would not be necessary that its contribution accounts for all the CS amplitude, but it should be intense enough to make anomalous the primordial fluctuation. In terms of the amplitude of the Gaussian model, the ISW contribution from the void represents a 13% with respect to the temperature at the centre of the CS. However, in terms of W_0, this fraction drops to 2.8%.

5.2.2 Ellipsoidal model

All previous conclusions are derived from a spherical void model, but we could wonder whether they remain when the void presents an ellipsoidal geometry. For this purpose, we decompose the radial coordinate $\mathbf{r}$ of the matter density profile, defined from the centre of the void, into a component parallel to the line of sight $r_{\parallel}$ and another orthogonal to it $\mathbf{r}_{\perp}$, which is a 2-dimensional vector in the normal plane, such that:

$$r = \sqrt{r_{\parallel}^2 \left(1 - e^2\right) + r_{\perp}^2}, \tag{5.8}$$

where e denotes the ellipticity. This toy model allows us to stretch the void along the line of sight in terms of the ellipticity, whereas the semi-minor axis is fixed to the scale of the density profile (R for the TH and r_0 for the Gaussian model, respectively), implying an increase of the volume. The centre position of the void is also kept at z_0. This configuration favours the increase of the ISW contribution due to the presence of the

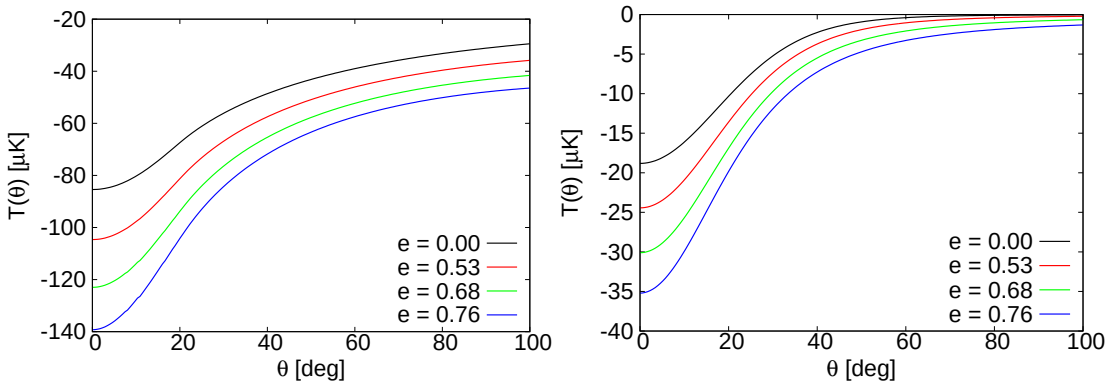

FIGURE 5.2: Comparison of CMB temperature profiles induced by the presence of an elliptical supervoid modelled as a TH (top panel) and a Gaussian model (bottom panel) with different values of ellipticity.

e	TH [μK]	Gaussian [μK]
0.00	-1.07	-0.54
0.53	-1.42	-0.71
0.68	-1.81	-0.85
0.76	-2.20	-1.03

TABLE 5.1: SMHW coefficients W_0 induced by elliptical voids modelled by TH and Gaussian profiles with different ellipticity. All coefficients correspond to a wavelet scale $R = 5°$. The W_0 computed at the CS location in the *Planck* temperature data is -19.3 ± 4.1 μK.

void, because the void influence is kept in a greater redshift interval along the line of sight.

Although the standard model imposes limits to the ellipticity (e.g. [173, 174]), three values are considered such that the semi-major axis is increased by one, two and three times the error bar of r_0 (the value of $35\mathrm{h}^{-1}$Mpc is taken in both models for simplicity). A comparison between CMB temperature profiles caused by supervoids with different ellipticity is shown in Figure 5.2. As expected, the absolute value of the amplitude at $\theta = 0$ increases as the ellipticity grows. In the case of the TH model, the radial profile at the centre of the void reaches a value close to the CS temperature decrease when an ellipticity of $e = 0.76$ is considered, whilst these values remain unreachable with the Gaussian model. However, all the SMHW coefficients lie within the 1σ level of the ISW contribution, as in the spherical case. This means that the shape of the profiles differs from that shown by the CS. The W_0 value for all cases are given in Table 5.1. They should be compared with the SMHW coefficient at the CS location in the *Planck* temperature data whose value is estimated in -19.3 ± 4.1 μK.

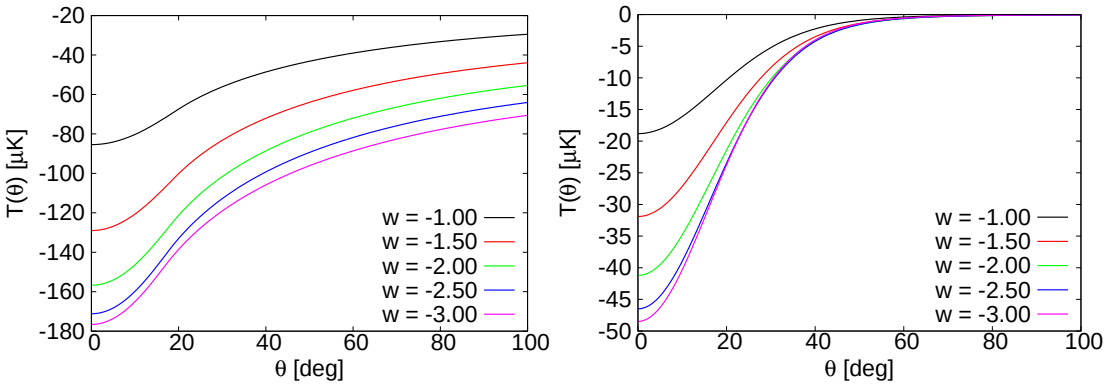

FIGURE 5.3: Comparison of CMB temperature profiles induced by the presence of a spherical supervoid modelled as a TH (top panel) and a Gaussian model (bottom panel) with different values of w.

5.2.3 Varying w in the dark energy equation of state

Assuming ΛCDM, Ω_Λ regulates the amplitude of the ISW effect produced by these void models. Considering dark energy, the ISW contribution also depends on its evolution. In this section, we extend the void models so that the dark energy equation of state parameter w can be set to another value different from -1. This dependence affects explicitly to the growth suppression factor $G(z)$ and the comoving distance $r(z)$. Decreasing the value of w causes a stronger evolution in the density parameter of the dark energy, implying a larger ISW imprint. Actually, for our purposes, the assumption that the w is different from -1 is only necessary at the redshift interval in which the CMB photon is suffering the effect of the void but not in the whole evolution of the Universe.

A comparison between CMB temperature profiles induced by the void corresponding to different values of w is given in Figure 5.3. The temperature at the centre reaches a similar value than that shown by the CS only for the TH model and considering a value of $w = -3.0$ which, obviously, is ruled out by current observations (e.g. [8]). Similar intervals in w does not correspond with similar increases of the absolute value of the amplitude of the profiles, but this increase is smaller as the values of w become more extreme. However, the W_0 values for these profiles also lie within the 1σ level with respect to the standard deviation of the ISW signal. They are shown in Table 5.2.

w	TH [μK]	Gaussian [μK]
-1.00	-1.07	-0.54
-1.50	-1.74	-0.96
-2.00	-2.13	-1.28
-2.50	-2.34	-1.49
-3.00	-2.38	-1.60

TABLE 5.2: SMHW coefficients W_0 induced by a spherical void as that detected by [136] modelled by TH and Gaussian profiles for different values of w. All coefficients correspond to a wavelet scale $R = 5°$. The W_0 computed at the CS location in the *Planck* temperature data is -19.3 ± 4.1 μK.

Chapter 6

Cross-correlation between the CMB and LSS tracers

In this Chapter, the large-scale structure of the Universe is studied in order to obtain a detection of the Integrated Sachs-Wolfe (ISW) effect from the cross-correlation between the CMB temperature field and the fluctuations in the number of counts derived from galaxy catalogues. In particular, the NRAO VLA Sky Survey (NVSS) [175] redshift distribution and angular power spectrum are modelled in order to have an appropriate theoretical description of the cross-correlation with the CMB temperature.

In Section 6.1, the halo model and a theoretical parametrization of the galaxy distribution and bias are introduced. Besides the parameters characterizing the Halo Occupation Distribution (HOD), the statistical properties of galaxy catalogues are modelled by the minimum mass of halos hosting the galaxies of the sample. This model and other parametrizations of the large-scale structure tracers are used to develop a code for the calculation of several galaxy angular power spectra and the cross-power between themselves and the CMB temperature in Section 6.2.

Moreover, in Section 6.3, the NVSS catalogue is described in terms of the model introduced in Section 6.1 by calculating the halo minimum mass and HOD parameters. In order to have a better characterization of the NVSS redshift distribution, the Combined EIS-NVSS Survey Of Radio Sources (CENSORS) [176, 177] data is included in the analysis.

Additionally, a methodology based on the MASTER estimation of the angular cross-power spectrum is presented in Section 6.4, in which a theoretical model of the covariance matrix for several surveys is given. This formalism is also extended to the covariance

matrix of different cross-correlation functions and estimators based on wavelet space [178].

Finally, some results published in the *Planck* papers on the integrated Sachs-Wolfe effect [179, 180] are presented in Section 6.5. Besides the cross-correlation analysis between temperature and LSS tracers, constraints on the dark energy parameters from the ISW effect are presented.

6.1 Halo mass function and galaxy bias

According to the halo model, galaxies are formed inside dark matter halos, and, consequently, it is important to characterize the dark matter distribution in order to describe the distribution of the observed galaxies. The simplest scenario of the halo formation process consists in consider that the collapse of the matter is isotropic, leading to a model which is referred to as the spherical collapse model. The advantage of this model is that the evolution of the collapsing matter overdensity is described by the equations of a close universe. After a simple calculation, it is obtained that a spherical mass distribution at redshift z whose linear matter overdensity δ is above a certain threshold $\delta_c(z)$ have already collapsed in the spherical collapse model. For the Einstein-de Sitter universe, the value of the critical overdensity does not depend on the redshift and corresponds to $\delta_c = \frac{3}{20}(12\pi)^{2/3} \approx 1.6865$, whereas models with cosmological constant predicts a slightly lower value at low redshifts [181, 182].

In order the select halos with a particular mass, the matter density is filtered by a top-hat function with scale R, corresponding to the radius of a sphere enclosing a mass m, and assuming that the matter density is constant. Since the matter distribution is considered to be Gaussian, the probability density function of the smoothed matter overdensity is parametrized only by the variance, which is given by

$$\sigma_R^2(z) = D(z)^2 \int \mathrm{d}k \, \frac{k^2}{2\pi^2} W_R(k)^2 P(k) \, , \tag{6.1}$$

where $P(k)$ is the linear matter power spectrum and $D(z)$ is the linear growth factor of the matter perturbations normalized at unity at $z = 0$. The function $W_R(k)$ is the Fourier transform of the smoothing function, which for the top-hat filter is given by

$$W_R(k) = \frac{3}{(kR)^3} \left[\sin kR - kR \cos kR\right] \, . \tag{6.2}$$

The smoothing scale depends on the halo mass as $R = (3m/4\pi\bar{\rho})^{1/3}$, where $\bar{\rho}$ is the mean density of the Universe.

In the Press-Schechter formalism [183], the mass distribution of halos at a given redshift is calculated by considering the fraction of the volume of the regions in which the matter overdensity is above the critical value $\delta_c(z)$. Since the density field is assumed to be Gaussian, the halo mass function depends on the redshift and the mass through the parameter $\nu(m,z) = \delta_c(z)/\sigma_m(z)$, where $\sigma_m(z)$ is the r.m.s. of matter perturbations at the scale associated with the mass m at redshift z (see eq. (6.1)). Under these considerations, the Gaussian halo mass function is given by

$$n(m,z) = \frac{\bar{\rho}}{m} f(\nu) \frac{\mathrm{d}\ln\nu}{\mathrm{d}m} \ , \tag{6.3}$$

where $f(\nu)$ is the multiplicity function, which represents the fraction of collapsed volume per logarithmic interval of ν. We adopt the Sheth-Tormen halo mass function [184], in which the multiplicity function is given by

$$f(\nu) = A\left(1 + \frac{1}{(a\nu^2)^p}\right)\sqrt{\frac{2a}{\pi}}\nu e^{-a\nu^2/2} \ . \tag{6.4}$$

The values for the parameters are: $a = 0.707$, $p = 0.3$, and $A = 0.322$ [184]. The parameter A is chosen such that the function $f(\nu)$ is normalized to unity. The Press-Schechter mass function [183] is recovered when $a = 1$, $p = 0$ and $A = 1/2$.

In the Lagrangian space, the overdensity of halos $\delta_h(m,z)$ of mass m is related to the matter overdensity δ through the bias relation. In the case of deterministic local linear bias, the halo overdensity is $\delta_h(m,z) = b(m,z)\delta$. It is natural to think that galaxies are formed inside halos where the conditions for galaxy formation exists. The relation between halos and galaxies is not straightforward due to the complexity of the galaxy formation process. In order to deal with this problem, the number of galaxies within a halo $N_g(m)$ is considered as a stochastic variable depending on the mass of the halo. The distribution of N_g is called the Halo Occupation Distribution (HOD) [185]. If in a catalogue there are only halos of mass greater than $M_{\min}$, the galaxy overdensity $\delta_g(z)$ is given by

$$\delta_g(z) = \frac{\int_{M_{\min}}^{\infty} \mathrm{d}m \ n(m,z)\langle N_g\rangle \delta_h(m,z)}{\int_{M_{\min}}^{\infty} \mathrm{d}m \ n(m,z)\langle N_g\rangle} \ , \tag{6.5}$$

where $n(m,z)$ is the halo mass function. The upper limit in the integrals is taken to be infinity, considering that there are halos of arbitrary large mass in the sample. In practice, the results are not strongly dependent on this maximum mass. As follows from eq. (6.5), we have that $\delta_g(z) = b_g(z)\delta$, where the galaxy bias $b_g(z)$ is given by:

$$b_g(z) = \frac{\int_{M_{\min}}^{\infty} \mathrm{d}m \ n(m,z)\langle N_g\rangle b(m,z)}{\int_{M_{\min}}^{\infty} \mathrm{d}m \ n(m,z)\langle N_g\rangle} \ . \tag{6.6}$$

In this equation, the halo bias $b(m, z)$ depends on the mass and the redshift of the halo, for which the expression in [184] is adopted:

$$b(m,z) = 1 + \frac{1}{D(z)\sigma(m)}\left(a\nu - \frac{1}{\nu} + \frac{2p/\nu}{1+(a\nu^2)^p}\right) , \tag{6.7}$$

where $D(z)$ is the linear growth factor of perturbations normalized to unity at $z = 0$. The eq. (6.6) depends on the average number of galaxies within a halo $\langle N_g \rangle$, which depends on the mass of the halo. We assume a power-law model [186]:

$$\langle N_g \rangle = \begin{cases} 0 & \text{if } M < M_{\min} \\ (M/M_0)^\beta & \text{if } M > M_{\min} \end{cases} . \tag{6.8}$$

The parameter β is positive definite in order to have an increasing number of galaxies with mass. In this formula the pivot of the power-law, M_0, represents the mass of the halos with an average number of galaxies equal to one. The eq. (6.6) does not depend on the parameter M_0, and therefore it can not be constrained from the power spectrum of the data and other observables have to be used. The cutoff mass $M_{\min}$ represents the minimum mass of halos with galaxies, which is considered to be the same as in eq. (6.6).

It is possible to deduce the galaxy distribution from the mass function of the halos and the HOD. Whereas the halo mass function gives the number of halos per unit volume and mass, the quantity $\langle N_g \rangle$ represents the average number of galaxies per halo, therefore, the number of galaxies per redshift interval within a solid angle Ω is obtained by integrating these quantities:

$$\frac{\mathrm{d}n}{\mathrm{d}z} = \Omega \frac{c\, r(z)^2}{H(z)} \int_0^\infty \mathrm{d}m \; n(m,z) \langle N_g \rangle , \tag{6.9}$$

where $r(z)$ is the comoving distance and $H(z)$ is the Hubble function. Notice that the factor before the integral is the volume per redshift interval.

6.2 Galaxy angular power spectrum

The galaxy angular auto and cross-power spectra for different surveys are calculated in this section. In order to study two-dimensional surveys in which the specific radial coordinates of individual galaxies are unknown, or averaged out by integrating along the line of sight, it is necessary to project all the tridimensional quantities on the sphere. In particular, the galaxy angular power spectra are calculated from the linear power

spectrum, once the redshift distributions of the galaxy surveys are provided:

$$C_\ell^{gg'} = 4\pi \int \frac{\mathrm{d}k}{k}\ \Delta_\ell^g(k)\Delta_\ell^{g'}(k)\ \Delta_\zeta^2(k)\ , \tag{6.10}$$

where the different galaxy surveys are labelled by the superscripts g and g', and $\Delta_\zeta^2(k)$ is the primordial power spectrum of the curvature ζ (see eq. (1.20)). In this equation, the galaxy transfer function $\Delta_\ell^g(k)$ of the survey g is given by

$$\Delta_\ell^g(k) = \frac{2}{3}k^2 T(k) \int_0^\infty \mathrm{d}z\ b_g(z) D(z) \frac{\mathrm{d}n}{\mathrm{d}z}(z)\ j_l(k\, r(z))\ , \tag{6.11}$$

where $\frac{\mathrm{d}n}{\mathrm{d}z}$ is the redshift distribution of galaxies (number of galaxies per redshift interval). Whilst the galaxy bias $b_g(z)$ is included in order to relate the galaxy and matter perturbations ($\delta_g = b_g\delta$), the growth factor $D(z)$ accounts for the linear evolution of δ. In this expression, the linear scale k is projected on the angular scale ℓ by using the spherical Bessel functions $j_\ell(kr)$, where $r(z)$ is the comoving distance as a function of redshift. Additionally, the matter transfer function $T(k)$ describes the suppression of the matter perturbations during the radiation-dominated era, as well as other physical effects which occur at scales smaller than the size of the horizon at the matter-radiation equality epoch.

The angular cross-power spectrum between the CMB temperature and the galaxy survey g is given by

$$C_\ell^{tg} = 4\pi \int \frac{\mathrm{d}k}{k}\ \Delta_\ell^t(k)\Delta_\ell^g(k)\ \Delta_\zeta^2(k)\ , \tag{6.12}$$

where $\Delta_\ell^t(k)$ is the CMB temperature transfer function. The correlation at large scales between the primordial CMB perturbations and the late-time matter distribution mainly arise due to the integrated Sachs-Wolfe effect. In this case, the temperature transfer function is simply given by:

$$\Delta_\ell^t(k) = \int_{\tau_*}^{\tau_0} \mathrm{d}\tau\ \left[\Phi'(k,\tau) + \Psi'(k,\tau)\right]\ j_l(k\,\tau)\ , \tag{6.13}$$

as can be deduced from eq. (1.39). The calculation of the source term $\Phi'(k,\tau)+\Psi'(k,\tau)$ can be done numerically by solving the Boltzmann equation for the different components of the Universe. One of the publicly available codes for the calculation of CMB temperature transfer functions is CAMB (Code for Anisotropies in the Microwave Background) [187]. This code has been modified for the calculation of the different galaxy angular power spectra $C_\ell^{gg'}$ and the cross-spectra C_ℓ^{tg}, in which the surveys are modelled as described above.

6.3 Modelling of the NRAO VLA Sky Survey

In this section, one of the most widely galaxy survey used up to date is studied: the NRAO VLA Sky Survey (NVSS) [175]. The strength of the NVSS radio galaxy catalogue comes from its large sky coverage and its relatively high redshift range. As a drawback, it does not posses individual redshift estimation of the sources, but just a statistical description. These characteristics make NVSS a suitable catalogue for cross-correlation studies with the CMB, and, also, to constrain large-scale features as, for instance, the gaussianity of the distribution of the initial perturbations.

The NVSS catalogue has been cross-correlated with WMAP to report the first detection of the integrated Sachs-Wolfe (ISW) effect [188]. Many subsequent analyses [178, 189–193] further explored different aspects of this cross-correlation. The ISW signal depends very much on the accurate description of the redshift distribution of the galaxies. However, NVSS is known to suffer from some systematics, especially at very large scales. These systematics are mostly reflected as an excess of power at scales greater than 20° [194, 195]. The aim of this work is, precisely, to study in detail the statistical properties of NVSS in terms of both the angular power spectrum and the redshift distribution, trying to explore further these incompatibilities in the catalogue. The NVSS model described in this section has been used in the studies of the ISW effect made by the *Planck* collaboration [179, 180], as well as in publications on the recovery of the ISW fluctuations [193, 196].

In order to calculate the theoretical angular power spectrum of NVSS, it is necessary to know the redshift distribution of the NVSS counts accurately and, for this reason, we used the Combined EIS-NVSS Survey Of Radio Sources (CENSORS) [176, 177] as additional dataset to constrain the distribution of the NVSS radio galaxies along the line of sight. Both NVSS and CENSORS data are described in the next subsections:

- *NVSS catalogue:*

  The NRAO VLA Sky Survey (NVSS) is a 1.4 Ghz survey of the northern equatorial part of the sky up to $-40°$ in declination [175]. The most important contribution at this frequency is provided by the Active Galactic Nuclei (AGN's). One important feature of NVSS is the large sky coverage compared with other galaxy surveys. This fact allows a better estimation of the angular power spectrum.

  Besides the unobserved sky, a region of width 14° around the galactic plane is also masked to avoid contamination from the Galaxy. In addition, some regions with high number of counts are masked with a disk of 0.6° of radius, obtaining that the total fraction of observed sky is $f_{\rm sky} = 0.73$. We chose a flux threshold equal to

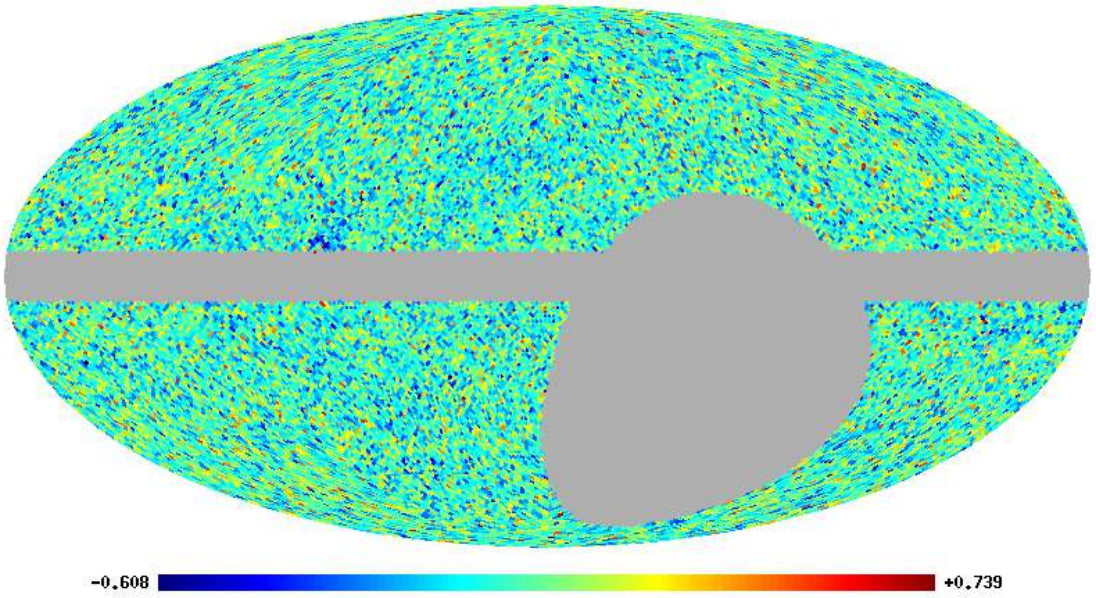

FIGURE 6.1: NVSS map of sources with flux above 2.5 mJy. The map is at HEALpix [159] resolution $N_{\rm side} = 64$ (pixel size $\sim 1°$). The masked pixel are shown in grey color.

2.5 mJy, in which case the total number of sources which are above this flux and outside the mask is 1.45×10^6. It is important to have a high number of counts in order to reduce the contribution of the shot noise.

The NVSS observations are made with two different array configurations of the VLA radio telescopes (D and Dnc). One or the other is used depending on the declination, introducing a declination systematic in the NVSS catalogue, in which the mean density of counts depends on the declination angle. In order to avoid this problem the NVSS sky map is corrected following a procedure similar to the one in [178]: The map is divided in 70 declination bands with the same area and the mean number of counts is calculated in each stripe. Therefore, it is obtained that this number depends on the declination due to the systematic. In order to correct this effect, the pixels in the bands are rescaled such that the mean number of counts in each band is equal to the full sky mean:

$$n'_{ai} = \frac{\bar{n}}{\bar{n}_a}\, n_{ai} \ , \tag{6.14}$$

where n_{ai} and n'_{ai} are the number of counts in the pixel i of the band a before and after the correction, respectively. Whilst the value of $\bar{n}_a$ represents the mean number of counts in the band a, the mean number of counts of the full sky is given by $\bar{n}$. Note that this transformation does not change the full-sky mean of the map, and therefore, the shot noise is not affected by this transformation. The resulting NVSS data after applying the correction and the corresponding mask are represented in Figure 6.1.

- *CENSORS catalogue:*

  For the modelling of the galaxy redshift distribution of the NVSS catalogue, the Combined EIS-NVSS Survey Of Radio Sources (CENSORS) [176, 177] is used . This survey contains all the NVSS sources above 7.2 mJy that are within a patch of 6 deg^2 in the ESO Imaging Survey (EIS), leading to a total number of 149 galaxies. Whereas the redshift of 44 sources are calculated using $K-z$ relation, the remainder 105 have spectroscopic redshift [177]. In the present analysis, CENSORS data will be used to constrain the redshift distribution of the NVSS radio galaxies.

  Since the modelling of the redshift distribution derived from the halo model (see eq. (6.9)) could be very restrictive, a more phenomenological parametrization in terms of the gamma distribution is also considered:

$$\frac{\mathrm{d}n}{\mathrm{d}z} = N\left(\frac{z}{z_0}\right)^{\alpha} e^{-\alpha z/z0} \,, \tag{6.15}$$

  which depends on two parameters: z_0 and α. The physical meaning of z_0 is the redshift at which the distribution has the maximum, while α is a shape parameter. The variance of the distribution is given by $\frac{\alpha+1}{\alpha^2}z_0^2$. The constant N is chosen such that the distribution is normalized to unity. In Figure 6.2, the CENSORS redshift distribution and different models considered in the literature [197–199] are represented. The best fit to the gamma distribution in eq. (6.15), given by the parameters $z_0 = 0.53^{+0.11}_{-0.13}$ and $\alpha = 0.81^{+0.34}_{-0.32}$, is also shown in this figure.

If the redshift distribution is modelled by eq. (6.9), the theoretical angular power spectrum can be completely given by the halo model and the HOD. The CENSORS catalogue is not well described by this parametrization of the galaxy redshift distribution derived from the halo model and, therefore, only the NVSS angular power spectrum is used for constraining the HOD parameters. This model only has two parameters: the halo minimum mass M_{min} and the slope parameter β (the pivot mass M_0 in eq. (6.8) cannot be constrained using power spectrum data due to the fact that the galaxy bias do not depend on it). In Figure 6.3 it is represented the posterior probability of these two parameters. With the NVSS data only an upper limit on the HOD slope parameter can be provided: $\beta < 0.24$ (1-σ confidence level). For this reason, we will assume that the slope parameter takes a negligible value in the following.

Since the accurate knowledge of the distribution of the galaxies along the line of sight is important for the theoretical calculation of the angular power spectrum, a joint fit of the CENSORS distribution and the NVSS power spectrum is performed in order to improve the determination of the free parameters appearing in that calculation. The angular

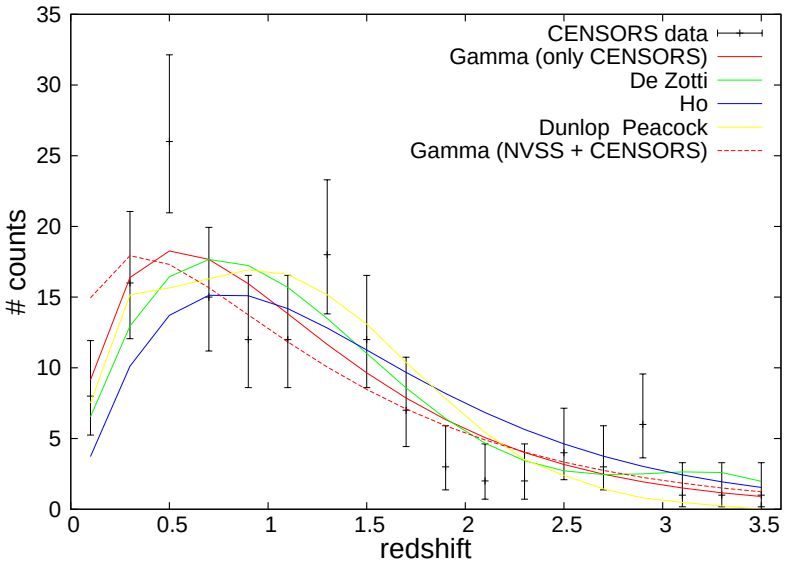

FIGURE 6.2: NVSS galaxy redshift distribution and the CENSORS data. The error bars correspond to 68% confidence level of the Poisson distribution (notice that they are not symmetric). All distributions are normalized such that the total number of counts correspond to that of CENSORS. The two red lines correspond to the gamma function model. Whereas the solid red line is a fit only to the CENSORS data, the dashed one also takes into account the NVSS power spectrum besides the CENSORS distribution. Different models for the NVSS redshift distribution proposed in the literature [197–199] are also shown.

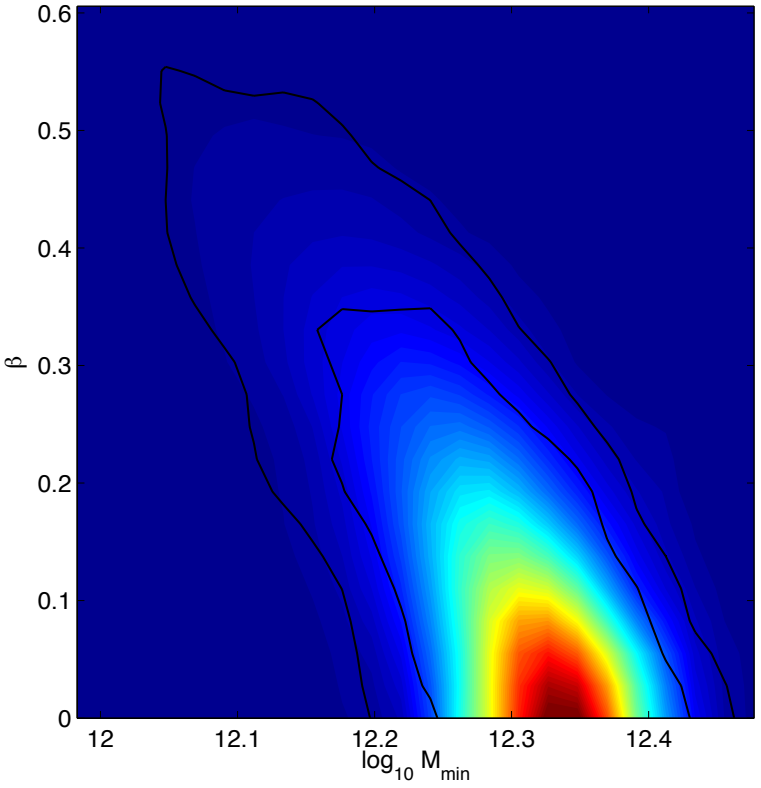

FIGURE 6.3: Probability contours of the halo minimum mass $M_{\rm min}$ and the slope parameter β of the HOD.

Parameter	best fit	Mean	σ
$\log_{10} M_{\rm min}$	12.66	12.63	0.19
z_0	0.33	0.34	0.04
α	0.37	0.40	0.09

TABLE 6.1: Best fit and marginalised mean values with the 1-σ errors of the three parameters in the NVSS model: the halo minimum mass $M_{\rm min}$ and the two parameters accounting for the redshift distribution, z_0 and α.

power spectrum is estimated from the NVSS data using the MASTER methodology described in [200] that accounts for the incomplete sky coverage. The presence of a mask in the data also introduces correlations between the different multipoles, which leads to a non-diagonal covariance matrix. In order to estimate the best fit model of the NVSS data, a Gaussian likelihood is considered in which the covariance is derived from the MASTER formalism [201, 202]. As mentioned above, the CENSORS data is modelled by the gamma distribution in eq. (6.15) instead of the one derived from the halo model (see eq. (6.9)) in order to have a better parametrization of the redshift distribution. Despite that the halo model is not applied to the CENSORS data, the modelling of the galaxy bias, which depends on the halo minimum mass $M_{\rm min}$, is considered to be given by eq. (6.6). The likelihood function of the number counts in each redshift bin is assumed to be Poissonian, as they are given by discretised quantities. Combining the two datasets, the best fit values obtained for the galaxy distribution parameters and the halo minimum mass are shown in Table 6.1.

The NVSS power spectrum data and theoretical models obtained from different redshift distributions are shown in Figure 6.4. Besides the parametrizations proposed in this work in terms of the gamma distribution, other models of the NVSS distribution proposed in the literature are depicted [197–199]. In this figure, the excess of power at large scales present in the NVSS data is observed. The only modelling capable of explaining, at least partially, the NVSS angular power spectrum in the full range of multipoles is the one obtained by combining the CENSORS and NVSS data, whose parameters are reported in the Table 6.1. However, it is worth mentioning that this is achieved by considering a redshift distribution which peaks at lower redshift (see eq. 6.2). This may reflect a tension between CENSORS and NVSS data or an evidence that there are more NVSS sources at low redshift than previously expected. Although, the possibility that the excess of power comes from systematic effects cannot be completely rule out, the joint fit allow a better parametrization of the NVSS power spectrum, which can be used in ISW analysis.

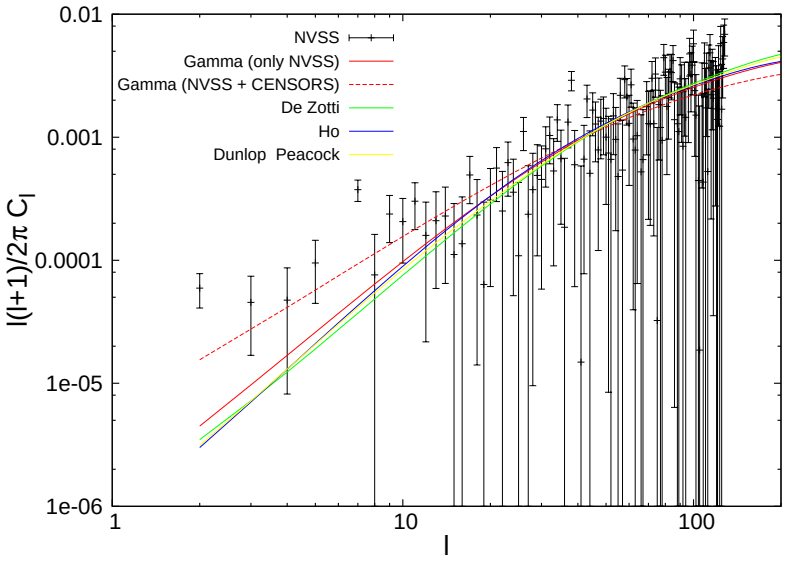

FIGURE 6.4: The angular power spectrum obtained from the NVSS data and the theoretical expectations derived from different redshift distributions. Besides the two models analysed in this work (labelled by gamma), other models proposed in the literature are considered [197–199]. The points with the error bars represent the power spectrum of the NVSS sources with flux above 2.5 mJy. Whereas the solid red line depicts the angular power spectrum obtained from a fit only to CENSORS data by using the gamma distribution, the dashed red line shows the power spectrum derived from the joint fit to both the NVSS and CENSORS data.

6.4 Estimation of the angular cross-correlation signal from several LSS tracers

In general, the data maps are masked due to Galactic contaminants or unobserved pixels and, therefore, a procedure similar to the one given in [200] is used to estimate the different angular cross-spectra. Additionally, the different multipoles of the cross-power spectrum are correlated due the partial sky coverage. In this work, the formula given in [201] (see also [202]) for calculating the covariance matrix of the different multipoles is extended in order to include more than one cross-power spectrum.

In the case of having full-sky coverage, the maximum likelihood estimator of the angular cross-spectrum is given by

$$\tilde{C}_\ell^{tg} = \frac{1}{2\ell+1} \sum_{m=-\ell}^{\ell} t_{\ell m}^* g_{\ell m} \ , \tag{6.16}$$

where $t_{\ell m}$ and $a_{\ell m}$ are the spherical harmonic coefficients of the CMB temperature and the number galaxy fluctuations, respectively (see eq. (1.33)). The estimated spectrum $\tilde{C}_\ell^{tg}$ is calculated by averaging the product of the spherical harmonics coefficients with different values of m. Since different orientations are represented by m, it is possible to see that the estimated cross-power spectrum is invariant under rotations. On the other

hand, the covariance matrix of the estimator in eq. (6.16), when different surveys are taken into account, is given by

$$C_{\ell g,\ell' g'} \equiv \langle \left(\tilde{C}_\ell^{tg} - C_\ell^{tg}\right)\left(\tilde{C}_{\ell'}^{tg'} - C_{\ell'}^{tg'}\right)\rangle = \frac{\delta_{\ell\ell'}}{2\ell+1}\left[C_\ell^{tg}C_{\ell'}^{tg'} + C_\ell^{tt}\left(C_\ell^{gg'} + N_\ell^{gg'}\right)\right] , \tag{6.17}$$

where we have included the shot noise power spectra $N_\ell^{gg'}$ as a source of error. If the noise contribution is considered to be Poissonian and independent between different surveys, the noise does not depend on ℓ and is given by $N_\ell^{gg} = 1/\bar{n}_g$, where $\bar{n}_g$ is number of galaxies per steradian. Notice that, since we are interested in large scales, the sensitivity and resolution of the *Planck* experiment allow one to neglect the noise contribution in the temperature field.

In contrast, the masking of both, CMB temperature and galaxy fields, makes that the estimator in eq. (6.16) and the covariance matrix in eq. (6.17) are not representative of the statistical properties of the angular cross-power spectrum. One of the most important effects due to the mask is that the multipoles are not independent, leading to an effective number of modes per multipole of $(2\ell+1)\sqrt{f_{\rm sky}^t f_{\rm sky}^g}$, where $f_{\rm sky}^t$ and $f_{\rm sky}^g$ are the fractions of observed sky in the temperature and galaxy fields, respectively. Therefore, at first order, the effect of the mask can be taken into account by dividing the expressions in eqs. (6.16) and (6.17) by the factor $\sqrt{f_{\rm sky}^t f_{\rm sky}^g}$. A more precise analysis of the masked fields by using convolution techniques in harmonic space leads to the following estimator [200]:

$$\hat{C}_\ell^{tg} = \sum_{\ell'=0}^{\ell_{\rm max}} \left(M^{tg}\right)^{-1}_{\ell\ell'} \tilde{C}_{\ell'}^{tg} , \tag{6.18}$$

where the coupling matrix M^{tg} is given by

$$M_{\ell\ell'}^{tg} = \frac{2\ell+1}{4\pi}\sum_{\ell''=0}^{2\ell_{\rm max}} W_{\ell''}^{tg}\begin{pmatrix} \ell & \ell' & \ell'' \\ 0 & 0 & 0 \end{pmatrix}^2 , \tag{6.19}$$

where W_ℓ^{tg} is the angular cross-power spectrum between the masks of the temperature and galaxy fields as calculated from eq. (6.16). The Wigner 3-j symbols in this expression account for the coupling of the different multipoles. The expression of the covariance presented in [201] and [202] is generalized for the case of dealing with more than one angular cross-power spectra:

$$C_{\ell g,\ell' g'} = K_\ell^{gg'}\frac{\left(M^{gg'}\right)^{-1}_{\ell\ell'}}{2\ell'+1}K_{\ell'}^{gg'} , \tag{6.20}$$

where

$$K_\ell^{gg'} = \left[C_\ell^{tg}C_\ell^{tg'} + C_\ell^{tt}\left(C_\ell^{gg'} + N_\ell^{gg'}\right)\right]^{1/2} . \tag{6.21}$$

Since the temperature mask affects to both spectra, $\hat{C}_\ell^{tg}$ and $\hat{C}_\ell^{tg'}$, a contribution of the mask to the correlation between the angular cross-power spectra of different surveys is observed. This coupling is given by the matrix $M^{gg'}$ in eq. (6.20), whose expression is similar to the one in eq. (6.19):

$$M_{\ell\ell'}^{gg'} = \frac{2\ell+1}{4\pi} \sum_{\ell''=0}^{2\ell_{\rm max}} W_{\ell''}^{tg,tg'} \begin{pmatrix} \ell & \ell' & \ell'' \\ 0 & 0 & 0 \end{pmatrix}^2 , \tag{6.22}$$

where $W_{\ell''}^{tg,tg'}$ are the cross-power spectra calculated as in eq. (6.16) of the different joint masks, which are obtained by multiplying the temperature mask with the ones corresponding to each survey (the LSS tracers labelled by g and g' in this case). Notice that the inverse matrix in eq. (6.20) is calculated with respect to the multipoles ℓ and ℓ', keeping the indices labelling the galaxy surveys g and g' as constants in the inversion process. In the full-sky limit, both coupling matrices M^{tg} and M^{gg} are the identity and, therefore, the full-sky estimator of the angular cross-power spectra and the covariance in eqs (6.16) and (6.17) are recovered.

In order to detect the ISW signal, several estimators of the correlation between the CMB temperature and the LSS can be considered. Besides the angular cross-power spectrum (denoted by CAPS in the following) discussed above, the cross-correlation function (CCF) and the covariance of the SMHW coefficients (SMHWcov) are also analysed within this formalism.

- *Cross-correlation function (CCF):*

  In real space, the correlation between two fields can be measured by the cross-correlation function $C^{tg}(\theta)$, which is related to the cross-power spectrum as

  $$C^{tg}(\theta) \equiv \langle \Delta T(\mathbf{n})\, \delta_g(\mathbf{n}') \rangle = \sum_{\ell=0}^{\infty} \frac{2\ell+1}{4\pi} C_\ell^{tg}\, P_\ell(\cos\theta) , \tag{6.23}$$

  where the angle θ represents the angular separation between the two points on the sphere ($\cos\theta = \mathbf{n}\cdot\mathbf{n}'$). The cross-correlation function can be estimated directly from the CMB temperature and number galaxy fluctuations maps by averaging over the product of pixels separated a distance θ within a bin. The covariance of the estimated cross-correlation functions can be calculated from eqs. (6.20) and (6.23):

  $$C_{gg'}(\theta,\theta') = \sum_{\ell,\ell'=0}^{\ell_{\rm max}} \frac{2\ell+1}{4\pi}\frac{2\ell'+1}{4\pi}\, C_{\ell g,\ell' g'}\, P_\ell(\cos\theta) P_{\ell'}(\cos\theta') , \tag{6.24}$$

  where the matrix $C_{\ell g,\ell' g'}$ is given in eq. (6.20).

- *Spherical Mexican Hat Wavelet covariance (SMHWcov):*

  Since the cross-correlation signal of the CMB temperature and the LSS is concentrated in scales of few degrees, wavelets provide a tool to analyse the ISW effect by considering a narrow range of scales [178]. In particular, the Spherical Mexican Hat Wavelet (SMHW) is considered [121] in this analysis. The estimator used to measured the cross-correlation is the covariance of the SMHW coefficient at a given scale R:

$$C^{tg}(R) = \sum_{\ell=0}^{\infty} \frac{2\ell+1}{4\pi}\, w_\ell^2(R)\, C_\ell^{tg}\ , \tag{6.25}$$

  where $w_\ell(R)$ are the SMHW window function (see Appendix D). The estimator in eq. (6.25) can be obtained by filtering the CMB temperature and the LSS maps with the window function $w_\ell(R)$, and calculating the cross-correlation of both maps by averaging the product of pixels. The covariance matrix of $C^{tg}(R)$ is calculated from the covariance matrix in eq. (6.20):

$$C_{gg'}(R,R') = \sum_{\ell,\ell'=0}^{\ell_{\max}} \frac{2\ell+1}{4\pi}\frac{2\ell'+1}{4\pi}\, w_\ell^2(R) w_{\ell'}^2(R')\, C_{\ell g,\ell' g'}\, P_\ell(\cos\theta)\ . \tag{6.26}$$

Finally, it is important to notice that several approximations are made in the derivation of this formalism [201]. This fact causes that the covariance matrix of the angular cross-spectra introduced in this section is not well-estimated when the sky coverage of one or some of the galaxy surveys considered is small. In this case, the best approach to the problem consists in performing Monte Carlo simulations for calculating the covariance of the different cross-spectra. For this reason, an accurate modelization of the galaxy surveys in terms of the different angular power spectra is needed to achieve a good description of the covariance matrix.

6.5 Detection of the Integrated Sachs-Wolfe effect from *Planck* and LSS data

In this section, the ISW signal is detected from the cross-correlation between the CMB temperature as measured by the *Planck* satellite and different LSS tracers. The results presented here have been published in the two papers of the *Planck* collaboration on the ISW effect [179, 180].

The ISW signal is measured from three different estimators of the cross-correlation: angular cross-power spectra (CAPS), cross-correlation function (CCF) and the covariance of the SMHW coefficients (SMHWcov). The ISW amplitude A is defined as the expected

LSS data	$\hat{\xi}_a^{xy}$	C-R		NILC		SEVEM		SMICA	
		$A^{T\phi}$	S/N	$A^{T\phi}$	S/N	$A^{T\phi}$	S/N	$A^{T\phi}$	S/N
NVSS	CAPS	0.86 ± 0.33	2.6	0.91 ± 0.33	2.8	0.90 ± 0.33	2.7	0.91 ± 0.33	2.7
	CCF	0.80 ± 0.33	2.4	0.84 ± 0.33	2.5	0.83 ± 0.33	2.5	0.84 ± 0.33	2.5
	SMHWcov	0.89 ± 0.34	2.6	0.93 ± 0.34	2.8	0.89 ± 0.34	2.6	0.92 ± 0.34	2.7
SDSS-CMASS/LOWZ	CAPS	0.98 ± 0.52	1.9	1.09 ± 0.52	2.1	1.06 ± 0.52	2.0	1.09 ± 0.52	2.1
	CCF	0.81 ± 0.52	1.6	0.91 ± 0.52	1.8	0.89 ± 0.52	1.7	0.90 ± 0.52	1.7
	SMHWcov	0.80 ± 0.53	1.5	0.89 ± 0.53	1.9	0.87 ± 0.53	1.6	0.88 ± 0.53	1.7
SDSS-MphG	CAPS	1.31 ± 0.57	2.3	1.43 ± 0.57	2.5	1.35 ± 0.57	2.4	1.42 ± 0.57	2.5
	CCF	1.00 ± 0.57	1.8	1.11 ± 0.57	2.0	1.10 ± 0.57	1.9	1.10 ± 0.57	1.9
	SMHWcov	1.03 ± 0.59	1.8	1.18 ± 0.59	2.0	1.15 ± 0.59	2.0	1.17 ± 0.59	2.0
All	CAPS	0.84 ± 0.31	2.7	0.91 ± 0.31	2.9	0.88 ± 0.31	2.0	0.90 ± 0.31	2.9
	CCF	0.77 ± 0.31	2.5	0.83 ± 0.31	2.7	0.82 ± 0.31	2.6	0.82 ± 0.31	2.7
	SMHWcov	0.86 ± 0.32	2.7	0.92 ± 0.32	2.9	0.89 ± 0.32	2.8	0.91 ± 0.32	2.9

TABLE 6.2: ISW best fit amplitudes, standard deviations and significances of the detection measured by the signal-to-noise ratio. The cross-correlation signal is calculated for the four CMB maps provided by the *Planck* collaboration [158], which are represented in the four main columns. The results obtained from the three galaxy catalogues and the combination of all of them by using the three estimators considered are given in the different rows. Reprinted from [179].

amplitude when the theoretical prediction is compared with the data. By assuming that the probability distribution of the three estimators is Gaussian, the best fit value of the amplitude and its standard deviation are given by

$$A = \frac{\hat{\xi} C_\xi^{-1} \xi}{\xi C_\xi^{-1} \xi} \,, \tag{6.27}$$

$$\sigma_A = \left(\xi C_\xi^{-1} \xi \right)^{1/2} \tag{6.28}$$

where $\hat{\xi}$ is a vector with components of the cross-correlation estimator obtained from the data, ξ is its theoretical expectation and C_ξ the corresponding covariance matrix.

In the first data release [179], two galaxy samples derived from the SDSS sample are analysed besides the NVSS data in order to detect the ISW signal. In Table 6.2, the results are shown for the three different estimator, CAPS, CCF and SMHWcov and the four CMB maps given by the *Planck* collaboration [158], for which different component separation methods are used. In this case, the ISW signal is detected with a significance about 3σ when the three galaxy catalogues considered in [179] are combined. The large sky coverage and the depth of redshift distribution of NVSS makes this survey to have most of the cross-correlation signal with the CMB temperature (about 2.7σ).

In the last paper of the *Planck* collaboration on the ISW effect [180], two galaxy surveys from WISE and the lensing potential map [203] are also considered in addition to the galaxy surveys analysed in the previous data released. In this paper, the cross-correlation analysis is focused on the angular cross-power spectrum, since this estimator provides the largest signal-to-noise ratio. The addition of new LSS tracers, especially the lensing

LSS data	COMMANDER		NILC		SEVEM		SMICA		Expected
	$A \pm \sigma_A$	S/N	$A \pm \sigma_A$	S/N	$A \pm \sigma_A$	S/N	$A \pm \sigma_A$	S/N	S/N
NVSS	0.95 ± 0.36	2.61	0.94 ± 0.36	2.59	0.95 ± 0.36	2.62	0.95 ± 0.36	2.61	2.78
WISE-AGN ($\ell_{\min} \geq 9$)	0.95 ± 0.60	1.58	0.96 ± 0.60	1.59	0.95 ± 0.60	1.58	1.00 ± 0.60	1.66	1.67
WISE-GAL ($\ell_{\min} \geq 9$)	0.73 ± 0.53	1.37	0.72 ± 0.53	1.35	0.74 ± 0.53	1.38	0.77 ± 0.53	1.44	1.89
SDSS-CMASS/LOWZ	1.37 ± 0.56	2.42	1.36 ± 0.56	2.40	1.37 ± 0.56	2.43	1.37 ± 0.56	2.44	1.79
SDSS-MphG	1.60 ± 0.68	2.34	1.59 ± 0.68	2.34	1.61 ± 0.68	2.36	1.62 ± 0.68	2.38	1.47
Kappa ($\ell_{\min} \geq 8$)	1.04 ± 0.33	3.15	1.04 ± 0.33	3.16	1.05 ± 0.33	3.17	1.06 ± 0.33	3.20	3.03
NVSS and Kappa	1.04 ± 0.28	3.79	1.04 ± 0.28	3.78	1.05 ± 0.28	3.81	1.05 ± 0.28	3.81	3.57
WISE	0.84 ± 0.45	1.88	0.84 ± 0.45	1.88	0.84 ± 0.45	1.88	0.88 ± 0.45	1.97	2.22
SDSS	1.49 ± 0.55	2.73	1.48 ± 0.55	2.70	1.50 ± 0.55	2.74	1.50 ± 0.55	2.74	1.82
NVSS and WISE and SDSS	0.89 ± 0.31	2.87	0.89 ± 0.31	2.87	0.89 ± 0.31	2.87	0.90 ± 0.31	2.90	3.22
All	1.00 ± 0.25	4.00	0.99 ± 0.25	3.96	1.00 ± 0.25	4.00	1.00 ± 0.25	4.00	4.00

TABLE 6.3: ISW best fit amplitudes, standard deviations and significances of the detection measured by the signal-to-noise ratio. The cross-correlation signal is calculated from the angular cross-power spectrum for the four CMB maps provided by the *Planck* collaboration [158], which are represented in the columns. The results obtained from the LSS tracers considered in the paper and different combinations of them are given in the rows. The expected signal-to-noise ratio is represented in the last column. Reprinted from [180].

potential, provides a detection of the ISW effect at the level of 4σ. In this case, the combination of only NVSS and the lensing potential gives most of the cross-correlation signal, since the redshift distribution of these two LSS tracers are the deepest.

Since the ISW effect is caused by the late-time evolution of the gravitational potential, the cross-correlation of the CMB temperature and the LSS fluctuations can be used to constrain the dark energy parameters. In particular, the density parameter of the cosmological constant Ω_Λ and the dark energy equation of state parameter w are constrained from the angular cross-power spectra between the CMB temperature and the most significant LSS tracers: NVSS and the lensing potential. The conditional probabilities of Ω_Λ and w are shown in Figure 6.5. The 68% confidence intervals of these two parameters are $0.49 < \Omega_\Lambda < 0.78$ and $-4.45 < w < -1.07$, with a best fit values $\Omega_\Lambda = 0.67$ and $w = -1.01$, which are in agreement with the ΛCDM model. Finally, the effect of the dark energy, as measured by the Ω_Λ parameter, is detected at 3σ level. More general parametrizations of the dark energy are analysed by including a time-dependent equation of state parameter w, however, the integrated Sachs-Wolfe effect is not capable to constrain this more general class of models.

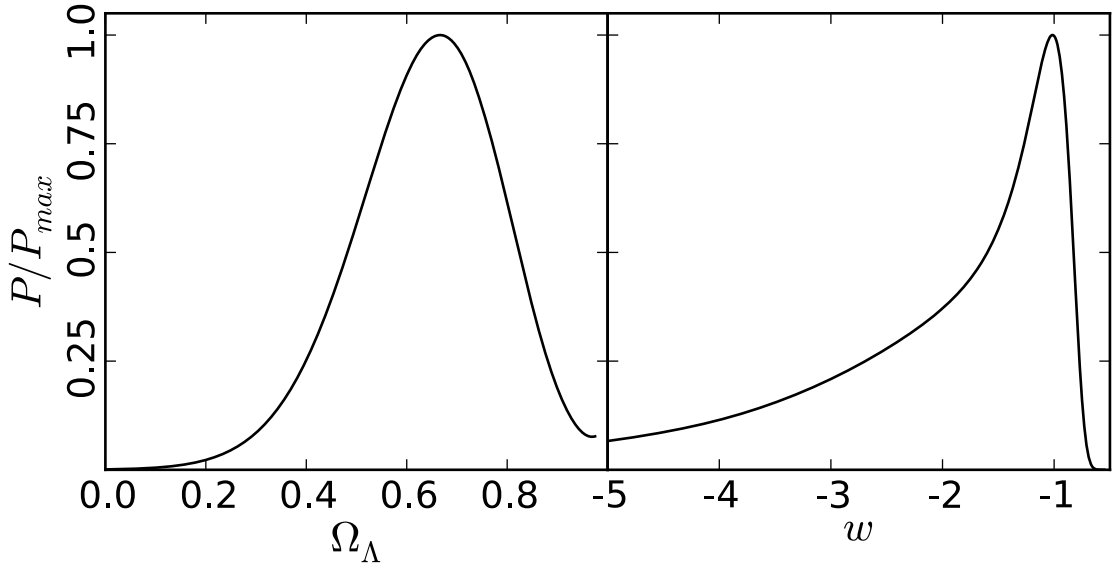

FIGURE 6.5: Conditional probability of Ω_Λ and the equation of state parameter w obtained from the angular cross-power spectrum between the CMB temperature and the two LSS tracers NVSS and the lensing potential.

Chapter 7

Conclusions

The large-scale anisotropies of the cosmic microwave background radiation and the peak theory are studied in this PhD thesis. After a general introduction on the cosmological standard model and the CMB in Chapter 1, different works are presented in the subsequent chapters. The theoretical background of peaks in a Gaussian random field on the sphere is studied in Chapter 2, applying this formalism to the case of CMB peaks in temperature and polarization. In order to describe the large-scale peaks on the CMB, a multiscale analysis of the derivatives up to second order is performed in Chapter 3, identifying the most extreme deviations and testing the isotropy of the CMB temperature field as given by the *Planck* data. In particular, four of the most prominent large-scale peaks, as well as the Cold Spot, are analysed in Chapter 4 in terms of the multipolar profiles. Moreover, the hypothesis that the Cold Spot is caused by a supervoid via the integrated Sachs-Wolfe effect is studied in Chapter 5. Finally, the ISW signal in terms of the cross-correlation between the CMB and the LSS tracers is analysed in Chapter 6. In particular, a theoretical modelization of the NRAO VLA Sky Survey (NVSS) is proposed in this chapter.

In the next sections, the main results and conclusions of the different chapters are presented. In addition, some comments on future work are given at the end of the chapter.

7.1 Chapter 2

In this chapter, the peak statistics and their shape on the sphere are presented. The description of the peaks is given by using the suitable properties of the spherical harmonic space. For this purpose, the peak degrees of freedom are expressed in terms of the

spherical harmonics coefficients. The peak variables, and the rest of the degrees of freedom of the field are subject to a decorrelation procedure, allowing an independent treatment of the peak and the rest of the fluctuating random field. In this procedure, the assumption of Gaussianity is essential, since the decorrelation does not guarantee statistical independence for non-Gaussian fields. The different peak shapes are obtained taking the expectation value of the random field, fixing the peak variables to some fiducial values.

The probability density of the peak variables is also calculated on the sphere. Some differences with respect to previous calculations are found [143], which may be important when the field is dominated by very large-scale peaks. The main difference with respect to the flat case is that the variances of the mean curvature (κ) and the eccentricity (ϵ) are not exactly the same. However, these variances are not independent since they are related through a constraint equation (see eq. (A.8)). In the small-scale limit, both variances have the same behaviour (they scale as ℓ^4) and the flat approximation is recovered. On the contrary, the variance of the eccentricity is suppressed with respect to the variance of the curvature for large-scale peaks. Therefore, the probability density of κ and ϵ is modified for large peaks on the sphere. However, this effect is only noticeable when the field is dominated by peaks whose size is $\gtrsim 45°$. Although these scales are not usually considered, it may be important in the study of the large-scale anomalies.

The peak shape in T, E and B fields for peaks selected in temperature can be understood as a biased version of the TT, TE and TB correlation functions, respectively. For high peaks, this bias is just a constant. However, when the peak height becomes smaller, the effect of the extremum constraint (minimum or maximum selection) and the peak eccentricity introduce a non-local bias. It is found that this bias is anisotropic due to the eccentricity. In the case in which the peaks are selected with spherical symmetry, then the non-local isotropic bias is recovered.

Throughout this work, we consider peaks selected in the temperature field allowing nonzero eccentricity. The non-spherical symmetry of peaks introduces a quadrupolar dependence on the azimuthal angle ϕ, which modifies their local shape. However, this asymmetry only affects to scales smaller than the sound horizon size. For larger scales, the peak shape is only affected by gravity, which is not sensitive to the local eccentricity at the centre. As it is expected, although the peaks are selected in the temperature field, the polarization around the peak location is also affected due to their correlation. The induced shape on the Stokes parameters, and on the E and B polarization fields, has been calculated for the general case of peaks with eccentricity. In the case of the Stokes parameters, we have used the polar coordinates around the peak, leading to the parameters Q_r and U_r [148]. When peaks have spherical symmetry, and there is no

physical effects introducing TB correlation, the induced U_r pattern vanishes. However, this is not the case when the peak eccentricity is considered. The asymmetrical photon flow converging or diverging to the potential well introduces a nonzero U_r contribution. The shape of U_r in this case is a quadrupole whose axes form an angle of 45° with respect to the peak principal axes. In addition, the Stokes parameter Q_r is also modified by the peak eccentricity. The differences in pressure and flow velocity in the directions of elongation and compression of the ellipse introduce a quadrupolar dependence in Q_r, in this case aligned with the principal axes.

Finally, the peak formalism in the spherical harmonic space developed in this chapter allows one to generate Gaussian random simulations with a given peak at some position on the sphere. The peak can be chosen with the desired characteristics (peak height, mean curvature and eccentricity). In particular, the extremum constraint can be imposed to the peak variables, generating in this case a minimum or maximum. This mechanism to simulate peaks may be useful for the analysis of particular peaks present in the data, taking into account the possible systematics, noise and mask.

In the next chapters, we will apply the formalism developed in this chapter to the *Planck* CMB data. In particular, we will test the standard cosmological model looking at the curvature and eccentricity of extrema.

7.2 Chapter 3

In this work, the CMB temperature field is analysed by calculating its derivatives up to second order at different scales. One of the problems is that the incomplete sky (due to the masking of the Galactic emission and the point sources) causes a wrong determination of the derivatives at the border of the mask. In addition, other systematics appear when a convolution is applied to the masked data, since the filtering introduces a smearing of the mask border which is proportional to the filter scale. Therefore, in a multiscale analysis of the derivative fields, the handling of the mask is important in order to have a correct characterization of the derivatives. Due to the fact that the mask breaks the statistical isotropy of the field, the covariance of the fields depends on the pixel location, following the geometry given by the particular mask considered. The calculation of the pixel covariance is achieved in Section 3.4 by doing Monte Carlo simulations in an efficient way in order the reduce the simulation errors. For this purpose, the covariance at a given pixel is expressed as a linear transformation of the theoretical pixel-independent covariance, using a Cholesky-like decomposition. Following this procedure, we have that the temperature (ν) and the local curvature (κ) at a given pixel are correlated in a way determined by the theoretical fiducial model and the mask geometry.

Besides, the components of the spinorial derivatives (the gradient and the eccentricity tensor), which are independent in an isotropic field, are correlated as a consequence of the incomplete sky.

Once the covariances between the different derivatives components have been determined at each pixel, an estimator of the theoretical full-sky covariances is proposed in Section 3.5, which generalizes the standard maximum likelihood estimator for full-sky data. A multiscale analysis is performed by calculating these covariances at different scales, finding that there is a systematic low variance preference at large scales in all the derivatives. Regarding the off-diagonal terms, an unusual low correlation between ν and κ is found when it is compared with its theoretical prediction. But, on the other hand, this effect disappears when the correlation term is normalized by the respective measured variances, indicating that the low correlation is directly related to the anomalous low variance.

Moreover, the isotropy of the field can be tested by looking at the variance of the gradient and the eccentricity tensor. If there is no preferred directions on the sky, the variances of each spinorial component must be the same, and the correlation between them should vanish. By comparing these assumptions as a function of the scale, no deviation from the isotropy is found in the CMB temperature. The statistical properties of the spinor components depend on the particular local system of reference used in their description, and therefore, this result is associated to the z axis of the standard Galactic coordinates. A more general analysis varying the azimuthal direction has to be performed in order to conclude that the derivatives are statistically isotropic.

The possible departure of the data from the standard model is quantified by looking at the deviation of the extreme values of the derivatives fields. The procedure consists in comparing the measured value of the derivative with the pixel covariance calculated in Section 3.4 using a χ^2 test. The deviations of the extreme values are quantified as the tail probability of finding that value in one realization. In this analysis, the observed low variance in the data has an important role in the determination of this quantity, which causes that the extrema have particularly small values. In order to correct by this effect, pixel covariances which take into account the mask geometry, as well as the observed low variances of the derivative fields, are introduced. Repeating the analysis with these modified covariances, the anomaly in the values of the extrema disappears in all the derivative fields, with the exception of κ, where deviations associated to the Cold Spot [123] and other large scale fluctuations are observed. In addition, a deviation at the scale $R = 10^\circ$ is highlighted in the combined analysis of the ν and κ whose p-value is comparable with the Cold Spot. The spatial location of the extrema is concentrated in the southern ecliptic hemisphere, a region which appear to be anomalous in other

estimators of the statistical isotropy, as the dipole modulation [105]. It is possible to conclude from these results that the significance of these anomalies in the CMB temperature at large scales may be related to the low variance of the field. When these deviations are referred to the variance calculated from the theoretical model instead of the ones obtained from the data, the compatibility of the deviations increase to a probability of 6%.

Finally, in Section 3.7, an estimator of the local isotropy of the field based on the geodesic projection is developed for spinorial quantities. The mathematical formalism can be reduced to the application of a given kernel to the spherical harmonic coefficients, which is a function of the particular spin of the quantity considered. This directional analysis depends on the sky area used for averaging the projected spinor, which allows an analysis of isotropy at different scales. Since we are interested in the large scales, we consider three cases in our study: full-sky, one hemisphere and 45° averaged areas. As in the previous section, deviations from the standard model are characterized by the directions of maximum anisotropy. The results indicate that these directions correspond to the largest structures observed in the CMB temperature. In particular, it is observed a deviation whose p-value is $\approx$ 0.2-0.9% which is centred in one of the largest peaks near the Galactic plane.

7.3 Chapter 4

In this work, we have studied the most prominent large-scale peaks in the CMB temperature in terms of the multipolar profiles for different values of m. Since the peaks are characterized by their derivatives up to second order at the centre, we pay special attention to the monopolar and quadrupolar profiles, which have expectation values different form zero in this situation. Once the theoretical mean profiles and covariances are calculated by conditioning the derivatives to the observed values, a χ^2 test is performed for each peak and value of m. The analysis suggests that the theoretical monopolar and quadrupolar profiles derived from the standard model present a good agreement with the profiles obtained from the data. Moreover, a broader analysis of the multipolar profiles concludes that there is no significant deviations in the profiles with m up to 10. These results implies that there is no anomalies in the shape of the peaks considered, at least once the values of the derivatives are conditioned.

The Cold Spot anomaly previously described in [123] is considered as a deviation in the Laplacian of the temperature field at the smoothing scale $R = 5°$. The analysis performed by conditioning both the peak height ν and the curvature κ does not indicate any anomaly in the Cold Spot monopolar profile, but, on the other hand, if only the

value of ν is fixed, the profile exhibits a 4.7σ deviation up to a radius $\theta = 10°$. This result shows that the Cold Spot anomaly is mainly caused by the extremely large value of κ at the centre, while the field around it seems to be compatible with the Gaussian correlations in the standard model. Moreover, it is observed that the hot ring in the Cold Spot around 15° is caused by a combination of the large value of κ with a comparatively small peak amplitude ν.

The study of the multipolar profiles is completed by analysing their phases, which take into account the orientation of the different multipolar shapes around the peaks. In general, even in the case of a statistically isotropic field, the phases of the multipolar profiles are correlated for different values of θ. For this reason, in this chapter, it is introduced an estimator which associates a phase-independent profile $\hat{T}_m(\theta)$ to each multipolar profile $T_m(\theta)$, given a fiducial model for its covariance. This allows one to define a Rayleigh random walk in terms of the phases of the profiles, which moves as the value of θ increases. Statistical deviations from the standard model are characterized by the total length travelled by the random walk at a given time. If the distance covered by the random walk associated to a given multipolar profile is too large (too small), it means that the corresponding multipolar profile of the peak has a correlation (anti-correlation) for different values of θ which is greater than the one expected in the standard model, and therefore the peak presents an alignment for that value of m not compatible with an isotropic field. Some alignments are observed in few multipolar profiles of some of the large-scale peaks considered. In particular, the Cold Spot presents an alignment of the $m = 5$ profiles which is maximum at the hot ring position (15°).

Finally, the peaks are directly analysed in the real space by considering 2-dimensional patches around them. This methodology allows taking into account a Galactic mask, which cannot be done in the multipolar profile expansion due to the spurious signal introduced in that case. As in the profile analysis, the peak field is compared with the theoretical expectation when the derivatives of the peak are conditioned. In particular, the direction of the elongation of each peak is fixed according to the observed eccentricity tensor. In this case, the results are compatible with the ones obtained in the multipolar profile analysis, concluding that the effect of the mask does not change the main conclusions already found with the multipolar profiles of the large-scale peaks.

7.4 Chapter 5

We have reviewed the ISW contribution from a supervoid as the one detected by [136] in the light of two different models previously considered: a top-hat (TH) matter density profile and a particular case of the Lemaître-Tolman-Bondi (LTB) model with a Gaussian

potential. The comparison between the feature induced on the CMB by the presence of a void as the one mentioned above and the CS has been focused both, on the amplitude of the induced CMB temperature decrement, and the shape of the radial profile. This is an important aspect that is related to the anomalous nature of the CS, which is manifested when the CMB is analysed in wavelet space. The shape of the CS radial profile is shown anomalous, and therefore the ability to relate this shape with the imprint of a supervoid would give weight to the hypothesis that there is a connection between both phenomena. However, an SMHW coefficient analysis shows that the imprint of the void does not fit the same pattern than the CS profile. All SMHW coefficients computed in this work lie within the 2.5σ level with respect to the standard deviation due to the ISW signal, even for extreme scenarios that, although discarded within the standard cosmological model, could provide CMB decrements at the centre of the CS of the order of the observed data. In the light of these models, it is important to recall that the ISW imprint from an individual void is indistinguishable from the primordial fluctuations.

Modifications of the LTB density profile have been considered to describe more accurately the particular shape of the CMB profile around the CS (see [137]). However, the shape is modified at the expense of a lower value of the amplitude at the centre, and therefore, this amplitude is not already significant. In fact, we have checked that the values of the wavelet coefficients at the centre of this feature are even smaller than those related to the cases considered in this work.

In conclusion, we have shown that the ISW effect within the standard model is not a plausible explanation for the CS, not even considering the Rees-Sciama effect. Nevertheless, any hypothetical physical connection between the void and the CS should rely either on deviations from the standard cosmological model (e.g. non-Gaussian primordial density fluctuations) or on new physics.

7.5 Chapter 6

The large-scale structure is the most important cosmological probe of the late Universe and the dark-energy physics. In particular, the cross-correlation between LSS tracers and the CMB temperature provides a way to quantify the evolution of the gravitational potential at the recent epoch and, therefore, information about the dynamics of the dark energy.

In this chapter, the NVSS catalogue has been studied in terms of both, the redshift distribution, and the angular power spectrum. A modelization of the NVSS bias based on the halo model and the halo occupation distribution is proposed, finding that the

mean number of NVSS galaxies per halo is almost flat. One of the problems of NVSS is that it suffer from a declination-dependent systematic, which mainly affects to sources with the lowest flux. The excess observed in the angular power spectrum at large scale could be caused by this systematic, however, this rise of power is present when higher flux thresholds are chosen. In order to obtain a description of the NVSS angular power spectrum, data from the CENSORS catalogue are used to characterize the redshift distribution. When both, the angular power spectrum and the redshift distribution, are combined to model the NVSS catalogue, the excess of power at large scales is better described at the expense of considering that there are more NVSS galaxies at low redshift than the expected from other models of the NVSS redshift distribution given in the literature.

By using information of several LSS tracers, the cross-correlation signal between the CMB temperature and the LSS is enhanced. Since the large-scale structure data, as well as the CMB temperature, are masked in order to remove foreground contaminants, systematic effects or unobserved pixels, the different multipoles of the angular cross-power spectra are correlated. In Section 6.4, the calculation of the covariance matrix obtained from the MASTER formalism [200, 201] is generalised including data from several LSS tracers. This methodology is also extended to other quantities as the cross-correlation function or wavelet-based estimators.

Finally, the results published in the *Planck* papers on the integrated Sachs-Wolfe effect are show. The combination of the NVSS catalogue, as it is described above, other galaxy samples (SDSS or WISE) and the lensing potential leads to a 4σ detection of the cross-correlation signal between the CMB temperature and the large-scale structure. Moreover, the ΛCMB model is tested by constraining the dark-energy parameters, finding that the dark-energy density parameter, Ω_Λ, is detected at 3σ level and the best fit value of w is very close to -1, despite the constraints on this parameter are not very tight.

7.6 Future work

The peak formalism presented in Chapter 2 provides a useful methodology to study the large-scale peaks on any Gaussian random field on the sphere. Although the analysis in this chapter are focused on the CMB peaks in temperature and polarization, a generalization to other fields is possible. In particular, the imprint on the CMB temperature of peaks selected in the number density field derived from large-scale catalogues can be analysed in order to study the ISW effect.

In Chapter 2, a methodology for simulating peaks with different amplitude, mean curvature and eccentricity is also presented. For instance, this formalism can be used for simulating specific peaks in the CMB, as the Cold Spot, and study its statistical properties. Additionally, this formalism allows one to remove the effect of a given peak on the observed CMB, keeping the rest of the field unaltered. The area of the sky where the peak was located could be filled with a Gaussian random simulation of the peak variables. By analysing the CMB maps where this particular peak is subtracted, it can be analysed whether this peak is responsible for some deviation observed in the data.

The methodology introduced in Chapter 3 for studying the directional isotropy of the gradient and the eccentricity tensor can be applied to any spinorial quantity. For instance, it is possible to study the CMB polarization field, in which case, this estimator is equivalent to applying a linear filter to the E and B polarization modes.

Moreover, the analysis of the large-scale peaks in the CMB temperature performed in Chapter 4 can be extended to include polarization. Since some of the secondary anisotropies do not induce an effect on the polarization field, this kind of tests are useful to study whether those peaks are primordial or not.

Finally, the hypothesis that the Cold Spot is caused by a supervoid can be also addressed from the perspective of the peak theory. Defining the Cold Spot as a large value of the curvature in the CMB temperature, as in Chapter 4, the peak theory can be used to estimate the induced ISW pattern.

Appendix A

Peaks formalism

A.1 Covariant derivatives on the sphere

A suitable approach to take derivatives on the sphere is by using the covariant derivatives. The components of a tensor field on the sphere can be expressed in the standard orthonormal basis of the tangent plane, $\mathbf{e}_\theta$ and $\mathbf{e}_\phi$. For convenience, we change this basis to the helicity basis $\mathbf{e}_\pm = (\mathbf{e}_\theta \pm i\mathbf{e}_\phi)/\sqrt{2}$. The interest of working in the helicity basis is that the covariant derivatives can be expressed in terms of the raising and lowering operators $\eth$ and $\eth^*$:

$$\nabla_+ = -\frac{1}{\sqrt{2}}\eth \ , \qquad \nabla_- = -\frac{1}{\sqrt{2}}\eth^* \ . \tag{A.1}$$

Throughout the paper, we use $\eth$ and $\eth^*$ as the derivative operators instead of the covariant derivatives, although the difference between both is only a normalization constant. In order to differentiate any field on the sphere, it is enough to see how $\eth$ and $\eth^*$ operate over the spin-weighted spherical harmonics:

$$\eth\,({}_sY_{\ell m}) = \sqrt{\ell(\ell+1) - s(s+1)}\ {}_{s+1}Y_{\ell m} \ , \tag{A.2a}$$

$$\eth^*\,({}_sY_{\ell m}) = -\sqrt{\ell(\ell+1) - s(s-1)}\ {}_{s-1}Y_{\ell m} \ . \tag{A.2b}$$

For simplicity, we are particularly interested in the value of the derivatives at the north pole. As the spherical coordinates present singularities at both poles, we have to take special care when expressions are evaluated at these points. The problem with the spherical coordinates is that, while θ takes the values 0 or π at the poles, the azimuthal angle ϕ is undetermined at these points. Different values of ϕ correspond to different orientations of the basis vectors $\mathbf{e}_\theta$ and $\mathbf{e}_\phi$. Therefore, the value of ϕ at the poles characterizes the orientation of the local system of reference. In the case of scalars, the system of reference is not important due to their invariant character. However, for higher

order tensors, the orientation modifies their components. In general, if we operate with $\eth$ and $\eth^*$ over the spherical harmonics and evaluate them at the north pole ($\theta = 0$), it is obtained that

$$(\eth^*)^a\ (\eth)^b\ Y_{\ell m}(0,\phi) = (-1)^b \sqrt{\frac{2\ell+1}{4\pi}} \sqrt{\frac{(\ell+a-b)!}{(\ell-a+b)!}} \frac{(\ell+b)!}{(\ell-b)!}\ e^{i(a-b)\phi}\ \delta_{m,a-b}\ , \tag{A.3}$$

where the ϕ dependence has been considered. The spinorial character of the derivatives causes that their values are complex numbers. As it is expected, the spin of $(\eth^*)^a\ (\eth)^b\ Y_{\ell m}$ is $a-b$. This fact is reflected in the exponential factor $e^{i(a-b)\phi}$, which determines its transformation under azimuthal rotations. The presence of ϕ in eq. (A.3) is nothing more than an indication of the non-zero spin of the derivatives and the ambiguity of the coordinates at the north pole. For this reason, we can understand the ϕ angle in this equation as a gauge parameter, caused by the lack of one-to-one mapping of the spherical coordinates and the sphere. In the following and throughout the calculations in this paper, we use the gauge $\phi = 0$ when we evaluate spinorial quantities at the north pole. This corresponds to a particular orientation of the system of reference, aligned with the x and y directions. In this case, we can ignore the factor $e^{i(a-b)\phi}$ in eq. (A.3). In particular, we are interested in some special values of eq. (A.3):

$$Y_{\ell m}(0,0) = \sqrt{\frac{2\ell+1}{4\pi}}\ \delta_{m0} \tag{A.4a}$$

$$\eth^* Y_{\ell m}(0,0) = \sqrt{\frac{2\ell+1}{4\pi}} \sqrt{\frac{(\ell+1)!}{(\ell-1)!}}\ \delta_{m1} \tag{A.4b}$$

$$\eth Y_{\ell m}(0,0) = -\sqrt{\frac{2\ell+1}{4\pi}} \sqrt{\frac{(\ell+1)!}{(\ell-1)!}}\ \delta_{m-1} \tag{A.4c}$$

$$\eth^* \eth Y_{\ell m}(0,0) = -\sqrt{\frac{2\ell+1}{4\pi}} \frac{(\ell+1)!}{(\ell-1)!}\ \delta_{m0} \tag{A.4d}$$

$$(\eth^*)^2 Y_{\ell m}(0,0) = \sqrt{\frac{2\ell+1}{4\pi}} \sqrt{\frac{(\ell+2)!}{(\ell-2)!}}\ \delta_{m2} \tag{A.4e}$$

$$(\eth)^2 Y_{\ell m}(0,0) = \sqrt{\frac{2\ell+1}{4\pi}} \sqrt{\frac{(\ell+2)!}{(\ell-2)!}}\ \delta_{m-2} \tag{A.4f}$$

Finally, in order to calculate the Stokes parameters, it is useful to obtain the expressions for the 2-spin spherical harmonics, in particular for $m = 0$ and $m = 2$:[1]

$${}_{\pm 2}Y_{\ell 0}(\theta,\phi) = Y_{\ell \pm 2}(\theta,\phi)\ e^{\mp i 2\phi} = \sqrt{\frac{2\ell+1}{4\pi}} \sqrt{\frac{(\ell-2)!}{(\ell+2)!}}\ P_\ell^2(\cos\theta)\ , \tag{A.5a}$$

[1] The spherical harmonics for $m = -2$ are calculated using the property ${}_{\pm s}Y_{\ell -m} = (-1)^{m+s}\ {}_{\mp s}Y^*_{\ell m}$.

$$ {}_{\pm 2}Y_{\ell 2}(\theta,\phi) = 2\sqrt{\frac{2\ell+1}{4\pi}\frac{(\ell-2)!}{(\ell+2)!}}\left(P_\ell^+(\cos\theta) \pm P_\ell^-(\cos\theta)\right)\ e^{i2\phi}\ , \tag{A.5b} $$

where the functions defined in eqs. (2.18) were used.

A.2 Peak degrees of freedom

In this appendix, we study the peak degrees of freedom and their connection to the operators defined in the previous appendix. Peaks are described by derivatives up to second order. Assuming that the field is given by its spherical harmonic expansion (see eq. (2.1)), and that the peak is located at the north pole, only the $m = 0$ spherical harmonic coefficients contribute to the value of ν (eq. (2.4a)). However, the first derivatives of T at the north pole are given by the real and imaginary parts of $\eth^* T$, which is a linear combination of the spherical harmonics coefficients with $m = 1$ (eq. (2.2b)). The second order derivatives are encoded in the Hessian matrix, which can be written in the following way:

$$ \begin{pmatrix} \partial_x^2 T & \partial_x\partial_y T \\ \partial_x\partial_y T & \partial_y^2 T \end{pmatrix} = \frac{1}{2}\begin{pmatrix} \nabla^2 T & 0 \\ 0 & \nabla^2 T \end{pmatrix} + \frac{1}{2}\begin{pmatrix} \mathrm{Re}\,(\eth^*)^2 T & -\mathrm{Im}\,(\eth^*)^2 T \\ -\mathrm{Im}\,(\eth^*)^2 T & -\mathrm{Re}\,(\eth^*)^2 T \end{pmatrix}\ , \tag{A.6} $$

where $\nabla^2 T$ is the Laplacian corresponding to the trace of the Hessian matrix. It can be written in terms of the operators described in the previous appendix: $\nabla^2 T = \eth^*\eth T$. The complex number $(\eth^*)^2 T$ is the traceless part and it describes the eccentricity of the peak. The Hessian matrix is separated in this form because the two parts transform in a different way. The Laplacian is invariant under rotations around the origin, while the $(\eth^*)^2 T$ transforms like a spin-2 tensor. The physical meaning of the Laplacian is the mean curvature of the peak when it is averaged over all directions. Whilst the modulus of $(\eth^*)^2 T$ is proportional to the square of the eccentricity of the peak, the orientation angle is encoded in its phase.

Throughout this paper, the peak variables ν, κ, η and ϵ are used. They are defined as the quantities T, $-\nabla^2 T$, $\eth^* T$ and $(\eth^*)^2 T$, normalized to unit variance. The variances of the peak variables are

$$ \sigma_\nu^2 = \langle T^2 \rangle = \sum_{\ell=0}^{\infty} \frac{2\ell+1}{4\pi} C_\ell^{TT}\ , \tag{A.7a} $$

$$ \sigma_\kappa^2 = \langle (-\nabla^2 T)^2 \rangle = \sum_{\ell=0}^{\infty} \frac{2\ell+1}{4\pi}\left[\frac{(\ell+1)!}{(\ell-1)!}\right]^2 C_\ell^{TT}\ , \tag{A.7b} $$

$$\sigma_\eta^2 = \langle |\eth^* T|^2 \rangle = \sum_{\ell=1}^{\infty} \frac{2\ell+1}{4\pi} \frac{(\ell+1)!}{(\ell-1)!} C_\ell^{TT} \ , \tag{A.7c}$$

$$\sigma_\epsilon^2 = \langle |(\eth^*)^2 T|^2 \rangle = \sum_{\ell=2}^{\infty} \frac{2\ell+1}{4\pi} \frac{(\ell+2)!}{(\ell-2)!} C_\ell^{TT} \ . \tag{A.7d}$$

In previous works [143, 145], it was implicitly assumed that σ_κ^2 and σ_ϵ^2 are equal, but we show that they are different if the exact calculation on the sphere is done. In particular, both variances have a ℓ^4 behavior at small scales ($\ell \gg 1$) and thus they tend to be equal. On the contrary, if the field is dominated by large-scale fluctuations, the variances σ_κ^2 and σ_ϵ^2 are different and this has an effect on the peak statistics. In addition, these two variances are not independent, as they are related through the following equation:

$$\sigma_\kappa^2 - \sigma_\epsilon^2 = 2\sigma_\eta^2 \ . \tag{A.8}$$

In the limit when $\sigma_\kappa^2, \sigma_\epsilon^2 \gg \sigma_\eta^2$ it is possible to consider that the variances σ_κ^2 and σ_ϵ^2 are equal. The peak variables ν, κ, η and ϵ are obtained normalizing by the respective variance. In this situation, the multipolar coefficients of the peak variables are

$$\nu_\ell = \sqrt{\frac{2\ell+1}{4\pi} \frac{C_\ell^{TT}}{\sigma_\nu^2}} \ , \tag{A.9a}$$

$$\kappa_\ell = \sqrt{\frac{2\ell+1}{4\pi} \frac{C_\ell^{TT}}{\sigma_\kappa^2} \frac{(\ell+1)!}{(\ell-1)!}} \ , \tag{A.9b}$$

$$\eta_\ell = \sqrt{\frac{2\ell+1}{4\pi} \frac{C_\ell^{TT}}{\sigma_\eta^2}} \sqrt{\frac{(\ell+1)!}{(\ell-1)!}} \ , \tag{A.9c}$$

$$\epsilon_\ell = \sqrt{\frac{2\ell+1}{4\pi} \frac{C_\ell^{TT}}{\sigma_\epsilon^2}} \sqrt{\frac{(\ell+2)!}{(\ell-2)!}} \ , \tag{A.9d}$$

where the factor C_ℓ^{TT} has been introduced in order to have normalized $a_{\ell m}$ coefficients. It is useful to calculate the covariance of the peak height, the mean curvature, the first derivative and the eccentricity. The covariance of ν, κ, η and ϵ is:[2]

$$S = \begin{pmatrix} 1 & \rho & 0 & 0 \\ \rho & 1 & 0 & 0 \\ 0 & 0 & 1 & 0 \\ 0 & 0 & 0 & 1 \end{pmatrix} \ , \tag{A.10}$$

[2]The covariance of complex variables $\{x_i\}$ is defined as $\langle x_i^* x_j \rangle - \langle x_i^* \rangle \langle x_j \rangle$.

where $\rho = \sigma_\eta^2/\sigma_\nu\sigma_\kappa$ is the correlation between ν and κ. We also consider the covariance of the scalar degrees of freedom ν and κ, which is a submatrix of S:

$$\Sigma = \begin{pmatrix} 1 & \rho \\ \rho & 1 \end{pmatrix} . \tag{A.11}$$

A.3 Flat approximation

In this appendix we see how to calculate the small-angle limit of the expressions developed throughout this paper. In particular, the expressions given in [145] are recovered. The dictionary between the sphere and the flat approximation is given by

$$(-1)^m \sqrt{\frac{(\ell-m)!}{(\ell+m)!}} P_\ell^m(\cos\theta) \quad \longrightarrow \quad J_m(\ell\theta) , \tag{A.12a}$$

$$\sum_{\ell=0}^{\infty} \frac{2\ell+1}{4\pi} \quad \longrightarrow \quad \int \frac{\mathrm{d}\ell}{\ell} \, \frac{\ell(\ell+1)}{2\pi} , \tag{A.12b}$$

$$\ell(\ell+1) \quad \longrightarrow \quad \ell^2 . \tag{A.12c}$$

These transformations are valid for large multipoles ($\ell \gg 1$) and small angles ($\theta \ll 1$) such that $\ell\theta \sim 1$. In this case, the associated Legendre functions $P_\ell^m(\cos\theta)$ are replaced by the Bessel function $J_m(\ell\theta)$ of order m. This relation can be deduced applying the small-angle limit to the fundamental equation of the Legendre functions. The sums over multipoles are replaced by an integral over ℓ with the appropriate volume factor.

Appendix B

Integrals of the spin-weighted spherical harmonics

The spatial average of the spin-weighted spherical harmonics are given by:

$$\frac{1}{4\pi}\int \mathrm{d}^2\mathbf{x}\ {}_sY_{\ell m}(\mathbf{x}) = s\sqrt{\frac{2\ell+1}{4\pi}}\sqrt{\frac{(\ell-|s|)!}{(\ell+|s|)!}}\ A^s_\ell\ \delta_{m0}\ , \tag{B.1}$$

where the coefficients A^s_ℓ satisfy the relation $A^{-s}_\ell = A^s_\ell$, and they are defined only for $\ell \geq |s|$. In particular, in the case of $s = 1, 2$ we have

$$A^1_\ell = \begin{cases} \frac{1}{4^{\ell+1}} \begin{pmatrix} \ell+1 \\ \frac{\ell+1}{2} \end{pmatrix}^2 \frac{\ell+1}{\ell}\frac{\pi}{2}\ , & \ell \text{ odd} \\ 0\ , & \ell \text{ even} \end{cases}\ , \tag{B.2a}$$

$$A^2_\ell = \begin{cases} 0\ , & \ell \text{ odd} \\ 1\ , & \ell \text{ even},\ \ell \neq 0 \end{cases}\ . \tag{B.2b}$$

The coefficients A^1_ℓ can be easily calculated by using the following recurrence relation:

$$A^1_{\ell+2} = \frac{\ell(\ell+2)}{(\ell+3)(\ell+1)}A^1_\ell\ , \tag{B.3}$$

with initial values $A^1_0 = 0$ and $A^1_1 = 1/2$.

Appendix C

Binning of the theoretical profiles

In order to compare with the data, the theoretical profiles have to be binned in intervals of θ. Since these profiles are expressed in terms of the associated Legendre functions, this operation can be done by calculating the following indefinite integrals:

$$I_\ell^m = \int \bar{P}_\ell^m(x)\ \mathrm{d}x = \sqrt{\frac{2\ell+1}{4\pi}}\sqrt{\frac{(\ell-m)!}{(\ell+m)!}}\int P_\ell^m(x)\ \mathrm{d}x\ , \tag{C.1}$$

where the normalised associated Legendre functions $\bar{P}_\ell^m$ are introduced in order to prevent from large numbers in the calculations. On the one hand, the integrals for $m = 0, 2$ are calculated from the Legendre polynomials [165]:

$$I_\ell^0(x) = \frac{1}{\sqrt{(2\ell+1)(2\ell+3)}}\bar{P}_{\ell+1}(x) - \frac{1}{\sqrt{(2\ell+1)(2\ell-1)}}\bar{P}_{\ell-1}(x)\ , \tag{C.2a}$$

$$I_\ell^2(x) = \frac{1}{\sqrt{(\ell+2)(\ell+1)\ell(\ell-1)}}\left[-2I_\ell^0(x) + (\ell+3)x\bar{P}_\ell(x) - (\ell+1)\sqrt{\frac{2\ell+1}{2\ell+3}}\bar{P}_{\ell+1}(x)\right]\ . \tag{C.2b}$$

On the other hand, in the case of $m = 1$, the integral can be determined recursively following the expressions in [165]:

$$I_\ell^1(x) = \frac{\ell-2}{\ell+1}\sqrt{\frac{(2\ell+1)\ell(\ell-2)}{(2\ell-3)(\ell+1)(\ell-1)}}I_{\ell-2}^1(x) + \frac{1}{\ell+1}\sqrt{\frac{(2\ell+1)(2\ell-1)}{(\ell+1)(\ell-1)}}\left(1-x^2\right)\bar{P}_{\ell-1}^1(x)\ , \tag{C.3}$$

where the initial conditions are given by

$$I_1^1(x) = -\frac{1}{4}\sqrt{\frac{3}{2\pi}}\left[x\sqrt{1-x^2} + \arcsin x\right]\ , \tag{C.4a}$$

$$I_2^1(x) = \frac{2}{3}\sqrt{1-x^2}\bar{P}_2^2(x)\ . \tag{C.4b}$$

Finally, the averaged value of the associated Legendre function P_ℓ^m in the interval $[\theta_1, \theta_2]$ is expressed as

$$\frac{1}{\cos\theta_2 - \cos\theta_1} \int_{\cos\theta_1}^{\cos\theta_2} \mathrm{d}x \; P_\ell^m(x) = \sqrt{\frac{4\pi}{2\ell+1}} \sqrt{\frac{(\ell+m)!}{(\ell-m)!}} \frac{I_\ell^m(\cos\theta_2) - I_\ell^m(\cos\theta_1)}{\cos\theta_2 - \cos\theta_1} \; . \quad \text{(C.5)}$$

Alternatively, these integrals can be evaluated using numerical quadrature methods, but the recursive expressions above are faster and more accurate.

Appendix D

The spherical mexican hat wavelet

The mexican hat wavelet in the Euclidean plane is defined as a 2-dimensional function proportional to the Laplacian of the Gaussian distribution:

$$\Psi(\mathbf{x}; R) = -\sqrt{2\pi} R^3 \nabla^2_{(x,y)} G(\mathbf{x}; R) \ , \tag{D.1}$$

where $G(\mathbf{x}; R)$ is the Gaussian distribution of standard deviation R:

$$G(\mathbf{x}) = \frac{1}{2\pi R^2} e^{-|\mathbf{x}|^2/2R^2} \ . \tag{D.2}$$

Hence, taking the derivatives in eq. (D.1), it is obtained that

$$\Psi(\mathbf{x}; R) = \frac{1}{\sqrt{2\pi R^2}} \left(2 - \frac{|\mathbf{x}|^2}{R^2}\right) e^{-|\mathbf{x}|^2/2R^2} \ . \tag{D.3}$$

The generalization of this wavelet to the sphere can be done by using the stereographic projection [121, 204], which, in the case that the wavelet is located at the North pole, is given by

$$\begin{aligned} x &= 2 \tan \frac{\theta}{2} \cos\phi \ , \\ y &= 2 \tan \frac{\theta}{2} \sin\phi \ , \end{aligned} \tag{D.4}$$

where (x, y) and (θ, ϕ) are the Cartesian and spherical coordinates, respectively. These transformations are similar to the mapping relating the Cartesian and polar coordinates, where the radial coordinate is given by $2 \tan \frac{\theta}{2}$. In this case, the Laplacian operator in

the Euclidean plane $\nabla^2_{(x,y)}$ and in the sphere $\nabla^2_{(\theta,phi)}$ are related by:

$$\nabla^2_{(x,y)} = \cos^4 \frac{\theta}{2} \, \nabla^2_{(\theta,\phi)} \ . \tag{D.5}$$

Therefore, the wavelet in eq. (D.1) can be generalised to the sphere as

$$\Psi(\theta, \phi; R) = -N(R) \nabla^2_{(\theta,\phi)} G(\theta, \phi) \ , \tag{D.6}$$

where $G(\theta, \phi)$ is the sterographic projection of the Gaussian distribution in eq. (D.2) and $N(R)$ is a normalization constant. Combining eqs. (D.3), (D.5) and (D.6), it is obtained that

$$\Psi(\theta, \phi) = \frac{N(R)}{2\pi R^4} \left(1 + \frac{r^2}{4}\right)^2 \left(2 - \frac{r^2}{R^2}\right) e^{-r^2/2R^2} \ , \tag{D.7}$$

where $r = 2 \tan \frac{\theta}{2}$. This expression is the same as the one obtained in [121], where the normalization constant is given by

$$N(R) = \sqrt{\frac{2\pi}{1 + \frac{R^2}{2} + \frac{R^4}{4}}} R^3 \ . \tag{D.8}$$

Although, this expression is derived assuming that wavelet is located at the North pole, the eq. (D.7) is still valid for any location of the wavelet, where, in this case, θ represents the angular distance from the centre of the wavelet. This is a direct consequence of the definition and that the Laplacian is invariant under rotations.

From the definition in eq. (D.6), it can be shown that the the spherical harmonic transform of eq. (D.7) is

$$w_\ell(R) = N(R) \, \ell \, (\ell + 1) \, e^{-\ell(\ell+1)R^2/2} \ , \tag{D.9}$$

where we have used the fact that the Laplacian in harmonic space consists in the multiplication of the spherical harmonic coefficients by the factor $-\ell \, (\ell + 1)$, and the expression of the Gaussian filter in harmonic space. Notice that the coefficients in eq. (D.9) are related with the standard spherical harmonic coefficients by $w_\ell = \sqrt{\frac{4\pi}{2\ell+1}} a_{\ell 0}$.

Resumen en castellano

En esta tesis doctoral, se analizan las anisotropías de la radiación del fondo cósmico de microondas (FCM) a gran escala. En particular, se estudia la teoría de picos que surgen en campos gaussianos aleatorios sobre una superficie esférica, incluyendo la excentricidad de los picos como parámetro. Dicha teoría se aplica al caso particular del la temperatura y la polarización de la radiación del FCM. Para poder caracterizar los picos, es necesario conocer los campos de las derivadas hasta segundo orden. Tomando como banco de pruebas los datos de la misión *Planck* de la ESA, se realiza un análisis de las derivadas a diferentes escalas, estudiando aquellos lugares que presentan una mayor desviación del modelo cosmológico estándar. Posteriormente, se realiza un análisis más detallado de los picos que forman las estructuras más grandes del FCM, además de la región conocida como el *Cold Spot* (mancha fría). El formalismo de los perfiles multipolares, desarrollado previamente, se aplica a dichos picos para poder caracterizar su forma y geometría particular. Finalmente, en los dos últimos capítulos, se procede a estudiar las anisotropías del FCM a gran escala producidas por el efecto Sachs-Wolfe Integrado (ISW). En el primero de ellos, se estudia el efecto producido por un supervacío alineado con el *Cold Spot*, considerando diferentes modelos de energía oscura y geometrías del vacío. Por otro lado, se estudia la correlación cruzada del la temperatura del FCM y de diferentes trazadores de la estructura a gran escala del Universo. En particular, se modeliza el catálogo de galaxias denominado *NRAO VLA Sky Survey* (NVSS) en términos de su espectro angular de potencias y de su distribución en *redshift*, para poder tener un modelo teórico adecuado para describir tanto su auto-correlación, como la cruzada con el FCM. Algunos de los resultados presentados en este último capítulo han sido publicados por la colaboración *Planck* en los artículos dedicados al estudio del efecto Sachs-Wolfe integrado.

1 Introducción

El modelo cosmológico estándar proporciona una descripción precisa de la evolución y geometría del Universo a grandes escalas. Dicho modelo se basa en el principio cosmológico, el cual establece que las propiedades estadísticas del Universo no dependen de la posición en el espacio. Las observaciones de la radiación del fondo cósmico de microondas y de la estructura a gran escala del Universo están de acuerdo con las predicciones del principio cosmológico a distancias cosmológicas.

La expansión del Universo, observada primeramente en las velocidades de alejamiento de las galaxias más distantes, indica que el Universo tenía que estar en estado muy denso y caliente en las etapas más tempranas. Medidas de las abundancias relativas de elementos atómicos ligeros sugieren que dichos elementos se formaron en el Universo primitivo cuando la temperatura era lo sufucientemente elevada como para poder desencadenar reacciones nucleares. El hecho de que la temperatura del Universo fue más alta en épocas más tempranas ha sido confirmado por el descubrimiento de la radiación del FCM, la cual fue generada en la época de la recombinación. El despazamiento al rojo, debido a la expansión del Universo, hace que dicha radiación sea observada en el rango de las microondas en la actualidad.

La evolución del Universo a escalas cosmológicas viene determinada por las ecuaciones de Friedmann, las cuales surgen al aplicar el principio cosmológico a la teoría de la relatividad general. Dichas ecuaciones relacionan la dinámica del Universo con su contenido energético. Sin embargo, el alto nivel de homogeneidad observado en la radiación del FCM no se puede explicar con el contenido de materia y energía que se observa en la actualidad. Dentro del esquema comúnmente aceptado, se propone que el Universo temprano experimentó una fase de expansión acelerada, resolviendo, de esta manera, el problema de la homegeneidad, además de explicar porqué el Universo que observamos tiene una geometría tan plana. El mecanismo que originó esta expansión repentina se denomina inflación, la cual es provocada por uno o varios campos escalares. Según este modelo, las fluctuaciones cuánticas de dicho campo fueron las semillas que crearon la estructura a gran escala que se observa en el Universo actual.

Como se ha mencionado anteriormente, en el modelo de *Big Bang*, la temperatura del Universo en el pasado era mucho mayor que en la actualidad. Como consecuencia de este hecho, la materia bariónica (compuesta por electrones y núcleos atómicos) debía estar ionizada en el Universo primitivo y, por lo tanto, las partículas libres con carga (principalmente los electrones) estaban fuertemente acopladas con los fotones, implicando que el recorrido libre medio de estos era pequeño comparado con las distancias cosmológicas típicas. En esta época, la información transportada por los fotones no puede viajar

entre regiones cuya distancia relativa es mayor que este recorrido libre medio. Una de las implicaciones de la evolución del Universo es que la temperatura cae cuando este se expande, provocando que se puedan formar átomos neutros cuando la temperatura es suficientemente baja. En este último estado, la probabilidad de que un fotón colisione con una partícula es pequeña debido a la ausencia de partículas libres cargadas en el medio. Este proceso, en el que los electrones son capturados por los núcleos atómicos, se denomina recombinación. Ya que la sección eficaz de los procesos de dispersión de los fotones se reduce después de la recombinación, los fotones experimentan una transición de fase en la que su recorrido libre medio crece hasta escalas cosmológicas. En este caso, los fotones son capaces de viajar libremente a lo largo del Universo y ser observados en la actualidad como la radiación del fondo cósmico de microondas.

En los siguientes apartados se resumen cada uno de los capítulos de la tesis, mostrando sus resultados y conclusiones principales.

2 La morfología de los picos en la temperatura y la polarización del FCM sobre la esfera

En este capítulo, se presentan la estadística y la forma de los picos sobre la esfera. La descripción de los picos se hace mediante las propiedades de los armónicos esféricos. Para este propósito, los grados de libertad que parametrizan los picos son expresados en términos de los armónicos esféricos. Las variables que definen el pico y el resto de grados de libertad del campo son sujetos de un proceso de decorrelación, permitiendo un tratamiento independiente del pico y del resto del campo aleatorio. En este procedimiento, la suposición de que el campo es gaussiano es esencial, ya que la decorrelación no garantiza la independencia para campo aleatorios no gaussianos. La respectivas formas de los picos se obtienen tomando el valor esperado del campo aleatorio, manteniendo las variables del pico fijadas a los valores deseados.

En este trabajo, calculamos la densidad de probabilidad de las variables del pico es calculada para el caso de la esfera, encontrando algunas diferencias con respecto a cálculos anteriores [143], las cuales pueden llegar a ser importantes cuando el campo está dominado por picos grandes. La principal diferencia con respecto al caso plano es que las varianzas de la curvatura media (κ) y del tensor de excentricidad (ϵ) no son exactamente iguales. Sin embargo, estas cantidades no son independientes y están relacionadas mediante un ligadura (ver ec. (A.8)). En el límite de pequeña escala, las dos varianzas tienen el mismo comportamiento (ambas escalan como ℓ^4) y la aproximación plana es válida, como era de esperar. Por el contrario, la varianza de la excentricidad disminuye

con respecto a la de la curvatura para picos grandes. Por lo tanto, la densidad de probabilidad de κ y ϵ se modifica para picos grandes en la esfera con respecto al caso plano. Sin embargo, este efecto solo se nota cuando el campo está dominado por picos cuyo tamaño es mayor que $\approx 45°$. Aunque estas escalas no son comúnmente analizadas, este hecho podría ser importante en el estudio de anomalias en las escalas más grandes.

La forma de los picos seleccionados en temperatura en los campos T, E y B pueden ser vistos como una versión sesgada de las funciones de correlación TT, TE y TB, respectivamente. Para los picos más altos este sesgo es simplemente una constante. Sin embargo, cuando la altura del pico es más pequeña, el efecto de la selección del pico como un extremo (mínimo o máximo) y su excentricidad introducen un sesgo no local. Se encuentra que este sesgo es anisótropo debido a la excentricidad. En el caso de que el pico seleccionado tenga simetría esférica, se recupera un sesgo isótropo.

A lo largo de este capítulo, se consideran picos seleccionados en el campo de temperatura, permitiendo que tengan una excentricidad diferente de cero. La asimetría de los picos introducen una dependencia cuadrupolar en el ángulo azimutal ϕ, la cual modifica su forma local. Sin embargo, esta asimetría sólo afecta a las escalas más pequeñas que el tamaño del horizonte de sonido. Para las escalas más grandes, la forma del pico solo viene dada por la gravedad, la cual no es sensible a la excentricidad local en el centro del pico. Tal y como se espera, aunque los picos estén seleccionados en temperatura, la polarización alrededor del pico también se ve afectada, debido a la correlación entre ambas cantidades. La morfología inducida en los parámetros de Stokes, así como en los campos de polarización E y B, se ha calculado para el caso general de picos con excentricidad. En el caso de los parámetros de Stokes, se han utilizado coordenadas polares alrededor del pico, dando lugar a los parámetros Q_r y U_r [148]. Cuando los picos tienen simetría esférica y no hay efectos físicos que introducen correlación TB, el patrón U_r inducido se anula. Sin embargo, este no es el caso cuando se consideran picos con excentricidad. El flujo asimétrico de los fotones que convergen o divergen en los pozos de potencial introduce una contribución diferente de cero en U_r. La forma de U_r es, este caso, un cuadrupolo que forma un ángulo de 45° con respecto a los ejes principales del pico. Además, el parámetro de Stokes Q_r también cambia por la excentricidad del pico. Las diferencias de presión y velocidad del flujo de fotones en la direcciones de elongación y compresión de la elipse introducen una dependencia cuadrupolar en Q_r, en este caso alineada con los ejes principales.

Finalmente, el formalismo de picos en el espacio de armónicos esféricos desarrollado en este capítulo permite generar simulaciones aleatorias gaussianas con un determinado pico en una posición dada de la esfera. El pico puede ser escogido con las características deseadas (altura del pico, curvatura media y excentricidad). En particular, la condición

de que sea un extremo puede ser impuesta a las variables que definen el pico, generando en este caso un máximo o un mínimo. Este mecanismo para simular picos puede ser útil en análisis de fluctuaciones concretas que aparecen en los datos, teniendo en cuenta los posibles efectos sistemáticos, el ruido y la máscara.

En los siguientes capítulos, se aplicará el formalismo desarrolado en este capítulo a datos del fondo cósmico de microondas. En particular, pondremos a prueba el modelo cosmológico estándar mirando a la curvatura y excentricidad de los extremos.

3 Análisis multiescala de las derivadas de la temperatura del FCM

En este trabajo, analizamos el campo de temperatura del FCM a través del cálculo de las derivadas, hasta segundo orden, a diferentes escalas. Uno de los problemas es que el hecho de tener un cielo incompleto (debido al enmascarmiento de la emisión galáctica y de las fuentes puntuales) hace que la derivadas estén mal estimadas en los bordes de la máscara. Además, otros efectos sistemáticos aparecen cuando se aplica una convolución a datos enmascarados, ya que el filtrado introduce un suavizado de la máscara que es proporcional a la escala del filtro. Por lo tanto, en un análisis multiescala de los campos de derivadas, el procesamiento de la máscara es importante para tener una caracterización correcta de las derivadas. Debido al hecho de que la máscara rompe la isotropía del campo, las matrices de covarianza dependen de la localización del píxel, según marca la geometría de la máscara considerada. El cálculo de la matriz de covarianza asociada a un píxel se presenta en la Sección 3.4 mediante la realización de simulaciones Monte Carlo de una manera eficiente para reducir los errores de simulación. Para este propósito, la matriz de covarianza en un píxel dado se expresa como una transformación lineal de la covarianza teórica, la cual es independiente del píxel, usando una descomposición tipo Cholesky. Siguiendo este procedimiento, se tiene que la temperatura ν y la curvatura local κ en un píxel dado están correlacionadas, no solo de una manera intrínseca (por el propio campo en sí), sino también por la geometría de la máscara. Además, las componentes de las derivadas con caracter espinorial (el gradiente y el tensor de excentricidad), las cuales son independientes en un campo isótropo, están correlacionadas como consecuencia de tener un cielo incompleto.

Una vez que las matrices de covarianza de las diferentes componentes de las derivadas se han determinado en cada píxel, se propone un estimador de las covarianzas que se obtendrían en el caso de cielo completo (ver Sección 3.5), el cual generaliza el estimador de máxima verosimilitud estándar empleado para datos sin máscara. Hemos realizado

un análisis multiescala calculando estas matrices de covarianza a diferentes escalas, y se encuentra que hay una varianza preferentemente más baja en las escalas más grandes en todos los campos de derivadas. Con respecto a los términos no diagonales, se encuentra una baja correlación entre ν y κ en los datos del FCM de *Planck*, cuando se compara con la predicción teórica. Pero, por otro lado, dicho efecto desaparece cuando el coeficiente de correlación es normalizado con las respectivas varianzas medidas en los datos, indicando que la baja correlación está relacionada directamente con la anomalía de baja varianza discutida previamente en la literatura.

Además, la isotropía del campo puede ser validada a través del gradiente y del tensor de excentricidad. Si no hay direcciones privilegiadas en el cielo, la varianza de cada componente del espinor debe ser la misma y la correlación entre ellas se debe anular. Comprobando estas hipótesis en función de la escala, no se observan desviaciones de la isotropía en la temperatura del FCM. Las propiedades estadísticas de las componentes del espinor dependen del sistema de referencia local usado para describirlas y, por lo tanto, este resultado está asociado al eje z de las coordenadas galácticas comúnmente utilizadas. Se ha realizado un análisis más preciso variando la dirección azimutal para poder concluir que los campos de derivadas son estadísticamente isótropos (ver Sección 3.7).

Las posibles desviaciones con respecto al modelo estándar son cuatificadas mirando a los valores extremos en los campos de derivadas. El procedimiento consiste en comparar los valores medidos de las derivadas con la matriz de covarianza dependiente del píxel calculadas en la Sección 3.4 usando el test χ^2. Las desviaciones de los valores extremos son cuantificadas mediante la probabilidad de encontrar ese valor o uno mayor en una realización. En este análisis, la baja varianza observada en los datos tiene un importante papel en la determinación de la cantidad estudiada, lo que causa que los extremos tengan valores particularmente pequeños. Para poder corregir este efecto, se introducen matrices de covarianza que tienen en cuenta, tanto la geometría de la máscara, como los valores observados de las covarianzas de la derivadas. Repitiendo el análisis con estas covarianzas modificadas, las anomalías en las valores de los extremos desaparece en todas las derivadas, con la excepción de κ, donde son observadas desviaciones asociadas con el *Cold Spot* [123] y otras flucuaciones a gran escala. Además, destaca una desviación a la escala $R = 10^\circ$ en el análisis combinado de ν y κ, cuyo p-valor es comparable al del *Cold Spot*. La localización espacial de los extremos está concentrada en el hemisferio sur eclíptico, una región que parece ser anómala en otros estimadores de la isotropía, como la modulación dipolar [105]. Se puede concluir a partir de estos resultados que la significancia de estas anomalías en la temperatura del FCM a grandes escalas podría estar relacionada con la baja varianza observada. Cuando estas desviaciones son referidas a las covarianzas calculadas a partir del modelo teórico, en lugar de las calculadas a partir

de los datos, la compatibilidad de las desviaciones incrementa hasta una probabilidad de 6%.

Finalmente, en la Sección 3.7, se desarrolla un estimador de la isotropía local para cantidades espinoriales. El formalismo matemático puede ser reducido a la aplicación de un núcleo a los coeficientes de armónicos esféricos, el cual es función del spin de la cantidad considerada. Este análisis direccional depende del área usada para promediar la proyección del espinor, lo cual permite un análisis de la isotropía a diferentes escalas. Ya que estamos interesados en las escalas más grandes, consideramos los tres casos siguientes: promediando a todo el cielo, en un hemisferio y en un casquete de 45°. Como en la sección anterior, las desviaciones del modelo estándar son caracterizadas a través de las direcciones de máxima anisotropía. Los resultados indican que estas direcciones se corresponden con las estructuras más grandes observadas en la temperatura del FCM. En particular, se observa una desviación cuyo p-valor es $\approx$ 0.2-0.9%, la cual está centrada en uno de los picos más grandes cerca del plano galáctico. Este análisis de la isotropía del FCM basado en cantidades espinoriales puede ser fácilmente generalizado para aplicarlo al espinor que define la polarización.

4 Propiedades locales de los picos más grandes en la temperatura del FCM

En este capítulo, se estudian los picos más grandes y prominentes de la temperatura del FCM en términos de los perfiles multipolares para diferentes valores de m. Ya que los picos están caracterizados por el valor de las derivadas hasta segundo orden en el centro, prestaremos especial atención a los perfiles monopolares y cuadrupolares, los cuales tienen valor experado diferente de cero en este caso. Una vez que calculamos los perfiles medios y las covarianzas teóricas (condicionando las derivadas a los valores observados, Capítulo 2), se realiza un test χ^2 para cada pico y valor de m. Los análisis sugieren que los perfiles monopolares y cuadrupolares teóricos derivados del modelo estándar presentan un buen acuerdo con los perfiles obtenidos a partir de los datos. Además, un análisis más amplio de los perfiles multipolares concluye que no hay desviaciones significativas en los perfiles hasta $m = 10$. Estos resultados implican que no hay anomalías en la forma de los picos considerados, al menos una vez que los valores de las derivadas son condicionados.

La anomalía del *Cold Spot*, previamente descrita en [123], se considera como una desviación del laplaciano del campo de temperatura suavizado con una gaussian de escala $R = 5°$. El análisis realizado condicionando tanto la altura de pico ν como la curvatura κ no

indica ninguna anomalía en el perfil monopolar del *Cold Spot*, pero, por otro lado, si solo el valor de ν es fijado, el perfil exhibe una desviación 4.7σ hasta un radio de $\theta = 10°$. Este resultado muestra que la anomalía del *Cold Spot* está principalmente causada por el valor extremadamente grande de κ en el centro, mientras que el campo a su alrededor parece ser compatible con las correlaciones gaussianas del modelo estándar. Además, se observa que el anillo caliente en el *Cold Spot* en torno a 15° es causado por una combinación de un valor alto de κ y un valor comparablemente pequeño de la altura del pico ν.

El estudio de los perfiles multipolares se completa con un análisis de sus fases, las cuales tienen información de la orientación de las diferentes formas multipolares alrededor de los picos. En general, incluso cuando el campo es estadísticamente isótropo, las fases de los perfiles multipolares están correlacionadas para diferentes valores de θ. Por esta razón, en este capítulo, se introduce un estimador que asocia un perfil $\hat{T}_m(\theta)$, cuyas fases son independientes, a cada perfil multipolar $T_m(\theta)$, una vez que se ha dado un modelo para sus covarianzas. Esto permite definir un caminante aleatorio de Rayleigh en términos de las fases de los perfiles, el cual se mueve según incrementa el valor de θ. Las desviaciones estadísticas del modelo estándar se caracterizan a través de la longitud total recorrida por el caminante aleatorio en un tiempo dado. Si la distancia recorrida por el caminante aleatorio asociada a un perfil multipolar dado es demasiado grande (o pequeña), significa que el perfil multipolar del pico correspondiente tiene una correlación (anticorrelación) para los diferentes valores de θ, la cual es mayor de la que se espera en el modelo estándar y, por lo tanto, el pico presenta un alineamiento en dicho multipolo m que no es compatible con un campo isótropo. Se observan alineamientos en unos cuantos multipolos de algunos de los picos considerados. En particular, el *Cold Spot* presenta un alineamiento del perfil multipolar con $m = 5$, que se maximiza en la posición del anillo caliente ($\theta = 15°$).

Finalmente, los picos son analizados en el espacio real considerando parches alrededor de ellos. Esta metodología permite tener en cuenta la máscara galáctica, lo cual no se puede hacer cuando se realiza la expansión en términos de los perfiles multipolares debido a la señal espuria introducida por la máscara en este caso. Como en el caso del análisis de los perfiles, el campo alrededor del pico se compara con el valor teórico esperado cuando las derivadas del pico son condicionadas. En partiular, la dirección de elongación de cada pico se fija conforme al valor observado del tensor de excentricidad. En este caso, los resultados son compatibles con los que se obtienen en el análisis de los perfiles multipolares, concluyendo que el efecto de la máscara no cambia las principales conclusiones que ya se encontraron en las secciones anteriores.

5 Sobre la explicación del *Cold Spot* como vacío

En este capítulo, se ha estudiado la contribución del efecto Sachs-Wolfe integrado (ISW) sobre el fondo cósmico de microondas debido a la presencia de un supervacío como el detectado en [136], comprobándose si este podría explicar la anomalía del *Cold Spot*. Se han considerado dos modelos previamente utilizados en la literatura para describir el perfil de densidad de materia del vacío: una función *tophat* y un perfíl compensado producido por un potencial gaussiano, el cual es un caso particular del modelo LTB (Lemaître-Tolman-Bondi). El análisis muestra que, incluso permitiendo diferentes valores de la elipticidad o variando el parámtro de la ecuación de estado de la energía oscura w, la contribución del efecto ISW debido a la presencia de un vacío no reproduce las propiedades del *Cold Spot*.

La comparación entre el patrón inducido en el FCM por la presencia de un vacío como el que se ha mencionado anteriormente y el *Cold Spot* se centra tanto en la amplitud del decremento de temperatura como en la forma del perfil radial. Este es un aspecto importante, el cual está relacionado con la naturaleza anómala del *Cold Spot* que se manifiesta cuando el FCM es analizado en el espacio de *wavelets*, en concreto con la SMWH. La forma del perfil radial del *Cold Spot* se muestra anómalo y, por tanto, la capacidad de relacionar esta forma con la que se deriva de un supervacío daría peso a la hipótesis de que hay una conexión entre ambos fenómenos. Sin embargo, un analisis de los coeficiente de la SMHW muestran que la forma del vacío no se ajusta al mismo patrón que el perfil del *Cold Spot*. Todos los coeficientes de la SMHW están dentro de un rango 2.5σ con respecto a la desviación estándar derivada del effecto ISW, incluso para los casos más extremos que, aunque están descartados dentro del modelo estándar, podrían proporcionar decrementos de temperatura en el centro del *Cold Spot* del orden del que se observa en los datos. A la luz de estos modelos, es importante recalcar que el efecto ISW de un solo vacío es indistinguible de las fluctuaciones primordiales del FCM.

Se han considerado modificaciones del perfil de densidad del modelo LTB para describir de una forma más precisa la forma del perfil del *Cold Spot* (ver [137]). Sin embargo, la forma se modifica a expensas de un valor más bajo de la amplitud en el centro, y por tanto su amplitud deja de ser significativa. De hecho, se ha comprobado que el valor del coeficiente de la SMHW asociado a este perfil es incluso más pequeño que los que se obtienen en los casos considerados en este trabajo.

En conclusión, se ha demostrado que el efecto ISW dentro del modelo estándar no es una explicación posible para el *Cold Spot*. Por tanto, cualquier conexión física entre el vacío y el *Cold Spot* debería basarse en, o bien desviaciones del modelo estándar (por ejemplo fluctuaciones primordiales que no sean gaussianas), o bien nueva física.

6 Correlación cruzada entre el FCM y trazadores de la estructura a gran escala

En este capítulo, se estudia la estructrua a gran escala del Universo con el objetivo de detectar el efecto Sachs-Wolfe Integrado (ISW) a partir de la correlación cruzada entre la temperatura del FCM y las fluctuaciones en el número de cuentas derivadas de catálogos de galaxias. En particular, se modelizan la distribución de *redshift* y el espectro de potencias angular del catálogo *NRAO VLA Sky Survey* (NVSS) [175] para poder tener una descripción teórica adecuada de la de correlación cruzada con la temperatura del FCM.

En la Sección 6.1, se introducen el modelo de halos y una parametrización teórica de la distribución de galaxias y del sesgo con respecto a la distribución de materia. Además de los parámetros que caracterizan la distribución de ocupación de los halos, se modelizan las propiedades estadísticas de los catálogos de galaxias a través de la masa mínima de los halos que albergan las galaxias de la muestra. Este tipo de modelos, y otras parametrizaciones de los trazadores de la estructura a gran escala, son utilizados para desarrollar un código que calcule el espectro de potencias angular para diferentes muestras y la correlación cruzada entre ellas y la temperatura del FCM (ver la Sección 6.2).

Además, en la Sección 6.3, se describe el catálogo NVSS a través del modelo introducido en la sección anterior, calculando la masa mínima y los parámetros de la distribución de ocupación de los halos. Para poder tener una mejor caracterización de la distribución de *redshift* de NVSS, se incluye en el análisis los datos del catálogo *Combined EIS-NVSS Survey Of Radio Sources* (CENSORS) [176, 177].

Adicionalmente, en la Sección 6.4, se presenta una metodología basada en la estimación del espectro de potencias cruzado a la MASTER [200, 201], en la cual se da una modelización teórica de la matriz de covarianza para más de una muestra de galaxias. Este formalismo se extiende para incluir la matriz de covarianza de diferentes funciones de correlación cruzada y estimadores basados en el espacio de *wavelets*.

Finalmente, en la Sección 6.5, se presentan algunos de los resultados publicados en los artículos de la colaboración *Planck* sobre el efecto Sachs-Wolfe integrado [179, 180]. Además de los análisis de la correlación cruzada entre la temperatura de FCM y de los trazadores de la estructura a gran escala, se presentan estimaciones de los parámetros de la energía oscura derivados del efecto ISW.

Bibliography

[1] A. Einstein. Die Grundlage der allgemeinen Relativitätstheorie. *Annalen der Physik*, 354:769–822, 1916. doi: 10.1002/andp.19163540702.

[2] E. Hubble. A Relation between Distance and Radial Velocity among Extra-Galactic Nebulae. *Proceedings of the National Academy of Science*, 15: 168–173, March 1929. doi: 10.1073/pnas.15.3.168.

[3] G. Lemaître. Un Univers homogène de masse constante et de rayon croissant rendant compte de la vitesse radiale des nébuleuses extra-galactiques. *Annales de la Société Scientifique de Bruxelles*, 47:49–59, 1927.

[4] F. Zwicky. Die Rotverschiebung von extragalaktischen Nebeln. *Helvetica Physica Acta*, 6:110–127, 1933.

[5] F. Zwicky. On the Masses of Nebulae and of Clusters of Nebulae. ApJ, 86:217, October 1937. doi: 10.1086/143864.

[6] H. W. Babcock. The rotation of the Andromeda Nebula. *Lick Observatory Bulletin*, 19:41–51, 1939. doi: 10.5479/ADS/bib/1939LicOB.19.41B.

[7] V. C. Rubin, W. K. J. Ford, and N. . Thonnard. Rotational properties of 21 SC galaxies with a large range of luminosities and radii, from NGC 4605 /R = 4kpc/ to UGC 2885 /R = 122 kpc/. ApJ, 238:471–487, June 1980. doi: 10.1086/158003.

[8] Planck Collaboration, P. A. R. Ade, N. Aghanim, M. Arnaud, M. Ashdown, J. Aumont, C. Baccigalupi, A. J. Banday, R. B. Barreiro, J. G. Bartlett, and et al. Planck 2015 results. XIII. Cosmological parameters. A&A, 594:A13, September 2016. doi: 10.1051/0004-6361/201525830.

[9] J. Lesgourgues and S. Pastor. Massive neutrinos and cosmology. Phys. Rep., 429:307–379, July 2006. doi: 10.1016/j.physrep.2006.04.001.

[10] G. Efstathiou, W. J. Sutherland, and S. J. Maddox. The cosmological constant and cold dark matter. Nature, 348:705–707, December 1990. doi: 10.1038/348705a0.

[11] S. Perlmutter, G. Aldering, M. della Valle, S. Deustua, R. S. Ellis, S. Fabbro, A. Fruchter, G. Goldhaber, D. E. Groom, I. M. Hook, A. G. Kim, M. Y. Kim, R. A. Knop, C. Lidman, R. G. McMahon, P. Nugent, R. Pain, N. Panagia, C. R. Pennypacker, P. Ruiz-Lapuente, B. Schaefer, and N. Walton. Discovery of a supernova explosion at half the age of the universe. Nature, 391:51, January 1998. doi: 10.1038/34124.

[12] P. M. Garnavich, R. P. Kirshner, P. Challis, J. Tonry, R. L. Gilliland, R. C. Smith, A. Clocchiatti, A. Diercks, A. V. Filippenko, M. Hamuy, C. J. Hogan, B. Leibundgut, M. M. Phillips, D. Reiss, A. G. Riess, B. P. Schmidt, R. A. Schommer, J. Spyromilio, C. Stubbs, N. B. Suntzeff, and L. Wells. Constraints on Cosmological Models from Hubble Space Telescope Observations of High-z Supernovae. ApJ, 493:L53–L57, February 1998. doi: 10.1086/311140.

[13] A. G. Riess, A. V. Filippenko, P. Challis, A. Clocchiatti, A. Diercks, P. M. Garnavich, R. L. Gilliland, C. J. Hogan, S. Jha, R. P. Kirshner, B. Leibundgut, M. M. Phillips, D. Reiss, B. P. Schmidt, R. A. Schommer, R. C. Smith, J. Spyromilio, C. Stubbs, N. B. Suntzeff, and J. Tonry. Observational Evidence from Supernovae for an Accelerating Universe and a Cosmological Constant. AJ, 116:1009–1038, September 1998. doi: 10.1086/300499.

[14] S. Perlmutter, G. Aldering, G. Goldhaber, R. A. Knop, P. Nugent, P. G. Castro, S. Deustua, S. Fabbro, A. Goobar, D. E. Groom, I. M. Hook, A. G. Kim, M. Y. Kim, J. C. Lee, N. J. Nunes, R. Pain, C. R. Pennypacker, R. Quimby, C. Lidman, R. S. Ellis, M. Irwin, R. G. McMahon, P. Ruiz-Lapuente, N. Walton, B. Schaefer, B. J. Boyle, A. V. Filippenko, T. Matheson, A. S. Fruchter, N. Panagia, H. J. M. Newberg, W. J. Couch, and T. S. C. Project. Measurements of Ω and Λ from 42 High-Redshift Supernovae. ApJ, 517:565–586, June 1999. doi: 10.1086/307221.

[15] M. Chevallier and D. Polarski. Accelerating Universes with Scaling Dark Matter. *International Journal of Modern Physics D*, 10:213–223, 2001. doi: 10.1142/S0218271801000822.

[16] E. V. Linder. Exploring the Expansion History of the Universe. *Physical Review Letters*, 90(9):091301, March 2003. doi: 10.1103/PhysRevLett.90.091301.

[17] E. R. Harrison. Fluctuations at the Threshold of Classical Cosmology. Phys. Rev. D, 1:2726–2730, May 1970. doi: 10.1103/PhysRevD.1.2726.

[18] Y. B. Zeldovich. A hypothesis, unifying the structure and the entropy of the Universe. MNRAS, 160:1P, 1972. doi: 10.1093/mnras/160.1.1P.

[19] C. W. Misner. Mixmaster Universe. *Physical Review Letters*, 22:1071–1074, May 1969. doi: 10.1103/PhysRevLett.22.1071.

[20] R. H. Dicke, editor. *Gravitation and the universe*, 1970.

[21] A. H. Guth and S.-H. H. Tye. Phase transitions and magnetic monopole production in the very early universe. *Physical Review Letters*, 44:631–635, March 1980. doi: 10.1103/PhysRevLett.44.631.

[22] A. H. Guth. Inflationary universe: A possible solution to the horizon and flatness problems. Phys. Rev. D, 23:347–356, January 1981. doi: 10.1103/PhysRevD.23.347.

[23] A. H. Guth and E. J. Weinberg. Could the universe have recovered from a slow first-order phase transition? *Nuclear Physics B*, 212:321–364, February 1983. doi: 10.1016/0550-3213(83)90307-3.

[24] A. D. Linde. A new inflationary universe scenario: A possible solution of the horizon, flatness, homogeneity, isotropy and primordial monopole problems. *Physics Letters B*, 108:389–393, February 1982. doi: 10.1016/0370-2693(82)91219-9.

[25] A. Albrecht and P. J. Steinhardt. Cosmology for grand unified theories with radiatively induced symmetry breaking. *Physical Review Letters*, 48:1220–1223, April 1982. doi: 10.1103/PhysRevLett.48.1220.

[26] V. F. Mukhanov and G. V. Chibisov. Quantum fluctuations and a nonsingular universe. *Soviet Journal of Experimental and Theoretical Physics Letters*, 33:532, May 1981.

[27] S. W. Hawking. The development of irregularities in a single bubble inflationary universe. *Physics Letters B*, 115:295–297, September 1982. doi: 10.1016/0370-2693(82)90373-2.

[28] A. H. Guth and S.-Y. Pi. Fluctuations in the new inflationary universe. *Physical Review Letters*, 49:1110–1113, October 1982. doi: 10.1103/PhysRevLett.49.1110.

[29] A. D. Linde. Scalar field fluctuations in the expanding universe and the new inflationary universe scenario. *Physics Letters B*, 116:335–339, October 1982. doi: 10.1016/0370-2693(82)90293-3.

[30] A. A. Starobinsky. Dynamics of phase transition in the new inflationary universe scenario and generation of perturbations. *Physics Letters B*, 117:175–178, November 1982. doi: 10.1016/0370-2693(82)90541-X.

[31] J. M. Bardeen, P. J. Steinhardt, and M. S. Turner. Spontaneous creation of almost scale-free density perturbations in an inflationary universe. Phys. Rev. D, 28:679–693, August 1983. doi: 10.1103/PhysRevD.28.679.

[32] M. N. Saha. On a Physical Theory of Stellar Spectra. *Proceedings of the Royal Society of London Series A*, 99:135–153, May 1921. doi: 10.1098/rspa.1921.0029.

[33] P. J. Steinhardt and M. S. Turner. Prescription for successful new inflation. Phys. Rev. D, 29:2162–2171, May 1984. doi: 10.1103/PhysRevD.29.2162.

[34] A. R. Liddle and D. H. Lyth. COBE, gravitational waves, inflation and extended inflation. *Physics Letters B*, 291:391–398, October 1992. doi: 10.1016/0370-2693(92)91393-N.

[35] D. Polarski and A. A. Starobinsky. Isocurvature perturbations in multiple inflationary models. Phys. Rev. D, 50:6123–6129, November 1994. doi: 10.1103/PhysRevD.50.6123.

[36] T. S. Bunch and P. C. W. Davies. Quantum field theory in de Sitter space - Renormalization by point-splitting. *Proceedings of the Royal Society of London Series A*, 360:117–134, March 1978. doi: 10.1098/rspa.1978.0060.

[37] P. D. Meerburg, J. P. van der Schaar, and P. S. Corasaniti. Signatures of initial state modifications on bispectrum statistics. J. Cosmology Astropart. Phys., 5: 018, May 2009. doi: 10.1088/1475-7516/2009/05/018.

[38] BICEP2 Collaboration, Keck Array Collaboration, P. A. R. Ade, Z. Ahmed, R. W. Aikin, K. D. Alexander, D. Barkats, S. J. Benton, C. A. Bischoff, J. J. Bock, R. Bowens-Rubin, J. A. Brevik, I. Buder, E. Bullock, V. Buza, J. Connors, B. P. Crill, L. Duband, C. Dvorkin, J. P. Filippini, S. Fliescher, J. Grayson, M. Halpern, S. Harrison, G. C. Hilton, H. Hui, K. D. Irwin, K. S. Karkare, E. Karpel, J. P. Kaufman, B. G. Keating, S. Kefeli, S. A. Kernasovskiy, J. M. Kovac, C. L. Kuo, E. M. Leitch, M. Lueker, K. G. Megerian, C. B. Netterfield, H. T. Nguyen, R. O'Brient, R. W. Ogburn, A. Orlando, C. Pryke, S. Richter, R. Schwarz, C. D. Sheehy, Z. K. Staniszewski, B. Steinbach, R. V. Sudiwala, G. P. Teply, K. L. Thompson, J. E. Tolan, C. Tucker, A. D. Turner, A. G. Vieregg, A. C. Weber, D. V. Wiebe, J. Willmert, C. L. Wong, W. L. K. Wu, and K. W. Yoon. Improved Constraints on Cosmology and Foregrounds from BICEP2 and Keck Array Cosmic Microwave Background Data with Inclusion of 95 GHz Band. *Physical Review Letters*, 116(3):031302, January 2016. doi: 10.1103/PhysRevLett.116.031302.

[39] G. Gamow. The Origin of Elements and the Separation of Galaxies. *Physical Review*, 74:505–506, August 1948. doi: 10.1103/PhysRev.74.505.2.

[40] G. Gamow. The Evolution of the Universe. Nature, 162:680–682, October 1948. doi: 10.1038/162680a0.

[41] R. A. Alpher and R. Herman. Evolution of the Universe. Nature, 162:774–775, November 1948. doi: 10.1038/162774b0.

[42] R. A. Alpher and R. C. Herman. Remarks on the Evolution of the Expanding Universe. *Physical Review*, 75:1089–1095, April 1949. doi: 10.1103/PhysRev.75.1089.

[43] A. A. Penzias and R. W. Wilson. A Measurement of Excess Antenna Temperature at 4080 Mc/s. ApJ, 142:419–421, July 1965. doi: 10.1086/148307.

[44] R. H. Dicke, P. J. E. Peebles, P. G. Roll, and D. T. Wilkinson. Cosmic Black-Body Radiation. ApJ, 142:414–419, July 1965. doi: 10.1086/148306.

[45] P. J. E. Peebles. Recombination of the Primeval Plasma. ApJ, 153:1, July 1968. doi: 10.1086/149628.

[46] Y. B. Zeldovich, V. G. Kurt, and R. A. Syunyaev. Recombination of Hydrogen in the Hot Model of the Universe. *Zhurnal Eksperimentalnoi i Teoreticheskoi Fiziki*, 55:278–286, July 1968.

[47] Planck Collaboration, R. Adam, P. A. R. Ade, N. Aghanim, Y. Akrami, M. I. R. Alves, F. Argüeso, M. Arnaud, F. Arroja, M. Ashdown, and et al. Planck 2015 results. I. Overview of products and scientific results. A&A, 594:A1, September 2016. doi: 10.1051/0004-6361/201527101.

[48] R. W. Ogburn, IV, P. A. R. Ade, R. W. Aikin, M. Amiri, S. J. Benton, J. J. Bock, J. A. Bonetti, J. A. Brevik, B. Burger, C. D. Dowell, L. Duband, J. P. Filippini, S. R. Golwala, M. Halpern, M. Hasselfield, G. Hilton, V. V. Hristov, K. Irwin, J. P. Kaufman, B. G. Keating, J. M. Kovac, C. L. Kuo, A. E. Lange, E. M. Leitch, C. B. Netterfield, H. T. Nguyen, A. Orlando, C. L. Pryke, C. Reintsema, S. Richter, J. E. Ruhl, M. C. Runyan, C. D. Sheehy, Z. K. Staniszewski, S. A. Stokes, R. V. Sudiwala, G. P. Teply, J. E. Tolan, A. D. Turner, P. Wilson, and C. L. Wong. The BICEP2 CMB polarization experiment. In *Millimeter, Submillimeter, and Far-Infrared Detectors and Instrumentation for Astronomy V*, volume 7741 of Proc. SPIE, page 77411G, July 2010. doi: 10.1117/12.857864.

[49] C. D. Sheehy, P. A. R. Ade, R. W. Aikin, M. Amiri, S. Benton, C. Bischoff, J. J. Bock, J. A. Bonetti, J. A. Brevik, B. Burger, C. D. Dowell, L. Duband, J. P. Filippini, S. R. Golwala, M. Halpern, M. Hasselfield, G. Hilton, V. V. Hristov, K. Irwin, J. P. Kaufman, B. G. Keating, J. M. Kovac, C. L. Kuo, A. E. Lange, E. M. Leitch, M. Lueker, C. B. Netterfield, H. T. Nguyen, R. W. Ogburn, IV, A. Orlando, C. L. Pryke, C. Reintsema, S. Richter, J. E. Ruhl, M. C. Runyan, Z. Staniszewski, S. Stokes, R. Sudiwala, G. Teply, K. L. Thompson, J. E. Tolan, A. D. Turner, P. Wilson, and C. L. Wong. The Keck Array: a pulse tube cooled CMB polarimeter. In *Millimeter, Submillimeter, and Far-Infrared Detectors and Instrumentation for Astronomy V*, volume 7741 of Proc. SPIE, page 77411R, July 2010. doi: 10.1117/12.857871.

[50] BICEP2 Collaboration, P. A. R. Ade, R. W. Aikin, M. Amiri, D. Barkats, S. J. Benton, C. A. Bischoff, J. J. Bock, J. A. Brevik, I. Buder, E. Bullock, G. Davis, P. K. Day, C. D. Dowell, L. Duband, J. P. Filippini, S. Fliescher, S. R. Golwala, M. Halpern, M. Hasselfield, S. R. Hildebrandt, G. C. Hilton, K. D. Irwin, K. S. Karkare, J. P. Kaufman, B. G. Keating, S. A. Kernasovskiy, J. M. Kovac, C. L. Kuo, E. M. Leitch, N. Llombart, M. Lueker, C. B. Netterfield, H. T. Nguyen, R. O'Brient, R. W. Ogburn, IV, A. Orlando, C. Pryke, C. D. Reintsema, S. Richter, R. Schwarz, C. D. Sheehy, Z. K. Staniszewski, K. T. Story, R. V. Sudiwala, G. P. Teply, J. E. Tolan, A. D. Turner, A. G. Vieregg, P. Wilson, C. L. Wong, and K. W. Yoon. BICEP2. II. Experiment and three-year Data Set. ApJ, 792:62, September 2014. doi: 10.1088/0004-637X/792/1/62.

[51] R. K. Sachs and A. M. Wolfe. Perturbations of a Cosmological Model and Angular Variations of the Microwave Background. ApJ, 147:73, January 1967. doi: 10.1086/148982.

[52] M. White and W. Hu. The Sachs-Wolfe effect. A&A, 321:8–9, May 1997.

[53] W. Hu and S. Dodelson. Cosmic Microwave Background Anisotropies. ARA&A, 40:171–216, 2002. doi: 10.1146/annurev.astro.40.060401.093926.

[54] W. Hu and M. White. Acoustic Signatures in the Cosmic Microwave Background. ApJ, 471:30, November 1996. doi: 10.1086/177951.

[55] W. Hu and N. Sugiyama. Anisotropies in the cosmic microwave background: an analytic approach. ApJ, 444:489–506, May 1995. doi: 10.1086/175624.

[56] J. Silk. Cosmic Black-Body Radiation and Galaxy Formation. ApJ, 151:459, February 1968. doi: 10.1086/149449.

[57] S. Weinberg. Entropy Generation and the Survival of Protogalaxies in an Expanding Universe. ApJ, 168:175, September 1971. doi: 10.1086/151073.

[58] W. Hu and N. Sugiyama. Small-Scale Cosmological Perturbations: an Analytic Approach. ApJ, 471:542, November 1996. doi: 10.1086/177989.

[59] U. Seljak. A two-fluid approximation for calculating the cosmic microwave background anisotropies. ApJ, 435:L87–L90, November 1994. doi: 10.1086/187601.

[60] A. Kosowsky. Cosmic microwave background polarization. *Annals of Physics*, 246:49–85, February 1996. doi: 10.1006/aphy.1996.0020.

[61] P. J. E. Peebles and J. T. Yu. Primeval Adiabatic Perturbation in an Expanding Universe. ApJ, 162:815, December 1970. doi: 10.1086/150713.

[62] C.-P. Ma and E. Bertschinger. Cosmological Perturbation Theory in the Synchronous and Conformal Newtonian Gauges. ApJ, 455:7, December 1995. doi: 10.1086/176550.

[63] A. Blanchard and J. Schneider. Gravitational lensing effect on the fluctuations of the cosmic background radiation. A&A, 184:1–6, October 1987.

[64] A. Lewis and A. Challinor. Weak gravitational lensing of the CMB. Phys. Rep., 429:1–65, June 2006. doi: 10.1016/j.physrep.2006.03.002.

[65] Planck Collaboration, R. Adam, N. Aghanim, M. Ashdown, J. Aumont, C. Baccigalupi, M. Ballardini, A. J. Banday, R. B. Barreiro, N. Bartolo, S. Basak, R. Battye, K. Benabed, J.-P. Bernard, M. Bersanelli, P. Bielewicz, J. J. Bock, A. Bonaldi, L. Bonavera, J. R. Bond, J. Borrill, F. R. Bouchet, F. Boulanger, M. Bucher, C. Burigana, E. Calabrese, J.-F. Cardoso, J. Carron, H. C. Chiang, L. P. L. Colombo, C. Combet, B. Comis, F. Couchot, A. Coulais, B. P. Crill, A. Curto, F. Cuttaia, R. J. Davis, P. de Bernardis, A. de Rosa, G. de Zotti, J. Delabrouille, E. Di Valentino, C. Dickinson, J. M. Diego, O. Doré, M. Douspis, A. Ducout, X. Dupac, F. Elsner, T. A. Enßlin, H. K. Eriksen, E. Falgarone, Y. Fantaye, F. Finelli, F. Forastieri, M. Frailis, A. A. Fraisse, E. Franceschi, A. Frolov, S. Galeotta, S. Galli, K. Ganga, R. T. Génova-Santos, M. Gerbino, T. Ghosh, J. González-Nuevo, K. M. Górski, A. Gruppuso, J. E. Gudmundsson, F. K. Hansen, G. Helou, S. Henrot-Versillé, D. Herranz, E. Hivon, Z. Huang, S. Ilić, A. H. Jaffe, W. C. Jones, E. Keihänen, R. Keskitalo, T. S. Kisner, L. Knox, N. Krachmalnicoff, M. Kunz, H. Kurki-Suonio, G. Lagache, A. Lähteenmäki, J.-M. Lamarre, M. Langer, A. Lasenby, M. Lattanzi, C. R. Lawrence, M. Le Jeune, F. Levrier, A. Lewis, M. Liguori, P. B. Lilje,

M. López-Caniego, Y.-Z. Ma, J. F. Macías-Pérez, G. Maggio, A. Mangilli, M. Maris, P. G. Martin, E. Martínez-González, S. Matarrese, N. Mauri, J. D. McEwen, P. R. Meinhold, A. Melchiorri, A. Mennella, M. Migliaccio, M.-A. Miville-Deschênes, D. Molinari, A. Moneti, L. Montier, G. Morgante, A. Moss, P. Naselsky, P. Natoli, C. A. Oxborrow, L. Pagano, D. Paoletti, B. Partridge, G. Patanchon, L. Patrizii, O. Perdereau, L. Perotto, V. Pettorino, F. Piacentini, S. Plaszczynski, L. Polastri, G. Polenta, J.-L. Puget, J. P. Rachen, B. Racine, M. Reinecke, M. Remazeilles, A. Renzi, G. Rocha, M. Rossetti, G. Roudier, J. A. Rubiño-Martín, B. Ruiz-Granados, L. Salvati, M. Sandri, M. Savelainen, D. Scott, G. Sirri, R. Sunyaev, A.-S. Suur-Uski, J. A. Tauber, M. Tenti, L. Toffolatti, M. Tomasi, M. Tristram, T. Trombetti, J. Valiviita, F. Van Tent, P. Vielva, F. Villa, N. Vittorio, B. D. Wandelt, I. K. Wehus, M. White, A. Zacchei, and A. Zonca. Planck intermediate results. XLVII. Planck constraints on reionization history. A&A, 596:A108, December 2016. doi: 10.1051/0004-6361/201628897.

[66] R. A. Sunyaev and Y. B. Zeldovich. Small-Scale Fluctuations of Relic Radiation. Ap&SS, 7:3–19, April 1970. doi: 10.1007/BF00653471.

[67] R. A. Sunyaev and I. B. Zeldovich. Microwave background radiation as a probe of the contemporary structure and history of the universe. ARA&A, 18:537–560, 1980. doi: 10.1146/annurev.aa.18.090180.002541.

[68] J. P. Ostriker and E. T. Vishniac. Generation of microwave background fluctuations from nonlinear perturbations at the ERA of galaxy formation. ApJ, 306:L51–L54, July 1986. doi: 10.1086/184704.

[69] Planck Collaboration, N. Aghanim, C. Armitage-Caplan, M. Arnaud, M. Ashdown, F. Atrio-Barandela, J. Aumont, C. Baccigalupi, A. J. Banday, R. B. Barreiro, J. G. Bartlett, K. Benabed, A. Benoit-Lévy, J.-P. Bernard, M. Bersanelli, P. Bielewicz, J. Bobin, J. J. Bock, J. R. Bond, J. Borrill, F. R. Bouchet, M. Bridges, C. Burigana, R. C. Butler, J.-F. Cardoso, A. Catalano, A. Challinor, A. Chamballu, H. C. Chiang, L.-Y. Chiang, P. R. Christensen, D. L. Clements, L. P. L. Colombo, F. Couchot, B. P. Crill, A. Curto, F. Cuttaia, L. Danese, R. D. Davies, R. J. Davis, P. de Bernardis, A. de Rosa, G. de Zotti, J. Delabrouille, J. M. Diego, S. Donzelli, O. Doré, X. Dupac, G. Efstathiou, T. A. Enßlin, H. K. Eriksen, F. Finelli, O. Forni, M. Frailis, E. Franceschi, S. Galeotta, K. Ganga, M. Giard, G. Giardino, J. González-Nuevo, K. M. Górski, S. Gratton, A. Gregorio, A. Gruppuso, F. K. Hansen, D. Hanson, D. L. Harrison, G. Helou, S. R. Hildebrandt, E. Hivon, M. Hobson, W. A. Holmes, W. Hovest, K. M. Huffenberger, W. C. Jones, M. Juvela, E. Keihänen, R. Keskitalo, T. S.

Kisner, J. Knoche, L. Knox, M. Kunz, H. Kurki-Suonio, A. Lähteenmäki, J.-M. Lamarre, A. Lasenby, R. J. Laureijs, C. R. Lawrence, R. Leonardi, A. Lewis, M. Liguori, P. B. Lilje, M. Linden-Vørnle, M. López-Caniego, P. M. Lubin, J. F. Macías-Pérez, N. Mandolesi, M. Maris, D. J. Marshall, P. G. Martin, E. Martínez-González, S. Masi, M. Massardi, S. Matarrese, P. Mazzotta, P. R. Meinhold, A. Melchiorri, L. Mendes, M. Migliaccio, S. Mitra, A. Moneti, L. Montier, G. Morgante, D. Mortlock, A. Moss, D. Munshi, P. Naselsky, F. Nati, P. Natoli, H. U. Nørgaard-Nielsen, F. Noviello, D. Novikov, I. Novikov, S. Osborne, C. A. Oxborrow, L. Pagano, F. Pajot, D. Paoletti, F. Pasian, G. Patanchon, O. Perdereau, F. Perrotta, F. Piacentini, E. Pierpaoli, D. Pietrobon, S. Plaszczynski, E. Pointecouteau, G. Polenta, N. Ponthieu, L. Popa, G. W. Pratt, G. Prézeau, J.-L. Puget, J. P. Rachen, W. T. Reach, M. Reinecke, S. Ricciardi, T. Riller, I. Ristorcelli, G. Rocha, C. Rosset, J. A. Rubiño-Martín, B. Rusholme, D. Santos, G. Savini, D. Scott, M. D. Seiffert, E. P. S. Shellard, L. D. Spencer, R. Sunyaev, F. Sureau, A.-S. Suur-Uski, J.-F. Sygnet, J. A. Tauber, D. Tavagnacco, L. Terenzi, L. Toffolatti, M. Tomasi, M. Tristram, M. Tucci, M. Türler, L. Valenziano, J. Valiviita, B. Van Tent, P. Vielva, F. Villa, N. Vittorio, L. A. Wade, B. D. Wandelt, M. White, D. Yvon, A. Zacchei, J. P. Zibin, and A. Zonca. Planck 2013 results. XXVII. Doppler boosting of the CMB: Eppur si muove. A&A, 571:A27, November 2014. doi: 10.1051/0004-6361/201321556.

[70] A. Challinor and F. van Leeuwen. Peculiar velocity effects in high-resolution microwave background experiments. Phys. Rev. D, 65(10):103001, May 2002. doi: 10.1103/PhysRevD.65.103001.

[71] G. F. Smoot, C. L. Bennett, A. Kogut, E. L. Wright, J. Aymon, N. W. Boggess, E. S. Cheng, G. de Amici, S. Gulkis, M. G. Hauser, G. Hinshaw, P. D. Jackson, M. Janssen, E. Kaita, T. Kelsall, P. Keegstra, C. Lineweaver, K. Loewenstein, P. Lubin, J. Mather, S. S. Meyer, S. H. Moseley, T. Murdock, L. Rokke, R. F. Silverberg, L. Tenorio, R. Weiss, and D. T. Wilkinson. Structure in the COBE differential microwave radiometer first-year maps. ApJ, 396:L1–L5, September 1992. doi: 10.1086/186504.

[72] J. C. Mather, E. S. Cheng, R. E. Eplee, Jr., R. B. Isaacman, S. S. Meyer, R. A. Shafer, R. Weiss, E. L. Wright, C. L. Bennett, N. W. Boggess, E. Dwek, S. Gulkis, M. G. Hauser, M. Janssen, T. Kelsall, P. M. Lubin, S. H. Moseley, Jr., T. L. Murdock, R. F. Silverberg, G. F. Smoot, and D. T. Wilkinson. A preliminary measurement of the cosmic microwave background spectrum by the

Cosmic Background Explorer (COBE) satellite. ApJ, 354:L37–L40, May 1990. doi: 10.1086/185717.

[73] J. C. Mather, E. S. Cheng, D. A. Cottingham, R. E. Eplee, Jr., D. J. Fixsen, T. Hewagama, R. B. Isaacman, K. A. Jensen, S. S. Meyer, P. D. Noerdlinger, S. M. Read, L. P. Rosen, R. A. Shafer, E. L. Wright, C. L. Bennett, N. W. Boggess, M. G. Hauser, T. Kelsall, S. H. Moseley, Jr., R. F. Silverberg, G. F. Smoot, R. Weiss, and D. T. Wilkinson. Measurement of the cosmic microwave background spectrum by the COBE FIRAS instrument. ApJ, 420:439–444, January 1994. doi: 10.1086/173574.

[74] D. J. Fixsen, E. S. Cheng, J. M. Gales, J. C. Mather, R. A. Shafer, and E. L. Wright. The Cosmic Microwave Background Spectrum from the Full COBE FIRAS Data Set. ApJ, 473:576, December 1996. doi: 10.1086/178173.

[75] D. J. Fixsen. The Temperature of the Cosmic Microwave Background. ApJ, 707: 916–920, December 2009. doi: 10.1088/0004-637X/707/2/916.

[76] R. Durrer, A. Gangui, and M. Sakellariadou. Doppler Peaks in the Angular Power Spectrum of the Cosmic Microwave Background: A Fingerprint of Topological Defects. *Physical Review Letters*, 76:579–582, January 1996. doi: 10.1103/PhysRevLett.76.579.

[77] J. Magueijo, A. Albrecht, P. Ferreira, and D. Coulson. Structure of Doppler peaks induced by active perturbations. Phys. Rev. D, 54:3727–3744, September 1996. doi: 10.1103/PhysRevD.54.3727.

[78] A. Albrecht, D. Coulson, P. Ferreira, and J. Magueijo. Causality, Randomness, and the Microwave Background. *Physical Review Letters*, 76:1413–1416, February 1996. doi: 10.1103/PhysRevLett.76.1413.

[79] A. D. Miller, R. Caldwell, M. J. Devlin, W. B. Dorwart, T. Herbig, M. R. Nolta, L. A. Page, J. Puchalla, E. Torbet, and H. T. Tran. A Measurement of the Angular Power Spectrum of the Cosmic Microwave Background from L = 100 to 400. ApJ, 524:L1–L4, October 1999. doi: 10.1086/312293.

[80] P. de Bernardis, P. A. R. Ade, J. J. Bock, J. R. Bond, J. Borrill, A. Boscaleri, K. Coble, B. P. Crill, G. De Gasperis, P. C. Farese, P. G. Ferreira, K. Ganga, M. Giacometti, E. Hivon, V. V. Hristov, A. Iacoangeli, A. H. Jaffe, A. E. Lange, L. Martinis, S. Masi, P. V. Mason, P. D. Mauskopf, A. Melchiorri, L. Miglio, T. Montroy, C. B. Netterfield, E. Pascale, F. Piacentini, D. Pogosyan, S. Prunet, S. Rao, G. Romeo, J. E. Ruhl, F. Scaramuzzi, D. Sforna, and N. Vittorio. A flat

Universe from high-resolution maps of the cosmic microwave background radiation. Nature, 404:955–959, April 2000.

[81] S. Hanany, P. Ade, A. Balbi, J. Bock, J. Borrill, A. Boscaleri, P. de Bernardis, P. G. Ferreira, V. V. Hristov, A. H. Jaffe, A. E. Lange, A. T. Lee, P. D. Mauskopf, C. B. Netterfield, S. Oh, E. Pascale, B. Rabii, P. L. Richards, G. F. Smoot, R. Stompor, C. D. Winant, and J. H. P. Wu. MAXIMA-1: A Measurement of the Cosmic Microwave Background Anisotropy on Angular Scales of $10' - 5°$. ApJ, 545:L5–L9, December 2000. doi: 10.1086/317322.

[82] N. W. Halverson, E. M. Leitch, C. Pryke, J. Kovac, J. E. Carlstrom, W. L. Holzapfel, M. Dragovan, J. K. Cartwright, B. S. Mason, S. Padin, T. J. Pearson, A. C. S. Readhead, and M. C. Shepherd. Degree Angular Scale Interferometer First Results: A Measurement of the Cosmic Microwave Background Angular Power Spectrum. ApJ, 568:38–45, March 2002. doi: 10.1086/338879.

[83] A. T. Lee, P. Ade, A. Balbi, J. Bock, J. Borrill, A. Boscaleri, P. de Bernardis, P. G. Ferreira, S. Hanany, V. V. Hristov, A. H. Jaffe, P. D. Mauskopf, C. B. Netterfield, E. Pascale, B. Rabii, P. L. Richards, G. F. Smoot, R. Stompor, C. D. Winant, and J. H. P. Wu. A High Spatial Resolution Analysis of the MAXIMA-1 Cosmic Microwave Background Anisotropy Data. ApJ, 561:L1–L5, November 2001. doi: 10.1086/324437.

[84] C. B. Netterfield, P. A. R. Ade, J. J. Bock, J. R. Bond, J. Borrill, A. Boscaleri, K. Coble, C. R. Contaldi, B. P. Crill, P. de Bernardis, P. Farese, K. Ganga, M. Giacometti, E. Hivon, V. V. Hristov, A. Iacoangeli, A. H. Jaffe, W. C. Jones, A. E. Lange, L. Martinis, S. Masi, P. Mason, P. D. Mauskopf, A. Melchiorri, T. Montroy, E. Pascale, F. Piacentini, D. Pogosyan, F. Pongetti, S. Prunet, G. Romeo, J. E. Ruhl, and F. Scaramuzzi. A Measurement by BOOMERANG of Multiple Peaks in the Angular Power Spectrum of the Cosmic Microwave Background. ApJ, 571:604–614, June 2002. doi: 10.1086/340118.

[85] C. L. Bennett, M. Bay, M. Halpern, G. Hinshaw, C. Jackson, N. Jarosik, A. Kogut, M. Limon, S. S. Meyer, L. Page, D. N. Spergel, G. S. Tucker, D. T. Wilkinson, E. Wollack, and E. L. Wright. The Microwave Anisotropy Probe Mission. ApJ, 583:1–23, January 2003. doi: 10.1086/345346.

[86] C. L. Bennett, D. Larson, J. L. Weiland, N. Jarosik, G. Hinshaw, N. Odegard, K. M. Smith, R. S. Hill, B. Gold, M. Halpern, E. Komatsu, M. R. Nolta, L. Page, D. N. Spergel, E. Wollack, J. Dunkley, A. Kogut, M. Limon, S. S. Meyer, G. S. Tucker, and E. L. Wright. Nine-year Wilkinson Microwave

Anisotropy Probe (WMAP) Observations: Final Maps and Results. ApJS, 208: 20, October 2013. doi: 10.1088/0067-0049/208/2/20.

[87] G. Hinshaw, D. Larson, E. Komatsu, D. N. Spergel, C. L. Bennett, J. Dunkley, M. R. Nolta, M. Halpern, R. S. Hill, N. Odegard, L. Page, K. M. Smith, J. L. Weiland, B. Gold, N. Jarosik, A. Kogut, M. Limon, S. S. Meyer, G. S. Tucker, E. Wollack, and E. L. Wright. Nine-year Wilkinson Microwave Anisotropy Probe (WMAP) Observations: Cosmological Parameter Results. ApJS, 208:19, October 2013. doi: 10.1088/0067-0049/208/2/19.

[88] D. N. Spergel, L. Verde, H. V. Peiris, E. Komatsu, M. R. Nolta, C. L. Bennett, M. Halpern, G. Hinshaw, N. Jarosik, A. Kogut, M. Limon, S. S. Meyer, L. Page, G. S. Tucker, J. L. Weiland, E. Wollack, and E. L. Wright. First-Year Wilkinson Microwave Anisotropy Probe (WMAP) Observations: Determination of Cosmological Parameters. ApJS, 148:175–194, September 2003. doi: 10.1086/377226.

[89] Planck Collaboration, N. Aghanim, M. Arnaud, M. Ashdown, J. Aumont, C. Baccigalupi, A. J. Banday, R. B. Barreiro, J. G. Bartlett, N. Bartolo, and et al. Planck 2015 results. XI. CMB power spectra, likelihoods, and robustness of parameters. *ArXiv e-prints*, July 2015.

[90] Planck Collaboration, P. A. R. Ade, N. Aghanim, C. Armitage-Caplan, M. Arnaud, M. Ashdown, F. Atrio-Barandela, J. Aumont, C. Baccigalupi, A. J. Banday, and et al. Planck 2013 results. XXIII. Isotropy and statistics of the CMB. A&A, 571:A23, November 2014. doi: 10.1051/0004-6361/201321534.

[91] Planck Collaboration, P. A. R. Ade, N. Aghanim, Y. Akrami, P. K. Aluri, M. Arnaud, M. Ashdown, J. Aumont, C. Baccigalupi, A. J. Banday, and et al. Planck 2015 results. XVI. Isotropy and statistics of the CMB. *ArXiv e-prints*, June 2015.

[92] J. M. Kovac, E. M. Leitch, C. Pryke, J. E. Carlstrom, N. W. Halverson, and W. L. Holzapfel. Detection of polarization in the cosmic microwave background using DASI. Nature, 420:772–787, December 2002. doi: 10.1038/nature01269.

[93] E. M. Leitch, J. M. Kovac, N. W. Halverson, J. E. Carlstrom, C. Pryke, and M. W. E. Smith. Degree Angular Scale Interferometer 3 Year Cosmic Microwave Background Polarization Results. ApJ, 624:10–20, May 2005. doi: 10.1086/428825.

[94] A. C. S. Readhead, S. T. Myers, T. J. Pearson, J. L. Sievers, B. S. Mason, C. R. Contaldi, J. R. Bond, R. Bustos, P. Altamirano, C. Achermann, L. Bronfman,

J. E. Carlstrom, J. K. Cartwright, S. Casassus, C. Dickinson, W. L. Holzapfel, J. M. Kovac, E. M. Leitch, J. May, S. Padin, D. Pogosyan, M. Pospieszalski, C. Pryke, R. Reeves, M. C. Shepherd, and S. Torres. Polarization Observations with the Cosmic Background Imager. *Science*, 306:836–844, October 2004. doi: 10.1126/science.1105598.

[95] A. Kogut, D. N. Spergel, C. Barnes, C. L. Bennett, M. Halpern, G. Hinshaw, N. Jarosik, M. Limon, S. S. Meyer, L. Page, G. S. Tucker, E. Wollack, and E. L. Wright. First-Year Wilkinson Microwave Anisotropy Probe (WMAP) Observations: Temperature-Polarization Correlation. ApJS, 148:161–173, September 2003. doi: 10.1086/377219.

[96] D. N. Spergel and M. Zaldarriaga. Cosmic Microwave Background Polarization as a Direct Test of Inflation. *Physical Review Letters*, 79:2180–2183, September 1997. doi: 10.1103/PhysRevLett.79.2180.

[97] H. V. Peiris, E. Komatsu, L. Verde, D. N. Spergel, C. L. Bennett, M. Halpern, G. Hinshaw, N. Jarosik, A. Kogut, M. Limon, S. S. Meyer, L. Page, G. S. Tucker, E. Wollack, and E. L. Wright. First-Year Wilkinson Microwave Anisotropy Probe (WMAP) Observations: Implications For Inflation. ApJS, 148:213–231, September 2003. doi: 10.1086/377228.

[98] L. Page, G. Hinshaw, E. Komatsu, M. R. Nolta, D. N. Spergel, C. L. Bennett, C. Barnes, R. Bean, O. Doré, J. Dunkley, M. Halpern, R. S. Hill, N. Jarosik, A. Kogut, M. Limon, S. S. Meyer, N. Odegard, H. V. Peiris, G. S. Tucker, L. Verde, J. L. Weiland, E. Wollack, and E. L. Wright. Three-Year Wilkinson Microwave Anisotropy Probe (WMAP) Observations: Polarization Analysis. ApJS, 170:335–376, June 2007. doi: 10.1086/513699.

[99] D. Hanson, S. Hoover, A. Crites, P. A. R. Ade, K. A. Aird, J. E. Austermann, J. A. Beall, A. N. Bender, B. A. Benson, L. E. Bleem, J. J. Bock, J. E. Carlstrom, C. L. Chang, H. C. Chiang, H.-M. Cho, A. Conley, T. M. Crawford, T. de Haan, M. A. Dobbs, W. Everett, J. Gallicchio, J. Gao, E. M. George, N. W. Halverson, N. Harrington, J. W. Henning, G. C. Hilton, G. P. Holder, W. L. Holzapfel, J. D. Hrubes, N. Huang, J. Hubmayr, K. D. Irwin, R. Keisler, L. Knox, A. T. Lee, E. Leitch, D. Li, C. Liang, D. Luong-Van, G. Marsden, J. J. McMahon, J. Mehl, S. S. Meyer, L. Mocanu, T. E. Montroy, T. Natoli, J. P. Nibarger, V. Novosad, S. Padin, C. Pryke, C. L. Reichardt, J. E. Ruhl, B. R. Saliwanchik, J. T. Sayre, K. K. Schaffer, B. Schulz, G. Smecher, A. A. Stark, K. T. Story, C. Tucker, K. Vanderlinde, J. D. Vieira, M. P. Viero, G. Wang, V. Yefremenko, O. Zahn, and M. Zemcov. Detection of B-Mode Polarization in the Cosmic Microwave

Background with Data from the South Pole Telescope. *Physical Review Letters*, 111(14):141301, October 2013. doi: 10.1103/PhysRevLett.111.141301.

[100] The Polarbear Collaboration: P. A. R. Ade, Y. Akiba, A. E. Anthony, K. Arnold, M. Atlas, D. Barron, D. Boettger, J. Borrill, S. Chapman, Y. Chinone, M. Dobbs, T. Elleflot, J. Errard, G. Fabbian, C. Feng, D. Flanigan, A. Gilbert, W. Grainger, N. W. Halverson, M. Hasegawa, K. Hattori, M. Hazumi, W. L. Holzapfel, Y. Hori, J. Howard, P. Hyland, Y. Inoue, G. C. Jaehnig, A. H. Jaffe, B. Keating, Z. Kermish, R. Keskitalo, T. Kisner, M. Le Jeune, A. T. Lee, E. M. Leitch, E. Linder, M. Lungu, F. Matsuda, T. Matsumura, X. Meng, N. J. Miller, H. Morii, S. Moyerman, M. J. Myers, M. Navaroli, H. Nishino, A. Orlando, H. Paar, J. Peloton, D. Poletti, E. Quealy, G. Rebeiz, C. L. Reichardt, P. L. Richards, C. Ross, I. Schanning, D. E. Schenck, B. D. Sherwin, A. Shimizu, C. Shimmin, M. Shimon, P. Siritanasak, G. Smecher, H. Spieler, N. Stebor, B. Steinbach, R. Stompor, A. Suzuki, S. Takakura, T. Tomaru, B. Wilson, A. Yadav, and O. Zahn. A Measurement of the Cosmic Microwave Background B-mode Polarization Power Spectrum at Sub-degree Scales with POLARBEAR. ApJ, 794:171, October 2014. doi: 10.1088/0004-637X/794/2/171.

[101] BICEP2 Collaboration, Keck Array Collaboration, P. A. R. Ade, Z. Ahmed, R. W. Aikin, K. D. Alexander, D. Barkats, S. J. Benton, C. A. Bischoff, J. J. Bock, R. Bowens-Rubin, J. A. Brevik, I. Buder, E. Bullock, V. Buza, J. Connors, B. P. Crill, L. Duband, C. Dvorkin, J. P. Filippini, S. Fliescher, J. Grayson, M. Halpern, S. Harrison, S. R. Hildebrandt, G. C. Hilton, H. Hui, K. D. Irwin, J. Kang, K. S. Karkare, E. Karpel, J. P. Kaufman, B. G. Keating, S. Kefeli, S. A. Kernasovskiy, J. M. Kovac, C. L. Kuo, E. M. Leitch, M. Lueker, K. G. Megerian, T. Namikawa, C. B. Netterfield, H. T. Nguyen, R. O'Brient, R. W. Ogburn, IV, A. Orlando, C. Pryke, S. Richter, R. Schwarz, C. D. Sheehy, Z. K. Staniszewski, B. Steinbach, R. V. Sudiwala, G. P. Teply, K. L. Thompson, J. E. Tolan, C. Tucker, A. D. Turner, A. G. Vieregg, A. C. Weber, D. V. Wiebe, J. Willmert, C. L. Wong, W. L. K. Wu, and K. W. Yoon. BICEP2/Keck Array VIII: Measurement of Gravitational Lensing from Large-scale B-mode Polarization. ApJ, 833:228, December 2016. doi: 10.3847/1538-4357/833/2/228.

[102] H. K. Eriksen, F. K. Hansen, A. J. Banday, K. M. Górski, and P. B. Lilje. Asymmetries in the Cosmic Microwave Background Anisotropy Field. ApJ, 605: 14–20, April 2004. doi: 10.1086/382267.

[103] F. K. Hansen, A. J. Banday, K. M. Górski, H. K. Eriksen, and P. B. Lilje. Power Asymmetry in Cosmic Microwave Background Fluctuations from Full Sky to

Sub-Degree Scales: Is the Universe Isotropic? ApJ, 704:1448–1458, October 2009. doi: 10.1088/0004-637X/704/2/1448.

[104] C. Gordon. Broken Isotropy from a Linear Modulation of the Primordial Perturbations. ApJ, 656:636–640, February 2007. doi: 10.1086/510511.

[105] J. Hoftuft, H. K. Eriksen, A. J. Banday, K. M. Górski, F. K. Hansen, and P. B. Lilje. Increasing Evidence for Hemispherical Power Asymmetry in the Five-Year WMAP Data. ApJ, 699:985–989, July 2009. doi: 10.1088/0004-637X/699/2/985.

[106] D. Hanson and A. Lewis. Estimators for CMB statistical anisotropy. Phys. Rev. D, 80(6):063004, September 2009. doi: 10.1103/PhysRevD.80.063004.

[107] K. Land and J. Magueijo. Is the Universe odd? Phys. Rev. D, 72(10):101302, November 2005. doi: 10.1103/PhysRevD.72.101302.

[108] J. Kim and P. Naselsky. Anomalous parity asymmetry of WMAP 7-year power spectrum data at low multipoles: Is it cosmological or systematics? Phys. Rev. D, 82(6):063002, September 2010. doi: 10.1103/PhysRevD.82.063002.

[109] A. Gruppuso, F. Finelli, P. Natoli, F. Paci, P. Cabella, A. de Rosa, and N. Mandolesi. New constraints on parity symmetry from a re-analysis of the WMAP-7 low-resolution power spectra. MNRAS, 411:1445–1452, March 2011. doi: 10.1111/j.1365-2966.2010.17773.x.

[110] J. Kim and P. Naselsky. Lack of Angular Correlation and Odd-parity Preference in Cosmic Microwave Background Data. ApJ, 739:79, October 2011. doi: 10.1088/0004-637X/739/2/79.

[111] P. Naselsky, W. Zhao, J. Kim, and S. Chen. Is the Cosmic Microwave Background Asymmetry due to the Kinematic Dipole? ApJ, 749:31, April 2012. doi: 10.1088/0004-637X/749/1/31.

[112] W. Zhao. Directional dependence of CMB parity asymmetry. Phys. Rev. D, 89 (2):023010, January 2014. doi: 10.1103/PhysRevD.89.023010.

[113] C. J. Copi, D. Huterer, D. J. Schwarz, and G. D. Starkman. Large-scale alignments from WMAP and Planck. MNRAS, 449:3458–3470, June 2015. doi: 10.1093/mnras/stv501.

[114] A. de Oliveira-Costa, M. Tegmark, M. Zaldarriaga, and A. Hamilton. Significance of the largest scale CMB fluctuations in WMAP. Phys. Rev. D, 69 (6):063516, March 2004. doi: 10.1103/PhysRevD.69.063516.

[115] C. Monteserín, R. B. Barreiro, P. Vielva, E. Martínez-González, M. P. Hobson, and A. N. Lasenby. A low cosmic microwave background variance in the Wilkinson Microwave Anisotropy Probe data. MNRAS, 387:209–219, June 2008. doi: 10.1111/j.1365-2966.2008.13149.x.

[116] M. Cruz, P. Vielva, E. Martínez-González, and R. B. Barreiro. Anomalous variance in the WMAP data and Galactic foreground residuals. MNRAS, 412: 2383–2390, April 2011. doi: 10.1111/j.1365-2966.2010.18067.x.

[117] C. R. Contaldi, M. Peloso, L. Kofman, and A. Linde. Suppressing the lower multipoles in the CMB anisotropies. J. Cosmology Astropart. Phys., 7:002, July 2003. doi: 10.1088/1475-7516/2003/07/002.

[118] C. Destri, H. J. de Vega, and N. G. Sanchez. Preinflationary and inflationary fast-roll eras and their signatures in the low CMB multipoles. Phys. Rev. D, 81 (6):063520, March 2010. doi: 10.1103/PhysRevD.81.063520.

[119] C. L. Bennett, M. Halpern, G. Hinshaw, N. Jarosik, A. Kogut, M. Limon, S. S. Meyer, L. Page, D. N. Spergel, G. S. Tucker, E. Wollack, E. L. Wright, C. Barnes, M. R. Greason, R. S. Hill, E. Komatsu, M. R. Nolta, N. Odegard, H. V. Peiris, L. Verde, and J. L. Weiland. First-Year Wilkinson Microwave Anisotropy Probe (WMAP) Observations: Preliminary Maps and Basic Results. ApJS, 148:1–27, September 2003. doi: 10.1086/377253.

[120] C. J. Copi, D. Huterer, D. J. Schwarz, and G. D. Starkman. Lack of large-angle TT correlations persists in WMAP and Planck. MNRAS, 451:2978–2985, August 2015. doi: 10.1093/mnras/stv1143.

[121] E. Martínez-González, J. E. Gallegos, F. Argüeso, L. Cayón, and J. L. Sanz. The performance of spherical wavelets to detect non-Gaussianity in the cosmic microwave background sky. MNRAS, 336:22–32, October 2002. doi: 10.1046/j.1365-8711.2002.05648.x.

[122] P. Vielva, E. Martínez-González, R. B. Barreiro, J. L. Sanz, and L. Cayón. Detection of Non-Gaussianity in the Wilkinson Microwave Anisotropy Probe First-Year Data Using Spherical Wavelets. ApJ, 609:22–34, July 2004. doi: 10.1086/421007.

[123] M. Cruz, E. Martínez-González, P. Vielva, and L. Cayón. Detection of a non-Gaussian spot in WMAP. MNRAS, 356:29–40, January 2005. doi: 10.1111/j.1365-2966.2004.08419.x.

[124] M. Cruz, M. Tucci, E. Martínez-González, and P. Vielva. The non-Gaussian cold spot in WilkinsonMicrowaveAnisotropyProbe: significance, morphology and

foreground contribution. MNRAS, 369:57–67, June 2006. doi: 10.1111/j.1365-2966.2006.10312.x.

[125] B. Czech, M. Kleban, K. Larjo, T. S. Levi, and K. Sigurdson. Polarizing bubble collisions. J. Cosmology Astropart. Phys., 12:023, December 2010. doi: 10.1088/1475-7516/2010/12/023.

[126] S. M. Feeney, M. C. Johnson, D. J. Mortlock, and H. V. Peiris. First Observational Tests of Eternal Inflation. *Physical Review Letters*, 107(7):071301, August 2011. doi: 10.1103/PhysRevLett.107.071301.

[127] J. D. McEwen, S. M. Feeney, M. C. Johnson, and H. V. Peiris. Optimal filters for detecting cosmic bubble collisions. Phys. Rev. D, 85(10):103502, May 2012. doi: 10.1103/PhysRevD.85.103502.

[128] M. Cruz, N. Turok, P. Vielva, E. Martínez-González, and M. Hobson. A Cosmic Microwave Background Feature Consistent with a Cosmic Texture. *Science*, 318: 1612–, December 2007. doi: 10.1126/science.1148694.

[129] J. C. Bueno Sánchez. The inflationary origin of the Cold Spot anomaly. *Physics Letters B*, 739:269–278, December 2014. doi: 10.1016/j.physletb.2014.11.001.

[130] K. Tomita. Second-order gravitational effects of local inhomogeneities on CMB anisotropies and non-Gaussian signatures. Phys. Rev. D, 72(10):103506, November 2005. doi: 10.1103/PhysRevD.72.103506.

[131] K. T. Inoue and J. Silk. Local Voids as the Origin of Large-Angle Cosmic Microwave Background Anomalies. I. ApJ, 648:23–30, September 2006. doi: 10.1086/505636.

[132] L. Rudnick, S. Brown, and L. R. Williams. Extragalactic Radio Sources and the WMAP Cold Spot. ApJ, 671:40–44, December 2007. doi: 10.1086/522222.

[133] M. Cruz, E. Martínez-González, P. Vielva, J. M. Diego, M. Hobson, and N. Turok. The CMB cold spot: texture, cluster or void? MNRAS, 390:913–919, November 2008. doi: 10.1111/j.1365-2966.2008.13812.x.

[134] M. N. Bremer, J. Silk, L. J. M. Davies, and M. D. Lehnert. A redshift survey towards the cosmic microwave background cold spot. MNRAS, 404:L69–L73, May 2010. doi: 10.1111/j.1745-3933.2010.00837.x.

[135] B. R. Granett, I. Szapudi, and M. C. Neyrinck. Galaxy Counts on the Cosmic Microwave Background Cold Spot. ApJ, 714:825–833, May 2010. doi: 10.1088/0004-637X/714/1/825.

[136] I. Szapudi, A. Kovács, B. R. Granett, Z. Frei, J. Silk, W. Burgett, S. Cole, P. W. Draper, D. J. Farrow, N. Kaiser, E. A. Magnier, N. Metcalfe, J. S. Morgan, P. Price, J. Tonry, and R. Wainscoat. Detection of a supervoid aligned with the cold spot of the cosmic microwave background. MNRAS, 450:288–294, June 2015. doi: 10.1093/mnras/stv488.

[137] F. Finelli, J. García-Bellido, A. Kovács, F. Paci, and I. Szapudi. Supervoids in the WISE-2MASS catalogue imprinting cold spots in the cosmic microwave background. MNRAS, 455:1246–1256, January 2016. doi: 10.1093/mnras/stv2388.

[138] BICEP2/Keck and Planck Collaborations, P. A. R. Ade, N. Aghanim, Z. Ahmed, R. W. Aikin, K. D. Alexander, M. Arnaud, J. Aumont, C. Baccigalupi, A. J. Banday, and et al. Joint Analysis of BICEP2/Keck Array and Planck Data. *Physical Review Letters*, 114(10):101301, March 2015. doi: 10.1103/PhysRevLett.114.101301.

[139] BICEP2 and Keck Array Collaborations, P. A. R. Ade, Z. Ahmed, R. W. Aikin, K. D. Alexander, D. Barkats, S. J. Benton, C. A. Bischoff, J. J. Bock, J. A. Brevik, I. Buder, E. Bullock, V. Buza, J. Connors, B. P. Crill, C. D. Dowell, C. Dvorkin, L. Duband, J. P. Filippini, S. Fliescher, S. R. Golwala, M. Halpern, S. Harrison, M. Hasselfield, S. R. Hildebrandt, G. C. Hilton, V. V. Hristov, H. Hui, K. D. Irwin, K. S. Karkare, J. P. Kaufman, B. G. Keating, S. Kefeli, S. A. Kernasovskiy, J. M. Kovac, C. L. Kuo, E. M. Leitch, M. Lueker, P. Mason, K. G. Megerian, C. B. Netterfield, H. T. Nguyen, R. O'Brient, R. W. Ogburn, IV, A. Orlando, C. Pryke, C. D. Reintsema, S. Richter, R. Schwarz, C. D. Sheehy, Z. K. Staniszewski, R. V. Sudiwala, G. P. Teply, K. L. Thompson, J. E. Tolan, A. D. Turner, A. G. Vieregg, A. C. Weber, J. Willmert, C. L. Wong, and K. W. Yoon. BICEP2/Keck Array V: Measurements of B-mode Polarization at Degree Angular Scales and 150 GHz by the Keck Array. ApJ, 811:126, October 2015. doi: 10.1088/0004-637X/811/2/126.

[140] J. M. Bardeen, J. R. Bond, N. Kaiser, and A. S. Szalay. The statistics of peaks of Gaussian random fields. ApJ, 304:15–61, May 1986. doi: 10.1086/164143.

[141] V. Desjacques. Local bias approach to the clustering of discrete density peaks. Phys. Rev. D, 87(4):043505, February 2013. doi: 10.1103/PhysRevD.87.043505.

[142] V. Desjacques. Baryon acoustic signature in the clustering of density maxima. Phys. Rev. D, 78(10):103503, November 2008. doi: 10.1103/PhysRevD.78.103503.

[143] J. R. Bond and G. Efstathiou. The statistics of cosmic background radiation fluctuations. MNRAS, 226:655–687, June 1987.

[144] R. B. Barreiro, J. L. Sanz, E. Martínez-González, L. Cayón, and J. Silk. Peaks in the Cosmic Microwave Background: Flat versus Open Models. ApJ, 478:1–6, March 1997.

[145] E. Komatsu, K. M. Smith, J. Dunkley, C. L. Bennett, B. Gold, G. Hinshaw, N. Jarosik, D. Larson, M. R. Nolta, L. Page, D. N. Spergel, M. Halpern, R. S. Hill, A. Kogut, M. Limon, S. S. Meyer, N. Odegard, G. S. Tucker, J. L. Weiland, E. Wollack, and E. L. Wright. Seven-year Wilkinson Microwave Anisotropy Probe (WMAP) Observations: Cosmological Interpretation. ApJS, 192:18, February 2011. doi: 10.1088/0067-0049/192/2/18.

[146] C. R. Contaldi. Imaging parity-violation in the CMB. *ArXiv e-prints*, October 2015.

[147] M. Galaverni, G. Gubitosi, F. Paci, and F. Finelli. Cosmological birefringence constraints from CMB and astrophysical polarization data. J. Cosmology Astropart. Phys., 8:031, August 2015. doi: 10.1088/1475-7516/2015/08/031.

[148] M. Kamionkowski, A. Kosowsky, and A. Stebbins. Statistics of cosmic microwave background polarization. Phys. Rev. D, 55:7368–7388, June 1997. doi: 10.1103/PhysRevD.55.7368.

[149] A. Stebbins. Weak Lensing On the Celestial Sphere. *ArXiv Astrophysics e-prints*, September 1996.

[150] D. Coulson, R. G. Crittenden, and N. G. Turok. Polarization and anisotropy of the microwave sky. *Physical Review Letters*, 73:2390–2393, October 1994. doi: 10.1103/PhysRevLett.73.2390.

[151] M. Zaldarriaga and U. Seljak. Reconstructing projected matter density power spectrum from cosmic microwave background. Phys. Rev. D, 59(12):123507, June 1999. doi: 10.1103/PhysRevD.59.123507.

[152] B. Rathaus and E. D. Kovetz. The CMB derivatives of Planck's beam asymmetry. MNRAS, 443:750–754, September 2014. doi: 10.1093/mnras/stu1214.

[153] A. Marcos-Caballero, E. Martínez-González, and P. Vielva. Local properties of the large-scale peaks of the CMB temperature (submitted to JCAP).

[154] Y. Wiaux, L. Jacques, and P. Vandergheynst. Correspondence Principle between Spherical and Euclidean Wavelets. ApJ, 632:15–28, October 2005. doi: 10.1086/432926.

[155] P. Vielva, Y. Wiaux, E. Martínez-González, and P. Vandergheynst. Steerable wavelet analysis of CMB structures alignment. New A Rev., 50:880–888, December 2006. doi: 10.1016/j.newar.2006.09.007.

[156] J. D. McEwen, B. Leistedt, M. Büttner, H. V. Peiris, and Y. Wiaux. Directional spin wavelets on the sphere. *ArXiv e-prints*, September 2015.

[157] A. Marcos-Caballero, R. Fernández-Cobos, E. Martínez-González, and P. Vielva. The shape of CMB temperature and polarization peaks on the sphere. J. Cosmology Astropart. Phys., 4:058, April 2016. doi: 10.1088/1475-7516/2016/04/058.

[158] Planck Collaboration, R. Adam, P. A. R. Ade, N. Aghanim, M. Arnaud, M. Ashdown, J. Aumont, C. Baccigalupi, A. J. Banday, R. B. Barreiro, and et al. Planck 2015 results. IX. Diffuse component separation: CMB maps. A&A, 594:A9, August 2016. doi: 10.1051/0004-6361/201525936.

[159] K. M. Górski, E. Hivon, A. J. Banday, B. D. Wandelt, F. K. Hansen, M. Reinecke, and M. Bartelmann. HEALPix: A Framework for High-Resolution Discretization and Fast Analysis of Data Distributed on the Sphere. ApJ, 622: 759–771, April 2005. doi: 10.1086/427976.

[160] A. Gruppuso, P. Natoli, F. Paci, F. Finelli, D. Molinari, A. De Rosa, and N. Mandolesi. Low variance at large scales of WMAP 9 year data. J. Cosmology Astropart. Phys., 7:047, July 2013. doi: 10.1088/1475-7516/2013/07/047.

[161] Y. Wiaux, P. Vielva, E. Martínez-González, and P. Vandergheynst. Global Universe Anisotropy Probed by the Alignment of Structures in the Cosmic Microwave Background. *Physical Review Letters*, 96(15):151303, April 2006. doi: 10.1103/PhysRevLett.96.151303.

[162] C. J. Copi, D. Huterer, D. J. Schwarz, and G. D. Starkman. On the large-angle anomalies of the microwave sky. MNRAS, 367:79–102, March 2006. doi: 10.1111/j.1365-2966.2005.09980.x.

[163] C. L. Bennett, R. S. Hill, G. Hinshaw, D. Larson, K. M. Smith, J. Dunkley, B. Gold, M. Halpern, N. Jarosik, A. Kogut, E. Komatsu, M. Limon, S. S. Meyer, M. R. Nolta, N. Odegard, L. Page, D. N. Spergel, G. S. Tucker, J. L. Weiland, E. Wollack, and E. L. Wright. Seven-year Wilkinson Microwave Anisotropy Probe (WMAP) Observations: Are There Cosmic Microwave Background Anomalies? ApJS, 192:17, February 2011. doi: 10.1088/0067-0049/192/2/17.

[164] A. Marcos-Caballero, E. Martínez-González, and P. Vielva. Multiscale analysis of the CMB temperature derivatives. J. Cosmology Astropart. Phys., 2:026, February 2017. doi: 10.1088/1475-7516/2017/02/026.

[165] A. R. DiDonato. Recurrence relations for the indefinite integrals of the associated legendre functions. *Mathematics of Computation*, 38(158):547–551, 1982. ISSN 00255718, 10886842.

[166] A. Kovács, I. Szapudi, and Z. Frei. Phase statistics of the WMAP 7 year data. *Astronomische Nachrichten*, 334:1020, November 2013. doi: 10.1002/asna.201211985.

[167] A. Stannard and P. Coles. Random-walk statistics and the spherical harmonic representation of cosmic microwave background maps. MNRAS, 364:929–933, December 2005. doi: 10.1111/j.1365-2966.2005.09627.x.

[168] J. R. Gott, W. N. Colley, C.-G. Park, C. Park, and C. Mugnolo. Genus topology of the cosmic microwave background from the WMAP 3-year data. MNRAS, 377:1668–1678, June 2007. doi: 10.1111/j.1365-2966.2007.11730.x.

[169] K.V. Mardia and P.E. Jupp. *Directional Statistics*. Wiley Series in Probability and Statistics. Wiley, 2009. ISBN 9780470317815.

[170] J. P. Zibin. Comment on "A Supervoid Imprinting the Cold Spot in the Cosmic Microwave Background". *ArXiv e-prints*, August 2014.

[171] S. Nadathur, M. Lavinto, S. Hotchkiss, and S. Räsänen. Can a supervoid explain the cold spot? Phys. Rev. D, 90(10):103510, November 2014. doi: 10.1103/PhysRevD.90.103510.

[172] Y.-C. Cai, S. Cole, A. Jenkins, and C. S. Frenk. Full-sky map of the ISW and Rees-Sciama effect from Gpc simulations. MNRAS, 407:201–224, September 2010. doi: 10.1111/j.1365-2966.2010.16946.x.

[173] V. Icke. Voids and filaments. MNRAS, 206:1P–3P, January 1984.

[174] J. M. Bardeen, J. R. Bond, N. Kaiser, and A. S. Szalay. The statistics of peaks of Gaussian random fields. ApJ, 304:15–61, May 1986. doi: 10.1086/164143.

[175] J. J. Condon, W. D. Cotton, E. W. Greisen, Q. F. Yin, R. A. Perley, G. B. Taylor, and J. J. Broderick. The NRAO VLA Sky Survey. AJ, 115:1693–1716, May 1998. doi: 10.1086/300337.

[176] P. N. Best, J. N. Arts, H. J. A. Röttgering, R. Rengelink, M. H. Brookes, and J. Wall. CENSORS: A Combined EIS-NVSS Survey Of Radio Sources - I.

Sample definition, radio data and optical identifications. MNRAS, 346:627–683, December 2003. doi: 10.1046/j.1365-2966.2003.07125.x.

[177] M. H. Brookes, P. N. Best, J. A. Peacock, H. J. A. Röttgering, and J. S. Dunlop. A Combined EIS-NVSS Survey Of Radio Sources (CENSORS) - III. Spectroscopic observations. MNRAS, 385:1297–1326, April 2008. doi: 10.1111/j.1365-2966.2008.12786.x.

[178] P. Vielva, E. Martínez-González, and M. Tucci. Cross-correlation of the cosmic microwave background and radio galaxies in real, harmonic and wavelet spaces: detection of the integrated Sachs-Wolfe effect and dark energy constraints. MNRAS, 365:891–901, January 2006. doi: 10.1111/j.1365-2966.2005.09764.x.

[179] Planck Collaboration, P. A. R. Ade, N. Aghanim, C. Armitage-Caplan, M. Arnaud, M. Ashdown, F. Atrio-Barandela, J. Aumont, C. Baccigalupi, A. J. Banday, and et al. Planck 2013 results. XIX. The integrated Sachs-Wolfe effect. A&A, 571:A19, November 2014. doi: 10.1051/0004-6361/201321526.

[180] Planck Collaboration, P. A. R. Ade, N. Aghanim, M. Arnaud, M. Ashdown, J. Aumont, C. Baccigalupi, A. J. Banday, R. B. Barreiro, N. Bartolo, and et al. Planck 2015 results. XXI. The integrated Sachs-Wolfe effect. A&A, 594:A21, September 2016. doi: 10.1051/0004-6361/201525831.

[181] V. R. Eke, S. Cole, and C. S. Frenk. Cluster evolution as a diagnostic for Omega. MNRAS, 282, September 1996. doi: 10.1093/mnras/282.1.263.

[182] F. Pace, J.-C. Waizmann, and M. Bartelmann. Spherical collapse model in dark-energy cosmologies. MNRAS, 406:1865–1874, August 2010. doi: 10.1111/j.1365-2966.2010.16841.x.

[183] W. H. Press and P. Schechter. Formation of Galaxies and Clusters of Galaxies by Self-Similar Gravitational Condensation. ApJ, 187:425–438, February 1974. doi: 10.1086/152650.

[184] R. K. Sheth and G. Tormen. Large-scale bias and the peak background split. MNRAS, 308:119–126, September 1999. doi: 10.1046/j.1365-8711.1999.02692.x.

[185] U. Seljak. Analytic model for galaxy and dark matter clustering. MNRAS, 318: 203–213, October 2000. doi: 10.1046/j.1365-8711.2000.03715.x.

[186] A. A. Berlind and D. H. Weinberg. The Halo Occupation Distribution: Toward an Empirical Determination of the Relation between Galaxies and Mass. ApJ, 575:587–616, August 2002. doi: 10.1086/341469.

[187] A. Lewis, A. Challinor, and A. Lasenby. Efficient Computation of Cosmic Microwave Background Anisotropies in Closed Friedmann-Robertson-Walker Models. ApJ, 538:473–476, August 2000. doi: 10.1086/309179.

[188] S. Boughn and R. Crittenden. A correlation between the cosmic microwave background and large-scale structure in the Universe. Nature, 427:45–47, January 2004. doi: 10.1038/nature02139.

[189] D. Pietrobon, A. Balbi, and D. Marinucci. Integrated Sachs-Wolfe effect from the cross correlation of WMAP 3year and the NRAO VLA sky survey data: New results and constraints on dark energy. Phys. Rev. D, 74(4):043524, August 2006. doi: 10.1103/PhysRevD.74.043524.

[190] J. D. McEwen, P. Vielva, M. P. Hobson, E. Martínez-González, and A. N. Lasenby. Detection of the integrated Sachs-Wolfe effect and corresponding dark energy constraints made with directional spherical wavelets. MNRAS, 376: 1211–1226, April 2007. doi: 10.1111/j.1365-2966.2007.11505.x.

[191] F. Schiavon, F. Finelli, A. Gruppuso, A. Marcos-Caballero, P. Vielva, R. G. Crittenden, R. B. Barreiro, and E. Martínez-González. An optimal estimator for the CMB-LSS angular power spectrum and its application to WMAP and NVSS data. MNRAS, 427:3044–3054, December 2012. doi: 10.1111/j.1365-2966.2012.21974.x.

[192] T. Giannantonio, R. Crittenden, R. Nichol, and A. J. Ross. The significance of the integrated Sachs-Wolfe effect revisited. MNRAS, 426:2581–2599, November 2012. doi: 10.1111/j.1365-2966.2012.21896.x.

[193] R. B. Barreiro, P. Vielva, A. Marcos-Caballero, and E. Martínez-González. Integrated Sachs-Wolfe effect map recovery from NVSS and WMAP 7-yr data. MNRAS, 430:259–263, March 2013. doi: 10.1093/mnras/sts600.

[194] C. Blake and J. Wall. Measurement of the angular correlation function of radio galaxies from the NRAO VLA Sky Survey. MNRAS, 329:L37–L41, January 2002. doi: 10.1046/j.1365-8711.2002.05163.x.

[195] C. Hernández-Monteagudo. Revisiting the WMAP-NVSS angular cross correlation. A skeptic's view. A&A, 520:A101, September 2010. doi: 10.1051/0004-6361/200913344.

[196] L. Bonavera, R. B. Barreiro, A. Marcos-Caballero, and P. Vielva. On the recovery of ISW fluctuations using large-scale structure tracers and CMB temperature and polarization anisotropies. MNRAS, 459:657–672, June 2016. doi: 10.1093/mnras/stw415.

[197] J. S. Dunlop and J. A. Peacock. The Redshift Cut-Off in the Luminosity Function of Radio Galaxies and Quasars. MNRAS, 247:19, November 1990.

[198] S. Ho, C. Hirata, N. Padmanabhan, U. Seljak, and N. Bahcall. Correlation of CMB with large-scale structure. I. Integrated Sachs-Wolfe tomography and cosmological implications. Phys. Rev. D, 78(4):043519, August 2008. doi: 10.1103/PhysRevD.78.043519.

[199] G. de Zotti, M. Massardi, M. Negrello, and J. Wall. Radio and millimeter continuum surveys and their astrophysical implications. A&A Rev., 18:1–65, February 2010. doi: 10.1007/s00159-009-0026-0.

[200] E. Hivon, K. M. Górski, C. B. Netterfield, B. P. Crill, S. Prunet, and F. Hansen. MASTER of the Cosmic Microwave Background Anisotropy Power Spectrum: A Fast Method for Statistical Analysis of Large and Complex Cosmic Microwave Background Data Sets. ApJ, 567:2–17, March 2002. doi: 10.1086/338126.

[201] G. Hinshaw, D. N. Spergel, L. Verde, R. S. Hill, S. S. Meyer, C. Barnes, C. L. Bennett, M. Halpern, N. Jarosik, A. Kogut, E. Komatsu, M. Limon, L. Page, G. S. Tucker, J. L. Weiland, E. Wollack, and E. L. Wright. First-Year Wilkinson Microwave Anisotropy Probe (WMAP) Observations: The Angular Power Spectrum. ApJS, 148:135–159, September 2003. doi: 10.1086/377225.

[202] J.-Q. Xia, C. Baccigalupi, S. Matarrese, L. Verde, and M. Viel. Constraints on primordial non-Gaussianity from large scale structure probes. J. Cosmology Astropart. Phys., 8:033, August 2011. doi: 10.1088/1475-7516/2011/08/033.

[203] Planck Collaboration, P. A. R. Ade, N. Aghanim, M. Arnaud, M. Ashdown, J. Aumont, C. Baccigalupi, A. J. Banday, R. B. Barreiro, J. G. Bartlett, and et al. Planck 2015 results. XV. Gravitational lensing. A&A, 594:A15, September 2016. doi: 10.1051/0004-6361/201525941.

[204] J-P. Antoine and P. Vandergheynst. Wavelets on the 2-sphere: A group-theoretical approach. *Appl. Comput. Harmon. Anal.*, 7:262–291, 1999. doi: 10.1006/acha.1999.0272.